On self-consistent determination of the quasi-average in statistical physics

Yu. M. Poluektov

National Science Center ''Kharkov Physicotechnical Institute,'' 310108 Kharkov, Ukraine*

The concept of quasi-average introduced by N. N. Bogoliubov for describing the states of many-particle systems with spontaneously broken symmetry (superfluid liquids, superconductors, crystals, etc.) is generalized so that the fields introduced into the initial Hamiltonian for breaking its symmetry are not presumed to be given from outside, but are determined by the properties of the physical object itself and can be found by solving the system of equations in the self-consistent field approximation. © *1997 American Institute of Physics.* [S1063-777X(97)00109-6]

1. INTRODUCTION

The concept of quasi-average was introduced by Bogoliubov[1,2] from an analysis of many-particle systems with a degenerate statistical equilibrium state. Such a state is inherent in various physical objects such as liquid helium in the superfluid phase, metals in the superconducting state, magnets in the ferromagnetic state, crystals and many other systems consisting of a large number of interacting particles. The states that can be described only by introducing the concept of quasi-average are characterized by observables which cannot be calculated on the basis of conventional averaging since the corresponding mean values vanish in view of the symmetry properties of the Hamiltonian. In order of obtain nonzero values of observables, Bogoliubov proposed that the initial Hamiltonian should be supplemented with a Hamiltonian (with a small coefficient ν) containing external fields breaking the symmetry responsible for zero mean values. Subsequent averaging should be carried out with the new Hamiltonian, going over to the limit $\nu \to 0$ after the thermodynamic limiting transition $V \to \infty$ (V is the volume of the system). The mean values obtained in this way are called quasi-average values and can differ from zero in a certain range of thermodynamic parameters. The states with nonzero quasi-averages are known as states with spontaneously broken symmetry.

The concept of quasi-average introduced by Bogoliubov is useful for studying phase transitions accompanied by a change in the symmetry of the static equilibrium state. However, a number of important interconnected factors are not touched upon when the concept of quasi-average is used in its present form. For example, the fact that the symmetry of the phase into which the system goes over from the symmetric state must be known beforehand is not quite convenient. The type of spontaneously broken symmetry cannot be determined by using the concept of quasi-average alone. It would be helpful if the concept of quasi-average included a method providing (at least in principle) information on the states with spontaneously broken symmetry, that are possible for given values of thermodynamic parameters. This would permit the construction of the phase diagram of a system

consisting of many interacting particles on the basis of the microscopic approach. This problem cannot be solved by assuming that the fields breaking the symmetry are given externally. The inclusion of auxiliary fields can violate any symmetry of the system arbitrarily, but not all of the possible combinations are admissible. It would be more natural if the type of symmetry breaking were determined (as is usually the case) not by external fields defined in a certain way or by additional boundary condition selecting the required symmetry in some other way, but by the many-particle system itself and the symmetry of interactions between particles. Naturally, the symmetry of the state of a system in real external fields is also determined by the symmetry of these fields.

For these reasons, it is natural to supplement the concept of quasi-average so that it would be possible to find all admissible phases with spontaneously broken symmetry for given thermodynamic parameters, which permits the construction of the phase diagram of the system. It will be proved here that this can be done by assuming that the symmetry-breaking fields must be determined self-consistently as a result of solution of equations describing the many-particle system in a certain approximation. The requirement of simplicity imposed on the Hamiltonian and the assumption that it should not contain terms whose order in field operators is higher than second virtually necessitate the self-consistent field approximation for determining the type and symmetry of this Hamiltonian. This specifies an exact algorithm for constructing a correction to the initial Hamiltonian that would break any of its symmetries in all admissible ways.

Since the symmetry of states of a many-particle system is determined by its type (in particular, the statistics of the particles) and by the symmetry of interactions between particles as well as by the interaction with external fields (but not by the intensity of interaction between particles), we have every reason to believe that all possible states of the system with spontaneously broken symmetry can be obtained even in the self-consistent field approximation. Additional inclusion of correlation interactions that are not contained in the mean field approximation changes the parameters of the

system, but does not lead to the formation of phases with a new symmetry.

In Sec. 2 of this paper, it is shown how selection rules for ordinary average values follow from the symmetry conditions for the Hamiltonian. The existence of such rules does not permit the employment of ordinary average values for describing states with spontaneously broken symmetry and necessitates the introduction of quasi-average values. In order to define quasi-average self-consistently, we introduce in Sec. 3 an auxiliary Hamiltonian of general form containing fields that determine the symmetry broken by the given Hamiltonian. The equations for these fields are obtained in the self-consistent field approximation. The problem of constructing the phase diagram for a many-particle system on the basis of the microscopic approach is considered briefly.

2. SYMMETRY OF HAMILTONIAN AND SELECTION RULES

We shall consider many-particle systems defined by the Hamiltonian

$$H = \int dq\, dq'\, \psi^+(q) H(q,q') \psi(q')$$
$$+ \frac{1}{2} \int dq\, dq'\, \psi^+(q)\psi^+(q') U(x,x')\psi(q')\psi(q),$$
$$(1)$$

where

$$H(q,q') = H_0(q,q') - \mu\,\delta(q-q'),$$
$$(2)$$
$$H_0(q,q') = -\frac{\hbar^2}{2m}\nabla^2_{x'}\delta(q-q') + U_0(x)\,\delta(q-q').$$

In formula (1), $\psi^+(q)$ and $\psi(q)$ are the operators of creation and annihilation of a particle with coordinates q, and $U(x,x')$ is the potential of many-particle interaction, which does not depend on spin variables. It should be noted that H contains the term with the chemical potential μ. In the one-particle Hamiltonian (2), m is the mass of the particle and $U_0(x)$ the external potential (for electrons in a solid, this can be the periodic potential of the lattice). Hamiltonian (1) describes both the Fermi and Bose particles, the field operators obeying the anticommutation and commutation relations, respectively. For Fermi particles, $q=(x,\sigma)$, where $x=\{r\}$ is the spatial coordinate, σ the spin component, and the integration symbol indicates integration with respect to spatial coordinates and summation over a discrete variable; in addition, $\delta(q-q') = \delta(x-x')\delta_{\sigma\sigma'}$. In the case of Bose particles, $q=x$.

Let us consider unitary transformations of field operators:

$$\psi \rightarrow T_\lambda \psi T_\lambda^+ ,$$
$$(3)$$

where $\lambda=(\lambda_1,\ldots,\lambda_p)$ is a set of continuous or discrete parameters. We assume that the new operators can be expressed linearly in terms of the old operators:

$$T_\lambda \psi(q) T_\lambda^+ = \int dq'\, T_\lambda(q,q')\psi(q'),$$
$$(4)$$

and

$$\int dq''\, T_\lambda(q,q'') T_\lambda^*(q',q'') = \delta(q-q'). \quad (5)$$

in view of the unitary property of the transformation. If the conditions

$$\int dq\, dq'\, H(q,q') T_\lambda^*(q,q_1) T_\lambda(q',q_2) = H(q_1,q_2), \quad (6)$$

$$\int dq\, dq'\, U(x,x') T_\lambda^*(q,q_1) T_\lambda^*(q',q_2) T_\lambda(q',q_3) T_\lambda(q,q_4)$$
$$= U(x_1,x_2)\,\delta(q_2-q_3)\,\delta(q_1-q_4), \quad (7)$$

are satisfied for the one-particle Hamiltonian (2) and for the particle interaction potential, the Hamiltonian (1) is invariant to unitary transformations T_λ:

$$T_\lambda H T_\lambda^+ = H. \quad (8)$$

The sequence of all the transformations for which conditions (6)–(8) are satisfied form the symmetry group of the Hamiltonian (1). The observed characteristics of the system can be calculated by averaging Hermitian operators expressed in terms of field operators with the statistical operator

$$\rho = e^{\beta(\Omega-H)}, \quad (9)$$

where $\beta=1/T$ is the reciprocal temperature and Ω the thermodynamic potential determined by the normalization condition $\mathrm{Tr}\,\rho=1$.

In order to consider the averages of the products of field operators, we introduce the new notation for these operators:

$$\xi_\alpha(q) = \begin{cases} \psi(q), & \alpha=1, \\ \psi^+(q), & \alpha=2. \end{cases} \quad (10)$$

In this notation, relation (4) can be presented in the form

$$T_\lambda \xi_\alpha(q) T_\lambda^+ = \int dq'\, T_\lambda^{(\alpha)}(q,q')\xi_\alpha(q'), \quad (11)$$

where

$$T_\alpha^{(1)}(q,q') = T_\lambda^{(2)*}(q,q') = T_\lambda(q,q').$$

Taking into account the symmetry of operator (8), we can write the average of the product of n field operators in the form

$$\langle \xi_{\alpha_1}(q_1)\ldots\xi_{\alpha_n}(q_n)\rangle = \mathrm{Tr}[e^{\beta(\Omega-H)}\xi_{\alpha_1}(q_1)\ldots\xi_{\alpha_n}(q_n)]$$
$$= \mathrm{Tr}[T_\lambda e^{\beta(\Omega-H)} T_\lambda^+ \xi_{\alpha_1}(q_1)\ldots\xi_{\alpha_n}(q_n)]$$
$$= \mathrm{Tr}[e^{\beta(\Omega-H)} T_\lambda^+ \xi_{\alpha_1}(q_1)\ldots\xi_{\alpha_n}(q_n) T_\lambda]$$
$$= \int dq_1'\ldots dq_n' T_\lambda^{(\alpha_1)*}(q_1',q_1)\ldots$$
$$\times T_\lambda^{*(\alpha_n)}(q_n',q_n)\langle\xi_{\alpha_1}(q_1')\ldots\xi_{\alpha_n}(q_n')\rangle.$$

Thus, the invariance of the Hamiltonian leads to the following selection rules for average values:

$$\int dq_1'\ldots dq_n'\{\delta(q_1-q_1')\ldots\delta(q_n-q_n')$$

$$-T_\lambda^{(\alpha_1)^*}(q_1',q_1)\ldots T_\lambda^{*(\alpha_n)}(q_n',q_n)\}$$
$$\times\langle\xi_{\alpha_1}(q_1')\ldots\xi_{\alpha_n}(q_n')\rangle=0. \tag{12}$$

Green's functions are linear forms of average values, and hence the same selection rules are also valid for them.

The state of the system in which only the observables that can be expressed in terms of average values allowed by the selection rules (12) differ from zero is known as the high-symmetry (or simply symmetric) state.

Let us consider transformations (4) that depend on continuous parameters λ chosen so that

$$T_{\lambda=0}(q,q')=\delta(q-q').$$

In the vicinity of $\lambda=0$, we have the expansion

$$T_\lambda(q,q')=\delta(q-q')+i\sum_{a=1}^{p}\delta\lambda_a G_a(q,q'),$$

where the generators of the transformation satisfy the condition

$$G_a(q,q')=G_a^*(q',q) \tag{13}$$

in view of (5).

Continuous linear symmetry transformations can be put in correspondence to Hermitian operators in the representation of second quantization:

$$G_a=\int dq\,dq'\,\psi^+(q)G_a(q,q')\psi(q'). \tag{14}$$

These operators are integrals of motion for transformations that leave Hamiltonian (1) invariant.[3]

In zero external fields and for the interaction potential depending on the magnitude of the difference in coordinates, Hamiltonian (1) is invariant to translations over an arbitrary vector, to rotations in the coordinate space and independently in the spin space through arbitrary angles, and to phase transformations.

Selection rules for average values also appear in the case when the Hamiltonian is invariant to transformations characterized by a discrete set of parameters λ in (2) Let us suppose, for example, that the Hamiltonian (1) is invariant to translations over the crystal lattice vectors

$$\mathbf{t}=\sum_j n_j\mathbf{t}_j,$$

in the presence of a periodic field $U_0(x)$, where $\mathbf{t}_j$ are basic vectors of the lattice, and n_j are integers, $j=1,2,3$. In this case, we obtain from (12) the condition of invariance of average values relative to translations over vectors $\mathbf{t}$. However, the law of conservation of a certain quantity does not operate here as in the case of continuous transformations. It can be seen from the above analysis that Gibbs' statistical mechanics based on the distribution (9) describes only the high-symmetry state and fails to describe the states with spontaneously broken symmetry, and hence phase transitions between states with different symmetries.

3. SELF-CONSISTENT DEFINITION OF QUASI-AVERAGE

Bogoliubov[1,2] proposed that, in order to describe the states of many-particle systems with spontaneously broken symmetry, the average values should be calculated by breaking preliminarily the symmetry of the initial Hamiltonian (1) with the help of an additional Hamiltonian. This approach can be used if we know beforehand the symmetry that must be broken and the way in which it should be done. It would be more consistent, however, if the concept of quasi-average permitted to establish the possible form of symmetry breaking for given thermodynamic parameters. In order to implement such a program following Bogoliubov's approach, we supplement Hamiltonian (1) with a certain additional Hamiltonian without specifying beforehand the symmetry of the initial Hamiltonian that must be broken. We assume, for simplicity, that this additional Hamiltonian contains terms of not higher than second order in field operators. In this case, the additional Hamiltonian has the form

$$H'=\int dq[F(q)\psi^+(q)+F^*(q)\psi(q)]$$
$$+\int dq\,dq'\bigg[\psi^+(q)W(q,q')\psi(q')$$
$$+\frac{1}{2}\psi^+(q)\Delta(q,q')\psi^+(q')$$
$$+\frac{1}{2}\psi(q')\Delta^*(q',q)\psi(q)\bigg]. \tag{15}$$

The Hamiltonian H' contains the so far unknown fields $F(q)$, $W(q,q')$, $\Delta(q,q')$ whose form just determines the symmetry broken by this Hamiltonian. The hermiticity of H' leads to the conditions

$$W(q,q')=W^*(q',q), \quad \Delta(q,q')=\mp\Delta(q',q) \tag{16}$$

(the minus sign corresponds to Fermi systems and the plus sign to Bose systems). The terms linear in field operators appear in (15) only for Bose systems, while $F(q)=0$ in the case of Fermi systems. Hamiltonian (15) is invariant to unitary transformations T_λ

$$T_\lambda H'T_\lambda^+=H', \tag{17}$$

if the fields satisfy the following conditions:

$$\int dq'F(q')T_\lambda^*(q',q)=F(q), \tag{18a}$$

$$\int dq''dq'''T_\lambda^*(q'',q)T_\lambda(q''',q')W(q'',q''')=W(q,q'), \tag{18b}$$

$$\int dq''dq'''T_\lambda^*(q'',q)T_\lambda^*(q''',q')\Delta(q'',q''')=\Delta(q,q'). \tag{18c}$$

We introduce the new Hamiltonian

$$H_\nu=H+\nu H' \tag{19}$$

(ν is a small real-valued parameter) and the statistical operator

687   Low Temp. Phys. **23** (9), September 1997

Yu. M. Poluektov   687

$$\rho_\nu = e^{\beta(\Omega_\nu - H_\nu)}, \quad \text{Tr } \rho_\nu = 1. \tag{20}$$

All arguments[1,2] concerning the necessity of introduction of the Hamiltonian H_ν for describing states with spontaneously broken symmetry remain completely applicable in this case also. The quasi-average of the operator a is defined by the formula

$$\langle a \rangle = \lim_{\nu \to 0} \lim_{V \to \infty} \text{Tr}(\rho_\nu a). \tag{21}$$

In addition to Bogoliubov's definition (21), we assume that the fields $F(q)$, $W(q,q')$, $\Delta(q,q')$ in (15) cannot be defined arbitrarily, and their symmetry and values are completely determined by the state of the system itself. If the symmetry of the fields in (19) is such that the Hamiltonian H' is invariant relative to the same transformations as the initial Hamiltonian (1), we are dealing with the situation when the symmetry is not broken spontaneously. In this case, average values can be calculated by using the statistical operator ρ (9). If, however, the symmetry of Hamiltonian H' is lower than that of H, we are dealing with a state with spontaneously broken symmetry, and nonzero quasi-average values are the order parameters of such a state.

The set of all possible states of a many-particle system with different symmetries is determined by the type of the system, the symmetry of potential of interaction between particles, and the symmetry of applied fields (if such fields exist) rather than by the intensity of the interaction between the particles. Consequently, it is natural to assume that the fields $F(q)$, $W(q,q')$, $\Delta(q,q')$, determining the symmetry of the phase can be obtained by using the self-consistent field approximation.

In order to go over to the self-consistent field approximation, we represent the initial Hamiltonian (1) as the sum of two terms:

$$H = H_0 + H_c, \tag{22}$$

where the first term is the Hamiltonian in the self-consistent field approximation,[4]

$$H_0 = \int dq\, dq'\, \psi^+(q) H(q,q') \psi(q') + H' + E_0 \tag{23}$$

(E_0 is a constant), and the second term

$$H_c = \frac{1}{2} \int dq\, dq'\, \psi^+(q) \psi^+(q') U(x,x') \psi(q') \psi(q)$$
$$- H' - E_0. \tag{24}$$

is the Hamiltonian taking into account the correlations of particles that were ignored in the self-consistent field approximation. The method of self-consistent field was generalized to Fermi systems with broken phase invariance by Bogoliubov.[5]

Untill now, all relations were valid both for Fermi and Bose systems. In further analysis, we shall consider only the systems of Fermi particles. In this case, we must put $F(q) = 0$ in H', and then the Hamiltonian H_0, which is quadratic in field operators, can be diagonalized through the Bogoliubov $u-v$ transformation.[4] As a result of diagonaliza-

tion, we arrive at the system of equations for the coefficients of canonical transformation, which have the meaning of one-particle wave functions of quasiparticles[4]:

$$-\frac{\hbar^2}{2m} \nabla_x^2 u_i(q) + [U_0(x) - \mu] u_i(q) - \int dq'\, U(x,x')$$
$$\times [\rho(q,q') u_i(q') - \rho(q',q') u_i(q)$$
$$- \tau(q,q') v_i(q')] = \varepsilon_i u_i(q), \tag{25a}$$

$$-\frac{\hbar^2}{2m} \nabla_x^2 v_i(q) + [U_0(x) - \mu] v_i(q) - \int dq'\, U(x,x')$$
$$\times [\rho^*(q,q') v_i(q') - \rho(q',q') v_i(q)$$
$$- \tau^*(q,q') u_i(q')] = -\varepsilon_i v_i(q). \tag{25b}$$

where the one-particle density matrices are defined as

$$\rho(q,q') = \langle \psi^+(q') \psi(q) \rangle_0$$
$$= \sum_i [u_i(q) u_i^*(q') f_i + v_i^*(q) v_i(q')(1 - f_i)], \tag{26a}$$

$$\tau(q,q') = \langle \psi(q') \psi(q) \rangle_0$$
$$= \sum_i [u_i(q) v_i^*(q') f_i + v_i^*(q) u_i(q')(1 - f_i)], \tag{26b}$$

$f_i \equiv f(\varepsilon_i) = [\exp(\beta \varepsilon_i) + 1]^{-1}$, i being the set of quantum numbers characterizing the state of a quasiparticle and ε_i the quasiparticle energy. The averaging in (26) is carried out with the statistical operator

$$\rho_0 = e^{\beta(\Omega_0 - H_0)}, \tag{27}$$

where the parameter Ω_0 is defined by the condition $\text{Tr } \rho_0 = 1$ and is the thermodynamic potential of the system in the self-consistent field approximation with an appropriate choice of the parameter E_0 in (23). The symmetry of Hamiltonian H_0 coincides with the symmetry of H' so that all the states with spontaneously broken symmetry, which are obtained by using the statistical operator ρ_ν (20), can be obtained by averaging with ρ_0 (27).

The fields appearing in H' are connected with the density matrices (26) through the following relations[4,6]:

$$W(q,q') = -U(x,x') \rho(q,q') + \delta(q - q')$$
$$\times \int dq''\, U(x,x'') \rho(q'',q''), \tag{28a}$$

$$\Delta(q,q') = U(x,x') \tau(q,q'). \tag{28b}$$

One-particle density matrices satisfy the system of equations which can be obtained, taking into account (26) and (27), from the system of self-consistent equations (25)[6]:

$$\int dq'' [H(q,q'') \rho(q'',q') - \rho(q,q'') H(q'',q')$$
$$+ W(q,q'') \rho(q'',q') - \rho(q,q'') W(q'',q')$$

$$-\Delta(q,q'')\tau^*(q'',q')+\tau(q,q'')\Delta^*(q'',q')]=0,$$
$$(29)$$

$$\int dq''[H(q,q'')\tau(q'',q')+\tau(q,q'')H^*(q'',q')$$
$$+W(q,q'')\tau(q'',q')+\tau(q,q'')W^*(q'',q')$$
$$-\Delta(q,q'')\rho^*(q'',q')-\rho(q,q'')\Delta(q'',q')]$$
$$+\Delta(q,q')=0. \qquad (30)$$

Thus, in addition to (20) and (21), the self-consistent definition of quasi-average includes the system of equations (29), (30) which allows us to find the fields breaking the symmetry of the initial Hamiltonian (1) and determining the symmetry of Hamiltonian (19).

Obviously, the system (29), (30) has solutions for which $\rho(q,q')\neq 0$ and $\tau(q,q')=0$ (accordingly, $W(q,q')\neq 0$ and $\Delta(q,q')=0$). For such solutions, the Hamiltonian H_ν is invariant to phase transformations, and the anomalous average values containing different numbers of creation and annihilation operators are equal to zero according to the selection rules (12). These solutions describe normal (nonsuperconducting and nonsuperfluid) systems for which certain symmetries (magnetically ordered, spatially inhomogeneous, and anisotropic states) can be broken depending on the form of $\rho(q,q')$. Another, more general type of solutions of the system (29), (30) with $\rho(q,q')\neq 0$ and $\tau(q,q')\neq 0$ (accordingly, $W(q,q')\neq 0$ and $\Delta(q,q')\neq 0$) describes states with broken phase invariance. Such states are characterized by the presence of anomalous average values with different numbers of creation and annihilation operators. In this case, the system possesses superfluidity (or superconductivity for charged particles). A transition to the superfluid phase can also be accompanied by breaking of other symmetries such as symmetries relative to rotations in the coordinate and/or spin spaces. Thus, superfluid phases with various symmetries can exist as in the case of ^{3}He.[7] Superconducting transitions in crystalline conductors can be accompanied with the breaking of spatial symmetry in the electron distribution in addition to the violation of phase invariance.[8]

It is well known that states with spontaneously broken symmetry are degenerate.[1,2] Let us show how this circumstance is manifested in the case of the self-consistent definition of quasi-average. Let T_{λ_0} be a unitary transformation relative to which the Hamiltonian H (8) is invariant, while H' is not invariant, i.e.,

$$H'_{\lambda_0}=T_{\lambda_0}H'T^+_{\lambda_0}\neq H'. \qquad (31)$$

We define the Hamiltonian

$$H_{\nu\lambda_0}=T_{\lambda_0}H_\nu T^+_{\lambda_0}=H+\nu H'_{\lambda_0}, \qquad (32)$$

which depends on the choice of the parameters λ_0. Using this expression, we can introduce the statistical operator

$$\rho_{\nu\lambda_0}=\exp[\beta(\Omega_{\nu\lambda_0}-H_{\nu\lambda_0})], \qquad (33)$$

which can be applied, as well as (20), for calculating quasi-average values. The values of energy calculated with statistical operators ρ_ν and $\rho_{\nu\lambda_0}$ coincide since

$$\mathrm{Tr}\{\exp[\beta(\Omega_{\nu\lambda_0}-H_{\nu\lambda_0})]H_{\nu\lambda_0}\}$$
$$=\mathrm{Tr}\{\exp[\beta(\Omega_\nu-H_\nu)]H_\nu\},$$

where $\Omega_{\nu\lambda_0}=\Omega_\nu$. Thus, the statistical equilibrium state is degenerate in the parameters λ_0. The Hamiltonian H'_{λ_0} can be obtained from (15) if we carry out the following substitution in H':

$$W(q,q')\to W_{\lambda_0}(q,q')$$
$$=\int dq_1 dq_2 T^*_{\lambda_0}(q_1,q)T_{\lambda_0}(q_2,q')W(q_1,q_2),$$
$$(34a)$$

$$\Delta(q,q')\to\Delta_{\lambda_0}(q,q')$$
$$=\int dq_1 dq_2 T^*_{\lambda_0}(q_1,q)T^*_{\lambda_0}(q_2,q')\Delta(q_1,q_2).$$
$$(34b)$$

The one-particle density matrices $\rho_{\lambda_0}(q,q')$ and $\tau_{\lambda_0}(q,q')$ defined in analogy with (34a) and (34b) are connected with $W_{\lambda_0}(q,q')$ and $\Delta_{\lambda_0}(q,q')$ through relations (28) and satisfy equations (29) and (30). When we use quasi-average values in practice, we must fix the set of parameters λ_0 which corresponds to a certain choice of the quantization axis in the case of degeneracy relative to rotations in the spin or coordinate space, the choice of the reference point in the case of degeneracy relative to translations, and the choice of a certain phase in the case of degeneracy relative to phase transformations.

Let us consider briefly the procedure of constructing the phase diagram for a many- particle system on the basis of the self-consistent determination of quasi-average values. Since we are using a large canonical ensemble, it is natural to choose the chemical potential μ and temperature T as thermodynamic variables. The solutions of self- consistent equations differing in the type of symmetry breaking exist in certain regions of the phase diagram. These regions can coincide or overlap so that a given point on the phase diagram usually corresponds to a large number of phases with different symmetries. From all the phases possible for given μ and T, the phase corresponding to the minimum thermodynamic potential is realized. If the regions of existence of two or more phases with spontaneously broken symmetry overlap, the thermodynamic potential minimum of the first phase can be observed in some part of the overlapping region and that of the second phase can be observed in another part. The curve of phase transition between these phases is determined from the condition of the equality of the thermodynamic potentials of the two phases and is a first-order transition curve since the order parameters of these phases have finite values on this curve.

It should be noted that the phase diagram of the system of particles calculated in the self- consistent field approximation can differ considerably from the actual phase diagram. Although the inclusion of the correlation Hamiltonian (24) does not lead to the formation of phases with a new symmetry, it can modify considerably the form of the phase diagram

since phases unstable in the mean self-consistent field approximation can become stable if we take into account the correlation interaction. This situation was encountered in an analysis of the stability of superfluid phases of ^{3}He. It is well known[7] that the B-phase has the thermodynamic potential minimum in the entire range of superfluidity in liquid ^{3}He according to calculations based on the mean-field approximation, but this contradicts the observations. The inclusion of interactions which were disregarded in the mean-field approximation leads to the stabilization of the A-phase in a certain region of thermodynamic parameters, which is in accord with the experimental results. As mentioned above, a first-order transition takes place at the boundary between the A and B phases.

4. CONCLUSIONS

The self-consistent generalization of the concept of quasi-average proposed here is based on the assumption that the type of symmetry breaking in the statistical equilibrium state of a many-particle system is determined by its intrinsic properties. For this reason, the fields appearing in the additional Hamiltonian must be determined from the solution of the system of equations obtained in the self-consistent field approximation. In fact, the self-consistent determination of quasi-average values is based on the assumption that all possible phases with spontaneously broken symmetry can be obtained even in the self-consistent field approximation, although this approximation is generally insufficient for determining their stability, and hence for constructing the phase diagram. In all probability, this assumption should be re-

garded as an additional consequence of the Gibbs statistical mechanics since the ordinary Gibbs distribution contains no information about the states whose symmetry is lower than the symmetry of the Hamiltonian, and the approach to an analysis of such states is not indicated (see, for example, Sec. 2 of this article). In view of this incompleteness, the standard statistical mechanics is suitable only for studying high-symmetry states and cannot be used for describing states with spontaneously broken symmetry, and hence phase transitions between such states. This circumstance inspired Bogoliubov to seek new approaches for a correct description of systems of many interacting particles with spontaneously broken symmetry on the basis of statistical mechanics, which led to the formulation of the concept of quasi-average.

[*]E-mail: kfti@kfti.kharkov.ua

[1] N. N. Bogoliubov, Physica **26S**, 1 (1960).
[2] N. N. Bogoliubov, in *Statistical Physics and Quantum Field Theory* [in Russian], Nauka, Moscow (1973).
[3] A. I. Akhiezer and S. V. Peletninskii, *Methods of Statistical Physics*, Pergamon, Oxford, 1981.
[4] Yu. M. Poluektov, Fiz. Nizk. Temp. **22**, 402 (1996) [Low Temp. Phys. **22**, 313 (1996)].
[5] N. N. Bogoliubov, Dokl. Akad. Nauk SSSR **119**, 224 (1958) [Sov. Phys. Doklady **3**, 292 (1958)].
[6] Yu. M. Poluektov, Czech. J. Phys. **46**, S2, 955 (1996).
[7] A. J. Leggett, Rev. Mod. Phys. **47**, 331 (1975).
[8] Yu. M. Poluektov, Fiz. Nizk. Temp. **21**, 183 (1995) [Low Temp. Phys. **21**, 138 (1995)].

Translated by R. S. Wadhwa

LOW-TEMPERATURE MAGNETISM

Peculiarities of domain walls with vertical Bloch lines at low temperatures

V. T. Dovgij, A. A. Kalkin, T. G. Astaf'eva, F. G. Bar'yakhtar, and G. I. Yampolskaya

A. Galkin Donetsk Physical and Technical Institute, National Academy of Sciences of the Ukraine, 340114, Donetsk, Ukraine*

The results of experimental studies of the vertical Bloch line (VBL) generation and stability in the epitaxial iron-garnet films (EIGF) with different compounds, anisotropy, implantation, and compensation temperatures are presented. It is shown that the critical fields of the VBL generation and annihilation in the stripe domain (SD) walls increase and that its values differ considerably (the VBL stability region increases) with decreasing temperature. The domain period increases as a result of magnetic inhomogeneities of the domain walls. The magnetic profile and the energy potential barrier account for the existence of the metastable domain structures with different periods. It is established that the VBL existence domains are limited by the region near the Néel temperature T_N and the compensation point temperature T_c (in films with T_c). © *1997 American Institute of Physics.* [S1063-777X(97)00209-0]

1. The static and dynamic properties of the VBL in domain walls have been studied extensively (see, for example, Refs. 1–4). Most of these studies were carried out at room temperature and some of them in the range from room temperature to the Néel temperature. The VBL stability in domain walls at low temperatures has been virtually ignored in all studies.

Our main goal was to investigate the H-T diagrams of generation and stability of the VBL at the SD boundaries and the effect of the easy magnetization axis tilt, orthorhombic anisotropy, compensation point, and the magnetic profile (nonuniformity of the film magnetic properties) on the regions of the VBL stability and generation at low temperatures.

2. The investigation of the VBL creation and stability in the SD boundaries was carried out in the EIGF obtained by the liquid-phase epitaxy on gadolinium-gallium garnet substrata with (111) orientation. The magnetic parameters of the film have been measured by the methods suggested in Refs. 5–7 and are presented in Table 1. The investigations were carried out using magnetooptic devices with the Faraday effect. The creation of straightforward domain walls with the VBL was carried out by spontaneous demagnetization of films at the current pulse in the current loop (two parallel applications with 30 μm diameter, the distance between conductors is 300 μm). The current pulse in the loop with the amplitude is $I_{max}=12$ A, the pulse time is $\tau_p=0.2$–10 μs, and the front slope of the increase and decay pulse up to $\tau_f=50$ ns was created by the pulse magnetic field with amplitude $H_{max}=200$ Oe directed along the easy magnetization axis of the sample and is essential for film saturation. In this way the stripe structure with domains perpendicular to the conductors was created. The wall hardness was defined by the collapse field of the bubble domains obtained by the SD cutting by means of the bias current short pulse.[8] The im-

pulse amplitude was minimally possible in order for the additional VBL not to be generated.

3. The typical H-T diagram of the VBL stability for the $(YSmLuCa)_3(FeGe)_5O_{12}$ film (film 1 in Table 1), which has a small tilt of the magnetization easy axis, and the orthorhombic anisotropy are presented on Fig. 1. Line *1* is the limit of the region of the VBL ''static'' stability (or the line of the VBL annihilation). The shaded region corresponds to the stable VBL existence in the SD boundaries. For determination of this line after spontaneous demagnetization of the film, the SD structure was influenced by the planar quasistatic field H_p, which was perpendicular to magnetization easy axis and parallel to the film plane. The VBL existence was then determined by the dispersing of the bubble domain collapse field. It is shown that the critical field H_{cr} (the VBL annihilation field), above which the hard bubble domain is not created, increases with decreasing temperature. Thus, each temperature has the corresponding value of the planar critical field H_{cr} (when the VBL are not created) and the critical temperature exists when the H_{cr} vanishes. The considerable increase of H_{cr} with decreasing temperature results primarily from the uniaxial anisotropy increase.

Line *2* in Fig. 1 corresponds to the limit of the VBL ''dynamic'' stability (or the VBL creation line). In order to determine this line, the quasistatic planar field H_0 must influence EIGF during its spontaneous demagnetization. After that the VBL presence in the SD boundaries was determined. Line *2* corresponds to the planar field value higher than the spontaneous which takes place without the VBL creation. The touched region corresponds to the stable VBL creation region.

It is shown that the critical planar field of the VBL annihilation in stripe domains is essentially higher than the critical planar field that prevents the VBL creation. The ''static'' region of the VBL stable existence is essentially greater then the ''dynamic'' region. The experimental values

	Compound	h, μm	P_0, μm	$4\pi M$, Gs	H_a, Oe	$A \cdot 10^{-7}$, erg/cm
1	$(YSmLuCa)_3(FeGe)_5O_{12}$	6.8	13.8	183	1840	2.0
2	$(YSmCa)_3(FeGe)_5O_{12}$	6.8	9.9	203	1420	4.0
3	$(YBi)_3(FeGa)_5O_{12}$	6.9	8.5	233	4300	2.7
4	$(YGdTm)_3(FeGa)_5O_{12}$	9.0	18.4	161	1580	2.9

of the static and dynamic critical fields H_{cr} exceed the theoretical value $8M$. Such great difference can be explained by the existence of magnetic profile in the film.[9] The profile causes the existence of the high potential barrier, which prevents the VBL annihilation.

The SD period-vs-temperature curves for various methods of the SD creation and the hysteresis of the SD period dependence from planar field value for the same film acknowledge the existence of the profile and the metastable states. In Fig. 2 line *1* characterizes the temperature dependence of the SD structure period created in the direct-displacement field with the alternating field. Curve *2* corresponds to the SD system created with the EIGF spontaneous demagnetization. Curve *3* corresponds to the SD structure formed by the quasistatic planar field. Line *1* describes the equilibrium structure, because domain structures 2 and 3 were transformed into first one after the influence of the pulse or alternating displacement field. We see that curve *2* is situated above line *1* and their difference increases with the temperature decrease. The equilibrium SD structure arises with the period determined by the dynamic energy of the domain boundaries and the demagnetization fields because the spontaneous demagnetization takes place without the external magnetic field (process develops after the end of current pulse). Thus, we can assume that the SD period increase is conditioned by the domain structure energy increase. The Bloch lines are one of the sources of this increase.

The density of the mean energy of the domain structure with the VBL can be determined by the expression[1]

$$\sigma = \sigma_0[1 + (\pi\Delta_0/s)^2 + (2Q)^{-1}]^{1/2},$$

where K_u is the uniaxial anisotropy constant; $Q = H_A/4\pi M_s$ is the quality factor; $\pi\Delta_0 = \pi(A/K_u)^{1/2}$; $\sigma_0 = 4(AK_u)^{1/2}$ are the thickness and the energy density of the

Bloch-type domain wall, and s is the distance between the VBLs. The VBL density in domain walls on spontaneous demagnetization can be determined by means of a theory which assuming that line *1* corresponds to the domain structure without VBL.

Line *1* in Fig. 3 is the dependence of the VBL density from temperature and line *2* characterizes the temperature dependence of the dispersion of the bubble domain collapse fields. Experiment shows that the domain walls have the high density of the VBL through spontaneous demagnetization. It leads to an increase in the domain structure period. The investigation of domain structures formed by the direct and alternating displacement fields has shown that the domain walls have very low density of Bloch lines (see line *1* in Fig. 2). As can be seen from Fig. 2, the period of the domain structures formed by the quasistatic plane magnetic field is almost independent of temperature. But it is always smaller than the equilibrium domain structure period and this difference increases with decreasing temperature. The decrease of the domain structure period can be explained by the potential barrier between the most equilibrium state of the boundary and other metastable states, as well as by the influence of the plane field. It is known[10] that the energy of domain wall decreases more quickly with increasing field than the demagnetization energy. It leads to a decrease in the domain structure period. The domain structure is frozen in one of the metastable states by a decrease in the plane field. The temperature is lower, the energy barrier is higher, and the difference in the periods from the equilibrium value is greater. The SD period-vs.-plane field dependence is shown in Fig. 4. The direction of the plane field change is indicated by the arrows. The period-vs.-plane field dependence was measured at the
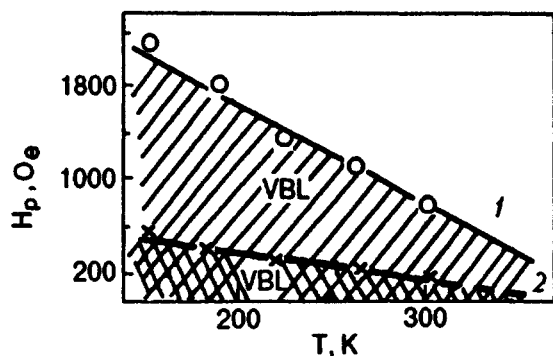

FIG. 1. The ''static'' and ''dynamic'' $H-T$ diagrams of the VBL stability in the SD boundaries (the VBL annihilation and generation $H-T$ diagram).
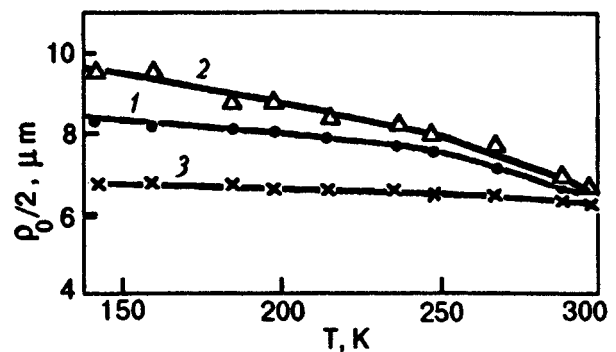

FIG. 2. Temperature dependence of the SD period for different generation methods in EIGF. Lines correspond to: *1*—The method of the displacement field with low-frequency modulation; *2*—spontaneous demagnetization method; *3*—method of the quasi-static plane field.
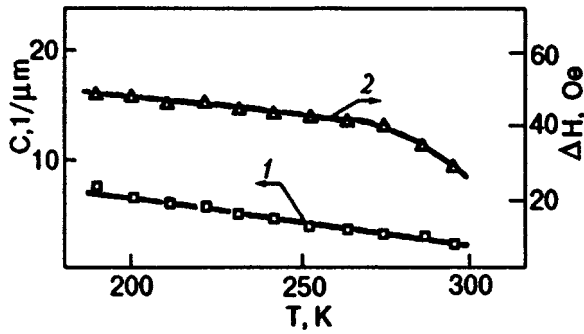
FIG. 3. Temperature dependences of the VBL density and the bubble domain collapse fields.

FIG. 5. Temperature dependence of the SD period for different generation methods in implanting EIGF. Lines *1*, *2*, and *3* are the same as those in Fig. 2.

fixed temperature of 133 K. The upper curve contains the large VBL quantity and corresponds to line *2* in Fig. 2. The lower curve contains the small VBL quantity and corresponds to line *3* in Fig. 2. Thus, the magnetic microprofile and the energy potential barrier account for the existence of the metastable states with different dimensions at the same temperature.

4. The same dependences of the SD period as a function of temperature for different methods of creation was measured in an implanted $(YSmCa)_3(FeGe)_5O_{12}$ film (see Fig. 5). In this film the collapse field dispersion ΔH is not revealed. This fact can be explained in the following way. During spontaneous demagnetization of EIGF the Bloch lines or loops are generating in the SD walls. They change the dynamic energy of the domain walls and increase the SD period. After termination of the film demagnetization the inhomogeneities disappear because they are unstable in the static state and the SD period does not change because of the high potential barrier which prevents the domain generation at low temperatures.

Thus, the Bloch line generation and existence lead to an increase in the domain structure period at low temperatures. The magnetic profile and the energy potential barrier lead to the existence of metastable domain structures with different periods and increase the VBL generation and stability region with decreasing temperature.

5. The influence of the easy-axis tilt and orthorhombic anisotropy is illustrated in Fig. 6 for the (110) orientation $(YBi)_3(FeGa)_5O_{12}$ film as the temperature is lowered. We see
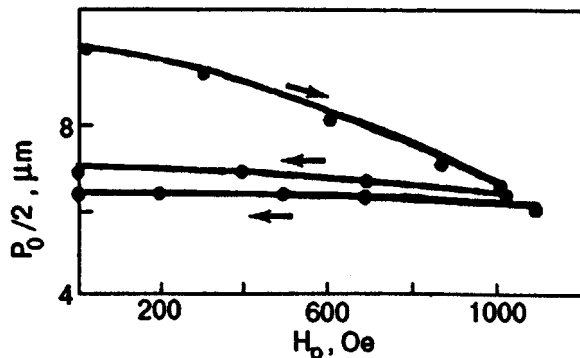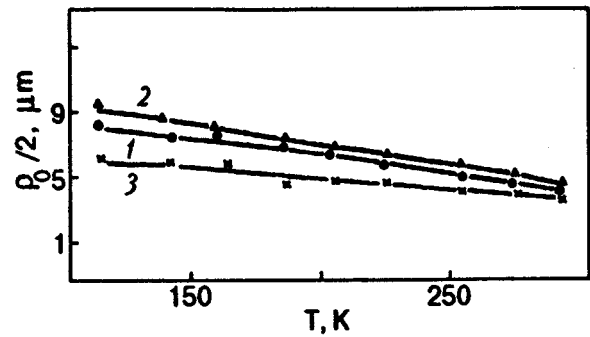
that the critical field of the VBL generation decreases with decreasing temperature, in contrast with the $H-T$ diagrams in Fig. 1 and the dH/dT derivative is different for in-plane film hard axis and easy-axis. Thus, the increase of the easy axis tilt and orthorhombic anisotropy leads to a change in the VBL generation and existence domain as the temperature is lowered.

The presence of the compensation point T_c in the film leads to cutting of the VBL existence domain near the T_c. The VBL generation and existence domain is shown in Fig. 7 for the $(YGdTm)_3(FeGa)_5O_{12}$ film with $T_c = 210$ K. This effect is connected with the magnetization decrease on approaching the compensation temperature and with the decrease in the demagnetizing field by the EIGF spontaneous demagnetization (a small quantity of the VBL is generated). For investigating EIGF with T_c the domain of the VBL stable existence is limited by the Néel temperature T_N and the compensation temperature T_c with some deviation ΔT from these critical points. Usually, ΔT is in the range 20–30 K.

6. Thus, the increase of the plane critical fields of the VBL generation and annihilation in the SD boundaries, as well as the considerable difference in its values takes place at
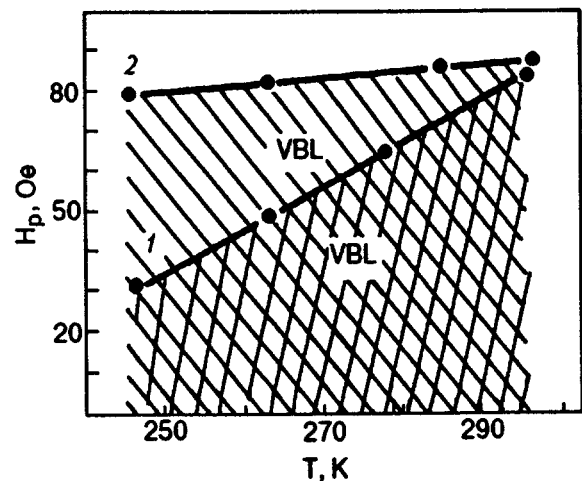

FIG. 4. The hysteresis of dependence of the SD period from the plane field value.

FIG. 6. The $H-T$ diagram of the VBL stability in the SD boundaries of the $(YBi)_3(FeGe)_5O_{12}$ film. Line *1* corresponds to the easy axis; line *2* corresponds to the hard axis.

693   Low Temp. Phys. **23** (9), September 1997
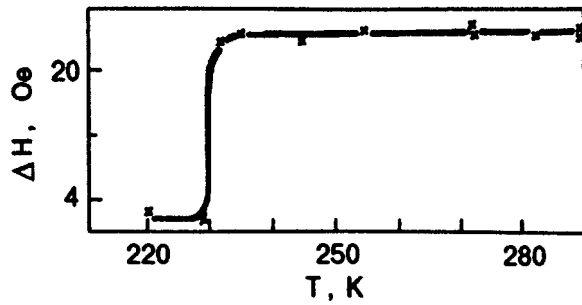
Dovgij *et al.*   693

FIG. 7. Temperature dependence of the bubble domain collapse field dispersion for the EIGF with the compensation point T_c.

low temperatures. The magnetic inhomogeneities in the domain walls cause the domain period to increase. The magnetic profile and the potential barrier existence lead to the existence of the metastable domain structures with different periods. The easy-axis tilt, the orthorhombic anisotropy, and the compensation point existence lead to a decrease of the

VBL generation and stability region in the EIGF.

*E-mail: sergey@gam.dipt.donetsk.ua

[1] A. P. Malosemoff and J. C. Slonczewski, *Magnetic Domain Walls in Bubble Materials*, Mir, Moscow (1982).
[2] A. Eschenfelder, *Magnetic Bubble Technology*, Mir, Moscow (1983).
[3] T. O'Dell, *Ferromagnetodynamics. The Dynamics of Magnetic Bubbles, Domains, and Domain Walls*, Mir, Moscow (1983).
[4] L. S. Uspenskaya and V. K. Vlasko-Vlasov, Zh. Éksp. Teor. Fiz. **101**, 944 (1992).
[5] R. F. Shaw, D. E. Hill, R. M. Sandford, and J. M. Moody, J. Appl. Phys. **44**, 2346 (1973).
[6] W. F. Druyvestein, F. W. Dorleijn, and R. F. Rinierse, J. Appl. Phys. **44**, 2397 (1973).
[7] A. Hubert, A. P. Malozemoff, and J. C. De Luca, J. Appl. Phys. **45**, 3562 (1974).
[8] H. Nishida, T. Kobayashi, and Y. Sugita, IEEE Trans. Magn. **MAG-9**, 517 (1973).
[9] V. T. Dovgij and A. A. Kalkin, Pis'ma Zh. Techn. Fiz. **15**, 89 (1989).
[10] T. R. Johunsen, D. J. Norman, and E. J. Toroh, J. Appl. Phys. **42**, 1715 (1971).

This article was published in English in the original Russian journal. It was edited by S. J. Amoretty.

A new type of spin density waves in quasi-one-dimensional antiferromagnetic metals

T. G. Petrova and A. S. Rozhavskii

B. Verkin Institute for Low Temperature Physics and Engineering, National Academy of Sciences of the Ukraine, 310164 Kharkov, Ukraine*

The model of a quasi-one-dimensional metal having antiferromagnetic order is considered. It is shown that the electron spectrum undergoes dielectrization in the ground state, accompanied by the emergence of a magnetic superstructure, i.e., spin density waves (SDW). In contrast to the triplet SDW observed in paramagnetic metals, the order parameter of SDW in this case is singlet-type. The dependence of the dielectric gap in the one-electron spectrum and the shape of the magnetic spiral on the commensurability parameter in a SDW is obtained. It is shown that, upon a transition to the SDW state, the rearrangement of the system occurs in such a way that its total magnetic moment remains equal to zero. © *1997 American Institute of Physics.* [S1063-777X(97)00309-5]

1. INTRODUCTION

It is well known that a decrease in temperature of quasi-one-dimensional metals leads to second-order phase transition to the insulating phase characterized by a complex order parameter. The magnitude of the order parameter is the gap in the spectrum of one- electron excitations, and the phase fluctuations determine, among other things, the response in the low-frequency range.

The metallic state of quasi-one-dimensional conductors is generally unstable. This instability is caused either by the interaction of conduction electrons with phonons having a momentum $\pm 2k_F$ (Peierls instability), or electron–electron interaction with scattering processes involving a momentum variation by $\pm 2k_F$ [formation of spin density waves (SDW)]. In both cases, the instability of the metal phase results from nesting of plane segments of the Fermi surface upon a translation by the vector $\pm 2k_F$. The Fourier components of the response function with vectors $\pm 2k_F$ diverge logarithmically, thus pointing towards a spontaneous breaking of symmetry and the emergence of a new ground state. In the case of Peierls instability, the polarization operator component diverges and the insulator emerges against the background of a lattice superstructure with a period π/k_F. In the case of SDW instability, the RKKY-exchange component diverges, and dielectrization is accompanied by the formation of a magnetic spiral with the same period (see the reviews in Refs. 1 and 2).

Recent years have been marked by a growing interest towards the analysis of SDW in different materials, particularly in quasi-one-dimensional organic salts with charge transfer, such as $(TMTSF)_2X$ ($X=ClO_4$, PF_6 etc.), $(MDTTF)_2X$ and $(DMET)_2X$ [$X=Au(CN)_2$],[1,2] as well as in a number of HTS cuprates in which one-dimensional HTS chains are formed for certain dopant concentrations.[3]

An interesting feature of quasi-one-dimensional organic metals is that they display nonlinear collective conductivity in the SDW state, caused by topological excitations of the order parameter[2] and by their nontrivial phase diagram in a strong magnetic field.[1,4,5] It is assumed that one-dimensional SDW chains in the cuprate matrix obstruct the superconduct-ing transition. All these circumstances make SDW an extremely interesting object for theoretical investigations which are indeed being carried out quite intensively.[6]

The traditional approach to the SDW problem is based on an analysis of the Hubbard model, using the mean field approach.[1,2,4,5] Such an approach provides a satisfactory description of the SDW formation in a paramagnetic metal. The SDW order parameter in this case is a triplet and is proportional to the mean Fourier component of electron density with momenta $\pm 2k_F$. The lattice site spin of the magnetic spiral is determined by the difference in order parameters with opposite electron spins. However, such a model does not exhaust all possible types of SDW since it does not provide any information about the stability of quasi-one-dimensional metals which already possess a magnetic order.

Earlier, it was shown by us[7] that a decrease in the temperature of a quasi-one- dimensional ferromagnetic metal also leads to transition to the insulating phase accompanied by the formation of a spiral magnetic structure. A new symmetry of the SDW order parameter is formed in this case: the order parameter is a singlet and proportional to $\langle a^+_{k_F\uparrow} a_{-k_F\downarrow}\rangle$ where $a^+_{k\sigma}$ is the creation operator for an electron with momentum k and spin σ.

In this article, we report on the first results of investigation of SDW formed in a one- dimensional antiferromagnetic (AFM) metal. Apart from the purely theoretical interest, this approach is also interesting in view of the experimental data[1,2] according to which a number of organic quasi-one-dimensional metals possess AFM order above the point of transition to the insulating SDW phase. It can also be construed that, in the compounds considered in Ref. 3, one-dimensional SDW are formed in the metallic AFM matrix.

The identical nature of the origin of spin- and charge density waves suggests that the formation of SDW in an AFM metal can be analyzed by using a scheme close to the one used for the Peierls problem, which would trace the nontrivial role of the umklapp processes that is usually masked in the Hubbard model. For this purpose, we shall use the Vonsovskii model[8] in which the electron–magnon interaction is introduced explicitly. It is found that the structure of

the SDW order parameter is reminiscent of the one obtained earlier[7] for a ferromagnetic metal. In other words, the dielectric state of SDW is due to electron umklapp processes involving a spin flip and emission/absorption of magnons with momenta $\pm 2k_F$. The approach followed by us is also advantageous in the sense that it can be used to formulate the field theory model of SDW suitable for subsequent investigation of inhomogeneous, soliton, and polaron states of the order parameter which probably play the major role[6,9] in explaining the experimental results presented in Ref. 3.

The approach described above is used here to study the ground state of a quasi-one- dimensional AFM metal. We shall show that the one-electron spectrum in this state undergoes dielectrization accompanied by the formation of a magnetic superstructure, viz., the SDW. The dependence of the dielectric gap and the shape of the magnetic spiral on the system parameters will be obtained for various commensurabilities. It is found that the rearrangement in the system during a transition to the SDW state occurs in such a way that its total magnetic moment remains equal to zero.

2. CONTINUAL MODEL OF A QUASI-ONE-DIMENSIONAL ANTIFERROMAGNETIC METAL. SDW LAGRANGIANS

In order to construct the theory of an SDW in a quasi-one-dimensional AFM metal at low temperatures, we proceed from the traditional Hamiltonian in the Vonsovskii model[8]:

$$H = -A \sum_{n,\sigma,\sigma'} (\mathbf{s}\cdot\mathbf{S}_n)_{\sigma\sigma'} a_{n\sigma}^+ a_{n\sigma'}' + B\sum_{n,\sigma} (a_{n\sigma}^+ a_{n+1,\sigma}$$

$$+ \text{h.c.}) - I\sum_n (\mathbf{S}_n \cdot \mathbf{S}_{n+1}), \tag{1}$$

where $a_{n\sigma}^+$ and $a_{n\sigma}$ are the operators of creation and annihilation of an electron with spin projection σ at the nth site of the chain, $\mathbf{s}$ and $\mathbf{S}_n$ are the electron and atomic spin operators respectively, $I<0$ is the integral of direct exchange between adjacent spins in the chain, $B<0$ the Bloch transport integral, and A the integral of exchange interaction between the spins of conduction electrons and magnetic atoms.

For $A=0$, the model (1) describes a conventional one-dimensional metal with the electron energy–momentum relation $\omega = -2|B|\cos ak$ (k is the electron momentum and a is the separation between atoms), and a magnetic atom chain that does not interact with electrons and whose ground state is assumed to be of the Néel type. The onset of interaction between the electron and magnetic subsystems results in their mutual rearrangement, which can be studied expediently in the continual model by averaging the microscopic Hamiltonian (1) over rapid oscillations with a period $(k_F n)^{-1}$.[7] A distinguishing feature of this procedure is that characteristic scales much larger than $a \sim k_F^{-1}$ over which components of the order parameter change are formed below a certain temperature $T_{SDW} < T_N$. Hence the system (1) can naturally be defined in terms of large-scale fields at $T < T_{SDW}$.

Following the procedure described by us earlier,[10] we can represent the electron operators in the form

$$a_{n\sigma} = \frac{1}{\sqrt{2}} \{W_\sigma(n) e^{ik_F na} + V_\sigma(n) e^{-ik_F na}\}, \tag{2}$$

where W and V are smooth functions of the coordinate na. The electron energy– momentum relation is linearized in the vicinity of $\pm k_F$, which corresponds to a replacement of the finite differences $W(n+1) - W(n)$, emerging in the second term of Eq. (1) upon a substitution of formulas (2), by the derivatives $\partial W(n)/\partial(an)$. In the following, we shall assume that the atomic chain along which the electrons move is directed along the x-axis, and hence carry out the substitution $an \to x$.

In the averaging of Eq. (1) over rapid oscillations, an important role is played by the condition which is always satisfied for metals and which assumes the following form for the system considered by us:

$$2ak_F = \pi/M_1, \quad (M_1 > 1). \tag{3}$$

This condition differs somewhat from the analogous relations used in the Peierls problem and in the problem of SDW in a one-dimensional ferromagnetic metal,[7,10] since the unit cell of a one-dimensional antiferromagnet contains two magnetic atoms. Formula (3) can be represented in the form

$$2k_F/P_B = 1/M_1. \tag{4}$$

Here $P_B = \pi/a$ is the size of the Brillouin zone of an antiferromagnetic chain. If M_1 is a rational number, i.e., if $M_1 = M/M_2$, where M and M_2 are integers ($M > M_2$), Eq. (4) expresses the condition of commensurability of the SDW phase in analogy with the Peierls phase.[10] An irrational M_1 corresponds to the noncommensurate case which will not be considered here. In the commensurate case, we can consider three possibilities $M=2$, $M=3$ and $M>3$ having Lagrangians of different structures corresponding to them in the continual limit.

Assuming that $S \gg 1$ (S is the spin of a magnetic atom), we present the atomic spin operators in Goldstein–Primakov form, for which we introduce two sublattices c and d corresponding to even sites m and odd sites l in the chain:

$$S_m^z = S - c_m^+ c_m, \quad S_m^+ = \sqrt{2S}c_m, \quad S_m^- = \sqrt{2S}c_m^+,$$

$$S_l^z = -S + d_l^+ d_l, \quad S_l^+ = \sqrt{2S}d_l^+, \quad S_l^- = \sqrt{2S}d_l. \tag{5}$$

Here $S^\pm = S^x \pm iS^y$, while c_m^+, c_m and d_l^+, d_l are magnon operators in each sublattice. In the ground state, the spins at even sites are parallel, and at odd sites, antiparallel, to the z-axis.

The specific nature of the one-dimensional problem enables us to confine the analysis to magnons with momenta $\pm 2k_F$, since such magnons lead to a logarithmic singularity in the effective indirect exchange integral,[8] analogous to the Cohn singularity in a one-dimensional electron–phonon system. This explains the inapplicability of the RKKY theory[11–13] for low-dimensional magnetic metals.

According to the principles of the self-consistent field theory, we introduce the quasimeans of magnon operators, which are order parameters of SDW:

$$\langle c_{2k_F} \rangle = \sqrt{2/N}\Delta e^{-i\varphi}, \quad \langle c_{-2k_F} \rangle = \sqrt{2/N}\rho e^{i\theta},$$

$$\langle d_{2k_F}\rangle=\sqrt{2/N}\Delta'\,e^{-i\varphi'},\quad \langle d_{-2k_F}\rangle=\sqrt{2/N}\rho'\,e^{i\theta'}, \qquad (6)$$

where N is the number of atoms in a chain, while the Fourier components of magnon operators are defined by formulas

$$c_q=\sqrt{2/N}\sum_m e^{iqam}c_m,\quad d_q=\sqrt{2/N}\sum_l e^{-iqal}d_l,$$

$$c_m=\sqrt{2/N}\sum_q e^{-iqam}c_q,\quad d_l=\sqrt{2/N}\sum_q e^{iqal}d_q, \qquad (7)$$

where q is the magnon momentum. It follows from Eq. (1) that formulas (6) and (7) lead to anomalous means of derivatives of electron operators $\langle a^+_{k\sigma}a_{k\pm 2k_F,\sigma}\rangle$, i.e. to the singlet order parameter of SDW. Retaining in Eqs. (7) terms with $q=\pm 2k_F$, we obtain in terms of parameters (6) the expression

$$c_m=\Delta\,\exp(-2ik_F am-i\varphi)+\rho\,\exp(2ik_F am+i\theta),$$

$$d_l=\Delta'\,\exp(2ik_F al-i\varphi')+\rho'\,\exp(-2ik_F al+i\theta').$$

For $m=2g$ and $l=2g+1$, it leads to the following expressions for the lattice site spin components

$$S^z_{2g}=S-\Delta^2-\rho^2-2\Delta\rho\,\cos(8k_F ag+\varphi+\theta),$$

$$S^x_{2g}=\sqrt{2S}[\Delta\,\cos(4k_F ag+\varphi)+\rho\,\cos(4k_F ag+\theta)],$$

$$S^y_{2g}=-\sqrt{2S}[\Delta\,\sin(4k_F ag+\varphi)-\rho\,\sin(4k_F ag+\theta)],$$

$$S^z_{2g+1}=-S+\Delta'^2+\rho'^2+2\Delta'\rho'\,\cos[4ak_F(2g+1)$$
$$-\varphi'-\theta'], \qquad (8)$$

$$S^x_{2g+1}=\sqrt{2S}\{\Delta'\,\cos[2ak_F(2g+1)-\varphi']$$
$$+\rho'\,\cos[2ak_F(2g+1)-\theta']\},$$

$$S^y_{2g+1}=-\sqrt{2S}\{\Delta'\,\sin[2ak_F(2g+1)-\varphi']$$
$$-\rho'\,\sin[2ak_F(2g+1)-\theta']\}.$$

As a result of the above transformations, the Hamiltonian (1) in the continual limit has Lagrangians that can be represented in the following form for various commensurabilities ($\hbar=1$):

$$L_{M=2}=\bar\psi\{i\tau_x\partial_t+(v_F\partial_x-i\gamma)\tau_y+A\sqrt{S/2}$$
$$\times[\Delta\,\exp(-i\tau_z\varphi)+\Delta'\,\exp(i\tau_z\varphi')]\}\psi$$
$$+\chi\{i\tau_x\partial_t+(v_F\partial_x+i\gamma)\tau_y$$
$$+A\sqrt{S/2}[\Delta\,\exp(i\tau_z\varphi)$$
$$-\Delta'\,\exp(-i\tau_z\varphi')]\}\chi-h_G, \qquad (9)$$
$$\gamma=A(\Delta'^2-\Delta^2),\quad h_G=4|I|S(\Delta^2+\Delta'^2);$$

$$L_{M>3}=\bar\psi\left\{i\tau_x\partial_t+(v_F\partial_x-i\gamma)\tau_y+\frac{A}{2}\sqrt{S/2}[\Delta\right.$$
$$\times\exp(-i\tau_z\varphi)+\Delta'\,\exp(i\tau_z\varphi')]\bigg\}\psi+\bar\chi\bigg\{i\tau_x\partial_t$$
$$+(v_F\partial_x+i\gamma)\tau_y+\frac{A}{2}\sqrt{S/2}[\rho\,\exp(-i\tau_z\theta)$$

$$+\rho'\,\exp(i\tau_z\theta')]\bigg\}\chi-h_G,$$
$$ \qquad (10)$$

$$\gamma=\frac{A}{4}\,(\Delta'^2+\rho'^2-\Delta^2-\rho^2),$$

$$h_G=|I|S\{\Delta^2+\rho^2+\Delta'^2+\rho'^2+2\,\cos 2ak_F[\Delta\Delta'$$
$$\times\cos(\varphi+\varphi')+\rho\rho'\,\cos(\theta+\theta')]\};$$

$$L^\pm_{M=3}=L_{M>3}+\frac{A}{4}\,\bar\psi\{\Delta\rho\tau_z\,\exp[i\tau_z(\varphi+\theta)]\pm\Delta'\rho'\tau_z$$
$$\times\exp[-i\tau_z(\varphi'+\theta')]\}\chi-\frac{A}{4}\,\bar\chi\{\Delta\rho\tau_z$$
$$\times\exp[i\tau_z(\varphi+\theta)]\pm\Delta'\rho'\tau_z$$
$$\times\exp[-i\tau_z(\varphi'+\theta')]\}\psi. \qquad (11)$$

Here, L is the Lagrangian density, h_H is the Heisenberg Hamiltonian density, $v_F=2a|B|\sin ak_F$, τ are the Pauli matrices, ψ and χ are spinors formed by components of the operators $a_{n\sigma}(\psi\equiv\psi^+\tau_x,\bar\chi\equiv\chi^+\tau_x)$:

$$\psi=\frac{1}{\sqrt2}\begin{pmatrix}W_\uparrow\\V_\downarrow\end{pmatrix},\quad \chi=\frac{1}{\sqrt2}\begin{pmatrix}W_\downarrow\\V_\uparrow\end{pmatrix}. \qquad (12)$$

While writing formula (9), we took into account the condition $c_{2k_F\pm\pi/a}=c_{2k_F}$, $d_{2k_F\pm\pi/a}=-d_{2k_F}$, which gives $c_{2k_F}=c_{-2k_F}$, $d_{2k_F}=-d_{-2k_F}$ for $k_F=\pi/4a(M=2)$, or, if we take into account Eqs. (6), $\Delta=\rho$, $\Delta'=-\rho'$, $\theta=-\varphi$ $\theta'=-\varphi'$.

The upper sign in formula (11) corresponds to the case $k_F=\pi/6a$ and the lower one to the case $k_F=\pi/3a$. It can be seen from formulas (11) that for $M=3$ the Lagrangian has a more complicated structure (nondiagonal in spinors ψ and χ) than for other commensurabilities. This constitutes a separate problem which we shall not discuss here since the main laws governing the transformation to the SDW phase have been studied extensively for $M=2$ and $M>3$. The Lagrangians (9) and (10) for these commensurabilities correspond to the well-known model of the type of $U(1)\otimes U(1)$ chiral model in the Gross–Navier quantum field theory.[14] The following sections of the present work will be devoted to the investigation of SDW ground state in the systems described by them.

3. ELECTRON SPECTRUM AND GROUND STATE ENERGY OF SDW

In the ground state, the quantities Δ, Δ', ρ, ρ', φ, φ', θ, θ' in (9) and (10) are independent of the coordinate, and the equations of motion $\partial L/\partial\bar\psi=0$ and $\partial L/\partial\bar\chi=0$ assume the following form:

for $M=2$

$$i\partial_t\psi+\{A\sqrt{S/2}[(\Delta\,\cos\varphi+\Delta'\,\cos\varphi')\tau_x+(\Delta'\,\sin\varphi'$$
$$-\Delta\,\sin\varphi)\tau_y]+i\tau_z v_F\partial_x+\gamma\tau_z\}\psi=0,$$

$$i\partial_t\chi+\{A\sqrt{S/2}[(\Delta\,\cos\varphi-\Delta'\,\cos\varphi')\tau_x+(\Delta'\,\sin\varphi'$$

$$+\Delta\,\sin\,\varphi)\tau_y]+i\tau_z v_F\partial_x-\gamma\tau_z\}\chi=0; \qquad (13)$$

$$i\partial_t\psi+\{(A/2)\sqrt{S/2}[(\Delta\,\cos\,\varphi+\Delta'\,\cos\,\varphi')\tau_x$$
$$+(\Delta'\,\sin\,\varphi'-\Delta\,\sin\,\varphi)\tau_y]+i\tau_z v_F\partial_x+\gamma\tau_z\}\psi=0,$$

$$i\partial_t\chi+\{(A/2)\sqrt{S/2}[\rho\,\cos\,\theta+\rho'\,\cos\,\theta')\tau_x+(\rho'\,\sin\,\theta'$$
$$-\rho\,\sin\,\theta)\tau_y]+i\tau_z v_F\partial_x-\gamma\tau_z\}\chi=0 \qquad (14)$$

for $M>3$.

Representing the Fourier transformation for electronic operators in the form

$$a_{n\sigma}=\frac{1}{\sqrt{N}}\sum_k e^{-ikan}a_{k\sigma}$$

$$=\frac{1}{\sqrt{N}}\Bigg[\sum_{k>0}e^{-i(k-k_F)an}e^{-ik_Fan}a_{k\sigma}^+$$

$$+\sum_{k<0}e^{-i(k+k_F)an}e^{ik_Fan}a_{k\sigma}\Bigg] \qquad (15)$$

and comparing the expressions (15) and (2), we obtain

$$W_\sigma(n)=\sqrt{2/N}\sum_{k<0}e^{-iQan}a_{k\sigma},$$

$$V_\sigma(n)=\sqrt{2/N}\sum_{k>0}e^{-iQan}a_{k\sigma}, \qquad (16)$$

where $Q=k+k_F$ for $k<0$ and $Q=k-k_F$ for $k>0$. Expressing formulas (13) and (14) in terms of the components (16), we obtain expressions for four lower branches of the electron spectrum for the time-independent problem:

$$\left.\begin{array}{l}\omega_{k>0,\downarrow}=\\ \omega_{k<0,\uparrow}=\end{array}\right\}-\sqrt{(v_FQ+\gamma)^2+\beta_1},$$
$$\left.\begin{array}{l}\omega_{k>0,\uparrow}=\\ \omega_{k<0,\downarrow}=\end{array}\right\}-\sqrt{(v_FQ-\gamma)^2+\beta_2}. \qquad (17)$$

Here, for $M=2$

$$(\kappa=\varphi+\varphi',\kappa'=\theta+\theta')$$

$$\beta_{1,2}=\frac{A^2S}{2}(\Delta^2+\Delta'^2\pm2\Delta\Delta'\,\cos\,\kappa) \qquad (18)$$

$$(\kappa=\varphi+\varphi',\kappa'=\theta+\theta')$$

and for $M>3$

$$\beta_1=\frac{A^2S}{8}(\Delta^2+\Delta'^2+2\Delta\Delta'\,\cos\,\kappa),$$

$$\beta_2=\frac{A^2S}{8}(\rho^2+\rho'^2+2\rho\rho'\,\cos\,\kappa'). \qquad (19)$$

Since the condition $\omega_{k>0,\sigma}=\omega_{k<0,\sigma}$ of joining of branches must be satisfied for $k=0$, we can write $\beta_1=\beta_2\equiv\beta$. Consequently, spectrum (17) contains only one gap $\Delta_0=\sqrt{\beta}$ as shown schematically in Fig. 1.

The total energy of the electron subsystem is determined by integrating formulas (17) over the spectrum, and has the form
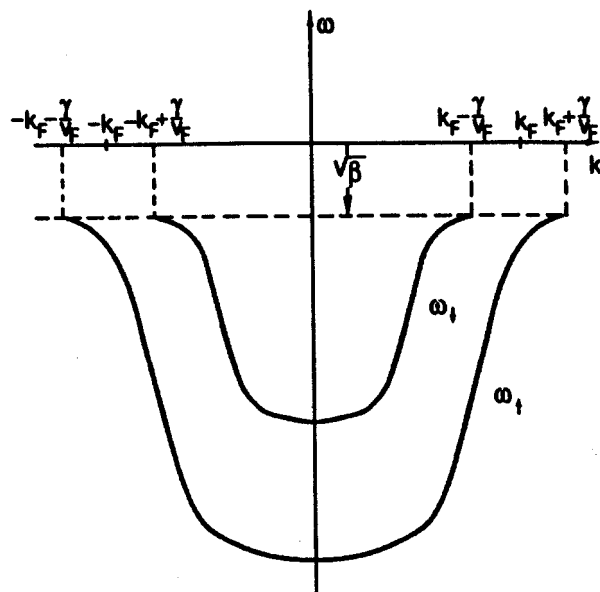

FIG. 1. Electron spectrum of the system (1) in the SDW state for $\gamma>0$.

$$W=-\frac{Na}{2\pi v_F}\{(\varepsilon_F+\gamma)\sqrt{(\varepsilon_F+\gamma)^2+\beta}+(\varepsilon_F-\gamma)$$
$$\times\sqrt{(\varepsilon_F-\gamma)^2+\beta}+\beta\,\ln\,\alpha\},$$
$$\alpha=\beta^{-1}[\sqrt{(\varepsilon_F+\gamma)^2+\beta}+\varepsilon_F+\gamma]$$
$$\times[\sqrt{(\varepsilon_F-\gamma)^2+\beta}+\varepsilon_F-\gamma], \qquad (20)$$

where $\varepsilon_F=v_Fk_F$ is the electron Fermi energy. Expansion of (20) in small parameters $\Delta^2/S\ll1$ and $AS/\varepsilon_F\ll1$ gives in the lowest approximation the following expression for the total energy of the system (1) ($\beta_1=\beta_2=\beta$):

$$E=W+Nh_G=-\frac{Na}{\pi v_F}\left[\varepsilon_F^2+\frac{\beta}{2}\left(1+\ln\frac{4\varepsilon_F^2}{\beta}\right)\right.$$
$$\left.-\frac{\pi v_F}{a}h_G\right]. \qquad (21)$$

In the case of double commensurability ($M=2$), the joining condition for formulas (18) has the form

$$\Delta\Delta'\,\cos\,\kappa=0, \qquad (22)$$

while the energy (21) becomes a function of only the parameters Δ and Δ'. The necessary conditions $\partial E/\partial\Delta=0$ and $\partial E/\partial\Delta'=0$ lead to the following relations:

$$\Delta\left(\ln\frac{4\varepsilon_F^2}{\beta}-2\lambda\right)=0,\quad\Delta'\left(\ln\frac{4\varepsilon_F^2}{\beta}-2\lambda\right)=0, \qquad (23)$$

where

$$\lambda=\frac{8\pi v_F|I|}{A^2a}. \qquad (24)$$

In all three cases following from the joining condition (22) ($\Delta=0$, $\Delta'=0$, $\cos\,\kappa=0$), the solution of Eqs. (23) gives the

same value of $\beta = 4\varepsilon_F^2 \exp^{-2\lambda}$. Hence the energy (21) is also the same for the three cases and has the value

$$E = -\frac{Na}{\pi v_F} \varepsilon_F^2 (1 + 2e^{-2\lambda}). \tag{25}$$

The spin configurations (8) corresponding to the energy (25) are different for the cases mentioned above. This degeneracy is removed by taking into account the terms $\sim \Delta^4/S^2$ in (1). This leads to the following correction to the Lagrangian (9):

$$\delta L = -A\sqrt{2/S}\{\bar\psi(\Delta^3 e^{-i\tau_z\varphi} + \Delta'^3 e^{i\tau_z\varphi'})\psi + \bar\chi(\Delta^3 e^{i\tau_z\varphi}$$
$$- \Delta'^3 e^{-i\tau_z\varphi'})\chi\} - \delta h_G, \tag{26}$$
$$\delta h_G = 16|I|\Delta^2\Delta'^2.$$

The introduction of the correction (26) leads to the same form of the expression (17) for the electron spectrum, but to different values of β_1 and β_2:

$$\beta_{1,2} = \frac{A^2 S}{2}(\Delta^2 + \Delta'^2 \pm 2\Delta\Delta'\cos\kappa) - 2A^2[\Delta^4 + \Delta'^4$$
$$\pm \Delta\Delta'(\Delta^2 + \Delta'^2)\cos\kappa]. \tag{27}$$

It follows from this expression that the joining condition (22) remains the same and gives

$$\beta = \beta_0 + \beta', \tag{28}$$
$$\beta_0 = \frac{A^2 S}{2}(\Delta^2 + \Delta'^2), \quad \beta' = -2A^2(\Delta^4 + \Delta'^4).$$

The total energy of the system can be represented to within terms of the order of Δ^4/S^2 in the form

$$E = -\frac{Na}{\pi v_F}\left[\varepsilon_F^2 + \gamma^2 + \beta_0/2 + \frac{\beta_0 + \beta'}{2}\ln\frac{4\varepsilon_F^2}{\beta_0}\right.$$
$$\left. - \frac{\pi v_F}{a}(h_G + \delta h_G)\right]. \tag{29}$$

Taking into account formulas (9), (26) and (28), we can present the necessary conditions for the minimum of energy (29) in the form

$$\Delta\left[(S - 8\Delta^2)\ln\frac{8\varepsilon_F^2}{A^2 S(\Delta^2 + \Delta'^2)} + 4\frac{3\Delta^4 - \Delta'^4}{\Delta^2 + \Delta'^2}\right.$$
$$\left. - 2\lambda(S - 4\Delta'^2)\right] = 0,$$
$$\tag{30}$$
$$\Delta'\left[(S - 8\Delta'^2)\ln\frac{8\varepsilon_F^2}{A^2 S(\Delta^2 + \Delta'^2)} + 4\frac{3\Delta'^4 - \Delta^4}{\Delta^2 + \Delta'^2}\right.$$
$$\left. - 2\lambda(S - 4\Delta^2)\right] = 0.$$

For $\Delta' = 0$, the above expression assumes the form

$$\ln\frac{8\varepsilon_F^2}{A^2 S\Delta^2} = 2\lambda + \frac{4\Delta^2}{S}(4\lambda - 3). \tag{31}$$

This leads to the solution

$$\Delta^2 = \frac{8\varepsilon_F^2}{A^2 S}e^{-2\lambda}\left[1 - \left(\frac{8\varepsilon_F}{AS}\right)^2\left(2\lambda - \frac{3}{2}\right)e^{-2\lambda}\right]. \tag{32}$$

Using formulas (31) and (32), we can express the energy (29) for $\Delta' = 0$ in the form

$$E_{\Delta'=0} = -\frac{Na}{\pi v_F}\varepsilon_F^2\left[1 + 2e^{-2\lambda} - (2\lambda - 1)\left(\frac{8\varepsilon_F}{AS}\right)^2 e^{-4\lambda}\right]. \tag{33}$$

For $\Delta = 0$, we can easily obtain in the same way an expression for the energy $E_{\Delta=0}$ which coincides exactly with $E_{\Delta'=0}$.

For $\cos\kappa = 0$ ($\Delta, \Delta' \neq 0$), Eqs. (30) will be compatible only if $\Delta^2 = \Delta'^2$, i.e., $\gamma = 0$ [see formula (9)]. This leads to the following relations:

$$\ln\frac{4\varepsilon_F^2}{A^2 S\Delta^2} = 2\lambda + 4\frac{\Delta^2}{S}(2\lambda - 1),$$

$$\Delta^2 = \frac{4\varepsilon_F^2}{A^2 S}e^{-2\lambda}\left[1 - \left(\frac{4\varepsilon_F}{AS}\right)^2(2\lambda - 1)e^{-2\lambda}\right]. \tag{34}$$

Using the expressions (34) and (28), we can write the energy (29) in the following form for $\Delta, \Delta' \neq 0$:

$$E_{\Delta,\Delta'\neq 0} = -\frac{Na}{\pi v_F}\varepsilon_F^2\left[1 + 2e^{-2\lambda} - \frac{\lambda}{2}\left(\frac{8\varepsilon_F}{AS}\right)^2 e^{-4\lambda}\right]. \tag{35}$$

A comparison of formulas (33) and (35) shows that $E_{\Delta=0} = E_{\Delta'=0} > E_{\Delta,\Delta'\neq 0}$, since $\lambda > 1$. Consequently, the ground state of the system (1) for $M = 2$ has a corresponding SDW with energy (35) and with a value of $\Delta^2 = \Delta'^2$ determined by formula (34). The gap in the electron spectrum is defined by

$$\Delta_0 = \sqrt{\beta} = 2\varepsilon_F e^{-\lambda}\left[1 - \lambda\left(\frac{4\varepsilon_F}{AS}\right)^2 e^{-2\lambda}\right]. \tag{36}$$

For other commensurabilities, it is sufficient to consider the energy to within terms of the order of Δ^2/S in order to obtain the ground state of the system (1). To simplify the problem, we observe that formula (7) gives

$$c_{2k_F}^+ c_{2k_F} = c_{-2k_F}^+ c_{-2k_F} \quad \text{and} \quad d_{2k_F}^+ d_{2k_F} = d_{-2k_F}^+ d_{-2k_F},$$

whence we obtain $\Delta^2 = \rho^2$ and $\Delta'^2 = \rho'^2$. Together with the joining condition, this leads to the following expressions for $M > 3$ [see formulas (10) and (19)]:

$$\beta = \frac{A^2 S}{8}(\Delta^2 + \Delta'^2 + 2\Delta\Delta'\cos\kappa),$$

$$h_G = 2|I|S(\Delta^2 + \Delta'^2 + 2\Delta\Delta'\cos\kappa\cos 2ak_F), \tag{37}$$

$$\Delta\Delta'\cos\kappa = \rho\rho'\cos\kappa'.$$

Thus, the energy (21) becomes a function of three variables Δ, Δ' and κ. This leads to the following necessary conditions for the energy minimum:

$$(\Delta+\Delta'\cos\kappa)\ln\frac{4\varepsilon_F^2}{\beta}-4\lambda(\Delta+\Delta'\cos\kappa\cos 2ak_F)=0, \tag{38}$$

$$(\Delta'+\Delta\cos\kappa)\ln\frac{4\varepsilon_F^2}{\beta}-4\lambda(\Delta'+\Delta\cos\kappa\cos 2ak_F)=0,$$

$$\Delta\Delta'\sin\kappa\left(\ln\frac{4\varepsilon_F^2}{\beta}-4\lambda\cos 2ak_F\right)=0,$$

where λ is defined by formula (24). The last of Eqs. (38) leads to three cases: $\Delta=0$, $\Delta'=0$, and $\sin\kappa=0$ (the case $\ln 4\varepsilon_F^2/\beta=4\lambda\cos 2ak_F$ does not satisfy the first two equations in (38) for Δ, $\Delta'\neq 0$).

For $\Delta=0$, we obtain the following solutions from (38) by using (37):

$$\cos\kappa=0,\quad \Delta'^2=\frac{32\varepsilon_F^2}{A^2S}e^{-4\lambda}. \tag{39}$$

Using (37) and (39), we can represent the energy (21) in the form

$$E_{\Delta=0}=-\frac{Na}{\pi v_F}\varepsilon_F^2(1+2e^{-4\lambda}). \tag{40}$$

Considering the case $\Delta'=0$ in an analogous manner, we find that $E_{\Delta'=0}=E_{\Delta=0}$.

For $\sin\kappa=0$ [$\cos\kappa=(-1)^p$, p being an integer], elimination of the first two equations in (38) gives $\Delta'=\Delta(-1)^p$. Using this relation and formulas (37), we arrive at the following solutions of Eqs. (38):

$$\Delta^2=\frac{8\varepsilon_F^2}{A^2S}e^{-4\lambda\cos^2 ak_F}. \tag{41}$$

Using this relation, we can present the energy (21) for $\sin\kappa=0$ in the form

$$E_{\sin\kappa=0}=-\frac{Na}{\pi v_F}\varepsilon_F^2(1+2e^{-4\lambda\cos^2 ak_F}). \tag{42}$$

It follows from a comparison of expressions (40) and (42) for energy that $E_{\sin\kappa=0}<E_{\Delta=0}=E_{\Delta'=0}$. In other words, the ground state of the system (1) for $M>3$ has a corresponding SDW with energy (42) and an electron spectrum gap

$$\Delta_0=2\varepsilon_F e^{-2\lambda\cos^2 ak_F}. \tag{43}$$

Since $\gamma=0$ for all commensurabilities considered above, the spectral branches for electrons with opposite spins shown in Fig. 1 collapse and the magnetic momentum of the electron subsystem in the ground state of the SDW remains equal to zero like in the initial metallic state.

4. SPIN STRUCTURE OF THE SDW GROUND STATE

In the ground state of the system (1), the spin components defined by formulas (8) assume the following form for $M=2$:

$$S_n^z=(-1)^n(S-4\Delta^2),$$

$$S_{2g}^x=2\sqrt{2S}\Delta(-1)^g\cos\varphi,$$

$$S_{2g}^y=-2\sqrt{2S}\Delta(-1)^g\sin\varphi, \tag{44}$$
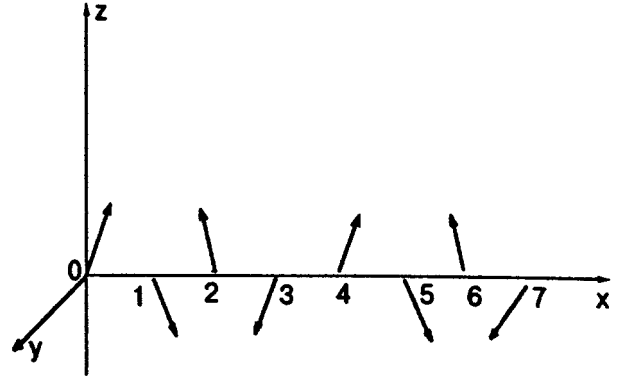

FIG. 2. Spin structure of the SDW ground state for $M=2$.

$$S_{2g+1}^x=\pm 2\sqrt{2S}\Delta(-1)^{g+f}\cos\varphi,$$

$$S_{2g+1}^y=\mp 2\sqrt{2S}\Delta(-1)^{g+f}\sin\varphi.$$

Here we have considered the fact that according to the results presented in Sec. 3, $\Delta'=\pm\Delta$ and $\varphi'=-\varphi+(\pi/2)\times(2f+1)$ (f is an integer) in the ground state of the system with a double commensurability. The quantity Δ in (44) is defined by formula (34), while the phase φ remains arbitrary and is fixed only in the presence of anisotropy in the XY plane. The state (44) corresponds to the energy (35) and is presented schematically in Fig. 2.

For $M>3$, the following relations are satisfied in the ground state of the system (1): $\Delta'=\Delta(-1)^p$, $\cos\kappa=(-1)^p$, $\rho^2=\rho'^2=\Delta'^2=\Delta^2$ (see Sec. 3). Together with the joining condition (37), this gives

$$\rho=\pm\Delta,\quad \rho'=\rho(-1)^f,\quad \cos\kappa'=(-1)^f. \tag{45}$$

Using these expressions, the spin components (8) can be represented for $M>3$ in the form

$$S_n^x=\sqrt{2S}\Delta[\cos(2k_Fan+\varphi)\pm\cos(2k_Fan+\theta)],$$

$$S_n^y=-\sqrt{2S}\Delta[\sin(2k_Fan+\varphi)\mp\sin(2k_Fan+\theta)],$$

$$S_n^z=(-1)^n\{S-2\Delta^2[1\pm\cos(4k_Fan+\varphi+\theta)]\}. \tag{46}$$

Here, the quantity Δ is defined by formula (41), while the upper and lower signs correspond to the cases $\rho=\Delta$ and $\rho=-\Delta$, respectively, If desired, the relation between φ and θ in (46) can be obtained from the condition of minimum "commensurability energy" which is a phase-dependent correction to the energy (21) arising when the magnon anharmonisms are taken into account in the Hamiltonian (1). However, as in the case $M=2$, one of the phases still remains undetermined in the absence of anisotropy in the XY-plane.

Thus, for all the commensurabilities considered here, the ground state of SDW corresponds to the spiral structures (44) and (46) emerging in the magnetic subsystem. The period of these spirals is determined from (46) as $\Pi=\pi/k_F$ or, if we take (3) into consideration, as $\Pi=2Ma/M_2$. For $k_F=\pi/4a$, the period is equal to $4a$ as shown in Fig. 2.

It also follows from (44) and (46) that all components of the total spin of the magnetic subsystem vanish in the ground state of the SDW for the approximation of averaging over

rapid oscillations with a period $(k_F n)^{-1}$. Together with the results obtained in Sec. 3 for the electron subsystem, this shows that the rearrangement of the ground state of the system (1) upon a transition to the SDW phase occurs in such a way that its total magnetic moment remains equal to zero.

5. CONCLUSIONS

In this work, we have studied for the first time the ground state of a quasi-one-dimensional metal possessing AFM order. It is shown that this state is an insulator with a spin density wave. The dependence of the insulating gap in a one-electron spectrum and the shape of the magnetic superstructure on the system parameters are obtained for various commensurabilities. The following result obtained in all the cases under consideration is quite interesting: the rearrangement of the ground state of an AFM metal during a transition to the SDW phase occurs in such a way that the total magnetic moment of the system remains equal to zero. The order parameter of the SDW generated by an AFM metal is found to be a singlet in contrast to the triplet SDW formed in a paramagnetic metal. Among other things, this should lead to the peculiar behavior of SDW in a magnetic field which will be considered in subsequent publications.

*E-mail: rozhavsky@ilt.kharkov.ua

[1] D. Jerome and H. J. Schultz, Adv. Phys. **31**, 300 (1982).

[2] G. Grüner, Rev. Mod. Phys. **66**, 1 (1994).

[3] J. M. Tranquada, D. J. Buttrey, V. Sachdev, and J. E. Lorenzo, Phys. Rev. Lett. **73**, 1003 (1994); J. M. Tranquada, B. J. Sternlieb, J. D. Axe *et al.*, Nature **375**, 561 (1995).

[4] L. P. Gor'kov, Usp. Phys. Nauk **144**, 381 (1984) [Sov. Phys. Uspekhi **27**, 809 (1984)].

[5] T. G. Petrova and A. S. Rozhavskii, Fiz. Nizk. Temp. **18**, 987 (1992) [Sov. J. Low Temp. Phys. **18**, 692 (1992)].

[6] V. J. Emery and S. A. Kivelson, Nature **374**, 434 (1995); S. A. Kivelson and V. J. Emery, Synth. Mat. **65**, 249 (1994).

[7] I. V. Krive, T. G. Petrova, and A. S. Rozhavskii, Pis'ma Zh. Éksp. Teor. Fiz. **44**, 127 (1987) [JETP Lett. **44**, 162 (1987)]; Zh. Éksp. Teor. Fiz. **92**, 1001 (1987) [Sov. Phys. JETP **65**, 568 (1987)].

[8] S. V. Vonsovskii, *Magnetism*, Wiley, New York, 1974.

[9] S. Nayak and F. Wilczek, unpublished, preprint Cond-mat. No. 9602112 (1996).

[10] I. V. Krive, A. S. Rozhavskii, and I. O. Kulik, Fiz. Nizk. Temp. **12**, 1123 (1986) [Sov. J. Low Temp. Phys. **12**, 635 (1986)].

[11] M. Ruderman and C. Kittel, Phys. Rev. **96**, 99 (1954).

[12] K. Yosida, Phys. Rev. **106**, 893 (1957).

[13] T. Kasuya, Progr. Theor. Phys. **16**, 45 (1956).

[14] I. V. Krive and A. S. Rozhavskii, Usp. Fiz. Nauk **152**, 33 (1987) [Sov. Phys. Uspekhi **30**, 370 (1987)].

Translated by R. S. Wadhwa

Effect of spontaneous magnetization on the electrical conductivity of ferromagnet-based metallic multilayers

Yu. A. Kolesnichenko

B. Verkin Institute for Low-Temperature Physics and Engineering, National Academy of Sciences of the Ukraine, 310164 Kharkov, Ukraine

L. V. Dekhtyaruk

Kharkov State University of Civil Engineering and Architecture, 310002, Kharkov, Ukraine

The conductivity of metallic magnetic multilayers (MML) in which the thickness of the ferromagnetic component exceeds the Larmor radius r of charge carrier trajectory in the field of spontaneous magnetic induction **B**, but is smaller than their mean free path l, is studied theoretically. It is shown that, if the electron scattering at the boundaries is negligible, the MML conductivity $\sigma_\perp$ at right angles to the field **B** depends significantly on the probability Q of tunneling of charge carriers from layer to layer, as well as on the ratio of radius r and thickness d of the nonmagnetic metal layers. A considerable decrease in the value of $\sigma_\perp$ upon a transition from antiferromagnetic to ferromagnetic ordering of spontaneous magnetic moments is predicted if the probability $Q \gg d/l$, r/l. The trajectory effects change the anisotropy of the conducting properties of MML in the plane parallel to the boundary. © *1997 American Institute of Physics.* [S1063-777X(97)00409-X]

1. INTRODUCTION

Conducting multilayers, which are periodic systems formed by alternating layers of different metals or semiconductors, are widely used as elements of modern microelectronic devices. This accounts for the growing interest towards the investigation of their electrical properties. The main feature of electron transport in multilayers distinguishing them from bulk conductors is the interaction of charge carriers with the internal boundaries, which affects significantly the dependence of the kinetic coefficients on layer thickness and external fields. Magnetic multilayers (MML) whose periodic structure contains a ferromagnet as an element (see the review in Ref. 1) display especially interesting properties. Giant magnetoresistance (GMR), involving a sharp decrease in the sample resistance (sometimes exceeding 100%!) in a quite weak magnetic field is without doubt among the most striking and significant effects displayed by MML. GMR was observed[2] for the first time in the MML Fe/Cr, and investigated subsequently for quite different combinations of ferromagnetic and nonmagnetic metals.

As a rule, the MML having an antiferromagnetic structure (spontaneous magnetic moments **M**$_s$ in adjacent ferromagnetic (F) layers separated by a nonmagnetic (N) layer are antiparallel) display GMR. This structure is determined by the thickness d of the N-layer and is formed as a result of indirect RKKY interaction between the F-layers. The application of a magnetic field **B**$_0$ parallel to the boundaries of an MML leads to an alignment of magnetic moments M_s in F-layers along the vector **B**$_0$. At the same time, the sample resistance decreases significantly. The most well-founded hypothesis about the origin of GMR can be the assumption about the dominating role of electron scattering at the internal boundaries which depends on the spin σ.[1,2] It is based on

the well-known fact that the cross-sections of scattering of charge carriers with different σ by impurities are different[3] in view of the dependence of the density of electron states at the Fermi surface on σ.[4]

A comparison of theoretical calculations[5–9] with the experimental results shows that GMR can be described quite accurately by using Boltzmann's kinetic equation for semiclassical electron distribution functions with boundary conditions in which the probability of scattering of charge carriers at the layer boundaries depends on spin. It should be observed that the theoretical works[5–9] mentioned above are a generalization of the Fuchs–Sondheimer theory of thin-film conductivity[10,11] to the case of MML, and do not take into account the spontaneous magnetization **M**$_s$ of a ferromagnet, which is responsible for magnetoresistance in an internal magnetic field **B** = 4π**M**$_s$ (see, for example, Refs. 12, 13). Such an approximation is fully justified for quite thin F-layers whose thickness d_f is much smaller than the characteristic radius r of the charge carrier trajectory in a field **B**. If r is comparable with the thickness d_f (for example, **B** ≅ 2.5 T for Fe at room temperature, and r is of the order of $10^{-4} - 10^{-3}$ cm) but smaller than the electron mean free path l, we must take into account the "intrinsic" magnetoresistance of MML.

In this work, we describe the results of theoretical investigations of the effect of internal magnetic field **B** on electron trajectories, which is manifested in the conductivity of ferromagnet-based MML. This effect may be due to a significant variation of the dynamics of charge carriers colliding with the boundary in a field **B**, just like the emergence of static skin effect in thin films caused by electrons "hopping" over the surface under the action of a magnetic field.[14–16] These ballistic effects, which are extremely sensitive to the mutual orientation of the electric current **J** and magnetization

M_s, may be manifested as anisotropy of GMR. We shall show that the experimental investigation of the MML for various angles between the vectors $\mathbf{J}$ and M_s can provide information about the probability of tunneling of charge carriers through the boundaries.

A consideration of such trajectory effects in ferromagnets with a domain structure[17,18] made it possible to explain the negative magnetoresistance observed in them.

2. MAGNETIC MULTILAYER MODEL AND COMPLETE SYSTEM OF EQUATIONS OF THE PROBLEM

Let us consider an infinite periodic system consisting of alternating layers of ferromagnetic and nonmagnetic metals. The boundary between the layers will be simulated by an ideal plane (in real systems, the width of the transition layer does not exceed 10Å as a rule). An electron having spin σ colliding with this plane has a probability Q_σ of tunneling into the adjoining metal without scattering, or a probability P_σ of specular reflection. The thicknesses d and d_f of the N- and F-layers are assumed to be much larger than the de Broglie wavelength of electrons. Combined with the fact that magnetic quantization of the energy spectrum of electrons in a ferromagnet can be disregarded for real values of spontaneous magnetic induction $\mathbf{B}$, this allows us to confine the analysis to the semiclassical approximation while calculating the conductivity of MML. Analyzing the role of trajectory effects, let us consider the case when the width d_f of the F-layer is much larger than the characteristic Larmor radius r of electron trajectories in the field $\mathbf{B}$ ($r \ll d_f \ll l$). The induction $\mathbf{B}_0$ of the external magnetic field required for transferring the system from the antiferromagnetic to ferromagnetic state is assumed to be quite low. Consequently, $r_0 \gg r$, l, and its effect on the orbits of charge carriers can be disregarded ($r_0 = c p_F / e B_0$, p_F being the Fermi momentum). For example, $B \simeq 2.5$ T for Fe, while GMR is observed in the Fe/Cr system in fields $B_0 \simeq 0.1$ T.

In order to compute the electric current in MML for a given potential difference across the endfaces of the sample ($y, z \rightarrow \infty$), we must solve the kinetic equation for the electron distribution function linearized with respect to the electric field $\mathbf{E}$:

$$f_i^{(\sigma)}(x, \mathbf{p}) = f_0(\varepsilon_i) - \frac{\partial f_0}{\partial \varepsilon_i} \psi_i^{(\sigma)}(x, \mathbf{p}). \tag{1}$$

This equation has the following form in the τ-approximation for the collision integral in the bulk of the sample:

$$\frac{\partial \psi_i^{(\sigma)}}{\partial t} + \frac{\psi_i^{(\sigma)}}{\tau_\sigma} = e \mathbf{v}_i \cdot \mathbf{E}. \tag{2}$$

Here, e is the electron charge, ε_i, $\mathbf{p}$ and $\mathbf{v}_i$ are its energy, quasimomentum, and velocity in the ith layer, $f_0(\varepsilon_i)$ the Fermi distribution function, the x-axis is at right angle to the interface, and τ_σ is the mean free time of electrons with spin σ. As usual,[19] we have introduced in Eq. (2) the time t of motion along the trajectory, defined as $t = x / v_x$ in a nonmagnetic metal and

$$t = c / e B \int dp_x / v_{yi} $$

in a ferromagnet.

The general solution of Eq. (2) is the function

$$\psi_i^{(\sigma)}(x, \mathbf{p}) = F_i^{(\sigma)}[x - x_i(t)] \exp\left(\frac{\lambda - t}{\tau_\sigma}\right) + \int_\lambda^t dt' \mathbf{v}_i(t')$$

$$\times \mathbf{E}[x - x_i(t) + x_i(t')] \exp\left(\frac{t' - t}{\tau_\sigma}\right), \tag{3}$$

in which the quantity $\lambda < t$ has the meaning of the moment of the last interaction of an electron with the boundary $x = x_s$, and λ is the root of the equation

$$x - x_i(t) = x_s - x_i(\lambda); \quad x_i(t) = \int^t dt' v_{x_i}(t'). \tag{4}$$

closest to t. The values of the functions $F_i^{(\sigma)}$ should be defined with the help of the boundary conditions[6,10] connecting the distribution function $\psi_{i, v_n > 0}^{(\sigma)}$ of electrons falling in the ith layer on the interface $x = x_s$ with the distribution functions of charge carriers incident on the boundary from the same layer $\psi_{i, v_n < 0}^{(\sigma')}$ or the adjacent layer $\psi_{k, v_n > 0}^{(\sigma'')}$:

$$\psi_{i, v_n > 0}^{(\sigma)}(x, \mathbf{p}) = P_{\sigma'} \psi_{i, v_n < 0}^{(\sigma')}(x, \mathbf{p}') + Q_{\sigma''} \psi_{k, v_n > 0}^{(\sigma'')}(x, \mathbf{p}''), \tag{5}$$

where $v_{i,n}$ is the projection of the velocity $\mathbf{v}_i$ on the inward normal to the boundary of the ith layer. The momenta $\mathbf{p}$, $\mathbf{p}'$, $\mathbf{p}''$ are connected through the conditions of conservation of energy and their tangential component relative to the plane $x = x_s$. In the case of MML with antiferromagnetic order of spontaneous magnetic moments M_s, the conditions $\sigma = \sigma' = -\sigma''$ and $\sigma = -\sigma' = \sigma''$ must be satisfied for electrons flying into the F-layer and for charge carriers falling into the N-layer, respectively. If the moments M_s are parallel (ferromagnetic order in MML), we should put $\sigma = \sigma' = \sigma''$.

For ''bulk'' electrons in F-layers, the value of $F_i^{(\sigma)}$ is obtained by requiring the periodicity of the function $\psi_i^{(\sigma)}(t) = \psi_i^{(\sigma)}(t + T_H)$ (T_H is the Larmor period).

The boundary condition (5) is valid if there is no diffusive scattering of electrons at the boundaries, i.e., $P_\sigma + Q_\sigma = 1$. If scattering does take place, the right-hand side of Eq. (5) acquires terms associated with the normalization of the chemical potential of reflected and tunneling electrons.[21] Consideration of the weak diffusivity of the boundary ($P_\sigma + Q_\sigma = 1 - \rho_\sigma, \rho_\sigma \ll r / l < 1$), which violates the ballistic motion of electrons causes just a slight decrease in the trajectorial contribution to the conductivity of MML. Note that the real boundary effectively scatters charge carriers colliding with it at fairly large angles, while the reflection of electrons at small incidence angles is nearly specular.[22]

The electric field $\mathbf{E} = -\nabla \varphi$ is obtained from the electroneutrality condition

$$\sum_\sigma \int \frac{dS_\mathbf{p}}{v_i} \psi_i^{(\sigma)}(x, \mathbf{p}) = 0, \tag{6}$$

where $dS_\mathbf{p}$ is an area element at the Fermi surface, and $v_i = |\mathbf{v}_i|$. It is obvious that in view of the homogeneity of the problem in the boundary plane, the potential
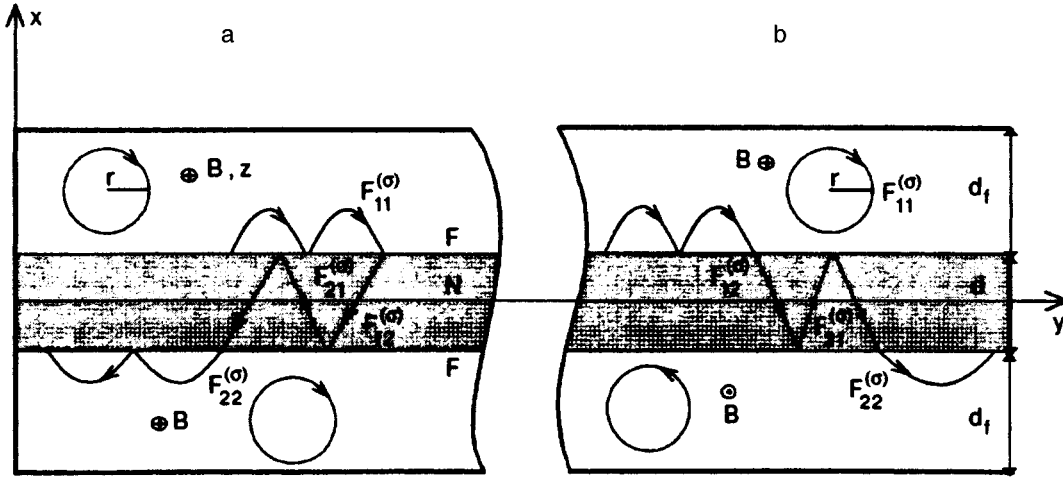
FIG. 1. Electron trajectory for ferromagnetic (a) and antiferromagnetic (b) structure of multilayer.

$\varphi(\mathbf{r}) = -yE_y - zE_z + \varphi_1(x)$, and Eq. (6) can be used for determining the field component $E_x(x)$ at right angles to the boundaries.

3. SOLUTION OF THE KINETIC EQUATION AND GENERAL EXPRESSION FOR ELECTRIC CURRENT IN MML

For ferromagnetic and antiferromagnetic structure of MML, which is preserved along the characteristic (4) of Eq. (2), the function $F_i^{(\sigma)}$ assumes (for a given σ) four values $F_{ik}^{(\sigma)}$ $(i,k=1,2)$, each corresponding to the motion along a certain segment of the trajectory (see Fig. 1a and b). Substituting the solution in the form (3) into the boundary conditions (5), we arrive at a system of eight algebraic equations, whose solution can be written in the form

$$F_{ii}^{(\sigma)} = D^{-1}\{\varphi_{ii}^{(\sigma)}[P_\sigma G_k^{(\sigma')} + (Q_\sigma^2 - P_\sigma^2)\alpha_{ik}^{(\sigma)}\alpha_{ki}^{(\sigma')}A_k^{(\sigma')}]$$

$$+ \varphi_{ik}^{(\sigma)}Q_\sigma\alpha_{ki}^{(\sigma')}A_k^{(\sigma')} + \varphi_{ki}^{(\sigma')}G_k^{(\sigma')}Q_\sigma$$

$$+ Q_\sigma Q_{\sigma'}\varphi_{kk}^{(\sigma')}\alpha_{ki}^{(\sigma')}\}; \quad i \neq k; \tag{7}$$

for parts of trajectory lying in the F-layer, and

$$F_{ik}^{(\sigma)} = D^{-1}\{\varphi_{ii}^{(\sigma)}G_k^{(\sigma')}Q_\sigma + \varphi_{ik}^{(\sigma)}\alpha_{ki}^{(\sigma')}A_k^{(\sigma')}A_i^{(\sigma)}$$

$$+ \varphi_{ki}^{(\sigma')}G_k^{(\sigma')}A_i^{(\sigma)} + Q_{\sigma'}\varphi_{kk}^{(\sigma')}\alpha_{ki}^{(\sigma')}A_i^{(\sigma)}\}; \quad i \neq k. \tag{8}$$

for parts of the trajectory lying in the N-layer.

Here,

$$D = G_k^{(\sigma')}G_i^{(\sigma)} - \alpha_{ik}^{(\sigma)}\alpha_{ki}^{(\sigma')}A_k^{(\sigma')}A_i^{(\sigma)}; \tag{9}$$

$$G_i^{(\sigma)} = 1 - P_\sigma\alpha_{ii}^{(\sigma)}; \tag{10}$$

$$A_i^{(\sigma)} = P_\sigma + (Q_\sigma^2 - P_\sigma^2)\alpha_{ii}^{(\sigma)}; \tag{11}$$

$$\alpha_{ik}^{(\sigma)} = \exp\left(\frac{\lambda_1^{(i)} - \lambda_2^{(k)}}{\tau_\sigma}\right); \tag{12}$$

$$\varphi_{ik}^{(\sigma)} = \int_{\lambda_1^{(i)}}^{\lambda_2^{(k)}} dt' \mathbf{v}_i(t') \cdot \mathbf{E} \exp\left(\frac{t' - \lambda_2^{(k)}}{\tau_\sigma}\right); \tag{13}$$

$\lambda_1^{(i)}$ and $\lambda_2^{(k)}$ are two successive instants $(\lambda_1^{(i)} < \lambda_2^{(k)})$ of collision of an electron with the same $(i=k)$ or different $(i \neq k)$ boundaries. The quantities $\alpha_{ik}^{(\sigma)}$ and $\varphi_{ik}^{(\sigma)}$ have the meaning of the probability of an electron moving without scattering in the bulk over the corresponding segment of the trajectory and the energy acquired by this electron in an electric field over this segment. For charge carriers moving in closed Larmor trajectories in the bulk of the ferromagnet, we should put $\lambda = -\infty$ in formula (3). Their contribution to the current can be calculated easily by using the well known magnetic conductivity tensor for an infinite metal.[19]

The current produced by electrons colliding with two adjacent MML boundaries can be presented in the form

$$I_\alpha = 2I_{11}^{(\alpha)} + I_{12}^{(\alpha)}, \quad \alpha = y, z; \tag{14}$$

where I_{11} is the current passing in the boundary region of width $2r (r = cp_F/eB)$ in the F-layer:

$$I_{11}^{(\alpha)} = -\frac{e^3 B}{ch^3} \sum_\sigma \int dp_z \int_0^{T_{H/2}} d\lambda v_{x_i}(\lambda) \int_0^{T_H} dt$$

$$\times \theta(t-\lambda)v_{\alpha_i}(t)\left\{F_{11}^{(\sigma)} \exp\left(\frac{\lambda - t}{\tau_\sigma}\right) + \int_\lambda^t dt'\right.$$

$$\times \mathbf{v}_i(t') \cdot \mathbf{E} \exp\left(\frac{t' - t}{\tau_\sigma}\right)\Bigg\} \tag{15}$$

and I_{12} is the current in the N-layer:

$$I_{12}^{(\alpha)} = \frac{2e^2}{h^3} \sum_\sigma \int \frac{dS_\mathbf{p}}{v_i} \theta(-v_{xi})v_{\alpha i}\left\{\mathbf{v}_i \cdot \mathbf{E}\tau_\sigma d + v_{xi}\tau_\sigma\right.$$

$$\times \left[1 - \exp\left(\frac{d}{v_{xi}\tau_\sigma}\right)\right](\mathbf{v}_i \cdot \mathbf{E}\tau_\sigma - F_{12})\Bigg\}, \tag{16}$$

where p_z is the momentum projection on the direction of the magnetic field $\mathbf{B}$. While writing the expression (15), we used Eq. (4) to go over from integration over the coordinate x to integration over the collision instants λ. Formula (16) describes the doubled electron current with negative velocity v_{ix}. It can easily be verified that, in view of the symmetry of
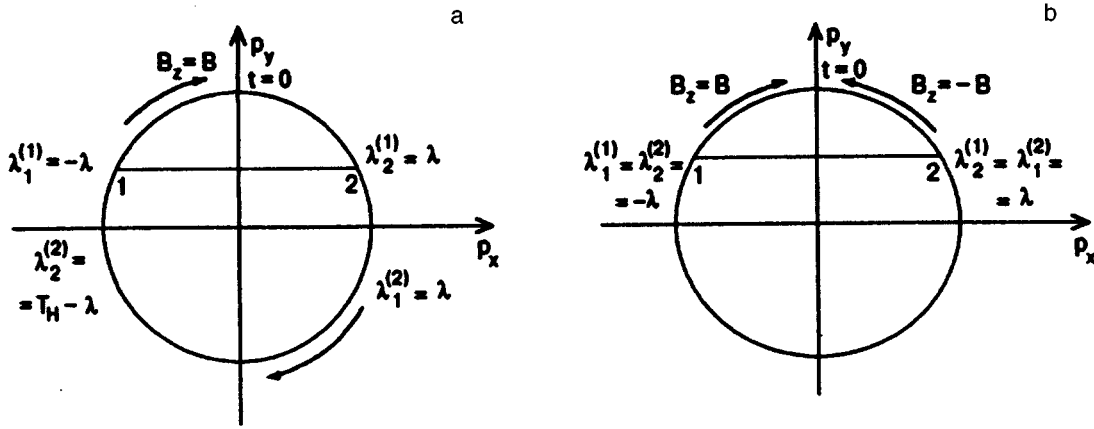
FIG. 2. Electron trajectory in the momentum space for ferromagnetic (a) and antiferromagnetic (b) order of spontaneous magnetic moments. Points *1* and *2* correspond to the motion at a constant velocity in the nonmagnetic layer.

the problem, the contributions from charge carriers with $v_{ix}>0$ and $v_{ix}<0$ to the conductivity of the N-layer are identical.

Formulas (15) and (16) are valid for any form of the Fermi surface of charge carriers. While calculating the current in the MML in the following analysis, we shall use the frequently employed model of a compensated metal with identical quadratic isotropic energy–momentum relations for electrons and holes. Naturally, such a simple model does not take into consideration a whole range of very fine effects associated with the existence of a contact potential difference at the boundaries, peculiarities of electron tunneling due to a difference in the Fermi surfaces in magnetic and nonmagnetic metals, etc. However, this model makes it possible to find the explicit form of the dependence of current on the thicknesses d and d_f and the magnetic induction **B**, and provides a qualitative description of the conductivity of an MML with an arbitrary closed Fermi surface just as in the case of a bulk conductor. The condition of compensation (equality of concentrations n_1 of electrons and n_2 of holes) allows us to neglect the Hall components of the MML conductivity and to disregard Eq. (5) for the field E_x which can be solved only numerically. Note that the strict equality $n_1=n_2$ which is quite normal for nonmagnetic metals is not satisfied for pure ferromagnets. However, it was shown by Kaganov and Peschansky[23] that so far as the galvanomagnetic properties are concerned, a metal for which the inequality $|n_1-n_2|/(n_1+n_2)\ll r/l$ is satisfied behaves like a compensated metal. Such a situation can be expected, for example, in $4f$-ferromagnetic metals.

4. MML CONDUCTIVITY PARALLEL TO THE BOUNDARIES

In the model of spherical constant energy surfaces, we obtain the following expressions for the components of electron (hole) velocities:

$$v_x=-v_\perp \sin \Omega t; \quad v_y=v_\perp \cos \Omega t; \quad v_z=p_z/m^*, \tag{17}$$

where

$$v_\perp=(1/m^*)(p_F^2-p_z^2)^{1/2}; \quad \Omega=(|e|B)/m^*c$$

is the cyclotron frequency, and m^* is the effective mass. For the instant $t=0$, we chose a point on the Fermi surface corresponding to charge carriers moving parallel to the boundaries (Fig. 2). In this reference system, the "instants" $\lambda_{1,2}^{(i)}$ of collisions are defined as

$$\lambda_1^{(1)}=-\lambda; \quad \lambda_1^{(2)}=\lambda_1^{(1)}=\lambda; \quad \lambda_2^{(2)}=T_H-\lambda;$$

$$(T_H=2\pi/\Omega); \tag{18}$$

for the ferromagnetic structure of MML, and

$$\lambda_1^{(1)}=\lambda_2^{(2)}=-\lambda; \quad \lambda_2^{(1)}=\lambda_1^{(2)}=\lambda. \tag{19}$$

for the antiferromagnetic structure.

Let us first consider the current flowing at right angles to the vector **B** and present it in the following form by using formula (14):

$$I_y=[4\sigma_{yy}^{(F)}r+\sigma_{yy}^{(N)}d]E_y, \tag{20}$$

where $\sigma_{yy}^{(F)}$ is the conductivity of the boundary region of the F-layer, and $\sigma_{yy}^{(N)}$ the conductivity of the N-layer. In order to pay special attention to the effect of the boundaries on the conductivity of MML, we can present the expression for $\sigma_{yy}^{(F,N)}$ for the case when the bulk relaxation frequencies in the layer are identical ($\tau_\sigma=\tau_{\sigma'}=\tau_{\sigma''}=\tau$):

$$\sigma_{yy}^{(F)}=\frac{9\pi}{64}\frac{\sigma_0}{1+\gamma^2}+\frac{3\sigma_0}{16\pi}\frac{\gamma^2}{(1+\gamma^2)^2}\sum_\sigma\int_0^\pi d\varphi \sin \varphi$$

$$\times\int_{-1}^1 du(1-u^2)^{3/2}D^{-1}[a_{11}\cos \varphi+\gamma(2-a_{22})$$

$$\times\sin \varphi]\{\sin \varphi[2Q_\sigma A_2^{(\sigma')}+Q_{\sigma'}(2-Q_\sigma a_{22})$$

$$+(2a_{12}-a_{12}^2)(2-3Q_\sigma)A_2^{(\sigma')}\mp Q_\sigma Q_{\sigma'}(1-a_{12})$$

$$\times(2-a_{22})]+\cos \varphi \gamma a_{12}Q_\sigma$$

$$\times[2A_2^{(\sigma')}+Q_{\sigma'}a_{22}-a_{12}A_2^{(\sigma')}]\}; \tag{21}$$

$$\sigma_{yy}^{(N)}=\sigma_0+\frac{3}{4\pi}\frac{\sigma_0}{1+\gamma^2}\sum_\sigma\int_0^\pi d\varphi \sin \varphi \cos \varphi\int_{-1}^1 du(1$$

$$-u^2)^{3/2}D^{-1}a_{12}\{\gamma \sin \varphi[Q_\sigma(2-a_{11})A_2^{(\sigma')}$$
$$\mp Q_{\sigma'}(1-a_{12})(2-a_{22})A_1^{(\sigma)}]$$
$$-\gamma^2 \cos \varphi[Q_\sigma Q_{\sigma'}(a_{11}+a_{22})+(Q_\sigma+Q_{\sigma'}$$
$$-3Q_\sigma Q_{\sigma'})a_{11}a_{22}-Q_{\sigma'}a_{12}a_{22}A_1^{(\sigma)}]\}, \tag{22}$$

where

$$D=Q_\sigma a_{11}A_2^{(\sigma')}+Q_{\sigma'}a_{22}A_1^{(\sigma)}+Q_\sigma Q_{\sigma'}a_{11}a_{22}-(2a_{12}$$
$$-a_{12}^2)A_1^{(\sigma)}A_2^{(\sigma')};$$
$$A_i^{(\sigma)}=Q_\sigma+(1-2Q_\sigma)\alpha_{ii}; \quad \gamma=\Omega\tau;$$
$$a_{12}=1-\exp(-(d/l)\sin \varphi \sqrt{1-u^2});$$
$$l=p_F\tau/m^*; \quad \sigma_0=(n_1+n_2)e^2\tau/m^*$$

is the conductivity of the bulk metal. For an MML with ferromagnetic structure, we should choose the upper sign in formulas (21) and (22) and put $\sigma=\sigma'$:

$$a_{11}=1-\exp(-2\varphi/\gamma); \quad a_{22}=1-\exp(-2(\pi-\varphi)/\gamma). \tag{23}$$

The antiferromagnet structure of MML corresponds to the lower sign and $\sigma\neq\sigma'$:

$$a_{11}=a_{22}=1-\exp(-2\varphi/\gamma). \tag{24}$$

The condition of strong magnetic field $\gamma=l/r\gg1$ allows us to expand a_{ii} up to the first nonvanishing term, and we shall treat these quantities to be small and of the order of γ^{-1}.

In spite of a number of simplifying assumptions, the expressions (21) and (22) remain quite cumbersome. We shall present below their asymptotic forms for the most interesting cases.

1. $Q_\sigma\ll r/l$. For such a low tunneling probability, there are practically no electron trajectories passing through two F-layers, and the conductivities $\sigma_{yy}^{(F,N)}$ are independent of the mutual orientation of magnetic moments $\mathbf{M}_s$:

$$\sigma_{yy}^{(F)}\simeq\sigma_0\begin{cases}\dfrac{9}{32}g-\dfrac{3}{8}(Q_\sigma+Q_{\sigma'})\gamma g_2, \\ Q_\sigma\ll d/l, \quad \sigma\neq\sigma' \\ \dfrac{9}{32}g-\dfrac{1}{4\pi}\dfrac{d}{2r}g_1, \quad Q_\sigma\gg d/l;\end{cases} \tag{25a, 25b}$$

$$\sigma_{yy}^{(N)}\simeq\sigma_0\begin{cases}1-\dfrac{3}{16}(Q_\sigma+Q_{\sigma'})\left(\dfrac{l}{d}\right)\left(1-\dfrac{g_2}{2}\right), \\ Q_\sigma\ll d/l, \quad \sigma\neq\sigma' \\ \dfrac{3}{4}\left(\dfrac{Q_\sigma+Q_{\sigma'}}{Q_\sigma Q_{\sigma'}}\right)\dfrac{d}{l}\ln\left(\dfrac{l}{d}\right), \quad Q_\sigma\gg d/l;\end{cases} \tag{26a, 26b}$$

where

$$g=\frac{1}{4}[3\mathrm{Si}(\pi)-\mathrm{Si}(3\pi)]; \quad g_1=\mathrm{Si}(2\pi);$$

$$g_2=\frac{3}{4}[\mathrm{Ci}(\pi)-\mathrm{Ci}(3\pi)]+\ln 3)$$

2. $r/l\ll Q_\sigma\ll d/l$. These inequalities mean that charge carriers freely penetrate the nonmagnetic metal from the ferro-

magnetic metal, but still the ballistic motion of electrons does not lead to a connection between F-layers because of a large thickness of the N-layer:

$$\sigma_{yy}^{(F)}=\sigma_0\frac{r}{l}\left(\frac{1}{Q_\sigma}+\frac{1}{Q_{\sigma'}}\right); \quad \sigma\neq\sigma' \tag{27a}$$

$$\sigma_{yy}^{(N)}=\sigma_0\left(1-\frac{3r}{8d}\right). \tag{27b}$$

3. $Q_\sigma\gg r/l, d/l$. In this case, the boundary is practically transparent to charge carriers, and the dominating role in the conductivity of MML is played by periodic trajectories intersecting two F-layers. The nature of these trajectories depends on the direction of the magnetic field $\mathbf{B}$ in F-layers because of which the asymptotic forms of the conductivities $\sigma_{yy}^{(F,N)}$ are found to be quite different for different types of magnetic order in MML.

The ferromagnetic structure of MML is characterized by the relations

$$\sigma_{yy}^{(F)}\simeq\sigma_0\sum_\sigma$$

$$\times\begin{cases}\dfrac{5}{8}(1-Q_\sigma)\dfrac{r}{l}+\dfrac{3}{16}(3Q_\sigma-2)\dfrac{rd}{l^2}, \quad d\gg r, \\ \dfrac{3}{16}\dfrac{(1-Q_\sigma)}{Q_\sigma}\dfrac{r}{l}, \quad d\ll r;\end{cases} \tag{28a, 28b}$$

$$\sigma_{yy}^{(N)}\simeq\sigma_0\begin{cases}1-\dfrac{3r}{8d}, \quad d\gg r, \\ \dfrac{3}{\pi}\dfrac{d}{r}\ln\left(\dfrac{l}{d}\right)+\dfrac{(1-Q_\sigma)}{Q_\sigma}\dfrac{r}{l}, \quad d\ll r,\end{cases} \tag{29a, 29b}$$

while for the antiferromagnetic structure of MML we can write

$$\sigma_{yy}^{(F)}\simeq\sigma_0\begin{cases}\dfrac{12}{10}\dfrac{r}{d}, \quad d\gg r, \\ \dfrac{9}{32}g, \quad d\ll r,\end{cases} \tag{30a, 30b}$$

$$\sigma_{yy}^{(N)}\simeq\sigma_0\begin{cases}1-\dfrac{3r}{8d}, \quad d\gg r, \\ \dfrac{4}{\pi}\dfrac{d}{r}\ln\left(\dfrac{l}{d}\right)+\dfrac{1}{\pi}g_1, \quad d\ll r.\end{cases} \tag{31a, 31b}$$

It is well known that the bulk conductivity $\sigma_{\perp b}$ of a compensated metal in a direction perpendicular to the magnetic field $\mathbf{B}$ is given by[18]

$$\sigma_{\perp b}=\sigma_0\left(\frac{r}{l}\right)^2 \quad \text{for } r\ll l. \tag{32}$$

Hence, for thicknesses $d_f\ll l$ of the F-layer, the main contribution to the MML conductivity comes from the N-layers and the boundary region of the ferromagnet.

Using formulas (15) and (16) to calculate the current flowing along the vector $\mathbf{B}$ in an MML, it can be easily verified that

$$\sigma_{zz}^{(F)}=\sigma_{zz}^{(N)}=\sigma_0 \tag{33}$$

706   Low Temp. Phys. **23** (9), September 1997

Yu. A. Kolesnichenko and L. V. Dekhtyaruk   706

for any value of the tunneling probability Q_σ.

5. DISCUSSION OF THE RESULTS

Let us now discuss the analytic results for conductivities $\sigma_{yy}^{(F,N)}$ (formulas (25)–(31)) obtained with the help of the exact formulas (21), (22) (within the limits of the model) using the concepts about the effective number of charge carriers n_{eff} and their mean free path l_{eff}. Such an approach, which allows a qualitative description of transport phenomena in conductors, is used frequently in the physics of normal metals.[19] It is based on the extremely simple assumption that the conductivity of a complex system can be described roughly by the simple Drude–Lorentz relation containing the relative number n_{eff} of electrons participating in the conduction, and the length l_{eff} characterizing the energy $\Delta\varepsilon = eEl_{\text{eff}}$ acquired during the mean free time τ:

$$\sigma = \frac{n_{\text{eff}}e^2 l_{\text{eff}}}{p_F} \equiv \sigma_0 \frac{n_{\text{eff}}l_{\text{eff}}}{nl}. \tag{34}$$

In the limit $Q \to 0$ (for simplicity, we shall assume that the tunneling probability Q does not depend on spin), the electrons interacting with the boundaries perform independent periodic motion in the N-layer (along a trajectory broken by mirror reflections) and in the F-layer (along a "hopping" trajectory). The path traversed by them along the electric field is defined as $l_{\text{eff}} \simeq l$, and the contribution to the conductivity is of the order of the conductivity σ_0 of the bulk sample. For $Q \neq 0$, however, $Q \ll r/l, d/l$, and most of the electrons fail to tunnel to the adjoining metal. However, as a result of each collision with the boundary, Qn charge carriers are left out from the conduction process and go over to another layer. The total number of such carriers is $\delta n = n - n_{\text{eff}} \simeq MQn$, where M is the number of collisions with the boundary during a time τ ($M \approx l/r$ for the F-layer and $M \approx l/d$ for the N-layer). Accordingly, the conductivities $\sigma_\perp^{(F)}$ and $\sigma_\perp^{(N)}$ of the boundary regions of F- and N-layers perpendicular to the magnetic field [see Eqs. (25a) and (26a)] are found to be of the order of

$$\sigma_\perp^{(F)} \approx \sigma_0\left(1 - \frac{Ql}{r}\right), \quad Q \ll r/l,\ d/l; \tag{35}$$

$$\sigma_\perp^{(N)} \approx \sigma_0\left(1 - \frac{Ql}{d}\right), \quad Q \ll r/l,\ d/l. \tag{36}$$

For $Q \gg d/l$ the electrons tunnel freely from N-layer to the F-layer, but their return during the mean free time is unlikely in view of the inequality $Q \ll r/l$. The situation arising in the N-layer is analogous to that in a thin plate with charge carriers scattered diffusely at the surface,[10,11] when l_{eff} is of the order of its thickness d, which leads to a decrease in the conductivity by a factor l/d. Before tunneling, the electrons manage to cover a distance $l_{\text{eff}} \approx d/Q$ in the N-layer, making a contribution

$$\sigma_\perp^{(N)} \simeq \sigma_0 \frac{d}{lQ} \ln\left(\frac{l}{d}\right), \quad d/l \ll Q \ll r/l. \tag{37}$$

to the conductivity [see (26b)]. As usual, $\ln(l/d)$ reflects the contribution to $\sigma_\perp^{(N)}$ from electrons flying nearly parallel to

the boundaries for which $l_{\text{eff}} \simeq l$. Conversely, the conductivity of the F-layer even becomes slightly higher since almost all of the $\delta n \simeq (l/r)Qn$ electrons tunneled through it return, and the difference between $\sigma_\perp^{(F)}$ and σ_0 is associated with a decrease in their effective mean free path by their path d/Q in the N-layer [see (25b)]:

$$\sigma_\perp^{(F)} \simeq \sigma_0\left(1 - \frac{d}{r}\right), \quad d/l \ll Q \ll r/l. \tag{38}$$

Conversely, if $r/l \ll Q \ll d/l$, the charge carriers in the ferromagnet go over to the N-layer after covering a path $l_{\text{eff}} = r/Q \ll l$ along the boundary, and the conductivity associated with them (see (27a)) is of the order of

$$\sigma_\perp^{(F)} \simeq \sigma_0 \frac{r}{Ql}, \quad r/l \ll Q \ll d/l. \tag{39}$$

The conductivity of the N-layer in the main approximation in the small parameter d/lQ coincides with the conductivity of a thin plate with mirror boundaries[10,11] (i.e., equal to σ_0). Its decrease is determined by the effective mean free path $l_{\text{eff}} = l - r/Q$ for $\delta n = (l/d)Qn$ electrons entering the F-layer (see (27b)):

$$\sigma_\perp^{(N)} \simeq \sigma_0\left(1 - \frac{r}{d}\right), \quad r/l \ll Q \ll d/l. \tag{40}$$

For a highly transparent boundary $Q \gg r/l,\ d/l$, a connection between F-layers is established due to trajectorial motion of electrons, and the conductivity of MML depends on the mutual orientation of magnetic field in them.

For the ferromagnetic structure of MML, electrons in different F-layers move in directions opposite to the electric field. In the limit $Q \to 1,\ d \to 0$, the magnetic field in the sample is uniform, and the conductivity $\sigma_\perp^{(F)}$ coincides with the corresponding value for an infinite conductor $\sigma_{\perp b}$ defined by Eq. (32). Proceeding from the concepts about the effective mean free path, the quantity $\sigma_{\perp b}$ can be estimated as follows. The displacement of an electron along the vector **E** over a period is equal to zero on account of its periodic motion, i.e., $l_{\text{eff}} = 0$ in the main approximation in r/l. However, taking into consideration the collisions and the fact that lengths l_1 and l_2 of trajectory segments along and against the field **E** are different ($|l_1 - l_2| \simeq r$), we obtain the following estimate for l_{eff}:

$$l_{\text{eff}} \simeq r\left|\exp\left(-\frac{l_1}{l}\right) - \exp\left(-\frac{l_2}{l}\right)\right| \simeq \frac{r^2}{l} \quad \text{for } r \ll l, \tag{41}$$

which corresponds to formula (32). For $Q \neq 1,\ d \neq 0$ (but for $Q \gg r/l, d/l$), the difference between the quantities $\sigma_\perp^{(F)}$ and $\sigma_{\perp b}$ is due to two reasons. First, as a result of reflection at the boundaries, $n_{\text{eff}} = (1-Q)n$ electrons have displacements in opposite directions, differing by a quantity of the order of $l_{\text{eff}}^{(1)} \approx r$. Second, bulk scattering at trajectory segments lying in the N-layer leads, as in a bulk metal, to a nonzero effective mean free path

$$l_{\text{eff}}^{(2)} \simeq r\left|\exp\left(-\frac{l_1}{l}\right) - \exp\left(-\frac{l_2 + 2d}{l}\right)\right| \simeq \frac{rd}{l},$$
$$\text{for } l \gg d \gg r. \tag{42}$$

707   Low Temp. Phys. **23** (9), September 1997

Yu. A. Kolesnichenko and L. V. Dekhtyaruk   707

The above processes define two contributions to the conductivity $\sigma_\perp^{(F)}$ of the F-layer (see (28a)):

$$\sigma_\perp^{(F)} \simeq (1-Q)\sigma_0 \frac{r}{l} + \sigma_0 \frac{dr}{l^2}, \quad Q \gg r/l, d/l. \tag{43}$$

In the case under consideration, the N-layer conductivity also contains two terms, one of which coincides with the first term in (46) and has the same origin. The second term is associated with the energy acquired by an electron directly in a nonmagnetic metal over a length $l_{\text{eff}} \simeq dM$, where M is the number of collisions with the boundary over a period τ. For transmission probabilities close to unity, $M \simeq l/(d+r)$. Hence the total conductivity $\sigma_\perp^{(N)}$ [see Eq. (29)] can be presented in the form

$$\sigma_\perp^{(N)} \simeq \sigma_0 \frac{d}{r+d} + (1-Q)\sigma_0 \frac{r}{l}, \quad Q \gg r/l, \, d/l. \tag{44}$$

If the MML has an antiferromagnetic structure, $Q \gg r/l, d/l$ for a high transparency of the boundaries, and electrons move along an open trajectory, being displaced along the electric field in the same direction. Their effective mean free path in the F-layer is $l_{\text{eff}} \simeq rM$, and the conductivity $\sigma_\perp^{(F)}$ [see (30)] is defined as

$$\sigma_\perp^{(F)} \simeq \sigma_0 \frac{r}{r+d}, \quad Q \gg r/l, \, d/l. \tag{45}$$

The conductivity of the N-layer in the case under consideration is weakly sensitive to the relation between d and r. Even for $r \gg d$, when charge carriers spend most of the mean free time in F-layers, moving in the same direction in these layers, they acquire energy in an electric field. Hence l_{eff} is always of the order of l, and the conductivity is comparable with the conductivity σ_0 of the bulk metal [see (31)]. It follows from formulas (43)–(45) that the change in the magnetic order in MML (under the action of the external field) leads to a considerable increase in the conductivity of both F- and N-layers in a direction perpendicular to the magnetic field.

6. CONCLUSION

Thus, if the radius r of the charge carrier trajectory in the magnetic field with spontaneous induction **B** is smaller than the ferromagnetic layer thickness, the conductivity of MML is sensitive to the direction of the current flowing parallel to the boundaries. The MML conductivity perpendicular to the vector **B** depends significantly on the probability of tunneling of electrons through the boundary, and also on the mutual orientation of the magnetic moments for quite large values of Q. The anisotropy of the MML resistance defined by these trajectory effects may well exceed the contribution emerging from a consideration of the anisotropy of matrix elements of spin-orbit interaction in a ferromagnet, which is usually of the order of a few percent.[1,8] Thus, the experimental investigation of the longitudinal and transverse resistance (relative to the intrinsic magnetic field) for different types of magnetic order in a multilayer can provide information about the nature of interaction of charge carriers with the boundaries between layers.

[1] R. E. Camley and R. L. Stamps, J. Phys. : Cond. Mat. **5**, 3727 (1993).
[2] M. N. Baibich, J. M. Broto, A. Fert *et al.*, Phys. Rev. Lett. **61**, 2472 (1988).
[3] A. Fert and I. A. Campbell, J. Phys. : Metal Phys. **6**, 849 (1976).
[4] S. V. Vonsovskii, *Magnetism*, John Wiley, New York, 1981.
[5] R. E. Camley and J. Barans, Phys. Rev. Lett. **63**, 664 (1989).
[6] J. Barans, A. Fuss, R. E. Camley *et al.*, Phys. Rev. **B44**, 8110 (1990).
[7] B. Dieny, J. Phys. : Cond. Mat. **4**, 8009 (1992).
[8] V. V. Ustinov, Zh. Éksp. Teor. Fiz. **106**, 207 (1994) [JETP **79**, 113 (1994)].
[9] V. I. Okulov, Fiz. Nizk. Temp. **20**, 100 (1994) [Low Temp. Phys. **20**, 81 (1994)].
[10] K. Fuchs, Cambridge Phil. Soc. **34**, 100 (1938).
[11] H. Sondheimer, Adv. Phys. **1**, 1 (1958).
[12] F. C. Schiwerer and J. Silcox, Phys. Rev. Lett. **20**, 101 (1968).
[13] L. Berge and A. R. de Vroomen, J. Appl. Phys. **36**, 2777 (1965).
[14] M. Ya. Azbel', Zh. Éksp. Teor. Fiz. **44**, 983 (1963) [JETP **17**, 667 (1963)].
[15] V. G. Peschansky, Sov. Sci. Rev. A: Phys. **16**, 1 (1992).
[16] O. V. Kirichenko, V. G. Peschansky, and S. N. Savel'eva, Zh. Éksp. Teor. Fiz. **77**, 2045 (1979) [Sov. Phys. JETP **50**, 976 (1979)].
[17] Yu. V. Zakharov and Yu. I. Mankov, Phys. Stat. Solidi (b) **125**, 197 (1986).
[18] Yu. V. Zakharov, Yu. I. Man'kov, and L. S. Titov, Fiz. Nizk. Temp. **12**, 408 (1986) [Sov. J. Low Temp. Phys. **12**, 232 (1986)].
[19] I. M. Lifshits, M. Ya. Azbel', and M. I. Kaganov, *Electron Theory of Metals*, Consultants Bureau, New York, 1973.
[20] M. I. Kaganov and V. B. Fiks, Zh. Éksp. Teor. Fiz. **73**, 753 (1977) [Sov. Phys. JETP **46**, 393 (1977)].
[21] V. V. Ustinov, Fiz. Metal Metalloved **49**, 31 (1980).
[22] L. A. Falkovsky, Adv. Phys. **32**, 753 (1983).
[23] M. I. Kaganov and V. G. Peschansky, Zh. Éksp. Teor. Fiz. **35**, 1052 (1958) [Sov. Phys. JETP **8**, 734 (1958)].

Translated by R. S. Wadhwa

Exchange metamagnetism in systems with triangular structure

Yu. D. Zavorotnev and L. I. Medvedeva

A. Galkin Physicotechnical Institute, National Academy of Sciences of the Ukraine, 340114 Donetsk, Ukraine[*]

The splitting of magnetization jumps in the metamagnetic phase of compounds based on iron phosphide in a magnetic field is obtained as a result of analysis of two models with the Landau potential with different degrees of complexity. The conditions for realization of transitions between the paramagnetic, metamagnetic, and ferromagnetic phases are established.
© *1997 American Institute of Physics.* [S1063-777X(97)00509-4]

INTRODUCTION

The expansion of the Landau potential in the complete rational basis of invariants (CRBI)[1] is expedient for describing the behavior of the magnetic order parameters depending on external conditions. Nine such invariants existing for crystals with the triangular arrangement of atoms permit 15 physical states.[2] In order to describe a specific state, we need to consider only a few of CRBI invariants. An analysis of the behavior of the ferromagnetic order parameter of structures with the triangular arrangement of magnetic atoms in a magnetic field on the basis of the Landau phenomenological theory was carried out in Ref. 3, where we took into account each of the mixed invariants, one by one. The results of the theoretical analysis were compared with the experimental data for compounds based on iron phosphide Fe_2P, which have the symmetry group D_{3h}^3.[4] Iron phosphide has a hexagonal crystalline structure whose unit cell contains six Fe atoms lying in two triply degenerate, crystallographically inequivalent positions Fe(1) and Fe(2),[5] which differ in that they lie in basal planes alternating along the c-axis. In each plane, these atoms form a triangular lattice.

When the stoichiometric composition deviates towards deficiency of iron atoms ($Fe_{2-\varepsilon}P$), or when the composition changes due to the substitution of Mn for Fe in $(Fe_{1-C}Mn_C)_2P$, the T vs. P, ε, and C diagrams reveal a certain metamagnetic phase MM_2 as under the effect of external pressure[6] (this phase differs from the phase MM_1 observed for $P, \varepsilon, C=0$),[7] which exhibits the metamagnetic behavior in a field. For a certain critical value of the field H_c, the MM_2 phase of the compounds $(Fe_{1-C}Mn_C)_2P$ and $Fe_{2-\varepsilon}P$ is characterized by a jump on the field dependence of magnetization. An increase in external pressure as well as in the parameter C leads to the splitting of this jump into two.[8] Such a behavior of the ferromagnetic order parameter in a field can be obtained by selecting an appropriate state from 15 physically admissible states and by retaining the required invariants in the expansion of the Landau potential into a power series in CRBI. It was found that the magnetization jumps in a field can take place if we choose the state $\mathbf{F} \| \mathbf{L}_1 (\mathbf{L}_2=0)$ for describing the magnetic structure of the MM_2 phase and include the term F^2L^4 into the Landau potential.[3] However, the splitting of the magnetization jump into two in a magnetic field upon a change of external conditions (T, P, C) as well as the behavior of the phase bound-

ary in the magnetic field were not analyzed in this case. The present publication is devoted to an analysis of these aspects.

NONSYMMETRIC MODEL (F^2, L^6)

It is well known[2] that the CRBI of a crystal with triangular structure consists of nine invariants, six of which are mixed, i.e., depend on three order parameters $\mathbf{F} = \mathbf{s}_1 + \mathbf{s}_2 + \mathbf{s}_3$; $\mathbf{L}_1 = \mathbf{s}_1 + \mathbf{s}_2 - 2\mathbf{s}_3$; $\mathbf{L}_3 = \sqrt{3}(\mathbf{s}_1 - \mathbf{s}_2)$, where $\mathbf{F}$ is the ferromagnetic and $\mathbf{L}_1$ and $\mathbf{L}_2$ are antiferromagnetic vectors, and $\mathbf{s}_i$ ($i=1,2,3$) is the spin moment of the ith ion. Among possible states, we single out a configuration for which $\mathbf{F} \| \mathbf{L}_1 (\mathbf{L}_2=0)$. Such a choice is based on the results of analysis carried our in Ref. 3. In order to explain the nontrivial behavior of the ferromagnetic order parameter as a function of H, we retain in the Landau potential only two out of six mixed invariants and write it in the form

$$\Phi = \frac{1}{2} a_1 F^2 + \frac{1}{2} b_1 L^2 + \frac{1}{4} b_2 L^4 + \frac{1}{6} b_3 L^6 + \nu_1 F^2 L^4$$
$$+ \nu_2 F L^3 - FH, \tag{1}$$

where H is the external magnetic field strength, and a_1, b_1, b_2, b_3, ν_1, ν_2 are phenomenological coefficients of exchange origin, of which all but a_1 and b_3 can be functions of external conditions. It should be noted that potential (1) is too simplified and hence cannot be used for describing the ferromagnetic (FM) state. For this reason, we consider only peculiarities in the behavior of the metamagnetic MM_2 state in the field as well as the phase transition (PT) between the MM_2 and the paramagnetic (PM) phases. The disregard of four mixed invariants leading to a change in the symmetry of the problem is admissible since the chosen structure $\mathbf{F} \| \mathbf{L}_1 (\mathbf{L}_2=0)$ corresponds to the triangular configuration of magnetic atoms,[2] while their inclusion leads to mismatching of the experimental and theoretical field dependences of the magnetization of the MM_2 state. It can be easily established from the relevant equations of state that the following relation holds for the MM_2 phase:

$$F = \frac{H - \nu_2 L^3}{a_1 + 2\nu_1 L^4}, \tag{2}$$

where L is the solution of a 12th degree equation. According to (2), the quantities F and L have opposite signs for $H=0$, i.e., $(\mathbf{F} \cdot \mathbf{L}) < 0$. The $F(H)$ curve obtained as a result of numerical solution of the corresponding system of equations
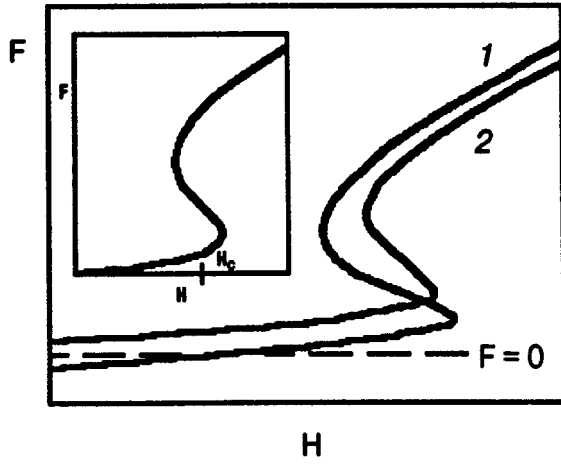
FIG. 1. Field dependences of branches of the ferromagnetic order parameter F for $\nu_2 \neq 0$. Branch 1 corresponds to positive values of L and branch 2 to negative values of L. The inset shows the field dependence of the ferromagnetic order parameter F for $\nu_2 = 0$.

FIG. 2. Field dependence of magnetization M for $\nu_2 = 0$ (curve 1) and $\nu_2 \neq 0$ (curve 2).

for $\nu_2 = 0$ is shown in the inset to Fig. 1. It can be seen that an S-shaped kink appears in the vicinity of the critical field H_c. It should be noted that for $\nu_2 = 0$, one curve $F(H)$ corresponds to two symmetric curves $\pm L(H)$. The inclusion of the invariant FL^3 into (1) leads to the emergence of two branches of the solutions F_1, F_2 and L_1, L_2 which are symmetric in zero field, and the splitting is proportional to the coefficient ν_2. This means that for $H = 0$, the crystal consists of two domains so that $\mathbf{F}_1 \uparrow \downarrow \mathbf{L}_1$, $\mathbf{F}_2 \uparrow \downarrow \mathbf{L}_2$, $\mathbf{F}_1$ and $\mathbf{F}_2$ being also antiparallel. As a result, the magnetization is equal to zero for $H = 0$. In this case, each of the $F(H)$ curves has S-shaped segments displaced relative to each other and having different hystereses (see Fig. 1). The magnetization M can be obtained by summing up the values of the branches of $F(H)$. The displacement of the S-shaped segments leads to splitting of a magnetization jump into two in the field. which is actually observed in experiments with Fe$_2$P under the action of pressure[8,9] or upon a change in the concentration C.[6] Hence, it follows that the coefficient ν_2 depends considerably on P or C. As the value of ν_2 increases, the magnetization jumps are displaced relative to each other upon an increase or decrease in H, the rate of this displacement being different. This leads to different values of hysteresis for the first and second jumps (Fig. 2).

In order to determine the stability boundary of the MM$_2$ phase, we have two equations

$$\frac{\partial \Phi}{\partial L} = L[L^{12} 4 \nu_1^2 b_3 + L^{10} 4 \nu_1^2 b_2 + L^9 (-6 \nu_2^2 \nu_1)$$

$$+ L^8 4 \nu_1 (a_1 b_3 + \nu_1 b_1) + L^6 2 \nu_1 (2 a_1 b_2 + 2 \nu_2^2$$

$$+ 3 \nu_2 H) + L^5 (-3 \nu_2^2 a_1) + L^4 (a_1^2 b_3 + 4 a_1 b_1$$

$$- 8 \nu_1 \nu_2 H) + L^2 (a_1^2 b_2 + 4 \nu_1 H^2 + 3 \nu_2 H a_1)$$

$$+ a_1^2 b_1] = 0, \qquad (3)$$

$$\frac{\partial^2 \Phi}{\partial L^2} = L[L^{11} 16 \nu_1^2 b_3 + L^9 8 \nu_1^2 b_2 + L^7 8 \nu_1 (2 a_1 b_3 + \nu_2^2)$$
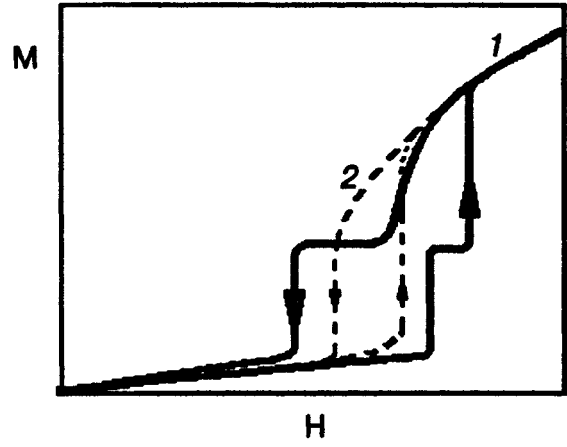
$$+ L^5 8 \nu_1 a_1 b_2 + L^4 (-10 \nu_1 \nu_2 H) + L^3 a_1 (4 a_1 b_3$$

$$- 3 \nu_2^2) + L^2 (a_1^2 b_2 + 4 \nu_1 H^2) + 3 \nu_2 a_1 H] = 0.$$

In zero field ($H = 0$), if $4 a_1 b_3 - 3 \nu_2^2 > 0$ ($a_1 > 0, b_2 > 0$), the only possible solution is $L = 0$, i.e., we have a second-order PT, and $b_1 = 0$ in this case. For $4 a_1 b_3 - 3 \nu_2^2 < 0$, two sign reversal are observed in the set of coefficients. In the equation of state, such a change of sign in the set of coefficients is associated with the coefficient ν_2. Consequently, a nonzero solution of system (3) can appear for $b_1 > 0$ ($T > T_N$, where T_N is the Néel temperature), i.e., we are dealing with a first-order PT between the PM and MM$_2$ phases. A situation leading to the sign reversal of the coefficient of L^3 in (3) (i.e., to a first-order PT) can also emerge under the action of pressure or upon a change in concentration. It should be noted that a first-order PT in $H = 0$ is also observed for $b_2 < 0$.

An interesting singularity is observed for $4 a_1 b_3 - 3 \nu_2^2 > 0$ ($b_2 > 0$). When the field is applied, the coefficient of L^4 in the brackets in (3) is nonzero and negative, i.e., the solution $L \neq 0$ appears for a certain value of the field, and the second-order PT changes to a first-order PT (tricritical point on the T–H plane). The change in the type of magnetic PT in the absence of structural distortions was predicted in the exchange-striction model,[10] in which pressure served as the external parameter. This effect is also possible when the concentration C changes (Mn$_{1-C}$Ti$_C$As).[11] In our case, the role of external parameter is played by the magnetic field.

NONSYMMETRIC MODEL (F^4, L^6)

The minimum complication of the model is associated with the addition of a fourth-order term in F to the potential. In this case, we have

$$\Phi = \frac{1}{2} a_1 F^2 + \frac{1}{4} a_2 F^4 + \frac{1}{2} b_1 L^2 + \frac{1}{4} b_2 L^4 + \frac{1}{6} b_3 L^6$$

$$+ \nu_1 F^2 L^4 + \nu_2 F L^3 - F H. \qquad (4)$$

Here all the coefficients except a_2 and b_3 can be functions of external conditions. Potential (4) describes a more realistic
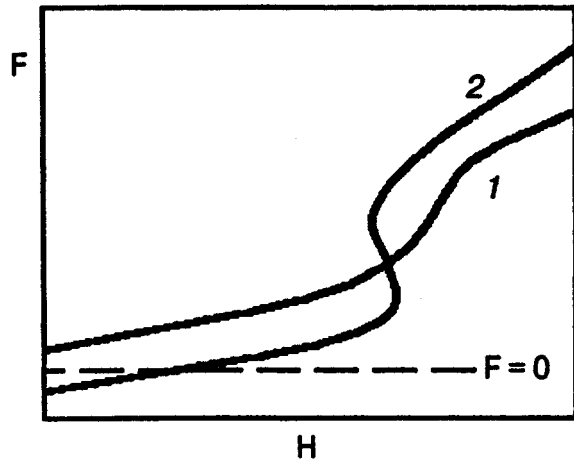
FIG. 3. Field dependences of the branches of ferromagnetic order parameter F for the nonsymmetric model ($F^4 L^6$), $L < 0$ (curve 1) and $L > 0$ (curve 2).

model as compared to (1) since it permits the ferromagnetic state also. The solutions of the system of equations of states were found numerically. For small values of the coefficient a_2, the dependences $F(H)$ and $L(H)$ are similar to those in Fig. 1. An increase in a_2 first leads to gradual smoothing of the branch of $F(H)$ corresponding to negative values of $L(H)$ (Fig. 3). Upon a further increase in a_2, the S-shaped region disappears on the second branch also.

Let us consider the PT between the MM$_2$ and FM phases. The stability curve of the FM phase can be described by a fifth-degree determinant, which can be easily evaluated and gives

$$a_1^3 = -\frac{27 a_2 H^2}{4}. \tag{5}$$

According to the stability condition for the metamagnetic phase, the relation

$$F^2 = -\frac{a_1 + 2\nu_1 L^4}{3 a_3}. \tag{6}$$

must be satisfied on the stability boundary. This equality necessitates the fulfillment of the condition $-a_1 \gg 2\nu_1 L^4$. Consequently, the stability curves of the FM and MM$_2$ phases do not coincide, and the PT between them is of first order. A numerical solution of Eq. (6) together with the system of equations of state for $H \neq 0$ shows that the temperature with increasing field difference determined from (5) and (6) increases in magnitude, i.e., the stability curves in the field do not intersect. Hence it follows that the PT between FM and MM$_2$ is of the first order irrespective of the magnitude of the field.

Let us consider the PT between the PM and MM$_2$ phases. A numerical analysis of the system of equations of state shows that the solutions $F(0)$ and $L(0)$ have opposite signs and the quantity $(\mathbf{F} \cdot \mathbf{L})$ is negative. This leads to a change in sign in the set of coefficients in the equations of state and in the stability condition for $b_1 > 0$. It then follows that, owing to the inclusion of the invariant FL^3, we have a solution with $L \neq 0$ for $b_1 > 0$ ($T > T_N$). At the same time, the stability curve for the PM phase ($L = 0$) corresponds to

$b_1 = 0$. This means that the PT from the MM$_2$ to the PM phase is of first order. An interesting situation occurs when a magnetic field is applied. In this case (see Fig. 1), one of the solutions of $F(H)$ changes sign for a certain value of the field. This means that no sign reversal is observed in strong fields in the equations determining the stability curve, and the only possible solution is $F = L = 0$. Consequently, for this solution we have a second-order PT from the PM to the MM$_2$ phase, while for the other branch this is a first-order transition.

It should be emphasized that splitting similar to that considered above also takes place for the invariant FL^5. However, this case should be analyzed by taking into account terms with a power higher than sixth in the power expansion of the Landau potential.

CONCLUSIONS

In our earlier publication,[3] we proposed that the MM$_2$ phase can be described by the structure $\mathbf{F} \| \mathbf{L}_1 (\mathbf{L}_2 = 0)$. Proceeding from this assumption, we analyzed successively two models with Landau potentials of different complexities. The analysis leads to the following conclusions.

(1) In the nonsymmetric model ($F^2 L^6$), the conditions under which the PM–MM$_2$ transition in iron phosphide is of first order are determined, and the splitting of the $F(H)$ curve into two branches is obtained. This is reflected in the formation of an additional step on the magnetization curve as a function of field in experiments on the samples of $(Fe_{1-C}Mn_C)_2 P$ or $Fe_2 P$ under pressure.

(2) In the nonsymmetric model ($F^4 L^6$), the conditions for a first-order PT between PM and MM$_2$ phases are established. It is found that in this approximation only one of the two domains experiences a transition from the MM$_2$ to the FM phase. The problem on the transition of the second domain into the FM phase can probably be solved by using the symmetric model ($F^6 L^6$).

[*]E-mail: kamenev@host.dipt.donetsk.ua

[1] Yu. M. Gufan, *Structural Phase Transitions* [in Russian], Nauka, Moscow (1982).
[2] A. V. Vedyashkin and Yu. M. Gufan, Fiz. Tverd. Tela (St. Petersburg) **34**, 714 (1992) [Sov. Phys. Solid State **34**, 382 (1992)].
[3] Yu. D. Zavorotnev and L. I. Medvedeva, Fiz. Tekh. Vys. Davl. **6**, 41 (1996).
[4] J. B. Goodenough, J. Solid State Chem. **7**, 428 (1973).
[5] R. Wappling, L. Haggstrom, and T. Ericsson, J. Solid State Chem. **13**, 258 (1975).
[6] L. I. Medvedeva and S. I. Khartsev, Fiz. Tverd. Tela (Leningrad) **31**, 78 (1989) [Sov. Phys. Solid State **31**, 43 (1989)].
[7] E. A. Zavadskii, L. I. Medvedeva, and A. E. Filippov, JMMM **43**, 54 (1984).
[8] H. Kadomatsu, M. Isoda, K. Tohma, *et al.*, J. Phys. Soc. Jpn. **54**, 2690 (1985).
[9] L. I. Medvedeva and S. I. Khartsev, Fiz. Tekh. Vys. Davl. **34**, 27 (1990).
[10] C. P. Bean and I. S. Rodbell, Phys. Rev. **126**, 104 (1967).
[11] E. G. Galkina, E. A. Zavadskii, V. I. Kamenev, and D. A. Yablonskii, Preprint Donetsk Physicotechnical Inst. No. 83-8(63), Donetsk (1983).

Translated by R. S. Wadhwa

711   Low Temp. Phys. 23 (9), September 1997

Yu. D. Zavorotnev and L. I. Medvedeva   711

ELECTRONIC PROPERTIES OF METALS AND ALLOYS

Point-contact-spectroscopy evidence of quasi-particle interactions in RNi$_2$B$_2$C (R=Ho, Y)

I. K. Yanson,[1,2] V. V. Fisun,[1,2] A. G. M. Jansen,[1] P. Wyder,[1] P. C. Canfield,[3] B. K. Cho,[3] C. V. Tomy,[4] and D. McK. Paul[4]

[1]*Grenoble High Magnetic Field Laboratory, Max-Planck-Institut für Festkörperforschung and Centre National de la Recherche Scientifique, B.P. 166, F-38042 Grenoble Cedex 9, France*
[2]*B. Verkin Institute of Low Temperature Physics and Engineering, National Academy of Sciences of Ukraine, 310164 Kharkov, Ukraine*[*]
[3]*Ames Laboratory, Iowa State University, Ames, Iowa 50011, U.S.A.*
[4]*Department of Physics, University of Warwick, Coventry CV4 7AL, UK*

The point-contact (PC) d^2V/dI^2-spectra of HoNi$_2$B$_2$C and YNl$_2$B$_2$C reveal structure at applied voltages corresponding to the phonon frequencies. At about 4 meV a maximum is observed in the phonon density of states by analogy to the soft-phonon structure in neutron scattering experiments for LuNi$_2$B$_2$C [P. Dervenagas *et al.*, Phys. Rev. B52, R9839 (1995)] and YNl$_2$B$_2$C [H. Kawano *et al.*, Czech. J. Phys. 46, S2-825 (1996), Phys. Rev. Lett. **77**, 4628 (1996)]. In the Ho compound the low-energy phonon peak is suppressed by an applied magnetic field in an anisotropic way, pointing to an interaction between the phonons and the magnetic systems. Surprisingly, in the nonmagnetic Y compound the 4-meV peak is also suppressed by a magnetic field. In the Ho-compound contacts which show the ⟨quasi-thermal⟩ behavior, the detailed magnetic-field and temperature dependences of PC spectra suggest that the magnetic order is destroyed due to the coupled phonon-magnon subsystem which is driven out of equilibrium by electrons that pass through the contact, by analogy with the nonequilibrium phonon-induced destruction of the superconducting state in point contacts [I. K. Yanson *et al.*, JETP Lett. **45**, 543 (1987)]. The PC electron-phonon interaction (EPI) spectral functions are reconstructed and the estimates for the λ-parameter yield the values of the order of 0.1. Comparison with PC EPI spectra of nonsuperconducting and nonmagnetic LaNi$_2$B$_2$C. [I. K. Yanson *et al.*, Phys. Rev. Lett. **78**, 935 (1997)], as well as the comparative study of PC EPI and Andreev-reflection spectra for various contacts with superconducting Ho and Y compounds suggest that the low-energy part of the electron-quasi-particle interaction spectral function is responsible for the Cooper pairing in these materials. © *1997 American Institute of Physics.* [S1063-777X(97)00609-9]

1. INTRODUCTION

The recently discovered intermetallic compounds[1,2] (RNi$_2$B$_2$C(R=rare earth, Y, Sc, Th) show a very rich interplay between superconductivity and magnetism with higher superconducting and magnetic critical temperatures compared with the rare-earth rhodium borides and molysulfides (selenides) magnetic superconductors.[3] These materials are now being studied intensively by various experimental techniques.[4–10] However, there are only a few reports concerning the application of the tunneling spectroscopy method.[11–14] All of them deal with the nonmagnetic compounds. This circumstance is probably attributable to the difficulties in preserving the fine balance between intra- and inter-layer magnetic interactions at the tunnel junction interfaces with the magnetic compounds.

The point-contact spectroscopy (PCS) involves studies of the nonlinearities of current-voltage characteristics of metallic constrictions with characteristic size d smaller than the inelastic electron mean free path l_{in}.[15,16] In contrast with a tunneling junction, an ideal point contact has no interfaces. In the case of a junction made of dissimilar electrodes, PCS has the advantage that the material is probed into the depth of the current spreading region, which is of the order of the constriction size. On one side, this size may be large enough to make a negligible contribution of the spoiled interface layers to the point-contact spectrum; on the other side it may be not too large with respect to the condition of the spectroscopic regime of current flow,

$$d \lesssim \min(l_{in}, \sqrt{l_{in}l_e}), \tag{1}$$

where l_e is the elastic scattering mean free path.

The voltage dependence of the differential resistance of a ballistic point contact reflects the energy-dependence of the scattering cross section of the conduction electrons, such that the point-contact spectra [$d^2V/dI^2(V)$ dependences] are proportional to the electron-phonon-interaction (EPI) spectral function. In the case of point contacts between different metals with strongly different Fermi velocities, only the spec-
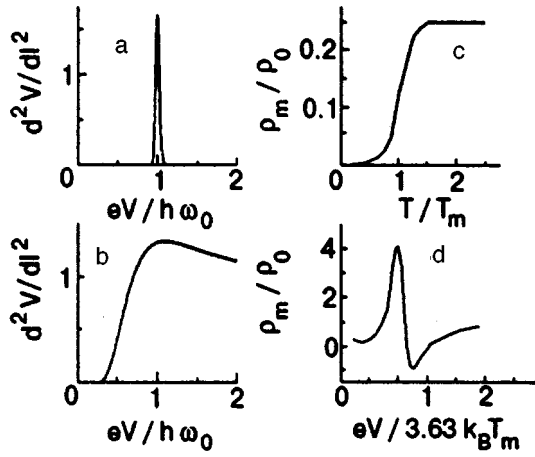
FIG. 1. Schematic diagrams of the PC d^2V/dI^2-spectra for an Einstein-type phonon spectrum for the spectroscopic (either ballistic or diffusive) (a) and thermal (b) regimes of current flow. Theoretical $d^2V/dI^2(V)$ dependence (d) calculated in the thermal limit for the $\rho_m(T)$ dependence[17] (c); ρ_0 is the residual resistivity of a metal.

trum of the material with the smaller Fermi velocity ν_F is seen:[16]

$$\frac{d \ln R}{dV}(V) = \frac{4}{3}\frac{ed}{\hbar v_F} g_{PC}(\omega)\bigg|_{\hbar\omega=eV}; \quad (T \simeq 0). \qquad (2)$$

The function $g_{PC}(\omega) = \alpha_{PC}^2 F(\omega)$ is similar to the Eliashberg function. Here $\alpha_{PC}^2(\omega)$ is the averaged EPI matrix element with kinematic restrictions imposed by the contact geometry, and $F(\omega)$ is the phonon density of states. The contact diameter d is determined by the normal-state resistance at zero bias R_0 via the Sharvin expression.[16] In the case of copper $d \simeq 30/\sqrt{R_0[\Omega]}$ nm, which we shall use for further estimates.

In the spectroscopic regime [Eq. (1)] no heating of the contact area occurs. However, if the contact size is large compared with the electron energy-relaxation length $\Lambda_\varepsilon = \min(l_{in}, \sqrt{l_{in}l_e})$, then there is a local heating of the contact with a maximum temperature T_0 at the center of the contact given by the Kohlrausch relation

$$V^2 = 4L(T_0^2 - T^2) \qquad (3)$$

for an applied voltage V across the contact at the bath temperature T. This relation transforms into $eV = 3.63k_B T_0$ or 1-mV applied voltage corresponds to 3.20-K temperature increase at the contact for the standard Lorentz number $L = 2.44 \cdot 10^{-8}$ V^2/K^2 (assuming $T=0$). In the thermal regime the PCS-spectrum of an Einstein oscillator $\hbar \omega_0$ looks like a smeared step with a shallow maximum at $eV = 1.09\hbar\omega_0$.[17,18] In Figs. 1a and 1b the point-contact spectra of the electron interaction with an Einstein phonon-mode are shown schematically for, respectively, the spectroscopic (either ballistic or diffusive) and the thermal regimes.

The thermal feature in the PC spectra can be quite sharp if a phase transition occurs at a particular temperature T_m, which leads to the jump-like increase of the temperature-dependent contribution $\rho_m(T)$ to the resistivity (see Fig. 1c). Such a situation holds, for example, for the ferromagnetic metals (Ni, Fe) at the voltages corresponding to the Curie

temperatures. In this case a maximum on the dV/dI curve and a sharp "N"-type feature on the second derivative d^2V/dI^2 (Fig. 1d appears at about $eV_m \simeq 3.63k_B T_m$).[17]

Similar peculiarities in the PC d^2V/dI^2 spectra of superconductors appear if the average concentration of quasiparticle excitations exceeds a critical value, destroying the superconducting order parameter in the contact region. It was found[19] that the voltage positions of these "N"-type features tend to coincide with the characteristic energies of slow phonons in a superconductor. These slow phonons are accumulated in the contact region, breaking effectively the Cooper pairs. This effect strongly enhances the intensity of the phonon spectral lines, which simultaneously modifies their shape. It is especially effective in the dirty contacts ($l_e \ll d$), where the intensity of the conventional phonon-induced backscattering processes are suppressed by the factor $\sim l_e/d$, and the slow phonon rate is further decreased by diffusion.

We will show below that in the HoNi$_2$B$_2$C contacts a similar effect on the phonon-structure occurs due to the destruction of the magnetic order by nonequilibrium phonons. To distinguish this nonequilibrium effect from the true thermal limit we shall call it the "quasi-thermal" limit. In this regime the nonequilibrium conduction electrons remain "cold", i.e., the Fermi distribution is smeared only by the environmental temperature[20] with an excess energy controlled by bias voltage.

In the present PCS study, we attempt to determine which interactions are the most efficient in the scattering of the conduction electrons in RNi$_2$B$_2$C. They are most likely the candidates to serve as mediators in the superconducting pairing mechanism. Although it was proposed that these materials fall into the class of common phonon-mediated superconductors,[21] there is disagreement as to which phonons play a major role. Mattheiss, Siegrist, and Cava[22] emphasize the role of high energy ($\hbar\omega = 106$ meV) boron A_{1g} vibrations, while Pickett and Singh[23] estimate the characteristic Debye energy to be rather low (about 300 K) and point out the importance of low-energy phonon branches. The first point of view finds confirmation in the observation of an appreciable boron-isotope effect in YNi$_2$B$_2$C,[24] while the second is consistent with the recent findings of phonon softening in LuNi$_2$B$_2$C.[25] The controversy can be continued by mentioning the temperature dependence of the heat capacity of the nonmagnetic compound YNi$_2$B$_2$C driven to the normal state by magnetic fields, which shows an apparent lattice stiffening.[26] Moreover, the recent comparative study of the normal-state transport and magnetic properties of non-superconducting LaNi$_2$B$_2$C and superconducting YNi$_2$B$_2$C and HoNi$_2$B$_2$C (Ref. 27) have questioned the phonon-mediated superconducting pairing mechanism.

We have found reproducible peaks in the d^2V/dI^2 spectra of Ag(Cu)$-$RNi$_2$B$_2$C (R=Ho, Y) point-contacts situated at energies of about 4–20 meV. The positions of these features on the voltage axis correlate well with the characteristic energies of slow phonons found in the neutron measurements on LuNi$_2$B$_2$C (Ref. 25) and YNi$_2$B$_2$C (Ref. 28). The intensity of the soft phonon peaks in the PC EPI spectra of HoNi$_2$B$_2$C can be suppressed by temperature and magnetic field, show-

ing the anisotropy expected from the magnetic phase diagram.[6] In nominally nonmagnetic YNi$_2$B$_2$C the intensity of the soft phonon mode also depends on the magnetic field. The linear background in the PC spectra of both compounds corresponds to a quadratic energy dependence of the contact resistance and could originate from electron-electron or electron-magnon (paramagnon) scattering.

The high energy part of the PC spectrum of the Ho and Y compounds is dominated for most contacts by a background signal. The saturation of this background signal at about $eV \simeq 100$ meV coincides with the high-frequency boron-vibration energy and points to an appreciable EPI at this energy, as predicted by theory.[22] Nonetheless, comparing the PC spectra of Ho and YNi$_2$B$_2$C contacts, which reveal different superconducting properties, and taking into account the results of our PCS study of nonsuperconducting LaNi$_2$B$_2$C (Ref. 29), we conclude that the low-energy part of the EPI spectra is mainly responsible for the Cooper pairing in these compounds.

2. METHODICAL DETAILS

The contacts are made by pressing together directly in the cryostat the sharp edge of a small silver (copper) bar to the ab-plane edge of HoNi$_2$B$_2$C or YNi$_2$B$_2$C single crystals, which were prepared via the Ni$_2$B flux-growth method developed at Aims Laboratory.[30] During one run, many contacts with different contact resistances (in the range from several tenths to several tens of an Ohm) at different sites of the crystal surface could be created. Typical contact resistances chosen for the extensive temperature- and magnetic-field-dependent measurements are about 1 Ω, which corresponds to a contact size d of about 30 nm. This is of the same order of magnitude as the electron mean free path in the starting material at low temperatures. Thus, one may expect the spectroscopic regime of current flow not to be violated in the best contacts studied. Such contacts were chosen among many trials by looking at the Andreev reflection (AR) spectra $dV/dI(V)$ at $T \ll T_c$, which for the selected junctions reveal critical temperatures and superconducting energy gaps close to the following typical values: $T_c = 15.4$ K, $\Delta = 2.4 \pm 0.07$ meV and $T_c = 8.5$ K, $\Delta = 1.04 \pm 0.06$ meV for, respectively, the Y- and Ho-based compounds.[31]

In Figs. 2a and 2b typical examples of the AR spectra for contacts with the Y and Ho compounds are shown, along with the fitting curves calculated according to the Blonder–Tinkham–Klapwijk–Dynes (BTKD) model.[32] The matching of the smearing parameter Γ (beyond the energy gap Δ_0 and barrier parameter Z) is essential in order to obtain a good fit for the two materials. The relatively large Γ values for the Ho compound are evidently connected with the magnetism in the superconducting state. Even for the nominally nonmagnetic Y-compound point contacts the BTKD-fit often does not follow the experimental points at energies greater than about 4 meV, as can be seen in Fig. 2a and Fig. 12c. As will be shown below, this energy corresponds to a maximum in the PC electron-phonon interaction spectral function for both YNi$_2$B$_2$C and HoNi$_2$B$_2$C. In HoNi$_2$B$_2$C point-contacts similar kinks on the $R(V)$ curves are often more smeared due to the larger Γ values, as is the case in Fig. 2b. It should be
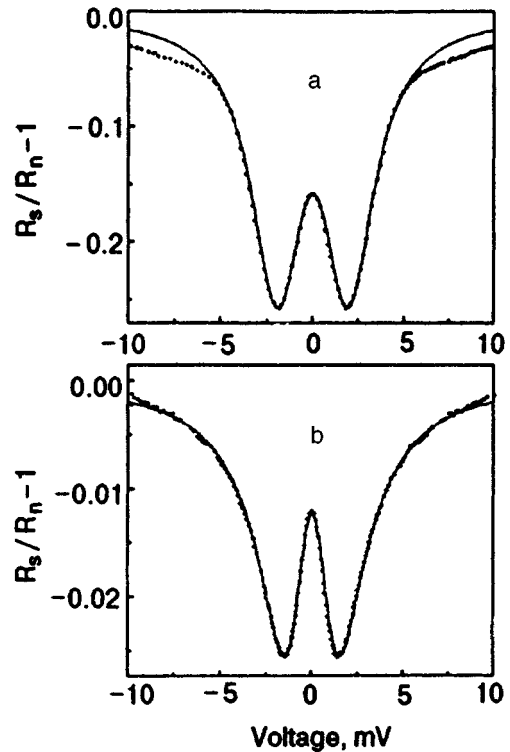

FIG. 2. Andreev reflection spectra in reduced units at $H=0$ for YNi$_2$B$_2$C-Cu (a) and HoNi$_2$B$_2$C-Ag (b) point contacts. R_s and R_m are the $dV/dI(V)$ characteristics in the superconducting and normal states, respectively. The contact parameters and measurement conditions are: (a) $R_0 = 16.6$ Ω, $T_c = 15.4$ K, $T = 4.2$ K; (b) $R_0 = 0.77$ Ω, $T_c = 8.5$ K, $T = 1.6$ K. The solid curves represent the BTKD fits with the following parameters (see text): (a) $\Delta_0 = 2.1$ meV, $\Gamma = 0.6$ meV, $Z = 0.5$, SF = 1.19; (b) $\Delta_0 = 1.05$ meV, $\Gamma = 1.35$ meV, $Z = 0.595$, SF = 0.58.

noted that actually the BTKD fitting procedure involves a fourth parameter, the scaling factor SF. This parameter scales the amplitude of the change in the dV/dI with a factor of order unity and may be due either to the nonhomogeneity of the boro-carbide compound in the contact region or to the asymmetry of the junction geometry.

Although for both compounds in Fig. 2 the barrier parameters Z do not differ much and the reduced temperatures T/T_c are both $\ll 1$, the distance between dV/dI minima for the Ho compound ($2V_{\min} = 1.48$ meV) differs noticeably from the energy gap $\Delta_0 = 1.05$ meV of the fitting curve due to extremely the large value of the Γ-parameter. Hence, one should be careful in identifying the energy gap parameter $2\Delta_0$ with $2V_{\min}$ in the case of a large Γ.

The contact axis which determines the preferred direction of current flow is nominally parallel to the ab-plane. Its orientation with respect to the $a(b)$-crystallographic axis remains uncertain. A magnetic field up to 10 T can be applied either along the ab-plane or perpendicular to it. In the first case both parallel ($I\|H$) and perpendicular ($I\perp H$) orientations, with respect to the contact axis, have been investigated with not much difference in the results. Many different contacts were investigated and for the selected contacts a number of different characteristics were measured. Among them are temperature and magnetic field variations of $dV/dI(V)$, AR spectra, zero-bias magnetoresistance curves at different

temperatures, point-contact spectra in the normal state [$d^2V/dI^2(V)$ characteristics] at various fields and temperatures.

In all the graphs we plot the second harmonic signal $V_{2F}(V)$, which is directly measured in experiments and which is connected with the $d^2V/dI^2(V)$ characteristics through the expression.[15]

$$d^2V/dI^2(V) = 2\sqrt{2}R^2 V_{2F}(V)/V_{\text{mod}}^2, \qquad (4)$$

where V_{mod} and $R = dV/dI$ are, respectively, the effective value of the modulation voltage and the differential contact resistance. The experimental data are scanned from $-V_{\text{max}}$ to $+V_{\text{max}}$ voltage bias to show the reproducibility of spectral features. The voltage polarity in all graphs corresponds to the polarity of the normal metal electrode (Cu,Ag). For plotting the EPI spectral function $g_{PC}(\omega)$ we use the odd part of the spectra $F_{\text{odd}}(V) = 1/2[F(+V) - F(-V)]$, which contains the spectral information that does not depend on the voltage polarity and in most cases nearly coincides with the original curve. The modulation voltage V_{mod} and the temperature T determine the smearing of an infinitely narrow spectral peak according to the standard formula.[16]

$$\delta V = \sqrt{(5.44 k_B T/e)^2 + (1.72 V_{\text{mod}})^2}. \qquad (5)$$

The results presented are representative of more than several hundred junctions that we have measured. While comparing our findings with the properties of bulk material one should keep in mind that the PC method probes a small volume with linear dimensions of the order of $d = 10$ -100 nm, located at the crystal surface. Due to the extreme sensitivity of the material properties to small variations of the composition[13,33] some contacts show no superconductivity at all. Those contacts are discarded. Those which remain after application of the selection criteria based on the AR spectra, still preserve some dispersion in composition and structural perfection of the material in the contact region, as well as in random deviations of the contact axis from the nominal orientation, which are probably the main cause of the variety of characteristics observed.

3. EXPERIMENTAL RESULTS

3.1. HoNi$_2$B$_2$C

Phonon structure for different regimes of current flow. In Fig. 3 we present the PC spectra for different HoNi$_2$B$_2$C-Ag contacts in the normal state at fields greater than $H_{c2}(0) \simeq 0.55$ T but less than $1-2$ T at which, judging from the magnetization measurements,[5,6,34] the magnetic order is not yet completely destroyed. There are some variations in the spectral line shapes which are due to the uncontrolled variations of the contact shape, the orientation of the probed crystallite, and the value of the elastic electron mean free path in the contact region, which leads to the different regimes of current flow. Judging from the width of the spectral lines compared with the expected smearing (Eq. (5)), one can tentatively assume the regime of current flow in contact 1 to be close to spectroscopic. On the other hand, the sharp ''N''-type feature around ± 5 mV, with a negative overshooting with respect to the background in the PC spectrum
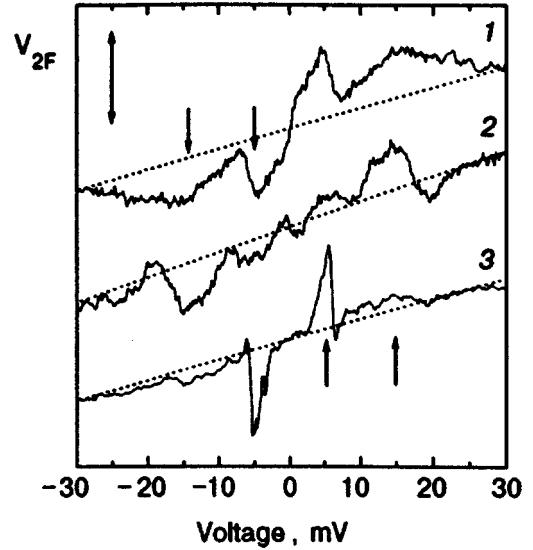

FIG. 3. Normal state point-contact spectra of HoNi$_2$B$_2$C-Ag contacts at $T = 1.6$ K. The contact resistance R, the magnetic field H, the modulation voltage V_{mod}, and the double-arrow bar for the calibration of the vertical axis are for each spectrum as follows: 0.7 Ω, 1.5 T, 0.7 mV, 0.21 μV (1); 0.53 Ω, 1 T, 0.9 mV, 0.55 μV (2); and 0.82 Ω, 0.7 T, 0.35 mV, 0.37 μV (3). Orientations of the contact axis (I) and magnetic field are for contacts 1 and 2 ($I\perp H)\perp c$, for contact 3 ($I\|H)\perp c$. The arrows mark the positions of the spectral bands common to all contacts. Dotted straight lines stand for the linear backgrounds. V_{2F} is the second harmonic signal which is proportional to the second derivative d^2V/dI^2 of the $I(V)$ characteristics [Eq. (4)]. For each curve $V_{2F} = 0$ at $V = 0$. Judging from the peak shapes the regimes of current flow can be classified as changing from spectroscopic (contact 1) to quasi-thermal (contact 3).

of contact 3, resembles the quasi-thermal lineshape shown in Fig. 1d. Similar negative overshooting is seen at about 20 meV in the spectrum of contact 2.

Despite these variations in lineshape, there are structures in the spectra of Fig. 3 at about 4–5 and 14–15 mV, which are common to all curves and which are marked by arrows. The lower energy is in striking correspondence with the characteristic energy of soft phonons, while the upper energy marks another characteristic phonon energy at which $\partial\omega/\partial q \simeq 0$ on the phonon dispersion curves of LuNi$_2$B$_2$C.[25] In some spectra the wide low-energy peak at about 6 mV is further resolved into bands at 4 and 8 mV, which nicely fit in more detail the neutron data (see below). These observations support the recent neutron findings[25] and prove that soft phonons are involved in the spectral structure of the EPI in these compounds.

The fine structure of the low-energy part of the HoNi$_2$B$_2$C EPI spectra is shown in Fig. 4 for two more contacts, which presumably corresponds to the spectroscopic conditions of the current flow. Besides demonstrating that the spectral features do not depend on the contact resistance (size), these curves are evidence of the independence of the spectra on the material of the counter electrode. The positions of the maxima in the PC EPI spectra marked by arrows lie close to the characteristic $\partial\omega/\partial q \simeq 0$ phonon energies of the low-temperature phonon dispersion curves of LuNi$_2$B$_2$C in the $[\zeta,0,0]$ direction,[25] which are 4, 8.5, 14, and 19 meV at 10 K. If the dispersion curves for other directions would be
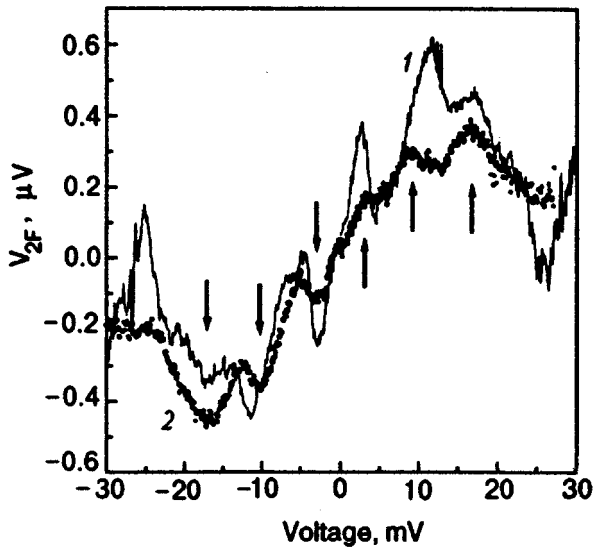
FIG. 4. Comparison of the phonon structure in the PC spectra of $HoNi_2B_2C$ with Ag (1) and Cu (2) counter electrodes at $T = 4.2$ K, $H = 1$ T. The parameters are: 1) $R = 0.85$ Ω, $V_{mod} = 0.6$ mV; 2) $R = 12$ Ω, $V_{mod} = 1$ mV. $I \| ab$, $H \| c$. The arrows mark the approximate peak positions common to both spectra.

FIG. 5. The magnetic field dependence of the PC spectra for a $HoNi_2B_2C$-Ag contact, which shows the strong suppression of the 4-meV peak for the spectroscopic regime of the current flow. The curves are shifted vertically. For each curve $V_{2F} = 0$ at $V = 0$. $H \|(ab)$. $R = 2.66$ Ω, $V_{mod} = 0.7$ mV, and $T = 1.65$ K.

known, a more detailed comparison with the total phonon density of states could be made. We emphasize that *all* PC EPI spectra of $HoNi_2B_2C$ contain the soft phonon maximum at about 4 meV.

Magnetic field dependence of phonon spectral peaks. Turning to the magnetic field dependence of the spectra, we first note that due to the preferential orientation of the Ho magnetic moments parallel to the ab-plane there is a strong anisotropy in magnetic properties of $HoNi_2B_2C$.[6,34,35] Bearing this in mind, we first describe the influence of the magnetic field H parallel to the direction of easy magnetization, i.e., $H \|(ab)$.

A magnetic field $H \|(ab)$ strongly influences the spectral features at low energies. For typical junctions we have observed a suppression of the 4-meV peak by magnetic fields of the order of several tesla. This behavior is illustrated in Fig. 5, where the peak positions are marked by an arrow. We disregard the zero-bias peak in the differential resistance, which does not show a systematic behavior in magnetic field and has no relevance for the electron-phonon interaction. The magnetic-field range of the soft-phonon-peak depression increases to 10 T. In Fig. 6 we show a contact with only a small influence of the field on the d^2V/dI^2-spectrum, where most of the phonon suppression occurs in fields up to about 2 T. Again, we regard the zero-bias anomaly as being nonessential for the phenomena considered here. Figure 7 shows a very strong magnetic field dependence for a contact with a spectrum similar to the one of contact 2 in Fig. 3, which clearly exhibits at 0.5 T the quasi-thermal-like ''N''-type feature at 19 mV. It follows from Fig. 7 that fields up to about 2 T strongly suppress the intensity of phonon lines, modifying their shape and position on the voltage scale. On the other hand, fields greater than 2 T (and up to 9 T) do not change dramatically the PC spectrum in Fig. 7, which con-
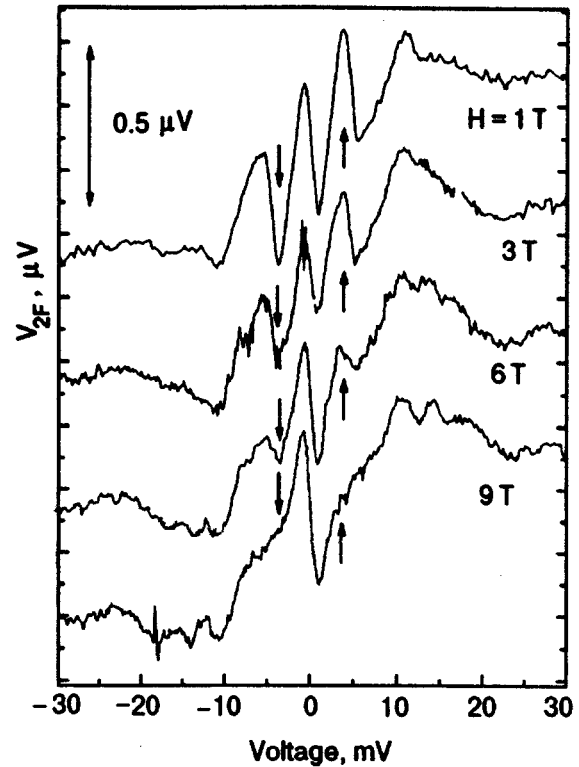
tains two maxima similar in shape, intensity, and energy position to those in Fig. 6.

The contacts with $HoNi_2B_2C$ showed very often a suppression of the phonon structures by an applied magnetic field along the (ab)-plane. For this field orientation, the magnetic order is destroyed above about 1–2 T.[5,6] Therefore, we conclude that our data show a strong interaction between the magnon and phonon branches of the excitation spectra, which enhances the electron-phonon interaction with low-energy phonons in $HoNi_2B_2C$, and which is suppressed by magnetic fields that destroy magnetic order in this compound.

For $H \| c$ the magnetic structure of $HoNi_2B_2C$ is much more robust and does not experience strong changes in the range of magnetic fields studied. The upper superconducting critical magnetic field $H_{c2}(0)$ in $\| c$ direction is about the same as for $H \perp c$.[34] Therefore, the superconductivity can be suppressed by $H \| c$ without influencing the magnetic order and without perturbing the phonon-magnon interaction. Two different junctions in Fig. 8 illustrate this behavior. The shape of the soft phonon feature at 3–5 mV remains almost unchanged in fields up to 7 T.

Temperature dependence of PC EPI spectra. The most trivial effect of the temperature on the PC spectra is related to the thermal smearing of spectral features according to expression (5). For increasing temperatures, this effect should lead to an increase of the peak width and a decrease of its intensity in such a way that the area under the peak remains
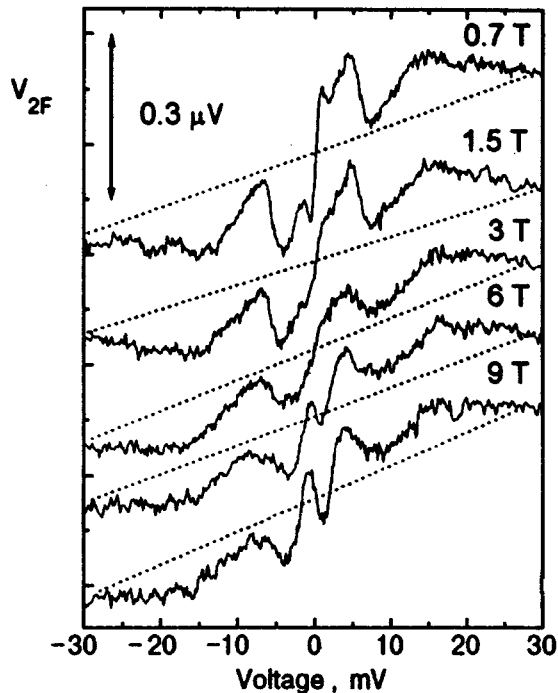
FIG. 6. The magnetic field dependence of the PC spectra for the HoNi$_2$B$_2$C-Ag point contact 1 in Fig. 3, which corresponds to the spectroscopic ("nonthermal") regime of current flow. $R = 0.7\ \Omega$, $T = 1.6$ K, $V_{mod} = 0.7$ mV. The curves are shifted vertically for clarity. For each curve $V_{2F} = 0$ at $V = 0$ and the assumed linear background is shown by the dotted line. Mutual orientation of the contact axis, the magnetic field, and the crystallographic basal plane corresponds to $(I \perp H) \| ab$.

FIG. 7. The magnetic field dependence for a HoNi$_2$B$_2$C-Ag point contact, which shows the "quasi-thermal" negative over-shooting beneath the linear background at fields of 0.5 and 1 T. $R = 0.5\ \Omega$, $V_{mod} = 0.8$ mV. The characteristics of this contact are very close to contact 2 in Fig. 3. The dotted straight lines represent the assumed backgrounds. For each curve $V_{2F} = 0$ at $V = 0$. Note the change of the phonon lineshape and the intensity the fields ≥ 2 T. $(I \perp H) \| ab$, $T = 4.2$ K.

approximately constant. The position of the spectroscopic structure should remain fixed on the voltage axis.

The spectrum of a HoNi$_2$B$_2$C-Ag has been plotted in Fig. 9 for temperatures from 4.2 to 13 K. With rising temperature, the structure at about 5–6 mV moves to lower voltages, which is still close to the characteristic soft phonon energy of 3–4 meV. The inset in Fig. 9 shows the position V_1 of the low-energy maximum on the $V_{2F}(V)$ curves as a function of temperature. The intensity of this maximum disappears suddenly between 11 and 12 K. Such an abrupt disappearance of the spectral peak in a narrow temperature interval cannot be attributed to a simple temperature-induced broadening. This points to a transition at $T_m \sim 12$ K, which is either a first- or very steep second-order transition. At higher temperatures, only a very wide and shallow PCS maximum at about 15 meV is seen, which is not surprising since the spectral smearing [see Eq. (5)] is rather large at these temperatures. Note also the change in the shape and the increase in the intensity of the soft phonon spectral peak while passing from the curve taken at $T = 8$ K and $H = 1$ T to $T = 8.4$ K and $H = 0$, which corresponds to the partial restoration of the magnetic order. Such behavior definitely proves that magnetism is involved in the observation of the electron-phonon interaction at low energies.

The observed shift of the lowest energy-peak at about 3 meV to higher energies, while lowering the temperature, contradicts the softening of the phonon energy observed in neutron-scattering experiments for the case of LuNi$_2$B$_2$C at low temperatures.[25] However, it corresponds to the tempera-
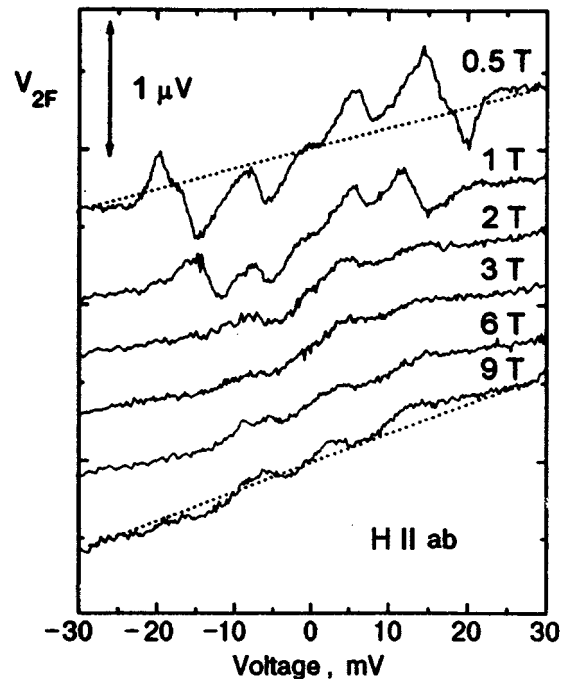
ture dependence of the 4-meV peak in neutron-scattering data on YNi$_2$B$_2$C.[28]

Since the position of a true spectral peak should not depend on the temperature, we can conclude that the temperature dependence of the lowest energy peak in Fig. 9 corresponds to an intermediate regime of the current flow. At low temperatures the regime is quasi-thermal (where there is a noticeable dependence of the peak position V_1 on the bath temperature) and for higher temperatures it gradually transforms into a spectral regime (where the peak position is fixed) due to the suppression of the magnetic order at higher temperatures and the disappearance of the nonequilibrium effects. Such transformations of the regimes of current flow in the strongly coupled electron-phonon-magnon system are probably due to the peculiar temperature dependences of the nonequilibrium phonon and magnon escape and relaxation rates in a contact.

Unfortunately, we were not able to study the point contacts which satisfy the spectroscopic conditions in the whole temperature range and which are stable enough to survive the whole series of temperature-dependent measurements.

3.2. YNi$_2$B$_2$C

Phonon structure at low energies and its magnetic field dependence. The PC spectra for the nonmagnetic Y compound reveal a broad phonon peak at about 12 meV, which does not depend on the magnetic field (Figs. 10a, and 10b). Because the same phonon structure is observed in Cu-YNi$_2$B$_2$C point contacts (Fig. 10b), it is not due to a

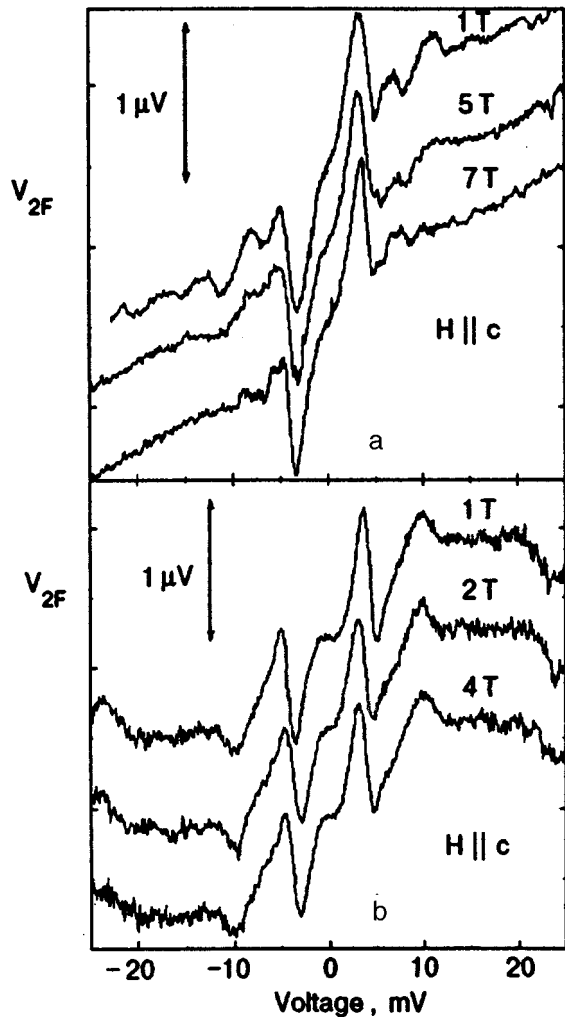FIG. 8. The magnetic field dependences of the HoNi$_2$B$_2$C PC spectra for $H\|c$ with Ag (a) and Cu (b) counter electrodes. The contact parameters and the measurement conditions are: (a) $R_0=1.51\,\Omega$, $V_{mod}=0.5$ mV, $T=4.2$ K; (b) $R_0=2.3\,\Omega$, $V_{mod}=0.7$ mV, $T=2.5$ K. Contact (b) is the same as in the lower panel of Fig. 13. For each curve $V_{2F}=0$ at $V=0$.

FIG. 9. The temperature dependence of the PC spectra for HoNi$_2$B$_2$C-Ag, which is similar to contact 2 in Fig. 3, and that shown in Fig. 7. $R=0.62\,\Omega$, $V_{mod}=0.95$ mV (for the uppermost curve $V_{mod}=1.0$ mV). $(I\perp H)\|ab$. The temperatures and fields are indicated. The dotted straight lines mark the assumed backgrounds. The curves are shifted vertically for clarity. For each curve $V_{2F}=0$ at $V=0$. The dashed lines are intended to follow the temperature dependence of the low-energy peak position V_1 as a guide to the eye (see the inset).

phonon contribution from the Ag electrode of the Ag-YNi$_2$B$_2$C contact. The absence of a Cu phonon band at 16–20 mV in the Cu-YNi$_2$B$_2$C contacts and the similarity of the PC spectra for the Cu-HoNi$_2$B$_2$C and Ag-HoNi$_2$B$_2$C contacts in Fig. 4 prove that the contribution of the noble metal electrodes to the spectra is strongly reduced, because the Fermi velocity in YNi$_2$B$_2$C and HoNi$_2$B$_2$C is substantially smaller than in Cu(Ag), as predicted by band structure calculations.[23]

In the YNi$_2$B$_2$C contacts a weaker structure at about 4 meV, indicated by the arrows in Figs. 10a and 10b is also observed. In order to study the normal state properties of these contacts, the applied magnetic field was above $H_{c2}=5-6$ T in order to suppress the superconductivity in YNi$_2$B$_2$C. In the spectrum of Fig. 10a a suppression of the low-energy phonon structure with a slight shift of the voltage position to lower values is observed in the limited field range from H_{c2} to 10 T. The spectrum in Fig. 10b shows a non-monotonic dependence on the magnetic field for the peak intensity, although without any change in the voltage posi-
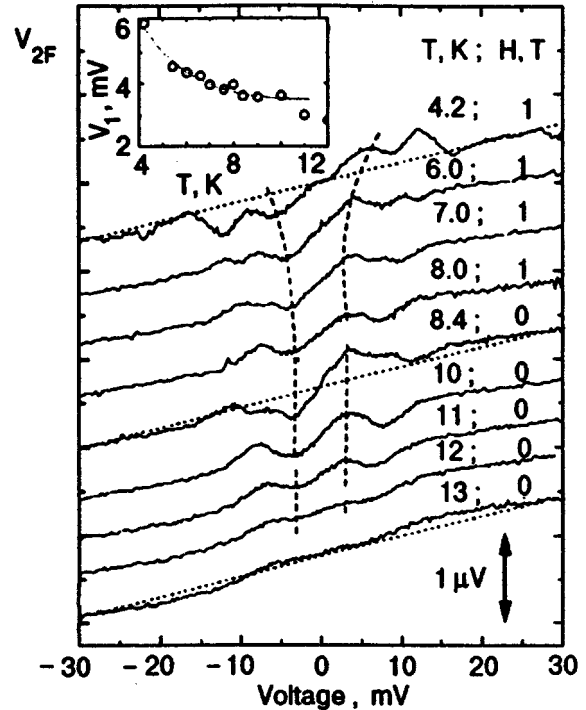
tion. A possible origin for the observed magnetic field dependence of this structure at low voltages could lay in the *magnetic interactions which would then even exist in the nominally nonmagnetic* YNi$_2$B$_2$C. Comparing the intensity of the 4-meV peak in YNi$_2$B$_2$C and HoNi$_2$B$_2$C PC spectra, one should note that to destroy superconductivity in YNi$_2$B$_2$C one has to apply a much higher field than that in the case of HoNi$_2$B$_2$C. The applied fields, for YNi$_2$B$_2$C being in the normal state could already suppress the observed structure at 4 meV.

The spectra of the YNi$_2$B$_2$C contacts shown in Fig. 10 illustrate the difference in the regimes of current flow corresponding to the contacts of different resistances (sizes). The rapid suppression of the low-energy phonon peak (marked by the arrow) in Fig. 10a and its shift to lower biases with increasing field resembles an analogous behavior of HoNi$_2$B$_2$C contacts (see Fig. 7) in the quasi-thermal regime of the current flow. The smaller contact (Fig. 10b) evidently is closer to the spectroscopic regime and, although the low-energy peak reveals a peculiar nonmonotonic dependence on the magnetic field, its position on the voltage scale remains fixed.

3.3. Evidence for high-frequency boron vibration mode

To cover the energy range including the A$_{1g}$ boron vibration mode with a characteristic frequency corresponding to 106 meV (Ref. 23), we have to extend our point-contact
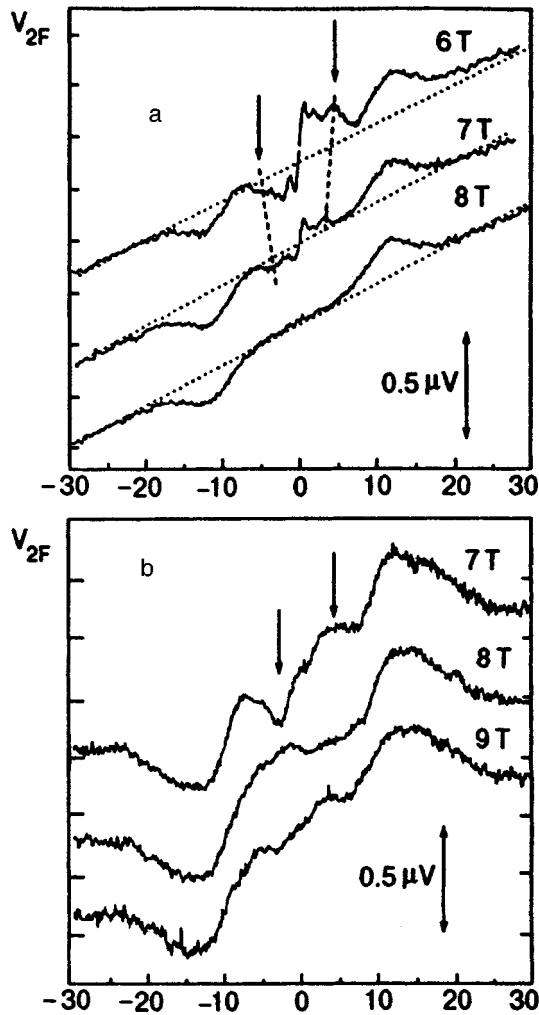
FIG. 11. The PC spectra where the boron vibrations at $eV \simeq 100$ mV take over at large biases, which presumably correspond to the thermal regime of the current flow. For the HoNi$_2$B$_2$C-Cu contact $R_0 = 1.91 \, \Omega$, $V_{mod}(V=0) = 0.55$ mV, and $H(\|c) = 0.6$ T; for the YNi$_2$B$_2$C-Cu contact $R_0 = 1.2 \, \Omega$, $V_{mod}(V=0) = 0.86$ mV, and $H(\perp c) \simeq 6$ T. $T = 4.2$ K.

FIG. 10. The low energy parts of the PC spectra of YNi$_2$B$_2$C with Ag (a) and Cu (b) counter electrodes at different magnetic fields and $T = 4.2$ K, which show the magnetic field evolution of the 4-meV phonon structure. The parameters are: (a) $R = 1.8 \, \Omega$, $V_{mod} = 0.6$ mV; (b) $R = 16.6 \, \Omega$, $V_{mod} = 1.1$ mV. In panel (a) the structure at zero-bias at $H = 6$ and 7 T is due to the not fully suppressed superconducting state. The dashed lines through the spectral maxima serve as a guide to the eye. For each curve $V_{2F} = 0$ at $V = 0$. The dotted straight lines indicate the assumed backgrounds. The contact in panel (b) is the same as in the upper panel of Fig. 13.

measurements to voltages about an order of magnitude larger than in the data presented above. The increase of bias voltage leads to a gradual departure from the spectroscopic regime that approaches the thermal limit. Therefore, in the PC spectra of the HoNi$_2$B$_2$C-Cu and YNi$_2$B$_2$C-Cu contacts shown in Fig. 11, the initial parts with the low-frequency phonon spectral peaks gradually transform into a background signal, which is linear up to 50–70 meV and either saturates or has a shallow maximum at about $= 100$ meV. This energy marks the end of the phonon spectrum and coincides roughly with the high-frequency boron vibration mode. The observation of clear features at this energy points to an appreciable electron-phonon interaction with the A$_{1g}$ boron mode.

4. DISCUSSION

4.1. The origin of the spectral structure

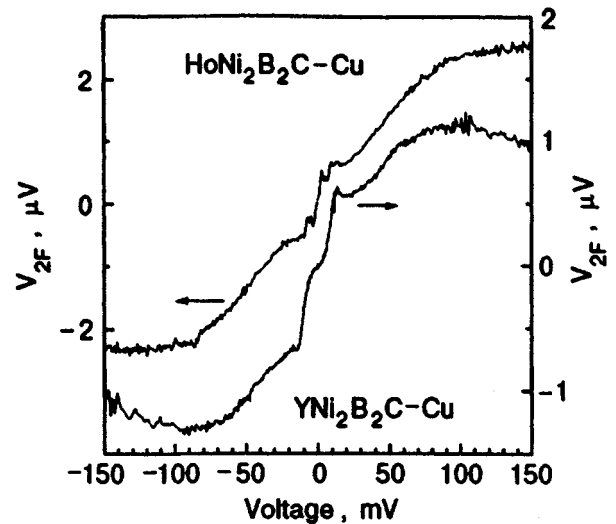*Low-energy phonons as a primary source of spectral structure.* The spectral structure at low bias voltages does not

depend on the counter electrode (Cu, Ag). Its position on the voltage scale is independent of the magnetic field and temperature, provided their origin can be classified as ''spectroscopic'', i.e., satisfying the conditions of PCS [see Eq. (1)] without noticeable contact heating or nonequilibrium effects (see below).

We can prove in several ways that the maxima in the PC spectra at 4–5 and 10–15 meV correspond to the low-energy *phonons* in RNi$_2$B$_2$C. First, they are situated at the characteristic phonon energies found in LuNi$_2$B$_2$C (Ref. 25) and YNi$_2$B$_2$C (Ref. 28) via neutron scattering experiments. Secondly, they are also observed at high fields, which completely destroy the magnetic order (Figs. 6 and 7) which excludes any magnetic origin of the observed structure (for instance, directly related to electron-magnon scattering).

Although we cannot measure the low-temperature PC spectra in the normal state unperturbed by the application of a magnetic field, there is evidence from the AR spectra at $H = 0$ that the 4-meV spectral structure is quite general for different RNi$_2$B$_2$C compounds, no matter which magnetic properties they possess. The typical examples for R=Ho, Er, and Y are demonstrated in Fig. 12. Although the shown AR spectra reveal quite different critical temperatures and superconducting energy gaps, they *deviate from the smooth BTKD behavior revealing a clear feature at* ~4 meV. The steep increase of the inelastic electron-scattering rate at this energy with a stepwise increase of the Γ-parameter could explain this feature. The characteristic energy is quite robust and does not depend on the contact resistance and the magnetic structure of the studied material, which proves its nonmagnetic origin.

It is interesting to note that in metallic Ho there is also a strong optical magnon band at $\hbar\omega = 4$ meV (Ref. 37). This suggests that in magnetically ordered HoNi$_2$B$_2$C the crossing of low-energy phonon and magnon branches might lead to the appearance of a low-energy mixed phonon-magnon

excitation-branch due to the repulsion of energy bands. Further investigations with polarized neutron scattering should clarify this point.

Quasi-thermal enhancement of phonon spectral line intensity. In many cases the observed peaks are not the conventional bell-shaped phonon peaks, but rather N-type shaped structures. After subtracting the linear background, the N-type shape corresponds more to maxima on the dV/dI curves than on the $d^2V/dI^2(V)$ dependences. These observations support our view that the N-shaped peaks, though located *close* to the characteristic phonon energies, are not simply due to the inelastic backscattering of conduction electrons by phonons, as is the case for the standard PCS.[15,16] The following observations relate these N-shaped phonon peaks to the destruction of magnetic order.

The positions and intensities of the N-shaped structures decrease with increasing magnetic field. At low fields the shape changes drastically and the intensity is strongly suppressed. At fields above the paramagnetic saturation field of about $1-2$ T,[5,6] the structure becomes only weakly magnetic-field dependent and looks as traditional, smeared PCS maxima. This described behavior is characteristic of the point-contact experiments with the magnetic $HoNi_2B_2C$. It originates from the strong coupling between the vibrational and magnetic degrees of freedom in this compounds. The strong phonon-magnon coupling easily leads to a large deviation from equilibrium in the phonon-magnon system, which is driven by the electrons that pass through the contact. The deviation from equilibrium is especially important in large and dirty contacts, since the escape rate of the nonequilibrium quasi-particles is hindered there by diffusion in the contact region. In small, clean contacts the nonequilibrium quasi-thermal effects are negligible due to the fast ballistic escape of the nonequilibrium quasi-particles from the contact region.

We propose the following explanation of the nonequilibrium phenomena observed in $HoNi_2B_2C$ point contacts which is, so to speak, a "magnetic" version of the earlier-found strong enhancement of the phonon structure by nonequilibrium phenomena in superconducting point contacts.[19] The ballistically injected nonequilibrium electrons generate *slow phonons* each time the bias voltage approaches an energy corresponding to the flattening of the phonon dispersion curves. At these biases the phonon branches have maxima in the density of state and their group velocities tend to zero. Those phonons cannot escape from the contact and thermalize through phonon-phonon collisions. Due to the *coupling between the phonon and magnon excitations*, which we assume to be strong, the magnon subsystem equilibrates with the phonons and the magnetic order is destroyed upon reaching the critical temperature of magnetic ordering in a given magnetic field. In fact, the thermalization of the phonon-magnon system is not necessary provided that the concentration of nonequilibrium magnetic excitations becomes large enough to destroy the magnetic order. Since the critical conditions depend on the complicated balance between the generation, escape, and decay rates of various quasi-particles (electrons, phonons, and magnons), where the phonons are only one of the few constituents in this picture, the position

of a "N"-type feature on the voltage scale is only approximately fixed around the characteristic phonon energies which become temperature- and magnetic-field dependent. At the corresponding critical bias voltages for the destruction of the magnetic order, the resistance of a point contact reveals a sharp increase. The resulting N-shaped structure in the PC spectra is similar to that found in the point contacts with the ferromagnetic metals of the iron group, where the magnetic transition is driven by Joule heating of the contact region at much larger biases.[17] Quantitatively, for a slow boson subsystem it is possible to be heated up to a temperature $\lesssim T_0$ $\sim (eV/4k_B)$ without temperature smearing of the electron distribution.[20] The steep rise of the contact resistance that occurs at about 5 mV then corresponds to T_0, which is roughly equal to the temperature at which the magnetic order is destroyed. Such an estimate gives the magnetic ordering temperature T_{mag} with an upper bound of 14.5 K, which roughly corresponds to our observations of $T_{mag} = 11-12$ K (see Fig. 9) and to the neutron powder-diffraction results of $T_{mag} \sim 8-10$ K. Since the point contacts are located close to the crystal surface, we compare our results with the neutron measurements on powders,[5,38] rather than with the bulk single-crystal results with $T_{mag} \sim 6$ K.[7]

Magnetic field dependence of the soft phonon branch. The low-energy phonon peak in the Ho compound appears to be very sensitive to the magnetic field parallel to the ab-plane, which points to the strong interaction between phonons and magnons. Our findings support the suggestion[25] that the phonon softening down to 4 meV is connected with the appearance of the incommensurate spin-density-wave along the $a(b)$ crystal axis in Er and Ho compound, since both occur at about the same wave vectors (close to a^* $= 0.55$[7,39]), which correspond to the nesting of the Fermi surface.[40] We have shown that the 4-meV spectral feature is also present in $ErNi_2B_2C$ (see Fig. 12). It is possible that the spin-density wave is present also in the Y compound, where a magnetic field could destroy the nesting feature that gives rise to the phonon softening.

In the above-described scenario, the lattice softening and the establishment of the magnetic order in the $a(b)$-direction cooperate with each other in lowering the total energy of a metal. If the soft phonon modes are important in the Cooper pairing, then the much stronger influence of magnetic field on the mixed electron-magnon-phonon interaction for $H \| ab$ should contribute to the anisotropy (or, more correctly, the apparent isotropy[34]) of H_{c2} in this material.

The dependence of the low-energy PCS phonon structure on magnetic field found in our experiments implies that the soft phonon modes *measured by neutrons* at low temperatures in $HoNi_2B_2C$ should reveal a strong sensitivity to the external magnetic field. It would be very interesting to check this prediction.

4.2. The linear background and interaction of electrons with non-phononic excitations

Many point-contact spectra on YNi_2B_2C, as well as on $HoNi_2B_2C$ (see, for example, Figs. 6, 7, and 10a), reveal a linear background signal starting from low bias voltages. Such a behavior is atypical for point contact spectra of con-
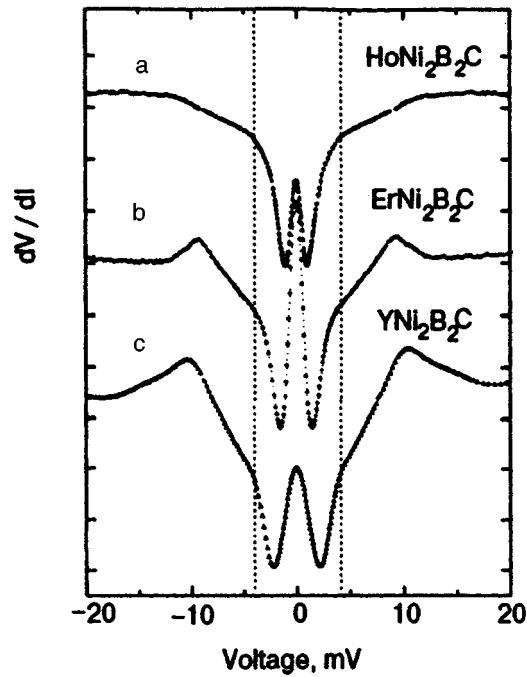
FIG. 12. The symmetrized Andreev reflection spectra [$dV/dI(V)$ dependences in the superconducting state] for the point contacts between Ag and RNi_2B_2C (R=Ho, Er, and Y). a) $HoNi_2B_2C$, $R(20\,mV)=15\,\Omega$, $T=1.6\,K$, 0.5 Ω per vertical division; b) $ErNi_2B_2C$, $R(20\,mV)=0.33\,\Omega$, $T=1.4\,K$, 0.023 Ω per division; c) YNi_2B_2C, $R(20\,mV)=0.82\,\Omega$, $T=4.2\,K$, 0.077 Ω per division. The vertical dotted lines mark the positions of the low-energy feature which is common to all spectra and which coincides with the lowest characteristic phonon energy in $LuNi_2B_2C$ (Ref. 25). $T \ll T_c$.

FIG. 13. The PC EPI spectral functions $g_{PC}(\omega)$ [see Eq. (2)] of YNi_2B_2C (upper panel) and $HoNi_2B_2C$ (lower panel) obtained as described in Ref. 29. The calculated λ_{PC} parameters are 0.05 and 0.1 for, respectively, YNi_2B_2C and $HoNi_2B_2C$.

ventional metals and alloys. If the electron-phonon interaction dominates, the background is due to the additional scattering of the conduction electrons on the generated nonequilibrium phonons in the contact area and results in a signal which corresponds to an energy integral of the phonon density of states. One of the reasons of the observed anomalous linear background signal could be that electron-electron (or electron-paramagnon[36]) interactions with a quadratic energy dependence in the scattering rate are strong scatters of the conduction electrons in these systems.

It follows from our measurements that the electron scattering by non-phononic excitations in YNi_2B_2C and $HoNi_2B_2C$ is essential up to energies of the order of 50 meV (Fig. 11), which correspond to the biases at which the contact resistance has an inflection point. This feature is clearly seen as a broad maximum at about 50 meV in the second harmonic signal for a number of contacts (not shown) along with another typical behavior of the background characterized by a saturation or wide shallow maximum at the boron vibration energy ~ 100 meV, shown in Fig. 11. In the thermal regime of the current flow the maximum temperature in the contact is $T_0 \simeq V/2\sqrt{L}$ [Eq. (3)]. This would correspond to a $\rho_{bulk}(T)$ dependence which has an inflection point at about 160 K, nicely fitting what is observed in the experiment.[27]

4.3. The boron vibrations, electron-phonon spectral functions, and λ parameters

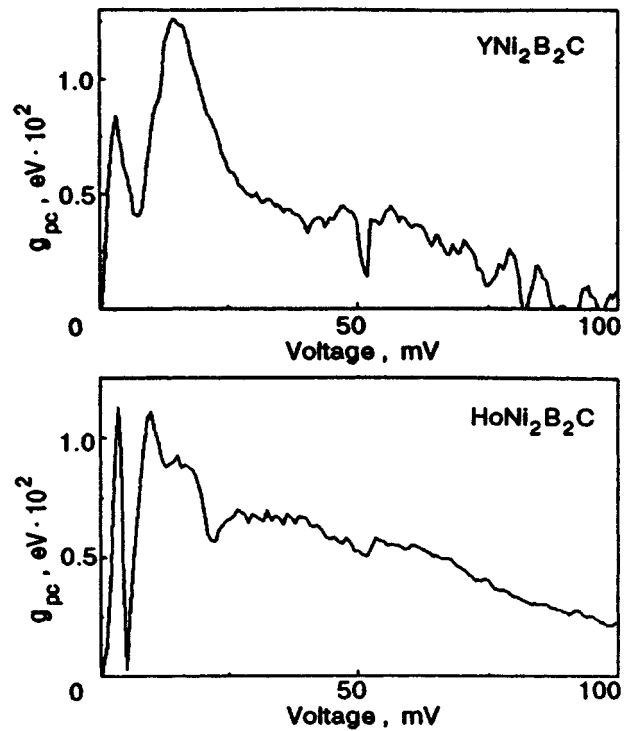After subtracting a smooth background from the measured d^2V/dI^2 spectra in the spectroscopic regime, the EPI spectral function $g_{PC}(\omega) = \alpha_{PC}^2(\omega)F(\omega)$ can be obtained using Eq. (2) for the scaling. The obtained EPI spectral functions for YNi_2B_2C and $HoNi_2B_2C$ are shown in Fig. 13 (Ref. 29). By analogy with the conventional EPI parameter $\lambda = 2\int \alpha^2 F(\omega)d\omega/\omega$, the $\lambda_{PC} = 2\int \alpha_{PC}^2 F(\omega)d\omega/\omega$ parameter can be calculated from the spectra.[16] The obtained values for λ_{PC} are of the order of 0.01 for typical spectra, which reach 0.1 for the most intensive spectrum, which is at least an order of magnitude smaller than expected from the band structure calculations.[23] This discrepancy may be partly due to the short electron mean free path l_e for elastic scattering, which leads to the diffusive regime of the current flow, $l_e \ll d \ll \sqrt{l_e l_{in}}$, in the contact region. In this case the contact diameter d in Eq. (2) should be replaced by l_e. The electron mean free path in the bulk is 10–100 nm (from $pl \sim 10^{-11}\,\Omega$ $\times cm^2$, as for a standard free electron metal, and the resistivity $\rho \sim 10^{-6} - 10^{-5}\,\Omega\cdot cm^4$) is of the same order of magnitude as the contact diameter calculated from the contact resistance, $R_0 \sim 1\,\Omega$, in the diffusive limit $d \sim \rho/R_0$. The maximum realistic shortening of l_e by static imperfections down to 1 nm can account for roughly an order-of-magnitude suppression of the spectral intensity.[18] The additional suppression may be due to unknown effects, which are related to the barrier at the contact interface or to a possibly small fraction of the contact that contributes to the phonon structure.

The boron vibrational spectral band at about the expected 100 meV is seen in many of the PC spectra as a broad maximum or as a change in the $d^2V/dI^2(V)$ slope that tends to saturation at voltages approximately equal to 100 mV (see

Fig. 11). The dominating role of the boron vibrations in the overall background behavior in many of the PC spectra clearly points to a contribution of the boron vibrational modes to the interaction parameter λ. However, we observed also spectra in which the prominent structure at 100 meV is absent, although a clear AR energy-gap structure suggests that the material under the contact is superconducting.[29] This may be due either to the strong anisotropy of the EPI (i.e., that for certain orientations of the contact axis the boron vibrations are not seen in the PC spectra) or to the fact that the high energy boron vibrations are not of great significance for the superconducting state. For some contacts with the YNi_2B_2C and $HoNi_2B_2C$ single crystals, with the contact axis oriented parallel to the c direction, we observed spectra (not shown here) with a strong boron feature at about 100 meV, but with neither low-frequency phonon peaks nor superconductivity under the contact. On the other hand, there are spectra of $HoNi_2B_2C$, in which any structure at about 100 meV is absent but the superconductivity under the contact is present, as revealed by the AR-dependences (together with the intensive low-frequency phonon peaks). These observations suggest that the EPI with the high-frequency boron mode, although being quite appreciable, is not vitally important for the superconductivity in these materials.

The quantitative estimates and even the relative comparison of the intensities of low-energy and high-energy phonon peaks cannot be made since the regime changes from the spectroscopic to the thermal one, while increasing the bias from the mV range to 100 mV. The developing fluctuations at $eV \gtrsim 100$ meV also point to a strong heating inside the contact region (Fig. 11).

CONCLUSIONS

We have shown the possibility of the application of point-contact spectroscopy to study the electron-quasiparticle-interaction spectral function in superconducting and magnetic rare-earth nickel boro-carbides. To the best of our knowledge, until now this is the only experimental technique able to yield information on the given issue. The dominating scattering mechanism for conduction electrons appears to be the electron-phonon interaction. The strong interaction with a soft phonon mode ($\hbar\omega \simeq 4$ meV) is clearly observed in the PC spectra. At low energies ($eV < 20$ meV) there is an enhancement of the electron-phonon interaction by magnetic order in $HoNi_2B_2C$, which may support the superconducting state in this material. The intensity of these phonon peaks is suppressed by the magnetic field in $HoNi_2B_2C$ in an anisotropic way, pointing to an interaction between the phonons and the magnetic system. Unexpectedly, in nominally nonmagnetic YNi_2B_2C a magnetic field was found to influence the intensity of the low-energy spectral peak, pointing to the existence of magnetic interactions in this compound. Comparing our results with the bulk resistivity measurements of Fisher et $al.$,[27] we suggest that the electron-magnon(paramagnon) interaction in $HoNi_2B_2C$ and YNi_2B_2C might be what distinguishes their $\rho_{bulk}(T)$ dependences from that for the nonsuperconducting $LaNi_2B_2C$.

The comparison of the EPI spectra of superconducting YNi_2B_2C and $HoNi_2B_2C$ with the nonsuperconducting $LaNi_2B_2C$,[29] as well as the comparative study of PC-EPI and AR spectra for various contacts with superconducting Ho- and Y-based compounds undertaken in this work, suggest that the low-energy part of electron-quasiparticle-interaction spectral function is responsible for the Cooper pairing in these materials. The strong electron-phonon-(para)magnon coupling observed in the case of magnetic $HoNi_2B_2C$ and nominally nonmagnetic YNi_2B_2C makes it problematic that these materials belong to the family of the ordinary electron-phonon-coupled superconductors, but rather attaches them to the high-T_c and heavy fermion systems.

[*]E-mail: fisun@ilt.kharkov.ua

[1] R. Nagarajan, C. Mazumdar, Z. Hossain, S. K Dhar, K. V. Gopalakrishnan, L. C. Gupta, C. Godart, B. D. Padalia, and R. Vijayaraghavan, Phys. Rev. Lett. **72**, 274 (1994).

[2] R. J. Cava, H. Takagi, H. W. Zandbergen, J. J. Krajewski, W. F. Peck, Jr., T. Siegrist, B. Batlogg, R. B. van Dover, R. J. Felder, K. Mizuhashi, J. O. Lee, H. Eisaki, and S. Uchida, Nature **367**, 146 (1994).

[3] O. Fisher, *Magnetic Superconductors in Ferromagnetic Materials*, E. P. Wohlfarth (Ed.), North-Holland, Amsterdam (1990), vol. 5.

[4] H. Elsaki H. Takagi, R. J. Cava, B. Batlogg, J. J. Krajewski, W. F. Peck, Jr., K. Mizuhashi, J. O. Lee, and S. Uchida, Phys. Rev. **B50**, 647 (1994).

[5] T. E. Grigereit, J. W. Lynn, Q. Huang, A. Santoro, R. J. Cava, J. J. Krajewski, and W. F. Peck, Jr., Phys. Rev. Lett. **73**, 2756 (1994).

[6] P. C. Canfield, B. K. Cho, D. C. Johnston, D. K. Finnemore, and M. F. Hundley, Physica **C230**, 397 (1994).

[7] A. I. Goldman, C. Stassis, P. C. Canfield, J. Zarestky, P. Dervenagas, B. K. Cho, D. C. Johnston, and B. Sternlieb, Phys. Rev. **B50**, 9668 (1994).

[8] M. E. Hanson, F. Lefloch, W. H. Wong, W. G. Clark, M. D. Lan, C. C. Hoellwarth, R. Klavins, and R. N. Shelton, Phys. Rev. **B51**, 674 (1995).

[9] T. Jacobs, B. A. Willemsen, S. Sridhar, R. Nagarajan, L. C. Gupta, Z. Hossain, C. Mazumdar, P. C. Canfield, and B. K. Cho, Phys. Rev. **B52**, R7022 (1995).

[10] L. P. Le, R. H. Heffner, J. D. Thompson, D. E. MacLaughlin, G. J. Nieuwenhuys, A. Amato, R. Feyerherm, F. N. Gygax, A. Schenck, P. C. Canfield, and B. K. Cho, Phys. Rev. **B53**, R510 (1996).

[11] T. Ekino, H. Fujii, M. Kosugi, Y. Zenitani, and J. Akimitsu, Physica **C235−240**, 2529 (1994).

[12] T. Hasegawa, M. Ogino, A. Takagi, E. Watanabe, M. Nantoh, H. Takagi, S. Uchida, R. J. Cava, and K. Kitazawa, Physica **C235−240**, 1859 (1994).

[13] E. Bar-Sadeh, I. Felner, U. Asaf, and O. Millo, Phys. Rev. **B52**, 6734 (1995).

[14] G. T. Jeong, J. I. Kye, S. H. Chun, Z. G. Khim, W. C. Lee, P. C. Canfield, B. K. Cho, and D. C. Johnston, Physica **C253**, 48 (1995).

[15] A. G. M. Jansen, A. P. van Gelder, and P. Wyder, J. Phys. **C13**, 6073 (1980).

[16] A. V. Khotkevich and I. K. Yanson, *Atlas of Point Contact Spectra of Electron-Phonon Interactions in Metals*, Kluwer Academic, New York (1995).

[17] B. I. Verkin, I. K. Yanson, I. O. Kulik, O. I. Shklyarevskii, A. A. Lysykh, and Yu. G. Naidyuk, Solid State Commun. **30**, 215 (1979).

[18] I. K. Yanson and O. I. Shklyarevskii, Sov. J. Low Temp. Phys. **12**, 509 (1986).

[19] I. K. Yanson, V. V. Fisun, N. L. Bobrov, and L. F. Rybal'chenko, JETP Lett. **45**, 543 (1987).

[20] I. O. Kulik, A. N. Omel'yanchuk, and I. K. Yanson, Fiz. Nizk. Temp. **7**, 263 (1981) [Sov. J. Low Temp. Phys. **7**, 129 (1981)].

[21] S. A. Carter, B. Batlogg, R. J. Cava, J. J. Krajewski, and W. F. Peck, Jr., Phys. Rev. **B50**, 4216 (1994).

[22] L. F. Mattheiss, T. Siegrist, and R. J. Cava, Solid State Commun. **91**, 587 (1994).

[23] W. E. Pickett and D. J. Singh, Phys. Rev. Lett. **72**, 3702 (1994).

[24] D. D. Lawrie and J. P. Frank, Physica **C245**, 159 (1995).

[25] P. Dervenagas, M. Bullock, J. Zarestky, P. Canfield, B. K. Cho, B. Harmon, A. I. Goldman, and C. Stassis, Phys. Rev. **B52**, R9839 (1995).

[26] N. M. Hong, H. Michor, M. Vybornov, T. Holubar, P. Hundegger, W. Perthold, G. Hilscher, and P. Rogl, Physica **C227**, 85 (1994).

[27] I. R. Fisher, J. R. Cooper, and R. J. Cava, Phys. Rev. **B52**, 15086 (1995).

[28] H. Kawano, H. Yoshizawa, H. Takeya, and K. Kadowaki, Czech. J. Phys. **46**, S2–825 (1996); Phys. Rev. Lett. **77**, 4628 (1996).

[29] I. K. Yanson, V. V. Fisun, A. G. M. Jansen, P. Wyder, P. C. Canfield, B. K. Cho, C. V. Tomy, and D. McK. Paul, Phys. Rev. Lett. **78**, 935 (1997).

[30] M. Xu, P. C. Canfield, J. E. Ostenson, D. K. Finnemore, B. K. Cho, Z. R. Wang, and D. C. Johnston, Physica **C227**, 321 (1994).

[31] L. F. Rybaltchenko, I. K. Yanson, A. G. M. Jansen, P. Mandal, P. Wyder, C. V. Tomy, and D. McK. Paul, Physica **B218**, 189 (1996).

[32] A. Plecenik, M. Grajcar, S. Benacka, P. Seidel, and A. Pfuch, Phys. Rev. **B49**, 10016 (1994).

[33] H. Schmidt, M. Weber, and H. F. Braun, Physica **C246**, 177 (1995); *ibid* **256**, 393 (1996).

[34] K. D. D. Rathnayaka, D. G. Naugle, B. K. Cho, and P. C. Canfield, Phys. Rev. **B53**, 5688 (1996).

[35] B. K. Cho, B. N. Harmon, D. C. Johnston, and P. C. Canfield, Phys. Rev. **B53**, 2217 (1996).

[36] D. L. Mills, *J. Phys. Chem. Solids* **34**, 679 (1973).

[37] M. W. Stringfellow, T. M. Holden, B. M. Powell, and A. D. B. Woods, J. Phys. C: Metal Phys. Suppl. No. 2, **3**, S189 (1970).

[38] J. W. Lynn, Q. Huang, A. Santoro, R. J. Cava, J. J. Krajewski, and W. F. Peck, Jr., Phys. Rev. **B53**, 802 (1996).

[39] J. Zarestky, C. Stassis, A. I. Goldman, P. C. Canfield, P. Dervenagas, B. K. Cho, and D. C. Johnston, Phys. Rev. **B51**, R678 (1995).

[40] J. Y. Rhee, X. Wang, and B. N. Harmon, Phys. Rev. **B51**, 15585 (1995).

Transition from strong to weak electron localization in a percolating gold film under the influence of an electric field

B. I. Belevtsev, E. Yu. Belyaev, Yu. F. Komnik, and E. Yu. Kopeichenko

*B. Verkin Institute for Low Temperature Physics and Engineering, National Academy of Sciences of the Ukraine, 310164 Kharkov, Ukraine**

The low-temperature (0.5–55 K) conductivity of a semicontinuous gold film near the percolation threshold is studied. It is found that the film resistance is very sensitive to the applied voltage U. By varying U, the film can be reversibly transformed from the insulating to the metallic type conductivity. This makes it possible to study the metal–insulator transition (MIT) by tuning the electric field. For low $U \leqslant 0.05$ V, the film behaves as an insulator with the sheet resistance $R_\square$ up to 10 MΩ. In this state, the dependences $R(T) \propto \exp(1/T)$ (for $T \leqslant 20$ K) and $R(U) \propto \exp(1/U)$ (for $T \leqslant 1$ K and $U > 0.1$ V) are observed. At high voltages ($U \simeq 10$ V), the film has the resistance $R_\square \simeq 5$ kΩ and behaves like a ''dirty'' metal. The magnetoresistance (MR) in the metallic state is positive and corresponds to the weak localization effect. In the insulating state, the MR is negative and is described by the formula $\Delta R(H)/R(0) \propto -H^2/T$. The negative MR manifests itself for nearest-neighbor hopping. Such behavior is unusual, and its nature is unclear. The dependences of resistance on temperature, voltage, and magnetic field as well as the general nature of the observed MIT are considered on the basis of the obtained results. © *1997 American Institute of Physics.* [S1063-777X(97)00709-3]

1. INTRODUCTION

An increase in disorder in the crystal lattice of metals leads to interference effects of weak localization (WL) and electron–electron interaction (EEI) in the electron conductivity.[1–3] In the case of strong disorder, electrons become localized (such a metal–insulator transition (MIT) is known as the Anderson transition).[1–5] The disorder responsible for these phenomena is associated with perturbations of the scattering potentials on the atomic scale (impurities, vacancies, and so on) and is often called microscopic. The MIT can also take place in heterogeneous systems in the form of disordered mixtures of a metal and an insulator. The conductivity of such systems differs from zero for $x > x_c$, where x is the relative fraction of the metal and x_c the critical fraction (percolation threshold). In the case of two-dimensional systems, x is the metallic surface coverage. The typical disorder scale in percolation systems is 10–100 nm and hence is known as macroscopic.

In the case of simultaneous influence of macroscopic and microscopic disorders, the conducting properties of heterogeneous systems is an interesting and important problem in the physics of conduction electrons in disordered systems. The well-known theoretical results obtained in Refs. 6 and 7 predict enhancement of Anderson localization near the percolation threshold. Various aspects of the influence of macroscopic disorder on WL and EEI effects as well as Anderson's transition were studied experimentally,[8–13] but this problem has been investigated insufficiently on the whole.

Here we report on the results of studies of peculiarities in the transition from weak to strong electron localization in semicontinuous gold films near the percolation threshold. The terms ''weak'' and ''strong'' localization should be

clarified. In the general case (both for homogeneous and heterogeneous systems), we shall assume that the system is under conditions of weak localization if it is a disordered metal whose conductivity at low temperatures is determined by the WL and EEI effects.[2,3] The temperature dependence of conductance for two-dimensional ($2D$) systems in this case is given by

$$G_\square(T) - G_\square(T_*) = a_T G_{00} \ln \frac{T}{T_*}, \tag{1}$$

where $G_\square = 1/R_\square$, $G_\square$ and $R_\square$ are the sheet conductance and resistance of a $2D$ system, $G_{00} = e^2/2\pi^2\hbar = 1/R_{00}$ ($R_{00} \approx 81$ kΩ); the quantity a_T of the order of unity depends on the mechanism of phase relaxation of electrons, and T_* is an arbitrary fixed temperature. In the case of strong localization, we shall assume that the system is an insulator whose conductivity is determined by thermally activated hops between localized states.[4,5]

Let us first consider the well-known regularities of a transition from weak to strong electron localization for homogeneous $2D$ systems. The conducting properties of such systems for $T > 0$ are determined by the relation between two lengths[2,14,15]: the localization length ξ_l and the phase relaxation length $L_\varphi(T) = (D_e \tau_\varphi)^{1/2}$, where D_e is the electron diffusion coefficient, $\tau_\varphi(T) \propto T^{-p}$ is the time of phase relaxation due to inelastic processes of electron scattering, and the quantity p is determined by the mechanism of inelastic relaxation and can vary from 1 to 4. We assume that electrons in $2D$ systems for which $\xi_l > L_\varphi(T)$ are localized weakly, while those in systems for which $\xi_l < L_\varphi(T)$ are localized strongly. A transition from weak to strong localization of electrons is characterized by the approximate equality $\xi_l \approx L_\varphi$. This transition in real systems can be carried out by

changing the degree of disorder (variation of ξ_l) or temperature ($L_\varphi \propto T^{-p/2}$). It was found during investigation of metal films[14–21] that a transition from a logarithmic to an exponential dependence of resistance upon an increase in disorder in the temperature range ~ 10 K occurs for the characteristic value of resistance $R_\square = R_\square^c$ whose value normally varies from 20 to 30 kΩ. This value of $R_\square^c$ was put in correspondence with the resistance quantum R_Q which is equal to $\hbar/e^2$ to within a numerical factor. For definiteness, we can assume[15] that $R_Q = \pi\hbar/e^2 \simeq 12.9$ kΩ. In this case, the experimental values of $R_\square^c$ can be presented in the form $R_\square^c = bR_Q$, where b is a factor of the order of unity.

Meir *et al.*[22] proved that the sign of magnetoresistance can serve as an accurate criterion of weak or strong electron localization in homogeneous $2D$ systems with a strong spin-orbit interaction (SOI). In the case of weak disorder, MR is positive in accordance with the WL theory,[2,3] while in the case of strong localization it must be negative. Such a transition was observed earlier for In films upon an increase in disorder.[19] According to Ref. 22, a transition from positive to negative MR must take place exactly for $\xi_l = L_\varphi(T)$. An analysis of ultrathin Cu, Ag, and Au films revealed[23] that this transition occurs for $R_c \simeq 75$ kΩ, which corresponds to the characteristic resistance $R_{00} = 2\pi^2\hbar/e^2 \simeq 81$ kΩ appearing in formula (1).

In percolating systems, the regularities of transition from weak to strong electron localization can be completely different and must be determined by the effect of "macroscopic" disorder to a considerable extent. This research is devoted to investigation of these effects. The objects of investigation were ultrathin semicontinuous gold films with resistance $R_\square$ of the order 10 kΩ under transient conditions between weak and strong electron localization. Films were prepared by vacuum deposition on a cold substrate (~ 50 K). The conductivity of such films was found to be very sensitive to the applied voltage U. At low temperatures, we could reversibly transform the films from weak to strong electron localization conditions by varying the value of U. It was found that apart from the change in the temperature dependence of resistance, such transition is also accompanied by the change in the sign (from positive to negative) of MR as in homogeneous systems. At the same time, some of peculiarities observed in the film conductivity (e.g., a transition from positive to negative MR upon an increase in temperature) do not correspond to homogeneous systems. In this paper, we analyze the results obtained for one of such films. It will be shown that the conducting properties of the film under strong localization conditions corresponds to a $2D$ granular metal. The observed transition to weak localization upon an increase in U is due to the effect of electric field on the probability of electron tunneling between metallic granules (percolation clusters). The observed difference from the behavior of homogeneous systems can be explained by joint effect of "microscopic" and "macroscopic" disorders. Negative magnetoresistance of the investigated film under strong localization was manifested in the regime of electron hopping between nearest neighbors. Such a case of negative magnetoresistance for insulators is unusual,[24] and its nature remains unclear. The obtained results can be used for devel-
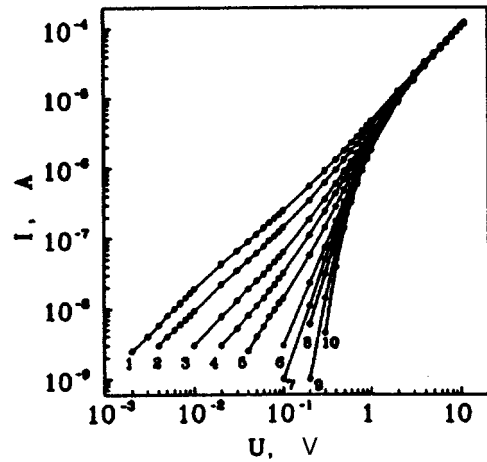

FIG. 1. Current-voltage characteristics at various temperatures T (in K): 10 (*1*), 8 (*2*), 6 (*3*), 5 (*4*), 4 (*5*), 3 (*6*), 2.5 (*7*), 2 (*8*), 1.4 (*9*), 0.51 (*10*).

oping a theoretical model of this interesting phenomenon.

2. EXPERIMENTAL TECHNIQUE

The preparation of percolating gold films and the measurement of their conducting properties *in situ* were carried out in a high-vacuum cryostat containing ^{3}He and a superconducting solenoid. The properties of one of the investigated films are described below.[1)] This film with effective thickness $L \simeq 3.25$ nm (determined by using a quartz pickup) was deposited under a pressure $\sim 10^{-6}$ Pa on a monocrystalline sapphire substrate at a deposition rate 0.015 nm/s at the substrate temperature ~ 54 K. The purity of the initial material was 99.99%. The resistance of the film immediately after its preparation was $R_\square \simeq 4.87$ kΩ. In order to stabilize the structural state of the film, it was heated to ~ 63 K, after which its resistance decreased to ~ 4.5 kΩ. The size of the regions of the film being measured was 2×0.1 mm. The conducting properties of the film were studied by recording the current-voltage characteristics (IVC) at various temperatures (in the range 0.5–55 K). The source of stabilized volt-
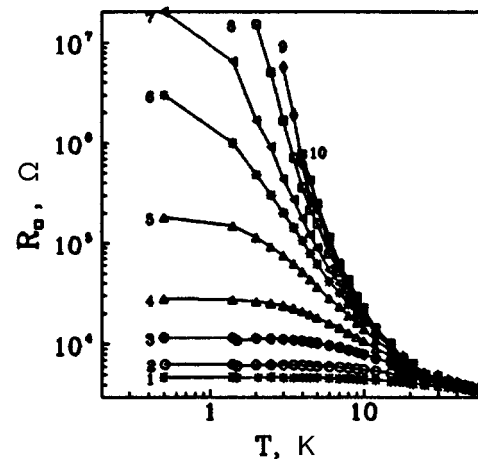

FIG. 2. Dependence of $R_\square(T)$ (in logarithmic coordinates) for various values of the applied voltage U (in V): 11 (*1*), 5 (*2*), 2 (*3*), 1 (*4*), 0.5 (*5*), 0.3 (*6*), 0.2 (*7*), 0.1 (*8*), 0.05 (*9*), 0.02 (*10*).
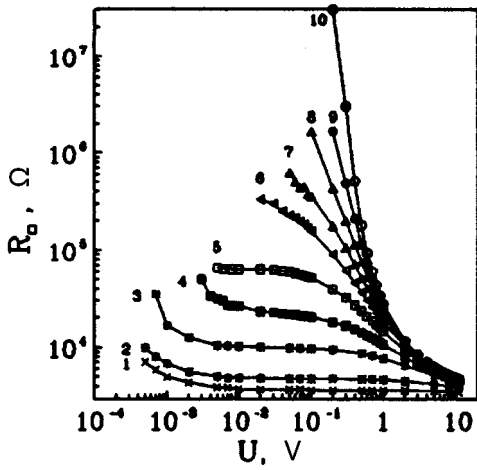
FIG. 3. Dependence of $R_\square(T)$ (in logarithmic coordinates) at various temperatures T (in K): 50 (*1*), 30 (*2*), 15 (*3*), 10 (*4*), 7 (*5*), 5 (*6*), 4 (*7*), 3 (*8*), 2 (*9*), 0.5 (*10*).

age used in the experiments made it possible to change the voltage U in steps from 11 to 0.001 V. Along with the IVC recording, we also measured MR in a magnetic field H of strength ~ 4.5 T normal to the film.

3. DISCUSSION OF RESULTS

3.1. Review of basic results

The film conductivity was essentially nonohmic, the IVC nonlinearity being enhanced upon a decrease in temperature (Fig. 1). The results of measurements can also be represented in the form of families of $R(T)$ curves (recorded for different values of U) as well as $R(U)$ curves (recorded at different temperatures) (Figs. 2 and 3). The figures show that the variation of $R(T)$ at low values of U and of $R(U)$ at low temperatures are exponentially large (for this reason, the curves are given in logarithmic coordinates). At the same time, the variations of resistance for large values of U and T are very small. The temperature dependence $R(T)$ for small $U(\leqslant 0.05$ V) corresponds to the simple exponential dependence

FIG. 5. Dependence $\ln R_\square = f(1/T)$ at $T = 0.51$ K.

$$R(T) \propto \exp(T_0/T) \qquad (2)$$

(Fig. 4), where $T_0 \simeq 20$ K. At low temperatures ($T < 1$ K), we have a similar dependence for $R(U)$:

$$R(U) \propto \exp(U_0/U) \qquad (3)$$

(Fig. 5), where $U_0 \simeq 2$ V.

As the value of U increases, the temperature dependence $R(T)$ becomes weaker (Fig. 6). For large values of $U \simeq 10$ V in the temperature range 5–55 K, this dependence approximately corresponds to the following expression:

$$R(T) - R(T_*) \propto \ln(T/T_*). \qquad (4)$$

A comparison of experimental dependence (4) with the theoretical formula (1) gives $a_T \simeq 3$. It should be noted that the experimental data in this temperature range are also in good agreement with the power dependence $R(T) \propto T^{-\beta}$, where $\beta = 0.3-0.5$.

Thus, the obtained results indicate that the film under investigation experiences a transition from strong to weak electron localization upon an increase in voltage. In this transition, the resistance $R_\square$ decreases from $\sim 10^7$ Ω to

FIG. 4. Dependence $\ln R_\square = f(1/T)$ for $U = 0.05$ V.

FIG. 6. Dependence $R_\square(T)$ for $U = 11$ V.

$\sim 5 \cdot 10^3$ Ω. Apart from a change in the temperature dependence of resistance, the transition is accompanied by a change in the nature and sign of magnetoresistance. For low-resistance states ($R_\square \lesssim 12$ kΩ) the value of MR was positive for high voltages ($\geqslant 5$ V). It is well known[11,13,25,26] that gold films under WL condition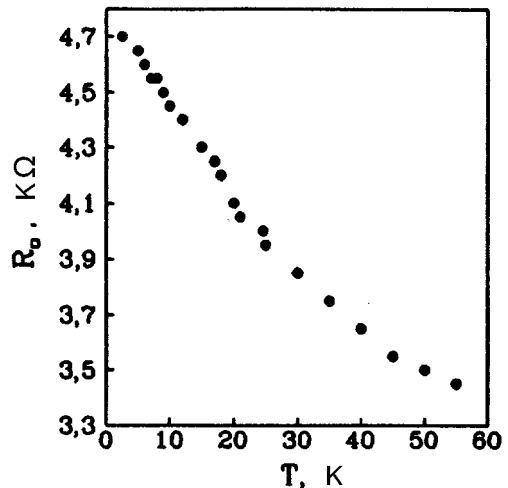s possess a positive MR due to strong SOI typical of gold. We can assume that it is also the case for low-resistance states of the film under investigation. In order to verify this assumption, we compared the experimental MR curves with the relevant theoretical expression[2,3]

$$\frac{\Delta R(H)}{R} = R_\square^{MR} \frac{e^2}{4\pi^2 \hbar} f\left(\frac{4eHL_\varphi^2}{\hbar c}\right), \tag{5}$$

where $f(x) = \psi(1/x + 1/2) + \ln x$, ψ being the digamma function. The application of this formula for heterogeneous and semicontinuous films requires certain stipulations. In such systems, we must take into account the relation between the length $L_\varphi(T)$ and the percolation correlation length ξ_p which is equal to the average size of percolating clusters[5] for $x < x_c$ and determines the scale of length above which the system is homogeneous for $x > x_c$. For example, the system is homogeneous relative to the WL effect for $L_\varphi(T) > \xi_p$ and heterogeneous for $L_\varphi(T) < \xi_p$.

In the case of homogeneous systems, the value of sheet resistance $R_\square$ measured for a $2D$ sample is usually substituted for $R_\square^{MR}$ in formula (5). Usually, the size of such a sample (except thickness) is much larger than the lengths ξ_p and L_φ, and hence we can refer to the resistance $R_\square$ being measured as "macroscopic." However, the substitution of this resistance into formula (5) is justified only for $L_\varphi > \xi_p$ since all the peculiarities of percolating structure in this case are averaged over the length L_φ. For percolating systems in which $L_\varphi \ll \xi_p$, the contribution to MR associated with the WL effect comes from metallic regions of the sample, whose size is larger than L_φ, but much smaller than ξ_p. The resistance of these regions can be much smaller than the "macroscopic" resistance $R_\square$. For this reason, the quantity $R_\square^{MR}$ in formula (5) must be a fitting parameter.[13,27] It is $R_\square^{MR}$ and not $R_\square$ that characterizes the "microscopic" disorder of the system in this case.

Taking into account the above arguments, we compared the experimental dependences $R(H)$ with formula (5). We used two fitting parameters for each theoretical curve: $R_\square^{MR}$ and the phase relaxation length L_φ. It was found that expression (5) is in good agreement with the measured field dependence of $\Delta G_\square$ (Fig. 7) in the entire range of fields used (up to ~ 4.5 T) for states of the film with $R_\square = 4.5$–11.5 kΩ in the temperature range[2)] 1.5–15 K and for voltages from the interval 5–11 V. The values of $R_\square^{MR}$ obtained as a result of such a data processing were within 800 ± 100 Ω and did not depend explicitly on temperature or applied voltage, in contrast to $R_\square$. It was found that the phase relaxation length L_φ at $T \leqslant 5$ K was independent of temperature and amounted to ~ 20 nm. As the temperature increases above 5 K, the values of L_φ decrease (to ~ 11.7 nm at $T = 12$ K).

The order of magnitude and the behavior of $R_\square^{MR}$ and L_φ are not unexpected. The value of $R_\square^{MR}$ as a measure of "microscopic" disorder should not depend noticeably on tem-
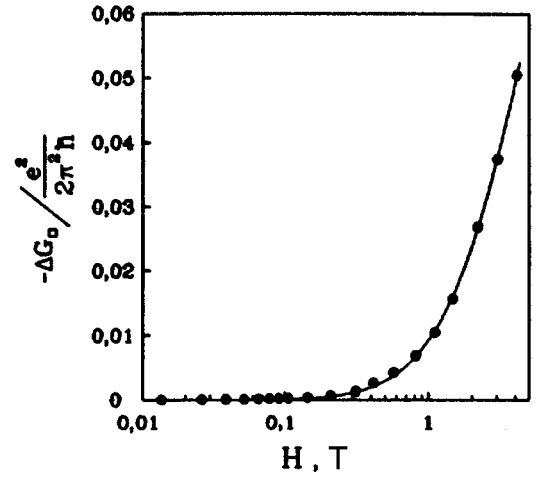

FIG. 7. Dependence of normalized correction to film conductivity on magnetic field at $T = 4$ K, $U = 5$ V. The solid curve corresponds to formula (5) for $R_\square^{MR} = 0.9$ kΩ. The measured "macroscopic" resistance $R_\square \approx 6$ kΩ.

perature or applied voltage. At the same time, the length $L_\varphi = (D_e \tau_\varphi)^{1/2}$ must decrease upon a considerable increase in temperature due to the effect of inelastic electron scattering.[2,3] The independence of L_φ on temperature at $T \leqslant 5$ K is in accord with a similar behavior of τ_φ observed for homogeneous gold films[25,26] prepared from the same initial material as in our experiments. This is associated with the dominating contribution of spin–spin scattering in this temperature range.

Thus, the MR of the film under investigation at high voltages (> 5 V) corresponds to the WL effects in percolating $2D$ systems for $L_\varphi < \xi_p$.[13,27] As the voltage decreases, the $R(T)$ dependences become stronger (Fig. 2) and approach the exponential dependence (2), i.e., a transition to a state with strong electron localization takes place. This transition is accompanied by the change in the sign of MR from positive to negative (Fig. 8). It should be emphasized that the sign reversal of MR with increasing temperature occurs at higher voltages (cf. Figs. 8a and b), and hence at lower values of $R_\square$. This is equivalent to a transition from positive to negative MR upon an increase in temperature for a fixed voltage U (Fig. 9).

At low values of U, a quadratic dependence of R on magnetic field was observed: $\Delta R(H)/R = -A(T)H^2$ (Fig. 10), where $A(T) \propto 1/T^n$, $n \simeq 1$. Consequently, the effect of magnetic field on resistance can be described by the formula

$$\frac{\Delta R_\square(H,T)}{R_\square(0,T)} = -B \frac{H^2}{T}, \tag{6}$$

where B is a positive numerical factor.

3.2. Nature of the observed metal–insulator transition

The obtained experimental results lead to quite definite assumptions concerning the nature of the observed MIT. The small effective thickness of the film (~ 3.25 nm), high values of $R_\square$ (~ 10 kΩ and higher) and strong nonohmicity of its conductivity indicate that the film is semicontinuous. This means that it consists of metallic islands (or percolating clus-
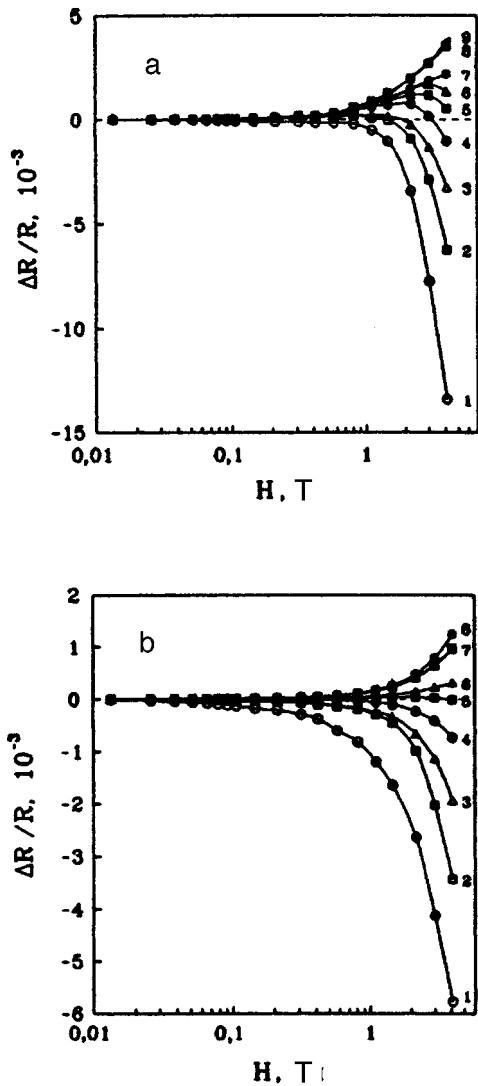
FIG. 8. Relative variation of resistance in a magnetic field at $T = 4$ K(a) and 15 K(b). The curves correspond to different values of the applied voltage U (in V): 0.5 (*1*), 0.8 (*2*), 1.0 (*3*), 1.2 (*4*), 1.5 (*5*), 1.7 (*6*), 2.0 (*7*), 3.0 (*8*), 5.0 (*9*) (a), and 0.1 (*1*), 0.5 (*2*), 1.0 (*3*), 2.0 (*4*), 3.0 (*5*), 4.0 (*6*), 8.0 (*7*), and 11.0 (*8*) (b).

FIG. 9. Relative variation of resistance in a magnetic field for $U = 2$ V. The curves correspond to different values of T (in K): 18.0 (*1*), 9.0 (*2*), 7.0 (*3*), 5.0 (*4*), 4.5 (*5*), 4.0 (*6*), 3.5 (*7*), 3.0 (*8*), 2.5 (*9*), 0.51 (*10*).

tunnelling and thermal activation. In this case, the probability of electron hopping from one granule to another is defined as

$$W \propto \exp(-2\chi s)\exp\left(-\frac{E_a}{kT}\right), \qquad (8)$$

where s is the tunneling length, $\chi = \hbar^{-1}(2m\varphi_i)^{1/2}$ (m is the electron mass and φ_i is the effective barrier height), χ^{-1} is the decay length of the wave function in the insulator, and E_a is the activation length.

The first theoretical explanation of dependence (7) for GM[28] was obtained under the assumption that $E_a = E_c$, where $E_c = e^2/\kappa r$ is the charging energy for granules (κ is the effective dielectric constant and r the granule radius). It was assumed that the density of charge carriers in GM is proportional to $\exp[-E_c/(2kT)]$ and electrons hop only between adjacent granules (nearest neighbors). In this case, the conductivity in the percolation approach is determined by the presence of optimal "chains" of granules with the maximum

ters) separated by tunnel barriers. Two types of barriers are possible: (a) vacuum gaps between adjacent islands on an insulating substrate, and (b) narrow and thin constrictions (bridges) between islands in the case of weak contacts between neighboring islands. In any case, such a system can be regarded as a two-dimensional granular metal (GM).

The insulating state of a GM is characterized by the following temperature dependence of conductivity σ[28–31]:

$$\sigma \in \exp[-(1/T)^{1/2}]. \qquad (7)$$

Sometimes, other dependences are also observed: the simple activation dependence (Arrhenius law) $\sigma \propto \exp(-1/T)$ or the dependences $\sigma \propto \exp(-1/T^\alpha)$ with a fractional index $\alpha = 1/4 - 1/3$ differing from $\alpha = 1/2$ in formula (7). The existing explanations of the conductivity of GM[28–31] are based on the Mott concept[4,5] according to which the hopping conductivity is determined by joint contribution of two processes:

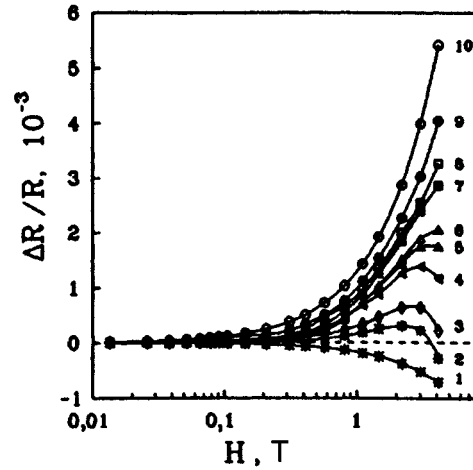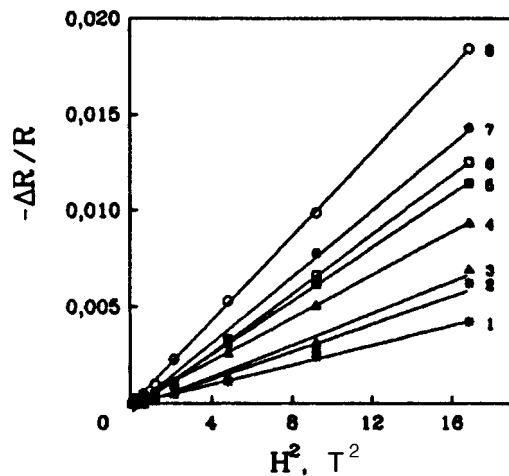FIG. 10. Dependences $\Delta R(H)/R = f(H^2)$ at various temperatures T (in K): 12 (*1*), 10 (*2*), 8 (*3*), 7 (*4*), 6 (*5*), 5 (*6*), 4 (*7*), 3 (*8*). At each temperature, this dependence corresponds to the minimum value of the applied voltage U.

total probability of activated tunneling for adjacent pairs of granules forming the chain (these probabilities are defined by formula (8)). It was concluded as a result of subsequent theoretical and experimental investigations[29,31] that dependence (7) is intermediate (or interpolating) between the temperature dependence of conductivity at high ($\ln \sigma \propto -1/T$) and low ($\ln \sigma \propto -1/T^{1/4}$) temperatures. High temperatures (~ 100 K and above) facilitate activation processes (the activation factor in (8) increases with temperature), and hence the hopping length is the limiting factor under these conditions. An optimal granular chain is characterized in this case by the minimum sum of hopping lengths. Then the temperature dependence of conductivity must be close to the Arrhenius law, and electrons must hop mainly between nearest neighbors. With decreasing temperature, activation is hampered, and the competition between the tunneling and activation factors in formula (8) results in an increase in the average hopping length upon a decrease in temperature.[4,5] This is the base of variable range hopping (VRH) mechanism of conductivity.[4,5] With such a mechanism, the following dependence can be expected:

$$\sigma \in \exp[-(1/T)^\alpha], \qquad (9)$$

where $\alpha = 1/(1+D)$, D being the system dimensionality. It follows from formula (9) that the value of α is equal to 1/4, 1/3, and 1/2 for $3D$, $2D$, and $1D$ systems, respectively. It is assumed that this statement is undoubtedly correct for $3D$ and $2D$ systems. For $1D$ systems, expression (9) does not hold in the case of long chains.[32,33] In such chains, "discontinuities" i.e., regions in which there are no impurity states with energies quite close to the Fermi level, are inevitable. Discontinuity regions make the largest contribution to the resistance of a $1D$ chain, and hence the temperature dependence of resistance must obey the Arrhenius law ($\alpha = 1$).[32,33] Such a situation can also emerge in narrow $2D$ conductors[34] as well as in GM at low temperatures in the case of a small number of possible hops.[31] In this case, an optimal chain of granules contains so-called difficult hops that cannot be avoided, and hence the $R(T)$ dependence must correspond to Arrhenius law.[31] The observed dependence (2) (see Fig. 4) is apparently associated with such a situation in the semicontinuous film under investigation.

It is well known[4] that in strong electric fields $F(eF\xi_l > kT)$, hopping conductivity is activationless and temperature independent. In this case, the following relation must hold for GM[28,35]:

$$\sigma \in \exp\left(-\frac{\chi \varphi_i}{eF}\right). \qquad (10)$$

This expression corresponds qualitatively to the dependence (3) observed for the film under investigation (see Fig. 5). Using the models described above,[28,35] we can explain qualitatively the observed transition from strong to weak electron localization upon an increase in applied voltage. The electric field exerts the dual effect on the GM conductivity: (1) it changes the shape and reduces the effective height and width of the potential barrier between granules, and thus affects the degree of electron localization in granules, and (2) it decreases the activation energy of jumps between granules

(so that the conductivity can become activationless). As a result, electrons can become nearly free in strong fields (the tunneling probability is close to unity). This can explain the transition from strong to weak localization upon an increase in applied voltage, which was described by us earlier.

3.3. Change in the sign of MR in metal–insulator transition

The behavior of the MR of the film under investigation reflects important peculiarities of the observed MIT occurring upon a change in applied voltage. In addition, we observed some peculiarities in the behavior of MR in the MIT, which differ from the behavior of homogeneous systems and are connected with heterogeneous structural state of the film.

For high values of U (5–11 V), the conducting properties of the film correspond to a ''dirty'' $2D$ metal. In this state, the film possesses a comparatively low resistance ($R_\square \simeq 5$ kΩ) and a weak negative temperature dependence of resistance (see Fig. 6). The MR of the film is positive in this case and corresponds to the WL effect (see Fig. 7). The results of numerical analysis of the MR curves show that the film behaves in this state as an aggregate of metallic islands or percolating clusters whose size is larger than the phase relaxation length $L_\varphi \simeq 20$ nm. The islands are connected through tunnel barriers which are very low in the case of high applied voltages so that electron tunneling through them is nonactivated. The presence of tunnel barriers nevertheless leads to a considerable (approximately an order of magnitude) difference between the ''microscopic'' and ''macroscopic'' resistances $R_\square^{MR}$ and $R_\square$. For lower values of U, the barrier height increases, the conductivity becomes activated (see Figs. 2 and 4), and the MR becomes negative (see Fig. 8).

The change in the sign of MR (from positive to negative) in homogeneous $2D$ systems with a strong SOI is used as a criterion of transition from weak to strong electron localization.[22,23] This effect was observed earlier in heterogenous systems also.[19,36] Thus, this criterion can be used with certain stipulations in the case of heterogeneous systems, which is also confirmed by our results for the MIT induced by electric field. In the case of homogeneous systems, this transition is assumed to occur exactly for $\xi_l = L_\varphi(T)$.[22] This condition for a transition is hardly valid for heterogeneous systems. It is also clear that in the case of heterogeneous $2D$ systems we cannot speak of a certain value of $R_\square^c \approx R_Q$ at which a transition from weak to strong localization should take place.[3)] The value of $R_\square^c$ for the film under investigation was a function of temperature and the applied voltage U. It was mentioned above that the change in the sign of MR upon an increase in temperature occurs at larger values of U and hence at smaller values of $R_\square$. For example, the change in the sign of MR was observed for $U = \simeq 0.8$ V and $R_\square \simeq 36$ kΩ at $T = 1.5$ K, $U \simeq 1.5$ V and $R_\square \simeq 16$ kΩ at $T = 3$ K and for $U \simeq 2.5$ V and $R_\square \simeq 5.7$ kΩ at $T = 15$ K.

Figures 11 and 12 supplementing each other give a general visual idea of the behavior of MR in the transition from weak to strong electron localization in the film under investigation. Figure 11 shows a family of curves $\Delta R(H)/R = f(U^{-1})$ corresponding to different fixed tem-
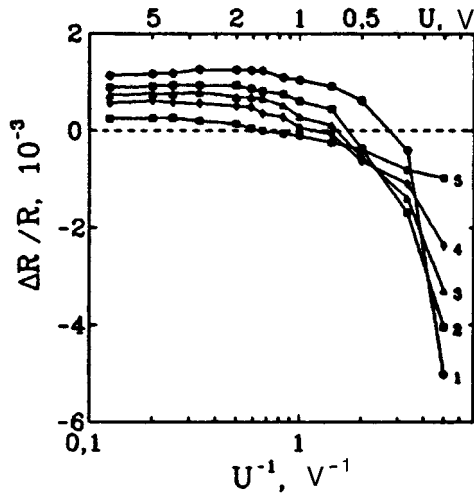
FIG. 11. Dependences $\Delta R(H)/R = f[\ln(1/U)]$ at $H = 1.1$ T and various temperatures T (in K): 2 (*1*), 3 (*2*), 4 (*3*), 5 (*4*), 10 (*5*).

peratures, while Fig. 12 presents a family of curves $\Delta R(H)/R = f(T^{-1})$ recorded at different fixed voltages. It can be seen from Fig. 11 that the value of MR is positive for large U, but becomes negative as the value of U decreases. It can also be seen that the change in the sign of MR upon an increase in temperature takes place for larger values of U. This is associated with the peculiar regularity mentioned above (see Figs. 9 and 12): the value of MR is positive in the intermediate region of U at low temperatures and negative at high temperatures. At first sight, this effect is unusual since an increase in temperature results to a decrease in resistance, i.e., a transition of the system to the metallic state characterized by positive MR. This obviously contradicts the above-mentioned criterion[22] of transition from weak to strong electron localization for homogeneous systems: a transition from negative to positive MR should be expected upon an increase in temperature. It will be proved below that the observed effect is associated with the heterogeneity (granular structure) of the film.
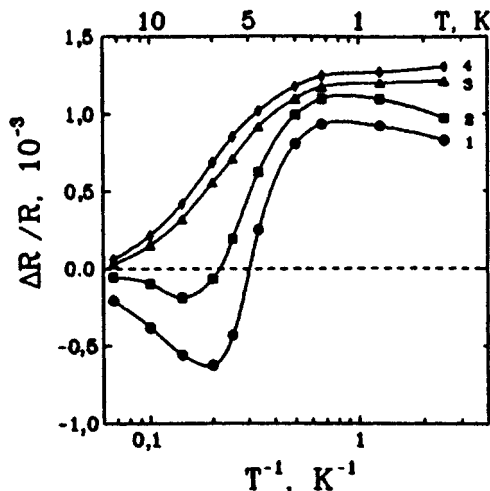

FIG. 12. Dependences $\Delta R(H)/R = f[\ln(1/T)]$ at $H = 1.1$ T and various values of the applied voltage U (in V): 0.5 (*1*), 1.0 (*2*), 2.0 (*3*), 3.0 (*4*).

On the basis of the obtained results, we can propose a simple qualitative explanation of the peculiarities in the behavior of MR mentioned above. We assume that the system under investigation can be approximated as a regular net formed by pairs of series-connected resistances R_M and $R_T(T,U)$, where R_M is the resistance of metal in a granule and $R_T(T,U)$ the tunnel resistance between adjacent granules. The value of sheet resistance R_G for such a net by the order of magnitude, coincides with the resistance of such a pair (i.e., $R_G \approx R_M + R_T(T,U)$). In this case, the variation of film resistance in a magnetic field in the entire range of value of T and U can be represented to a sufficiently good approximation as the sum of two components:

$$\Delta R = \Delta R_{WL}(H,T) + \Delta R_{SL}(H,T,U), \tag{11}$$

where $\Delta R_{WL}(H,T)$ is the positive contribution to the MR from the WL effect in metallic islands, and $\Delta R_{SL}(H,T,U)$ is the negative contribution to the MR associated with the effect of magnetic field on activated electron tunneling between islands. The first term is defined only by the ''microscopic'' disorder of metallic islands which does not depend on U. This is confirmed by the absence of any dependence of the ''microscopic'' resistance $R_\square^{MR}$ on T or U. Hence this term depends only on H and T. The second term is determined by the properties of tunnel barriers between islands and depends not only on H and T, but also on U. The first term can be written in the form

$$\Delta R_{WL}(H,T) = AR_M \frac{H^2}{T^{2p}}, \tag{12}$$

where $A = \text{const}$. While writing formula (12), we took into account the fact that the function $f(x)$ in formula (5) defining the contribution of the WL effect to MR can be presented for $x < 1$ in the form[4) $f(x) \approx x^2/24$.[3] It follows hence that $\Delta R_{WL}(H,T)/R \propto H^2 \tau_\varphi^2 \propto H^2/T^{2p}$. For continuous gold films prepared from the same starting material, $p = 1$ or 2 depending on the temperature and resistance $R_\square$.[25,26] Taking the value $p = 1$ for the sake of definiteness, we obtain $\Delta R_{WL}(H,T)/R \propto H^2/T^2$ However, it was shown above that $\Delta R_{SL}(H,T,U)/R = -BH^2/T$ for small U. Hence the second term in formula (11) can be presented in the form

$$\Delta R_{SL}(H,T,U) = -BR_T(T,U) \frac{H^2}{T}. \tag{13}$$

Going over to the relative correction, we obtain

$$\frac{\Delta R(H)}{R_M + R_T(T,U)} = \frac{A}{(1+\gamma)} \frac{H^2}{T^2} - \frac{B}{(1+1/\gamma)} \frac{H^2}{T}, \tag{14}$$

where $\gamma = R_T(T,U)/R_M$. For small values of U, formula (14) in the limit $\gamma \gg 1$ is reduced to formula (13) for negative MR in the strong localization regime. With increasing U, both $R_T(T,U)$ and γ decrease at a fixed temperature, and formula (14) in the limit $\gamma \ll 1$ is reduced to formula (12) for positive MR in the weak localization regime. The change of the sign of MR in such a case inevitably occurs at a certain intermediate value of U.

Formula (14) also illustrates the possibility of the observed transition from positive to negative MR upon an increase in temperature for fixed U (Figs. 11 and 12). Indeed,

it was shown above that $\Delta R_{WL}(H,T)/R \propto H^2/T^2$. At the same time, $\Delta R_{SL}(H,T,U)/R \propto -H^2/T$ for small U. Thus, as the temperature increases, the first term in (14) decreases more rapidly than the second, thus leading to a change in the sign of MR from positive to negative.[5]

3.4. Magnetoresistance in the nearest-neighbor hopping conduction

In the insulating state, the temperature dependence of the conductivity of the film under consideration was defined by the Arrhenius law (Fig. 4) corresponding to the nearest-neighbor hopping. Under such conditions, negative MR defined by formula (6) was detected. Earlier, Pakhomov et al.[24] reported on negative MR under conditions of nearest-neighbor hopping in a three-dimensional granular metal (a mixture of Al and Al_2O_3), in which it was found that $\Delta R(H) \propto -H$ (i.e., linear dependence on H), but the temperature dependence of MR could not be established. For the percolating gold film investigated by us, a quadratic dependence on H was observed and the temperature dependence was also determined (see formula (6)). In order to explain the negative MR in this case, we cannot use the interference models[37-39] taking into account the interference of contributions to the hopping probability from various trajectories of electron tunneling, including the acts of scattering at intermediate impurities. This approach is valid only for VRH.

With the exception of Ref. 40, we are not aware of any publication about the theoretical models of negative MR in disordered systems under conditions of hopping between nearest neighbors. The prediction of this model ($\Delta R(H) \propto -H^2/T$ under the Arrhenius law $R(T) \propto \exp(1/T)$) is formally in complete accord with our results. However, this model was worked out for weakly doped $3D$ semiconductors, and it is not clear whether it is applicable for GM. Moreover, Bötger et al.[40] presumed the ''high-temperature'' mechanism of the Arrhenius law indicated in Sec. 3.2, where the spread of energy levels of localized states at quite high temperatures was disregarded. In contrast to this, for the semicontinuous films investigated by us the Arrhenius law is valid only at low ($\leqslant 15$ K) temperatures and is associated (see above) with a limited number of localized states (a small number of hopping versions) and consequently with the existence of ''difficult'' hops in optimal conducting chains. Hence there are no justifications for using the model described in Ref. 40 to explain the obtained results. Thus, the nature of negative MR in GM under conditions of hopping between nearest neighbors remains practically unclear. We hope that the experimental results presented in this work will facilitate the development of theoretical models for this interesting phenomenon.

CONCLUSION

In this work, we have detected a transition from strong to weak localization in a semicontinuous (island) gold film upon a change in the applied voltage. This transition is accompanied by a change in the sign of MR. The obtained results can be explained by using modern concepts about the conductivity of granular systems. By the order of magnitude

the localization effects in the temperature dependence of resistance are determined by simple addition of the granule resistance and the resistance created by tunnel barriers between granules. The former obeys the laws of the WL theory. Since the phase relaxation length is less than the granule size, this resistance is not sensitive to division of the sample into granules. The second resistance decreases exponentially upon an increase in temperature or voltage. Hence both these agencies lead to a change in the temperature dependence of resistance from strong to weak localization. The magnetoresistance behaves in a more complex manner. It is shown that at relatively high temperatures, the weak localization region corresponds to positive MR which is described quite accurately by the WL theory. The region of strong localization corresponds to negative MR. This relation is violated in favor of the positive MR upon a decrease in temperature. This fact can be understood on the phenomenological level by comparing the temperature dependence of the negative MR obtained by us with the known temperature dependence of MR within grains, for which the WL theory is valid, and the latter contribution predominates at low temperatures. The negative MR of the investigated film under strong localization conditions was manifested for electron hops between nearest neighbors. The origin of this effect remains unclear. The obtained results can be used for working out theoretical models for this interesting phenomenon.

[1)]A similar behavior of conductivity was also observed by us in other gold films obtained under the conditions described in this paper.

[2)]At $T > 15$ K, the positive MR was quite small [$\Delta R(H)/R < 10^{-3}$ for $H \simeq 4$ T], and hence its behavior could not be compared with formula (5) very accurately.

[3)]For example, the change of the sign of MR in inhomogeneous In_2O_3 films occurred for $R_\square^c \simeq 1$ MΩ.[36]

[4)]Estimates show that for the films investigated by us, this corresponds to $H < 1$ T.

[5)]In a more rigorous approach, we must also take into account the decrease in $R_T(T,U)$ with increasing temperature, which causes a further weakening of the temperature dependence of the contribution of the second term in (14). However, we observed a change of the sign of MR upon an increase in temperature for quite low-resistive states of the samples ($R_\square \leqslant 10$ kΩ), for which the dependence of R_T on temperature is not very strong and hence the negative contribution dominates at quite high temperatures.

[1]E. Abrahams. P. W. Anderson, D. C. Licciardello, and T. V. Ramakrishnan, Phys. Rev. Lett. **42**, 673 (1979).

[2]P. A. Lee and T. V. Ramakrishnan, Rev. Mod. Phys. **57**, 287 (1985).

[3]B. L. Altshuler and A. G. Aronov, in: *Electron–Electron Interactions in Disordered Systems* (Ed. by A. L. Efros and M. Pollak), North-Holland, Amsterdam (1985).

[4]N. F. Mott and E. A. Davis, *Electron Processes in Noncrystalline Materials*, Clarendon Press, Oxford (1979).

731   Low Temp. Phys. **23** (9), September 1997

Belevtsev *et al.*   731

[5] B. I. Shklovskii and A. L. Efros, *Electronic Properties of Doped Semiconductors*, Springer-Verlag, Berlin (1984).

[6] D. E. Khmel'nitskii, Pis'ma Zh. Éksp. Teor. Fiz. **32**, 248 (1980) [JETP Lett. **32**, 229 (1980)].

[7] Y. Gefen, D. J. Thouless, and Y. Imry, Phys. Rev. **B28**, 6677 (1983).

[8] G. Deutscher, A. M. Goldman, and H. Micklitz, Phys. Rev. **B31**, 1679 (1985).

[9] A. Palevskii and G. Deutscher, Phys. Rev. **B34**, 431 (1986).

[10] A. A. Moshenskii and M. A. Spasova, Fiz. Nizk. Temp. **17**, 517 (1991) [Sov. J. Low Temp. Phys. **17**, 273 (1991)].

[11] G. Dumpich and A. Carl, Phys. Rev. **B43**, 12074 (1991).

[12] N. Papandreou nd P. Nedellec, J. Phys. (France) **2**, 707 (1992).

[13] M. E. Gershenson, P. M. Echternach, and H. M. Bozler, Phys. Rev. Lett. **74**, 446 (1995).

[14] Y. Imry and M. Strongin, Phys. Rev. **B24**, 6353 (1981).

[15] H. White and G. Bergmann, Phys. Rev. **B40**, 11594 (1989).

[16] R. C. Dynes, J. P. Garno, and J. M. Rowell, Phys. Rev. Lett. **40**, 479 (1978).

[17] Z. Ovadyahu and Y. Imry, J. Phys. **C16**, L471 (1983).

[18] B. I. Belevtsev, Yu. F. Komnik, and A. V. Fomin, Fiz. Tverd. Tela (Leningrad) **28**, 2038 (1986) [Sov. Phys. Solid State **28**, 1139 (1986)].

[19] B. I. Belevtsev, Yu. F. Komnik, and A. V. Fomin, Fiz. Nizk. Temp. **12**, 821 (1986) [Sov. J. Low Temp. Phys. **12**, 465 (1986)].

[20] B. I. Belevtsev, Yu. F. Komnik, and A. V. Fomin, Fiz. Tverd. Tela (Leningrad) **30**, 2773 (1988) [Sov. Phys. Solid State **30**, 1598 (1988)].

[21] Y. Liu, B. Nease, K. A. McGreer, and A. M. Goldman, Europhys. Lett. **19**, 409 (1995).

[22] Y. Meir, N. S. Wingreen, O. Entin-Wohlman, and B. L. Altshuler, Phys. Rev. Lett. **66**, 1517 (1991).

[23] S.-Y. Hsu and J. M. Valles, Jr., Phys. Rev. Lett. **74**, 2331 (1995).

[24] A. B. Pakhomov, D. S. MacLachlan, I. I. Oblakova, and A. M. Virnik, J. Phys.: Condens. Matter 5, 5313 (1993).

[25] B. I. Belevtsev, E. Yu. Belyaev, V. V. Bobkov, and V. I. Glushko, Fiz. Nizk. Temp. **21**, 763 (1995) [Low Temp. Phys. **25**, 592 (1995)].

[26] B. I. Belevtsev, Yu. F. Komnik, and E. Yu. Belyaev, Fiz. Nizk. Temp. **21**, 839 (1995) [Low Temp. Phys. **25**, 646 (1995)].

[27] A. V. Butenko, E. I. Bukhshtab, and V. V. Pilipenko, Fiz. Nizk. Temp. **10**, 773 (1984) [Sov. J. Low Temp. Phys. **10**, 407 (1984)].

[28] B. Abeles, P. Sheng, M. D. Coutts, and Y. Arie, Adv. Phys. **24**, 407 (1975).

[29] P. Sheng and J. Klafter, Phys. Rev. **B27**, 2583 (1983).

[30] C. J. Adkins, J. Phys.: Condens. Matter 1, 1253 (1989).

[31] P. Sheng, Philos. Mag. **B65**, 357 (1992).

[32] J. Kurkijarvi, Phys. Rev. **B8**, 922 (1973).

[33] M. E. Raikh and I. M. Ruzin, in: *Mesoscopic Phenomena in Solids* [Ed. by B. L. Altshuler, P. A. Lee, and R. A. Webb], North-Holland, Amsterdam (1991).

[34] M. E. Raikh and I. M. Ruzin, Phys. Rev. **B17**, 11203 (1990).

[35] M. Mostefa, D. Bourbie, and G. Olivier, Physica **B160**, 186 (1989).

[36] Y. Shapir and Z. Ovadyahu, Phys. Rev. **B40**, 12441 (1989).

[37] V. L. Nguen, B. Z. Spivak, and B. I. Shklovskii, Pis'ma Zh. Éksp. Teor. Fiz. **41**, 35 (1985) [JETP Lett. **41**, 42 (1985)].

[38] B. I. Shklovskii and B. Z. Spivak, in *Hopping Transport in Solids* [Ed. by M. Pollak and B. I. Shklovskii], Elsevier Sci. Publ., New York (1991).

[39] U. Sivan, O. Entin-Wohlman, and Y. Imry, Phys. Rev. Lett. **60**, 1566 (1988).

[40] H. Bötger, V. V. Bryskin, and F. Schulz, Phys. Rev. **B49**, 2447 (1994).

Translated by R. S. Wadhwa

One exactly solvable random spin-1/2 *XY* chain

O. V. Derzhko and T. M. Verkholyak

Institute for Condensed Matter Physics, 1 Svientsitskii St., L'viv-11, 290011, Ukraine[*]
(Submitted October 23, 1996; revised January 4, 1997)
Fiz. Nizk. Temp. **23**, 977–982 (September 1997)

Considering one-dimensional spin-1/2 isotropic *XY* model with Dzyaloshinski–Moriya interaction in random Lorentzian transverse field we have calculated exactly thermodynamic quantities of the model. We used the derived average single-particle density of states to examine the validity of coherent potential approximation. © *1997 American Institute of Physics.*
[S1063-777X(97)00809-8]

1. INTRODUCTION

Random models that can be solved exactly are of great importance in understanding the effects of disorder because they do not contain uncontrolled errors that are introduced by approximate treatment. One such model has been known for almost thirty years. Considering a model of tight-binding electrons, P. Lloyd was first to recognize that Lorentzian diagonal disorder allows one to perform the averaging of one-electron Green's functions over random variables with the help of contour integrals without making any approximation.[1] This idea was exploited by H. Nishimori for spin-1/2 isotropic *XY* chain which is related to Lloyd's model via the Jordan–Wigner transformation.

In the present paper our aim is to extend the consideration given in Ref. 2 by introducing additional Dzyaloshinskii–Moriya spin-spin interaction. By analogy with Ref. 2, we obtained exactly average, single-particle density of states and hence the thermodynamic quantities (Sec. 2). Moreover, the average density of states which we obtained enables us to discuss the applicability of coherent potential approximation which is usually used to describe realistic quenched systems for which exact solutions do not exist[3,4] (Sec. 3).

2. DENSITY OF STATES AND THERMODYNAMIC QUANTITIES

We consider N interacting spins 1/2 in a random transverse field that are governed by the Hamiltonian

$$H = \sum_{j=1}^{N} (\Omega_0 + \Omega_j) s_j^z + \sum_{j=1}^{N} [J(s_j^x s_{j+1}^x + s_j^y s_{j+1}^y)$$

$$+ D(s_j^x s_{j+1}^y - s_j^y s_{j+1}^x)] = \sum_{j=1}^{N} (\Omega_0 + \Omega_j)\left(s_j^+ s_j^- - \frac{1}{2}\right)$$

$$+ \sum_{j=1}^{N} \left(\frac{J+iD}{2} s_j^+ s_{j+1}^- + \frac{J-iD}{2} s_j^- s_{j+1}^+\right),$$

$$s_{N+j}^\alpha = s_j^\alpha, \tag{1}$$

with the Lorentzian probability distribution density

$$p(...,\Omega_j,...) = \prod_{j=1}^{N} \frac{1}{\pi} \frac{\Gamma}{\Omega_j^2 + \Gamma^2}.$$

The introduced Hamiltonian (1) contains the interaction terms proportional to D which describe the Dzyaloshinskii–Moriya interactions of the neighbouring spins.

The Jordan–Wigner transformation[5]

$$c_1 = s_1^-, c_1^+ = s_1^+, c_j = P_{j-1} s_j^-, c_j^+ = P_{j-1} s_j^+,$$

$$P_j \equiv \prod_{n=1}^{j} (-2s_n^z), \quad j = 2,...,N$$

converts (1) into a Hamiltonian of noninteracting spinless fermions

$$H = H^- + BP^+,$$

$$H^- = \sum_{j=1}^{N} (\Omega_0 + \Omega_j)\left(c_j^+ c_j - \frac{1}{2}\right) + \sum_{j=1}^{N}$$

$$\times \left(\frac{J+iD}{2} c_j^+ c_{j+1} - \frac{J-iD}{2} c_j c_{j+1}^+\right),$$

$$c_{N+j} = c_j, \quad c_{N+j}^+ = c_j^+,$$

$$B = -[(J+iD)c_N^+ c_1 - (J-iD)c_N c_1^+],$$

$$P^+ = \frac{1+P_N}{2}. \tag{2}$$

The boundary term B may be omitted since it does not influence thermodynamic quantities[6]. Hence, the thermodynamics of spin model (1) is determined by the average one-fermion Green's functions $\overline{G_{nm}^\mp(E)}$, where

$$G_{nm}^\mp(t) = \frac{1}{2\pi} \int_{-\infty}^{\infty} dE e^{-iEt} G_{nm}^\mp(E \pm i\varepsilon), \quad \varepsilon \to +0,$$

$$G_{nm}^\mp(t) \equiv \mp i\Theta(\pm t)\langle\{c_n(t), c_m^+\}\rangle,$$

$$\overline{(...)} \equiv \int_{-\infty}^{\infty} d\Omega_1 ... \int_{-\infty}^{\infty} d\Omega_N p(...,\Omega_j,...)(...),$$

via the average density of states

$$\overline{\rho(E)} = \mp \frac{1}{\pi} \, \text{Im} \, \overline{G_{jj}^{\mp}(E)},$$

and, therefore, the main goal is to find $\overline{G_{nm}^{\mp}(E)}$.

The equation of motion for $G_{nm}^{\mp}(t)$ that follows from (2) leads to the following set of equations for $G_{nm}^{\mp}(E \pm i\varepsilon)$:

$$(E \pm i\varepsilon) G_{nm}^{\mp}(E \pm i\varepsilon) = \delta_{nm} + (\Omega_0 + \Omega_n) G_{nm}^{\mp}(E \pm i\varepsilon)$$

$$+ \frac{J - iD}{2} G_{n-1,m}^{\mp}(E \pm i\varepsilon) + \frac{J + iD}{2} G_{n+1,m}^{\mp}(E \pm i\varepsilon). \quad (3)$$

To average (3), it can be assumed that Ω_j are complex variables and contour integration can be used in complex planes $\Omega_j s$. Following the paper by John and Schreiber,[7] we can rewrite Eq. (3) in the form

$$(\mathbf{A} \pm i\mathbf{B}^{\mp}) \mathbf{G}^{\mp}(E \pm i\varepsilon) = \mathbf{I},$$

where

$$\mathbf{A} \equiv \begin{pmatrix} E - \Omega_0 - \text{Re} \, \Omega_1 & -\dfrac{J+iD}{2} & 0 & \dots \\[2mm] -\dfrac{J-iD}{2} & E - \Omega_0 - \text{Re} \, \Omega_2 & -\dfrac{J+iD}{2} & \dots \\[2mm] 0 & -\dfrac{J-iD}{2} & E - \Omega_0 - \text{Re} \, \Omega_3 & \dots \\[2mm] \vdots & \vdots & \vdots & \end{pmatrix},$$

$$\mathbf{B}^{\mp} \equiv \begin{pmatrix} \varepsilon \mp \text{Im} \, \Omega_1 & 0 & 0 & \dots \\ 0 & \varepsilon \mp \text{Im} \, \Omega_2 & 0 & \dots \\ 0 & 0 & \varepsilon \mp \text{Im} \, \Omega_3 & \dots \\ \vdots & \vdots & \vdots & \end{pmatrix},$$

$$\mathbf{G}^{\mp}(E \pm i\varepsilon)$$

$$\equiv \begin{pmatrix} G_{11}^{\mp}(E \pm i\varepsilon) & G_{12}^{\mp}(E \pm i\varepsilon) & G_{13}^{\mp}(E \pm i\varepsilon) & \dots \\ G_{21}^{\mp}(E \pm i\varepsilon) & G_{22}^{\mp}(E \pm i\varepsilon) & G_{23}^{\mp}(E \pm i\varepsilon) & \dots \\ G_{31}^{\mp}(E \pm i\varepsilon) & G_{32}^{\mp}(E \pm i\varepsilon) & G_{33}^{\mp}(E \pm i\varepsilon) & \dots \\ \vdots & \vdots & \vdots & \end{pmatrix},$$

$$\mathbf{I} \equiv \begin{pmatrix} 1 & 0 & 0 & \dots \\ 0 & 1 & 0 & \dots \\ 0 & 0 & 1 & \dots \\ \vdots & \vdots & \vdots & \end{pmatrix}.$$

Evidently, the poles of $\mathbf{G}^{\mp}(E \pm i\varepsilon)$ are determined by the zeros of $\det(\mathbf{A} \pm i\mathbf{B}^{\mp})$. If all eigenvalues λ_s of $\mathbf{B}^{\mp}$ are positive $\mathbf{B}^{\mp} = (\mathbf{b}^{\mp})^2$, where $\mathbf{b}^{\mp}$ is symmetric, $(\mathbf{b}^{\mp})^{-1}$ is symmetric, $(\mathbf{b}^{\mp})^{-1} \mathbf{A} (\mathbf{b}^{\mp})^{-1}$ is Hermitian, and therefore,

$$\det(\mathbf{A} \pm i\mathbf{B}^{\mp}) = \det\mathbf{B}^{\mp} \det[(\mathbf{b}^{\mp})^{-1} \mathbf{A} (\mathbf{b}^{\mp})^{-1} \pm i\mathbf{I}] \neq 0.$$

Relying on Gershgorin criterion[8] for the matrix $\mathbf{B}^{\mp}$, we see that at least one of the inequalities

$$|\varepsilon \mp \text{Im} \, \Omega_j - \lambda| \leqslant 0, \quad j = 1, \dots, N$$

must be true. Therefore, the retarded Green's function $G_{nm}^{-}(E + i\varepsilon)$ [the advanced Green's function $G_{nm}^{+}(E - i\varepsilon)$] does not have the poles for $\text{Im} \, \Omega_j \leqslant 0$ ($\text{Im} \, \Omega_j \geqslant 0$). While averaging (3) one must close the contours of integration in these planes and compute the residua originating from the Lorentzian probability distribution density at $\mp i\Gamma$, obtaining finally

$$(E - \Omega_0 \pm i\Gamma) \overline{G_{nm}^{\mp}(E)} - \frac{J - iD}{2} \overline{G_{n-1,m}^{\mp}(E)}$$

$$- \frac{J + iD}{2} \overline{G_{n+1,m}^{\mp}(E)} = \delta_{nm}. \quad (4)$$

It is worthwhile to note that Eqs. (4) may be obtained in a slightly different manner. According to (3), we can rewrite $G_{nm}^{\mp}(E \pm i\varepsilon)$ as a series in degrees of $(J \pm iD)/2$. Due to a magic property of the Lorentzian distribution

$$\overline{(E - \Omega_0 - \Omega_j \pm i\varepsilon)^{-s}} = (E - \Omega_0 \pm i\Gamma \pm i\varepsilon)^{-s}$$

the averaging is straightforward and after summation of the series we again obtain (4).

Equations (4) are translationally invariant and can be solved in a standard way with the result

$$\overline{G_{nm}^{\mp}(E)} = \frac{1}{2\pi} \int_{-\pi}^{\pi} \frac{d\kappa \, e^{i(n-m)\kappa}}{E - [\Omega_0 + (J^2 + D^2)^{1/2} \cos(\kappa + \varphi)] \pm i\Gamma}$$

$$= \frac{e^{i\varphi(n-m)}}{(J^2 + D^2)^{1/2}} \frac{[x - (x^2 - 1)^{1/2}]^{|n-m|}}{(x^2 - 1)^{1/2}}, \quad (5)$$

where

$$\tan \varphi = \frac{D}{J}, \quad x = \frac{E}{(J^2 + D^2)^{1/2}} - \omega_0 \pm i\gamma,$$

$$\omega_0 = \frac{\Omega_0}{(J^2 + D^2)^{1/2}}, \quad \text{and} \quad \gamma = \frac{\Gamma}{(J^2 + D^2)^{1/2}}.$$

From (5) it follows that

$$\overline{\rho(E)} = \mp \frac{1}{\pi} \, \text{Im}((E - \Omega_0 \pm i\Gamma)^2 - (J^2 + D^2))^{-1/2}$$

$$= \frac{1}{\pi} \left[\frac{(A^2 + B^2)^{1/2} - A}{2(A^2 + B^2)} \right]^{1/2}, \quad (6)$$

where $A \equiv (E - \Omega_0)^2 - \Gamma^2 - J^2 - D^2$, $B = 2\Gamma(E - \Omega_0)$. Hence, the introduction of the Dzyaloshinskii–Moriya interaction from the viewpoint of thermodynamics results in the renormalization of the spin-spin interaction: $J^2 \to J^2 + D^2$. Thermodynamic quantities of the spin model (1) are determined by the average density of states (6) in a standard way. The corresponding formulas for entropy $\overline{s}$, specific heat $\overline{c}$, transverse magnetization $\overline{m_z} \equiv \langle (1/N) \Sigma_{j=1}^{N} s_j^z \rangle$, and static transverse susceptibility $\overline{\chi_{zz}} \equiv \partial \overline{m_z} / \partial \Omega_0$ are

$$\overline{s} = \int dE \overline{\rho(E)} \left[\ln\left(2 \cosh \frac{E}{2kT} \right) - \frac{E}{2kT} \tanh \frac{E}{2kT} \right],$$

$$\overline{c} = \int dE \overline{\rho(E)} \left(\frac{E/2kT}{\cosh(E/2kT)} \right)^2,$$

$$\overline{m_z} = -\frac{1}{2} \int dE \overline{\rho(E)} \tanh \frac{E}{2kT},$$
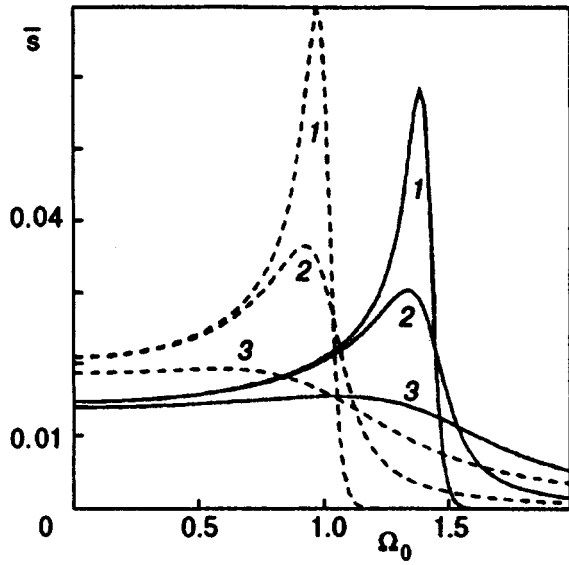
FIG. 1. $\overline{s}$ versus Ω_0 at $T=0.02$; $D=0$ (dashed curves), $D=1$ (solid curves), $\Gamma=0(1)$, 0.1 (2), 0.5 (3).
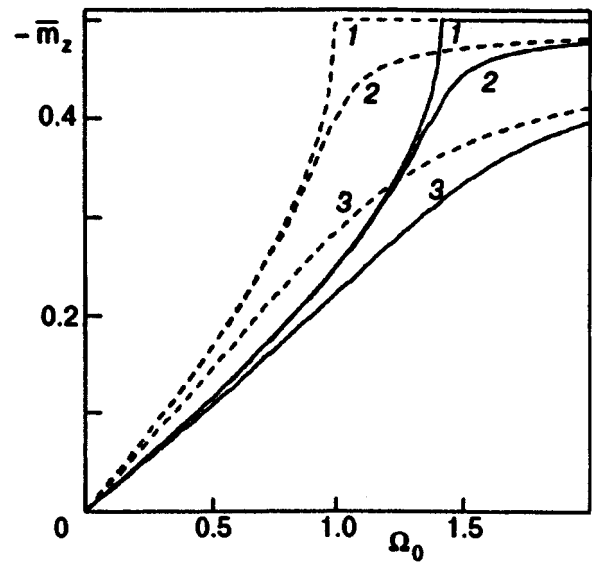

FIG. 3. $\overline{-m_z}$ versus Ω_0 at $T=0$; $D=0$ (dashed curves), $D=1$ (solid curves), $\Gamma=0(1)$, 0.1 (2), 0.5 (3).

$$\overline{\chi_{zz}}=-\frac{1}{kT}\int dE\,\overline{\rho(E)}\,\frac{1}{[2\cosh(E/2kT)]^2}.$$

In the numerical calculations of thermodynamic quantities J was set to 1. Figures 1–4 show the dependences of the entropy $\overline{s}$, specific heat $\overline{c}$, transverse magnetization $\overline{m_z}$, and static transverse susceptibility $\overline{\chi_{zz}}$ on Ω_0 at low temperatures. The temperature dependences of $\overline{m_z}$ and $\overline{\chi_{zz}}$ at $\Omega_0=0.5$ are shown in Figs. 5 and 6. The dashed curves correspond to $D=0$, and the solid curves correspond to $D=1$; 1 refers to the nonrandom case $\Gamma=0$, 2 refers to $\Gamma=0.1$, and 3 refers to $\Gamma=0.5$. It can be seen how some of the pronounced features of the plotted dependences disappear due to randomness. Dzyaloshinskii–Moriya interaction leads only to quantitative changes in thermodynamic quantities.

The importance of the two-spin correlation functions is obvious; it was recognized by Kontorovich and Tsukernik[9] in connection with a possibility for the appearance of the spiral structure in nonrandom spin-1/2 isotropic XY chain with Dzyaloshinskii–Moriya interaction. Although the average one-fermion Green's functions (5) yield the average fermion correlation function $\langle c_m^+ c_n(t)\rangle$,[10] and at $t=0$ and $T=0$ the latter quantity can be calculated explicitly[11]

$$\overline{\langle c_m^+ c_n\rangle}=\frac{1}{\pi|n-m|}\,\mathrm{Im}\left\{e^{i\varphi(n-m)}\left[-\omega_0\right.\right.$$
$$\left.\left.+\left(\frac{(\mathscr{C}^2+\mathscr{D}^2)^{1/2}+\mathscr{C}}{2}\right)^{1/2}\right.\right.$$
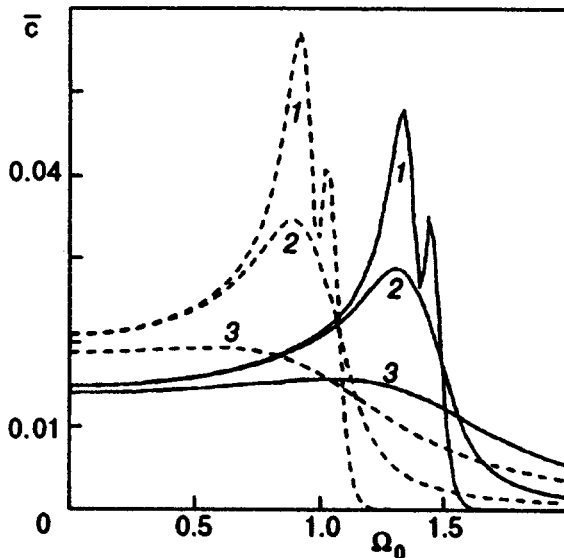

FIG. 2. $\overline{c}$ versus Ω_0 at $T=0.02$; $D=0$ (dashed curves), $D=1$ (solid curves), $\Gamma=0(1)$, 0.1 (2), 0.5 (3).
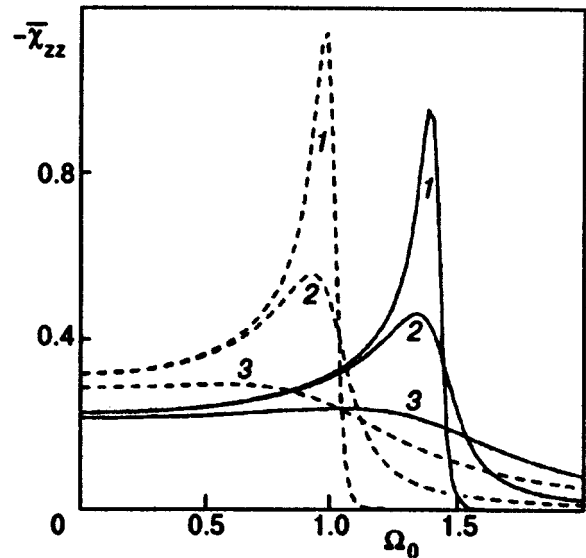

FIG. 4. $\overline{-\chi_{zz}}$ versus Ω_0 at $T=0.02$; $D=0$ (dashed curves), $D=1$ (solid curves), $\Gamma=0(1)$, 0.1 (2), 0.5 (3).
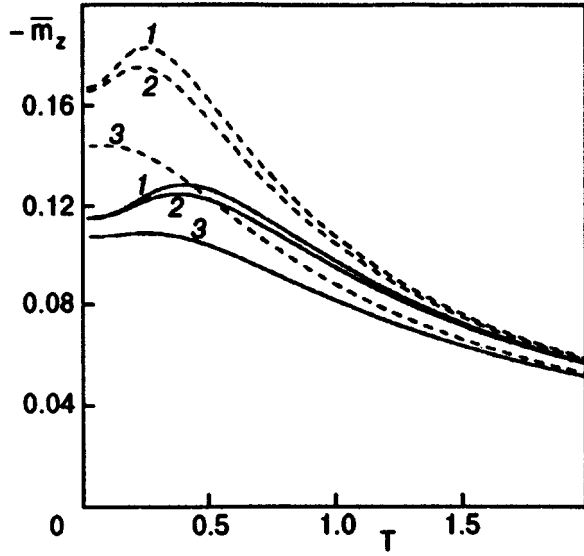
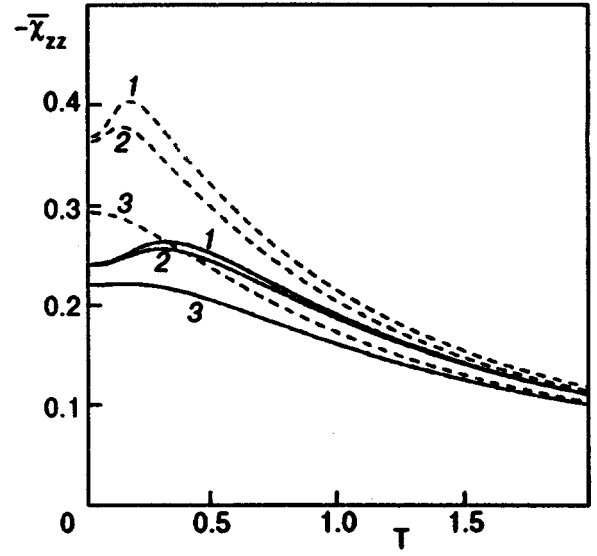FIG. 5. $\overline{-m_z}$ versus T at $\Omega_0 = 0.5$; $D = 0$ (dashed curves), $D = 1$ (solid curves), $\Gamma = 0$ (*1*), 0.1 (*2*), 0.5 (*3*).

FIG. 6. $\overline{-\chi_{zz}}$ versus T at $\Omega_0 = 0.5$; $D = 0$ (dashed curves), $D = 1$ (solid curves), $\Gamma = 0$ (*1*), 0.1 (*2*), 0.5 (*3*).

$$+ i\gamma - i\left(\frac{(\mathscr{C}^2 + \mathscr{D}^2)^{1/2} - \mathscr{C}}{2}\right)^{1/2}\Big]^{|n-m|}\Bigg\},$$

where $\mathscr{C} = \omega_0^2 - \gamma^2 - 1$, and $\mathscr{D} = 2\omega_0\gamma$, this does not allow us to obtain the spin correlation functions. The simplest equal-time zz spin correlation function in fermion representation has the form

$$\overline{\langle s_j^z s_{j+n}^z \rangle} = \overline{\langle c_j^+ c_j \rangle \langle c_{j+n}^+ c_{j+n} \rangle} + \overline{\langle c_j^+ c_{j+n} \rangle \langle c_j c_{j+n}^+ \rangle}$$

$$- \overline{\langle c_j^+ c_j \rangle} + \frac{1}{4},$$

and hence its evaluation requires the knowledge of the average products of two fermion correlation functions. Similar difficulties arose in the calculation of the electric conductivity for Lloyd's model[12].

3. COHERENT POTENTIAL APPROXIMATION

Consider the spin model (1) with arbitrary (not necessarily Lorentzian) random transverse field in the framework of coherent potential approximation. Choosing the random part of (1) and introducing a coherent transverse field $\hat{\Omega}$, we rewrite (3) in the form of a propagator expansion

$$G_{gm}^{\mp}(E) = \hat{G}_{gm}^{\mp}(E) + \hat{G}_{gn}^{\mp}(E)(\Omega_n - \hat{\Omega})\hat{G}_{nm}^{\mp}(E) + \ldots$$

where $\hat{G}_{gm}^{\mp}(E)$ is determined by (5) with $\Gamma = 0$ and $\Omega_0 + \hat{\Omega}$ instead of Ω_0, and then as an expansion in degrees in the $\hat{t}$-matrix

$$G_{gm}^{\mp}(E) = \hat{G}_{gm}^{\mp}(E) + \hat{G}_{gn}^{\mp}(E)\hat{t}_n\hat{G}_{nm}^{\mp}(E) + \ldots .$$

Here $\hat{t}_n \equiv (\Omega_n - \hat{\Omega})/(1 - \hat{G}_{nn}^{\mp}(E)(\Omega_n - \hat{\Omega}))$. The coherent field is determined from the condition

$$\overline{\hat{t}_n} = \int d\Omega_1 \ldots \int d\Omega_N p(\ldots, \Omega_j, \ldots)$$

$$\times \frac{\Omega_n - \hat{\Omega}}{1 - \hat{G}_{nn}^{\mp}(E)(\Omega_n - \hat{\Omega})} = 0, \tag{7}$$

where $\hat{G}_{nn}^{\mp}(E) = [(E - \Omega_0 - \hat{\Omega} \pm i\varepsilon)^2 - (J^2 + D^2)]^{-1/2}$ (see Refs. 3 and 4).

In the case of a Lorentzian transverse field Eq. (7) has a solution $\hat{\Omega} = \mp i\Gamma$ and, therefore, $\hat{G}_{nn}^{\mp}(E)$ coincides with the exact expression (5).

Consider another probability distribution density

$$p(\ldots, \Omega_j, \ldots) = \prod_{j=1}^{N} [x\delta(\Omega_j) + (1-x)\delta(\Omega_j - \Omega)],$$

$$0 \leqslant x \leqslant 1.$$

Equation (7) will then reduce to a cubic equation for $\hat{\Omega}$. Its solutions yield the Green's functions and the density of states $\overline{\rho(E)} \approx \mp (1/\pi)\mathrm{Im}\,\hat{G}_{nn}^{\mp}(E)$. In Fig. 7 the quantity $R(E^2) = (\rho(E) + \rho(-E))/2|E|$, which follows from the coherent potential approximation (dashed curves), is compared with the result of exact finite-chain computation of this quantity (solid curves)[13]. A good agreement between approximate and exact results apparently is contingent on the fact that thermodynamic averaging for noninteracting fermions has been performed exactly.

4. CONCLUSIONS

We have presented exact calculations of the thermodynamic quantities of spin-1/2 isotropic XY chain with the Dzyaloshinskii–Moriya interaction in random Lorentzian transverse field. The approach exploits reformulation in terms of fermions and the possibility of averaging exactly the equations for one-fermion Green's functions that yield thermodynamics. Such scheme is essentially limited by Lorent-

O. V. Derzhko and T. M. Verkholyak   736
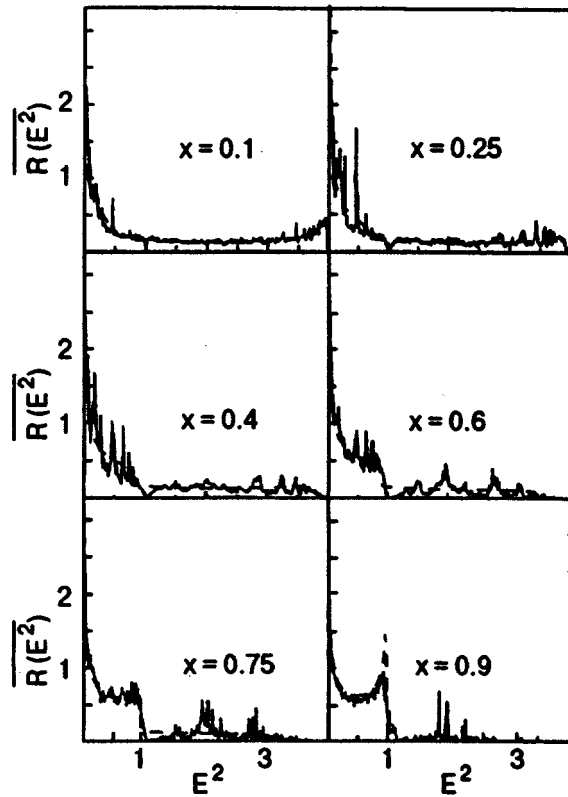
FIG. 7. $\overline{R(E^2)}$ versus E^2: the results of exact calculation (solid curves) and coherent potential approximation (dashed curves).

zian disorder. The results obtained by us supplement to some extent the existing exact analytical results for random spin-1/2 XY chains.[14–20] The comparison of the density of states obtained within the coherent potential approximation and the exact result illustrates that the region of validity of more sophisticated approaches of disordered spin systems theory can be tested.

*E-mail: derzhko@icmp.lviv.ua

[1] P. Lloyd, J. Phys. **C2**, 1717 (1969).
[2] H. Nishimori, Phys. Lett. **A100**, 239 (1984).
[3] R. J. Elliot, A. Krumhansl, and P. L. Leath, Rev. Mod. Phys. **46**, 465 (1974).
[4] K. Handrich and S. Kobe, *Amorphe Ferro-und Ferrimagnetika*, Akademie-Verlag, Berlin (1980) (in German).
[5] E. Lieb, T. Schultz, and D. Mattis, Ann. Phys. **16**, 407 (1961).
[6] Th. J. Siskens and P. Mazur, Physica **A71**, 560 (1974).
[7] W. John and T. Schreiber, Phys. Status Solidi **B66**, 193 (1974).
[8] F. R. Gantmachjer, *Tjeorija matriz*, Nauka, Moskwa (1967) (in Russian).
[9] V. M. Kontorovich and V. M. Tsukernik, Zh. Éksp. Teor. Fiz **52**, 1446 (1967) (in Russian).
[10] D. N. Zubarev, Usp. Fiz. Nauk **71**, 71 (1960) (in Russian).
[11] O. V. Derzhko and T. M. Verkholyak, Preprint ICMP-96-25E, Lviv (1996).
[12] M. Saitoh, Prog. Theor. Phys. **45**, 746 (1971).
[13] O. Derzhko and T. Korkhmalskii, *Ferroelectrics* **153**, 55 (1994).
[14] E. R. Smith, J. Phys. **C3**, 1419 (1970).
[15] E. Barouch and B. M. McCoy, Stud. Appl. Math. **51**, 57 (1972).
[16] R. O. Zaitsev, Zh. Éksp. Teor. Fiz. **63**, 1487 (1972) (in Russian).
[17] F. Matsubara and S. Katsura, Prog. Theor. Phys. **49**, 367 (1973).
[18] E. Barouch and I. Oppenheim, Physica **76**, 410 (1974).
[19] K. Okamoto, J. Phys. Soc. Jpn. **59**, 4286 (1990).
[20] O. Derzhko and J. Richter, Phys. Lett. **A222**, 338 (1996).

Persistent current in a ballistic ring with a quantum dot

M. V. Moskalets

Il'ich Prospect 93a, Flat 48, 310020 Kharkov, Ukraine

The influence of temperature and chemical potential on the persistent resonant current in a ballistic ring with a quantum dot connected to an electron reservoir is considered. © *1997 American Institute of Physics.* [S1063-777X(97)00909-2]

In a recent communication, Yacoby *et al.*[1] described the results of simultaneous experimental measurements of the amplitude and phase of the coefficient of transmission of an electron through a potential barrier during resonance tunneling. For this purpose, the authors used an interferometer (mesoscopic ring pierced by a magnetic flux Φ) one of whose arms contained a quantum dot (QD). Conductance oscillations of the ring in a magnetic field $G(\Phi)$ (Aharonov–Bohm (AB) oscillations with a period $\Phi_0 = h/e$) were measured. By applying a potential V_p to the QD, the authors ensured the fulfillment of the resonance tunneling condition $E_F = E_n + V_p$ (here, E_F is the Fermi energy of electrons in the ring, and E_n the electron energy level in the QD). In this case, the conductance G of the system increases sharply [resonance peaks are observed on the dependence $G(V_p)$]. It was found that the phase shift $\delta\varphi$ of AB oscillations of the conductance $G(\Phi)$ must depend on the variation of the phase of the electron wave function during tunneling through QD. A sharp variation in phase (by π) of the AB oscillations within a resonance peak was observed experimentally.

Theoretical investigations revealed[2–5] that the symmetry requirement $G(\Phi) = G(-\Phi)$[6] restricts the possible values of the oscillation phase shift to $\delta\varphi = 0$ or $\delta\varphi = \pi$. This led Yacobi *et al.* to the conclusion[3] that it is not possible in principle to measure directly the phase of the transmission coefficient in *two-terminal* interference experiments. It should be observed that the possibility of violation of this symmetry under conditions of nonlinear response ($V \neq 0$) was predicted in Ref. 4 as well as the dependence of the AB oscillations phase on the relative position of the resonance level.

However, the position of the resonance level affects the amplitude of AB oscillations. The observed phase variation by π of AB oscillations is due to vanishing and sign reversal of the amplitude of the first harmonic[3,5] as the level E_n passes through resonance. The vanishing of the first harmonic amplitude indicates that the dependence $G(\Phi)$ becomes periodic in magnetic flux with a period $\Phi_0/2$,[3,5] which is confirmed by the experimental observations.[3]

The amplitude of the thermodynamically equilibrium (persistent) current depends on the transparency of the potential barrier existing in the ring.[7,8] Hence the amplitude of the current must increase significantly during resonance tunneling. This was first shown by Büttiker and Stafford[9] for an insulated ring containing a quantum dot.[9] In this work, we shall consider the AB oscillations of persistent current in such a ring connected with an electron reservoir which maintains the preset chemical potential level. We shall also study the effect of temperature on the current and position of the chemical potential relative to the electron energy level in the ring.

It is well known that a significant role in transport phenomena in quantum dots is played by Coulomb blocking caused by electrostatic interaction of charged particles.[10,11] This effect determines the separation between the electron energy levels in QD and hence the separation between the resonance peaks. However, the peculiarities of an individual resonance peak can be described in the framework of the one-particle approximation[3,6] which we shall use in this work.

Let us consider a one-dimensional ballistic ring of length L ($L \ll L_\varphi$, where L_φ is the length of the electron phase breakdown) in which a solenoid with magnetic flux Φ is inserted. The x-axis is directed along the perimeter of the ring. The quantum dot can be described by the potential

$$U(x) = \frac{\hbar^2}{m^*} \Omega[\delta(x) + \delta(x-a)] + V_p \Theta(x)\Theta(a-x). \quad (1)$$

Here V_p is the QD potential relative to the remaining part of the ring, and m^* is the electron effective mass. For a ring in contact with the electron reservoir having chemical potential E_F and temperature T, the persistent current $I = -\partial\omega/\partial\Phi$ (ω is the thermodynamic potential of the electron system in the ring, the electron spin is disregarded) can be represented in the form

$$I = -\sum_l f_0\left(\frac{E_l - E_F}{T}\right) \frac{\partial E_l}{\partial\Phi}. \quad (2)$$

Here $f_0(E/T)$ is the Fermi distribution function, the index l marks the electron energy level in the ring and in the QD. In order to determine the levels E_l, we use the transfer-matrix technique[7] which leads to a simple eigenvalue equation for the electron wave vector k:

$$\text{Re}\{T_k^{-1} \exp[-ik(L-a)]\} = \cos\left(2\pi \frac{\Phi}{\Phi_0}\right), \quad (3)$$

where T_k is the coefficient of transmission of a free electron through the potential barrier (1).

In the limit $\Omega \to \infty$, the spectrum consists of two parts corresponding to the position of the electron in potential wells (with infinitely high walls) of size a and $L - a$, respectively. For a nonzero tunneling probability, the position of levels becomes dependent on the magnetic flux, and a current is produced in the ring. It follows from formula (2) that

the magnitude of the current is proportional to the variation δE_0 in the position of the energy level upon a change in the magnetic flux. In the general case, $\delta E_0 \simeq 1/\Omega^2$. However, the value of δE_0 increases considerably at resonance ($E_m = E_n + V_{p0}$, where E_m is the energy level of an electron in the ring: $\delta E_0 \simeq 1/\Omega$. This is associated with the formation of a resonance doublet:

$$E_{1,2} = E_m - \frac{\delta V_p}{2} - \frac{B_0}{2B_0'} - \frac{\Delta_m A_0'}{2\pi B_0'} \pm \delta E_0 D(\delta V_p, \Phi),$$

$$D = \left\{ \frac{\pi \Delta_m^{-1}}{8|B_0'|} \left(B(\delta V_p) + \frac{\Delta_m A_0'}{\pi} \right)^2 - \frac{1}{2} \left(\cos(\theta_{nm}(\Phi)) \right. \right.$$

$$\left. \left. + \operatorname{sgn}(B_0') A(\delta V_p) \right) \right\}^{1/2}. \tag{4}$$

Here, $\delta V_p = (V_{p0} - V_p)$; $E_m = (\hbar k_m)^2/(2m^*)$; $k_m = \pi m/(L - a)$; $\Delta_m = 2E_m/m$ is the separation between the energy levels of an electron in the ring near E_m, $\delta E_0 = (2\Delta_m/(\pi|B_0'|))^{1/2}$; $\theta_{nm}(\Phi) = \pi(n+m) + \pi + 2\pi\Phi/\Phi_0$ is the phase variation of the wave function of an electron passing around the ring at resonance. The quantities A and B are defined as follows: $\tau(E) = A(E) + iB(E)$, where $\tau(E) = T_k^{-1}$; $E = (\hbar k)^2/(2m^*) = E_m - V_p$. Near the resonance ($V_p = V_{p0}$), we have used the decomposition $\tau(\delta V_p) = \tau_0 + \tau_0' \delta V_p$, where the prime indicates differentiation with respect to energy. The quantities A and B for potential (1) are defined as $A_0 = (-1)^n$; $B_0 = (-1)^n 2\Omega/k_m$; $A_0' = (-1)^n a\Omega/E_n$; $B_0' = (-1)^n a\Omega^2/(k_m E_n)$. Formula (4) is derived under the assumption $\delta E_0 \ll \Delta_m$, which imposes constraints on the parameters of the unit δ-functional barrier [see Eq. (1)]:

$$t_n \ll \pi(a/L)^{1/2}, \tag{5}$$

where $t_n = \pi n/(a\Omega)$ is the magnitude of the tunneling coefficient of an electron with energy E_n. This is the case of weak coupling between the ring and the QD, when not more than one level E_m exists in resonance with the level E_n.

Substituting formula (4) into (2), we obtain for the potential (1) the following expression for current in the vicinity of the resonance:

$$I_{nm} = \frac{\pi \delta E_0}{2\Phi_0} \frac{f_0[(E_2 - E_F)/T] - f_0[(E_1 - E_F)/T]}{D\{\delta V_p, \Phi\}}$$

$$\times \sin[\theta_{nm}(\Phi)]. \tag{6}$$

It follows from the above expression that the main contribution to the current $I = \Sigma I_{nm}$ (summation is carried out over all pairs of levels (n,m) satisfying the condition $E_m - E_n = V_p$) comes from resonance levels lying near the Fermi level: $|E_m - E_F| \simeq T$. Consequently, as the potential V_p of the quantum dot varies, the amplitude of the current in the ring will increase resonantly as the quantum dot level ($E_n + V_p$) crosses the Fermi level E_F, which is in conformity with the results obtained in Ref. 9.

The amplitude of the current (6) reverses its sign at successive peaks $(n,m),(n,m+1),(n+1,m)$, and so on. Such a sign reversal is the well known parity effect,[7,12] since the total number of spinless electrons in the system (ring plus
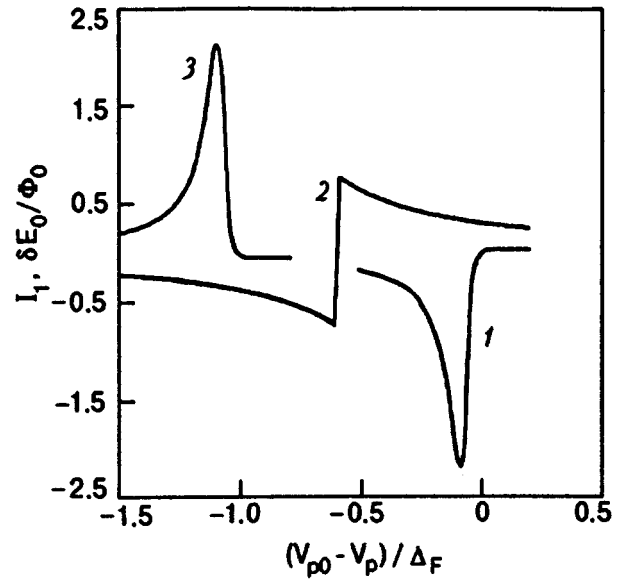

FIG. 1. Dependence of the amplitude of the first harmonic of current I_1 for $T=0$ on the quantum dot potential for different values of the chemical potential: $E_F = E_m(1)$, $E_F = (E_{m+1} + E_m)/2(2)$, $E_F = E_{m+1}(3)$. The ordinate of graph (2) is magnified fivefold. The parameters have the following values: $t_F = 0.03; L/a = 11$, $\Delta_F = 0.02\varepsilon_F, E_n = E_m$.

quantum dot) varies by unity upon a transition from one resonance peak to another, and the current is actually determined by the uppermost populated level in the system. Note that for an isolated ring in which the total number of particles is conserved, the current amplitude does not change sign upon a transition from one resonance peak to the next.[9]

The shape and position of the resonance peak peculiarities depends significantly on the position of the Fermi level E_F relative to the electron energy levels in the ring (or, in other words, on the product $k_F L$). Figure 1 shows the dependence of the amplitude of the first (predominant) harmonic of the current I_1 (for $T=0$) on V_p upon variation of E_F in the interval $E_m < E_F < E_{m+1}$.

If the Fermi level lies at the middle between the electron energy levels in the ring, i.e. $E_F = (E_{m+1} + E_m)/2$, the current amplitude reverses its sign within a resonance peak. This happens when the condition $E_F = E_n + V_p$ is satisfied and the total number of electrons in the system varies. In this case, the current is calculated numerically by using formula (2) and taking into account the solution of Eq. (3). Note that in this case, the "resonance peak" (situated at $V_p = E_F - E_n$) is away from the resonance levels in the ring and in the QD [defined by the condition $V_p = E_m - E_n$, hence the current is low (see Fig. 1)]. However, the dependence of current on the transparency of the potential barrier ($I \simeq 1/\Omega$) allows us to speak about the "resonance" peak, since the magnitude of the nonresonance current $I_{nr} \simeq 1/\Omega^2$. In this case, the characteristic temperature at which current starts decreasing is the same as in a pure ring: $T \simeq \Delta_F$, where Δ_F is the separation between the energy levels of electrons in the ring near the Fermi level, since the separation between electron energy levels in the region of the resonance peak is of the order of Δ_F.

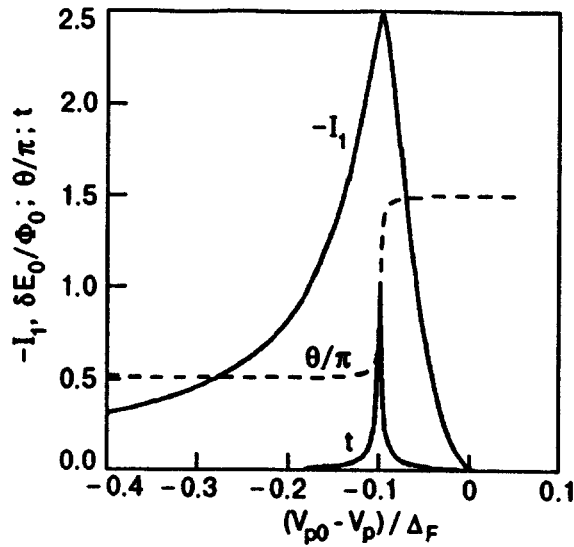The situation is quite different for $E_F = E_m$. In this case,

FIG. 2. Dependence of the amplitude of the first harmonic of current I_1 for $T=0$ (in units of $\delta E_0/\Phi_0$), phase θ/π, and magnitude t of the transmission coefficient on the quantum dot potential. The parameters have the following values: $t_F=0.03; L/a=11$, $\Delta_F=0.02\varepsilon_F$, $E_n=E_m=E_F$.

the current is determined by the contribution of only two (resonance) levels E_n and E_m (Eq. (6)). The current amplitude increases right up to the resonance: $E_m=E_n+V_p$ and then decreases to zero since the contributions from levels E_m and E_n compensate each other. Figure 2 shows the dependence $I_1(V_p)$ at $T=0$ as well as the variation, in the vicinity of the resonance, of the magnitude t and phase $\theta=\arctan(-B/A)$ of the coefficient T_k of transmission of an electron at the Fermi level through the potential barrier (1) (in the expression for the phase θ, the term πn that does not depend on V_p has been disregarded). Mathematically, the position of the peak I_1 is associated with the minimum of the quantity $D(\delta V_p,\Phi)$ [see Eqs. (4) and (6)]. For $L \gg a$, the position of this minimum is determined by the condition $B(\delta V_p)=0$. The same condition determines the position of the peak of the magnitude and of the phase jump in the transmission coefficient T_k. It should be observed that for magnetoresistance oscillations in such a system, the position of the first harmonic amplitude peak does not coincide with the peak of the tunneling coefficient [i.e., the position of the resonance peak on the dependence $G(V_p)$].[3,5]

Near the resonance peak, the separation between the doublet levels (4) oscillates in a magnetic field with the amplitude

$$\delta E_0 = \Delta_F t_F (L/a\pi^2)^{1/2}, \tag{7}$$

where t_F is the magnitude of the coefficient of tunneling through a unit potential barrier [appearing in Eq. (1)] for

electrons with energy $E_n=E_F-V_p$. The quantity δE_0 defines the characteristic temperature in the system $T_0=\delta E_0$. For $T \gtrsim T_0$, the population densities of the levels E_n and E_m become equal, which leads to a decrease in the value of the current (6) at resonance, as well as to a more symmetric form of the resonance curve. Note that in the limit of weak coupling between the ring and the QD under consideration, the condition $t_F \ll 1$ is satisfied and the quantity $T_0 \ll \Delta_F$.

For $T>T_0$, the dependence $I(\Phi)$ at the peak of the resonance curve is sinusoidal. The amplitude of the current is equal to $I=\pi I_0 T_0/(4T)$ (where $I_0=\delta E_0/\Phi_0$). At low temperatures ($T \ll T_0$), the dependence $I(\Phi)$ departs from sinusoidal. However, the first harmonic I_1 of the current dominates. The temperature dependence of I_1 can be represented in the form

$$I_1^{\max}(T) = \frac{I_1^{\max}(0)}{1+(\pi T/T_0)\exp[-T_0/(\pi T)]}, \tag{8}$$

where $I_1^{\max}(0) \simeq I_0 \pi/\sqrt{2}$. Note the power dependence of the decrease in current with temperature as compared to the exponential dependence for a ballistic ring without a potential barrier.[7]

Thus, we have considered the effect of temperature T and the chemical potential E_F of the electron reservoir on the persistent resonance current I in a ballistic ring containing a quantum dot in the weak bond limit.

It is shown that the phase of AB-oscillations of current within a resonance peak is conserved, or varies by π depending on the position of the chemical potential level relative to the electron energy levels in the ring.

It is also shown that, if E_F coincides with one of the electron energy levels in the ring, the temperature dependence of the resonance current is determined by the parameter δE_0, viz., the splitting of the resonance doublet (4), which is small in comparison with the separation between the electron energy levels near the Fermi energy.

[1] A. Yacoby, M. Heiblum, D. Mahalu, and H. Shtrikhman, Phys. Rev. Lett. **74**, 4047 (1995).
[2] A. Levy Yeyati and M. Büttiker, Phys. Rev. **B52**, R14360 (1995).
[3] A. Yacoby, R. Schuster, and M. Heiblum, Phys. Rev. **B53**, 9583 (1996).
[4] C. Bruder, R. Fazio, and H. Schoeller, Phys. Rev. Lett. **76**, 114 (1996).
[5] G. Hackenbroich and H. A. Weidenmüller, Phys. Rev. **B53**, 16379 (1996).
[6] M. Büttiker, IBM J. Res. Dev. **32**, 317 (1988).
[7] H. F. Cheung, Y. Gefen, E. K. Riedel, and W. H. Shih, Phys. Rev. **B37**, 6050 (1988).
[8] A. O. Gogolin and N. V. Prokofiev, Phys. Rev. **B50**, 4921 (1994).
[9] M. Büttiker and C. A. Stafford, Phys. Rev. Lett. **76**, 495 (1996).
[10] M. A. Kastner, Rev. Mod. Phys. **64**, 849 (1992).
[11] D. V. Averin, A. N. Korotkov, and K. K. Likharev, Phys. Rev. **B44**, 6199 (1991).
[12] A. A. Zvyagin and I. V. Krive, Fiz. Nizk. Temp. **21**, 687 (1995) [Low Temp. Phys. **21**, 533 (1995).

Translated by R. S. Wadhwa

QUANTUM EFFECTS IN SEMICONDUCTORS AND DIELECTRICS

Quantized vortices in systems with pairing of spatially separated electrons and holes

S. I. Shevchenko

B. I. Verkin Institute for Low Temperature Physics and Engineering, National Academy of Sciences of Ukraine, Kharkov, 310164, Ukraine[*]

It is predicted that in systems with pairing of spatially separated electrons and holes the planar vortices, in which the electron-hole pairs rotate in the plane of the structure, can become energy-advantageous in a nonuniform magnetic field. In this case the vortices should form an ordered, though translation-noninvariant, structure. © *1997 American Institute of Physics.* [S1063-777X(97)01009-8]

The possibility Bose condensation of real excitons, i.e., excitons whose size is smaller than the distance between them, was first pointed out in Ref. 1. Later, this subject was discussed in connection with exciton insulators,[2] in which the excitons are large compared with the electron-electron distance. By analogy with He-II and superconductors, it was assumed that Bose condensation of excitons would lead to the appearance of superfluid properties in exciton system. Since an exciton is an electroneutral excitation, it cannot transfer either a charge or mass. There is, however, the possibility of a nondissipative transfer of energy and possibly of dipole and magnetic moments. This statement does not imply the true superfluidity. It only means that dissipation of the energy flow (or polarization) does not occur below the Bose condensation temperature during times shorter than the electron-hole recombination time τ_r. It was shown later[3] that the interband transitions responsible for the value of τ_r lift the degeneracy of phase of the order parameter and cause a gap in the excitation spectrum, bringing the system from the superfluid state to the insulator state. Since it takes about τ_r for gap to form, the later statement is true for times longer than τ_r. As a result, steady superfluidity in the exciton gas does not take place.

The problem of superfluidity of electron-hole gas was approached from a new standpoint in the publications,[4,5] which called attention to the possibility of pairing of spatially separated electrons and holes (PSSEH). In systems with PSSEH the interband transitions coincide with the interlayer transitions and the probability of interlayer transitions can be easily changed by varying the thickness d of a dielectric layer, which separates layers with electron and hole conductivities. Since the probability of interlayer transitions decreases exponentially with increasing d, and since the binding energy of electrons with holes falls off algebraically with d, the binding energy can reach 10^2 K, at $d \approx 10^{-6}$ cm, but interband transitions can be completely disregarded. As a result, in systems with PSSEH, electron-hole pairs can go into a truly superfluid state. Moreover, in systems with PSSEH there is no local compensation of the electron current by a hole current, which makes it possible to observe supercurrents equal and opposite in direction, in layers with electron and hole conductivities. This means that in systems with PSSEH, a rather unusual superconductivity mechanism can be realized. In this connection, it was proposed to call superfluidity of electron-hole pairs in such systems «condenser superconductivity».[6]

The predictions made in Refs. 4–6 became of great interest when the progress in microelectronics resulted in the creation of the required structures. Many experimental[7–11] and theoretical[12–16] studies, in which the systems with PSSEH were analyzed, were published. However, in contrast to the $3D$ systems, in which a considerable progress in obtaining degenerate gas of excitons, and perhaps Bose condensation of excitons[17] has recently been achieved, for systems with PSSEH it is impossible at present to say with confidence that condenser superconductivity is realized under experimental conditions. Additional difficulties in recording of this superconductivity stem from the electrical neutrality of the pairs and the impossibility of using a traditional technique of measurement of the transport phenomena.

In the present paper we describe a new phenomenon in condenser superconductors, the observation of which is perhaps a more simple experimental problem than direct measurement of conductivity currents in electron and hole layers. We show that a nonuniform magnetic field can lead to the appearance of quantized vortices in the system in which electron-hole pairs rotate in the plane of the structure. We also show that although these vortices are very similar to the Onsager–Feynman and Abrikosov vortices, under certain conditions the structure formed by them differs radically from the structures formed by Onsager–Feynman and Abrikosov vortices.

Note that the behavior of the systems with PSSEH in a uniform field normal to a structure plane was considered many times. It was observed for the first time in Ref. 18, then in a series of studies,[19] and quite recently in Refs. 20 and 21. In all those studies, the influence of a strong magnetic field H on the pairing of electrons with holes was considered for the case in which the cyclotron radius $(c\hbar/eH)^{1/2}$ is lower than the Bohr radius $\varepsilon\hbar^2/me^2$. The possibility of inducing planar vortices by a nonuniform magnetic field has not been considered until now. We consider here the case of weak

magnetic fields $[(c\hbar/eH)^{1/2}\gg\varepsilon\hbar/me^2)]$ in which the effect of the field on pairing can be ignored.

The system under consideration is a three-layer structure: two conducting two-dimensional layers are separated by a thin insulator layer. For definiteness, we assume that the lower layer has electron conductivity and the upper layer has hole conductivity. The Coulomb interaction leads to electron-hole pairing, and the pairs form Bose gas which becomes superfluid below T_c.[6] In the coherent phase the supercurrent is $\mathbf{j}_e=-en_s\mathbf{v}_s\delta(z+d/2)$ in the electron layer, and $\mathbf{j}_h=en_s\mathbf{v}_s\delta(z-d/2)$ in the hole layer. Here n_s is the two-dimensional superfluid density and $-e$ is the electron charge. We assume that the conducting layers are infinitely thin, which leads to a δ function dependence of the current density on the z coordinate. The superfluid velocity of the electron-hole pairs, in general, is[4]

$$\mathbf{v}_s=\frac{\hbar}{m}\,\nabla\varphi-\frac{e}{mc}\,(\mathbf{A}_h-\mathbf{A}_e). \tag{1}$$

Here m is the pair mass; φ is the order parameter phase; $\mathbf{A}_e$ and $\mathbf{A}_h$ are the vector potentials in the electron and hole layers, respectively.

Here we assume that the thickness of the insulator layer, d, is small in comparison with the distance in which the vector potential $\mathbf{A}$ changes, so that the difference $\mathbf{A}_h-\mathbf{A}_e$ is

$$\mathbf{A}_h-\mathbf{A}_e=\frac{\partial\mathbf{A}}{\partial z}\,d. \tag{2}$$

On the other hand, we consider d large enough to ignore the tunnel transitions of the electrons between the conducting layers.

Our primary interest is in the velocity field of the planar vortex and the magnetic field created by the vortex. For the vortex, whose center is at $\rho=0$, the phase is

$$\varphi=\arctan\frac{y}{x}. \tag{3}$$

Because of the spatial separation of the electrons and holes, the rotation of the pairs generates a magnetic field in the surrounding space. To find the magnetic field, we must solve a Maxwell's equation

$$\nabla\times\mathbf{H}=\frac{4\pi}{c}\,\mathbf{j}(z). \tag{4}$$

Substituting the corresponding currents in the electron or hole layer instead of $\mathbf{j}$ in Eq. (4), writing $\mathbf{H}$ as $\mathbf{H}=\nabla\times\mathbf{A}$, and using the condition $\nabla\cdot\mathbf{A}=0$, we obtain

$$-\Delta\mathbf{A}+\gamma\left(\frac{\partial\mathbf{A}}{\partial z}-\frac{\mathbf{S}}{d}\right)[\delta(z-d/2)-\delta(z+d/2)]=0. \tag{5}$$

Here the vector $\mathbf{S}=\hbar c\nabla\varphi/e$ has only the θth component for the phase φ from Eq. (3) and $S_\theta=\hbar c/e\rho$. We also introduce the dimensionless quantity $\gamma=4\pi n_s e^2 d/mc^2$.

To solve Eq. (5), we take the Fourier-transformation of the vector potential

$$\mathbf{A}(\rho,z)=\int\mathbf{A}(\mathbf{q},k)\exp\{i\mathbf{q}\rho+ikz\}d^2qdk/(2\pi)^3. \tag{6}$$

Substitution of Eq. (6) into Eq. (5) gives the integral equation

$$(q^2+k^2)\mathbf{A}(\mathbf{q},k)-2\gamma\int\frac{d\rho}{2\pi}\,p\,\sin[(p-k)d/2]\mathbf{A}(\mathbf{q},p)$$

$$=-2i\,\frac{\gamma}{d}\,\sin\frac{kd}{2}\,\mathbf{S}(\mathbf{q}). \tag{7}$$

Its solution is

$$\mathbf{A}(q,k)=-\frac{2i\gamma}{d}\,\frac{\sin kd/2}{q^2+k^2}\,\frac{\mathbf{S}(\mathbf{q})}{1+(\gamma/2)\exp\{-qd\}}. \tag{8}$$

Before finding the potential $\mathbf{A}(\rho,z)$ from Eq. (8), it is useful to estimate γ numerically. It is $\gamma\approx 2\pi\cdot10^{-5}$ for the electron density $n\simeq10^{12}$ cm^{-2}, the insulator layer thickness $d\approx10^{-6}$ cm, and the effective mass of the pair $m\simeq0.1\,m_0$, where m_0 is the free electron mass. The γ value is even lower for smaller n and larger m. The condition $\gamma\ll1$ is therefore oversatisfied for the experimental conditions. Equation (8) can therefore be restricted to the terms of the order of γ. Substituting the $\mathbf{A}(\mathbf{q},k)$, calculated with this accuracy in Eq. (8), into Eq. (6), we obtain

$$A_\theta=\frac{2\pi e\hbar n_s}{mc\rho}\left[\sqrt{\rho^2+(z-d/2)^2}-|z-d/2|\right.$$
$$\left.-\sqrt{\rho^2+(z+d/2)^2}+|z+d/2|\right]. \tag{9}$$

We can now easily find the magnetic field excited by the planar vortex. The projection of the magnetic field normal to the conducting layers is $H_z=\rho^{-1}\partial(\rho A_\theta)/\partial\rho$, i.e.,

$$H_z=2\pi\,\frac{e\hbar n_s}{mc}\{[\rho^2+(z-d/2)^2]^{-1/2}$$
$$-[\rho^2+(z+d/2)^2]^{-1/2}\}. \tag{10}$$

It is evident that H_z is an odd function of z. The maximum value of H_z is attained in the conducting layers, i.e., at $z=\pm d/2$. The magnetic flux through the $z=d/2$ plane, which is related to the electron-hole vortex, is

$$\Phi\equiv\int H_z\rho d\rho\,d\theta=\frac{4\pi^2 e\hbar n_s d}{mc}\equiv\gamma\Phi_0. \tag{11}$$

The flux is not universal and depends on the superfluid density n_s and the insulator thickness d. It constitutes only a small part of the flux quantum, $\Phi_0\equiv hc/2e$, produced by a vortex in ordinary superconductors.

The magnetic field component $H_\rho=-\partial A_\theta/\partial z$ is

$$H_\rho=2\pi\,\frac{e\hbar n_s}{mc\rho}\left[\operatorname{sign}\left(z-\frac{d}{2}\right)\right.$$
$$-\frac{z-d/2}{[\rho^2+(z-d/2)^2]^{1/2}}-\operatorname{sign}\left(z+\frac{d}{2}\right)$$
$$\left.+\frac{z+d/2}{[\rho^2+(z+d/2)^2]^{1/2}}\right]. \tag{12}$$

Far from the vortex center or, more exactly, at $\rho\gg d$, the field H_ρ between the conducting layers decreases as $1/\rho$. As a result, the H_ρ contribution to the superfluid velocity $\mathbf{v}_s$ in

Eq. (1) and the term proportional to $\nabla\varphi$ decrease as $1/\rho$. The $1/\rho$ decrease in the velocity $\mathbf{v}_s$ implies that the energy U_v of the interaction between the vortices of opposite circulations is proportional to $\ln|\rho_1-\rho_2|$, where ρ_1 and ρ_2 are the vortex coordinates. We can show that the renormalization of the proportionality coefficient in U_v due to the spatial electron-hole separation is about γ. But the energy U_v determines the T_c at which the pairs of vortices of opposite circulation dissociate, i.e., the temperature of the superfluid Berezinskii–Kosterlitz–Thouless transition. For this reason, the renormalization of T_c is of the same order of magnitude. The spatial electron-hole separation therefore has virtually no effect on the temperature of the superfluid transition of the electron-hole pairs.

It is very important that because of the spatial electron-hole separation, the pairs which are electroneutral as a whole interact with the external magnetic field. As a result, the external field can lead to the vortex formation. The appearance of vortices in the external magnetic field H_0 is controlled by the energy

$$E=\int d^2\rho\left[\frac{n_s}{2m}\left(\hbar\nabla\varphi+\frac{e}{c}\,d\hat{z}\times\mathbf{H}\right)^2\right.$$
$$\left.+\left(\frac{H^2}{8\pi}-\frac{\mathbf{H}\cdot\mathbf{H}_0}{4\pi}\right)d\right]. \tag{13}$$

The local field $\mathbf{H}$ consists of the external field $\mathbf{H}_0$ and the field created by the moving electron-hole pairs. In Eq. (13) we take into account that the main part of the energy of the field created by the pairs is concentrated in the space between the conducting layers. In this region the field $\mathbf{H}$ may be assumed equal to $\mathbf{H}_0+4\pi en_s\hat{\mathbf{z}}\times\mathbf{v}_s/c$ [cf. Eqs. (10) and (12)]. Using this expression and discarding the corrections on the order of γ^2, we obtain the following expression from Eq. (13):

$$E=\int d^2\rho\left[\frac{\hbar^2n_s}{2m}\left(\nabla\varphi\right)^2+\frac{\hbar n_s ed}{mc}\nabla\varphi\left(\hat{\mathbf{z}}\times\mathbf{H}_0\right)\right]. \tag{14}$$

It can be concluded that with an appropriate strength and direction of the field $\mathbf{H}_0$, the second term can compensate for the vortex-related energy loss, $\int(\hbar^2n_s/2m)(\nabla\varphi)^2d^2\rho$. The vortex generation in the system thus becomes energy advantageous, as in the case of type-II superconductors at $H_0>H_{c1}$.

The magnetic field excited by the two-dimensional current that circulates around the origin of coordinates is perhaps the most favorable field for generation of vortices. A schematic representation of this field is shown in Fig. 1. If the two-dimensional density of the azimuthal current is I, then the magnetic field which is generated by the current at some distance from the edge of the structure is

$$\mathbf{H}_{0\rho}=\frac{2\pi I}{c}\left[\left(1+\frac{(z-l)^2}{\rho^2}\right)^{1/2}-\frac{|z-l|}{\rho}\right]\text{sign}(z-l). \tag{15}$$

Here l is the distance to the plane with the current I reckoned from the midpoint of the insulator layer in the electron-hole structure.

Substituting the phase

$$\varphi=\sum_i\ \arctan[(y-y_i)/(x-x_i)]$$

(x_i, y_i are the coordinates of the ith vortex) into Eq. (14), we find the energy E of the vortices in the field H_0. The energy E depends essentially on the size and shape of the system as the velocity v_s decreases slowly from the vortex center. If the condenser superconductor is a three-layer disk of radius R, whose center coincides with the center of the structure shown in Fig. 1, and if the distance l between this structure and the disk is much shorter than R, then the vortex energy will be

$$E=\sum_{i=1}^N F_v(\rho_i)+\frac{1}{2}\sum_{i\neq j}^N U(\rho_i,\rho_j). \tag{16}$$

Here E_v is the energy of one vortex, and U is the energy of interaction between the vortices:

$$E_v(\rho)=\frac{\pi\hbar^2n_s}{m}\left(\ln\frac{R^2-\rho^2}{R\xi}-\frac{R-\rho}{\lambda}\right), \tag{17}$$

$$U(\rho_i,\rho_j)$$
$$=\frac{\pi\hbar^2n_s}{m}\ln\frac{R^2-2\rho_i\rho_j\cos(\theta_i-\theta_j)+\rho_i^2\rho_j^2/R^2}{\rho_i^2-2\rho_i\rho_j\cos(\theta_i-\theta_j)+\rho_j^2}. \tag{18}$$

The first term in Eq. (17) is the intrinsic vortex energy in the absence of the external magnetic field and the second term is the vortex-field interaction energy. Here we have introduced the notation

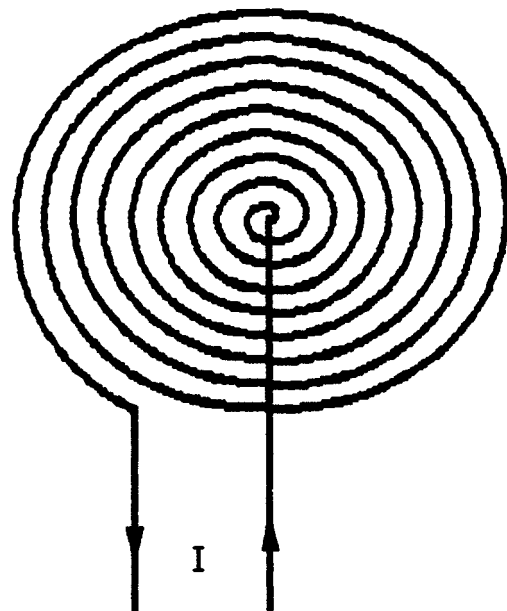$$\lambda^{-1}=\frac{4\pi Ied}{\hbar c^2}. \tag{19}$$

FIG. 1. Schematic diagram with two-dimensional azimuthal current.

Equation (18) takes into account the direct interaction between the vortices and their interactions with the images whose presence turns the v_s component normal to the disk bound into zero.

In Eq. (17) the term proportional to λ^{-1} makes the vortex state advantageous for small λ (large currents I). To find the current I_{c1} at which the vortex creation becomes energy advantageous, we should take the number of vortices $N=1$ and the vortex coordinate $\rho_1=0$. Setting $E_v=0$, we have

$$\lambda_{c1}^{-1} \equiv \frac{4\pi I_{c1}ed}{\hbar c^2} = \frac{1}{R}\ln\frac{R}{\xi}. \tag{20}$$

Substituting $d=10^{-6}$ cm into Eq. (20) and taking into account that $H_{0\rho}=2\pi I/c$ at $\rho \gg d$, we find $H_{0\rho}^{c1} \approx 1$ Gs for $R=1$ cm.

At $I>I_c$ the system has a finite number of vortices, which can be easily found for $I \gg I_{c1}$. In this case the vortices may be considered continuously distributed. Introducing the vortex density $n_v(\rho)$, we obtain

$$E = \int E_v(\rho)n_v(\rho)d^2\rho$$
$$+ \frac{1}{2}\int n_v(\rho_1)U(\rho_1,\rho_2)n_v(\rho_2)d^2\rho_1 d^2\rho_2. \tag{21}$$

Varying Eq. (21) in $n_v(\rho)$ and setting the result equal to zero, we obtain the equation for the dependence of the vortex density on ρ. We can solve the equation exactly and thus show that at $\rho \gg l$

$$n_v(\rho) = (4\pi\lambda\rho)^{-1}. \tag{22}$$

The result is drastically different from that known for neutral superfluid systems and ordinary superconductors. In both cases the equilibrium vortex concentration (Onsager–Feynman and Abrikosov, respectively) is spatially uniform. We clearly see from Eq. (22) that n_v in our case decreases with increasing ρ.

It is known that the Onsager–Feynman and Abrikosov vortices form a triangular lattice. The question then arises whether the vortices considered in this paper also form a lattice. Since $n_v(\rho)$, according to Eq. (22), decreases with increasing distance from the disk center, it is evident that the vortices cannot form a structure invariant under translations. Equation (22), however, admits a structure invariant against rotations. As such a structure we choose the structure where vortex cores are situated on the circumferences whose centers coincide with that of the disk. The number of vortices on the ith circumference is N_i, and its radius is ρ_i. Performing in Eq. (16) summation over the vortex coordinates on the ith circumference by the Poisson summation formula, we obtain the following expression for the vortex energy:

$$E = \sum_i \left\{ E_v(\rho_i) + \frac{\pi\hbar^2 n_s}{M}\left[2\sum_{j(<i)}N_j\left(\ln\frac{R}{\rho_i}+\frac{1}{N_i}\right.\right.\right.$$
$$\times \ln\frac{1-\exp\{-N_i\ln R^2/\rho_i/\rho_j\}}{1-\exp\{-N_i\ln\rho_i/\rho_j\}}\right) - \ln N_i + (N_i-1)\ln\frac{R}{\rho_i}$$
$$\left.\left.\left.+ \ln\left(1-\exp\left\{-2N_i\ln\frac{R}{\rho_i}\right\}\right)\right]\right\}N_i. \tag{23}$$

This exact expression can be simplified considerably at $N_i \gg 1$. In the case the main contribution to the last sum in Eq. (23) is made by the terms for which $|\ln\rho_j/\rho_i| \ll 1$. For these terms $|\ln\rho_j/\rho_i| \approx (\rho_{i+1}-\rho_i)|j-i|/\rho_i$. The terms with $\ln R^2/\rho_i\rho_j$ may be discarded far from the disk edge. Varying the resulting expression in N_i and ρ_i and setting the result equal to zero, we obtain a set of equations for these quantities. The solution for $R \gg \rho_i \gg \lambda$ is

$$N_i = \frac{\rho_{i+1}-\rho_i}{2\lambda}, \tag{24}$$

$$(\rho_{i+1}-\rho_i)^2 = 4\lambda\rho_i.$$

Both results of Eq. (24) readily follow from simple physical considerations. The number of vortices on the ith circumference is

$$N_i = \int_{\rho_i}^{\rho_{i+1}}\int_0^{2\pi} n_v(\rho)\rho d\rho d\theta. \tag{25}$$

Substitution of $n_v(\rho)$ from Eq. (22) into this expression gives $N_i=(\rho_{i+1}-\rho_i)/2\lambda$. To obtain the other result of Eq. (24), we should take into account that the repulsion forces between the vortices of the same circulation are isotropic. It is therefore expected that the spatial distribution of vortices is locally isotropic. In this case the mean vortex spacing $2\pi\rho_i/N_i$ for the particular circumference coincides with the mean vortex spacing $\rho_{i+1}-\rho_i$ on the neighboring circumferences. Substituting the value for N_i, we obtain $4\pi\lambda\rho_i/(\rho_{i+1}-\rho_i)=\rho_{i+1}-\rho_i$, which coincides with Eq. (24) with an accuracy up to the multiplier π.

We have considered thoroughly the case of generation of planar vortices by the field of two-dimensional circular current. It is inferred that in an arbitrary magnetic field, within the limit where vortices are assumed continuously distributed, the vortex density is $n_v(\rho)=(ed/2\pi\hbar c)|\partial H_{0z}/\partial z|$. In summary, a nonuniform magnetic field can, in general, excite vortices in the PSSEH systems. The nature of the vortex distribution in space needs to be studied.

*E-mail: shevchenko@ilt.kharkov.ua

[1] S. A. Moskalenko, Fiz. Tverd. Tela **4**, 276 (1962); J. M. Blatt, K. W. Boer, and W. Brandt, Phys. Rev. **126**, 1691 (1962).

[2] L. V. Keldysh and Yu. V. Kopaev, Fiz. Tverd. Tela **6**, 2791 (1964); B. I. Halperin and T. M. Rice, Solid State Phys. **21**, 116 (1968).

[3] R. R. Guseinov and L. V. Keldysh, Zh. Teor. Éksp. Fiz. **63**, 2255 (1972) [Sov. Phys. JETP **36**, 1193 (1972)].

[4] S. I. Shevchenko, Fiz. Nizk. Temp. **2**, 505 (1976) [Sov. J. Low Temp. Phys. **2**, 251 (1976)].

[5] Yu. E. Lozovik and V. I. Yudson, Zh. Éksp. Teor. Fiz. **71**, 738 (1976) [Sov. Phys. JETP **44**, 389 (1976)].

[6] S. I. Shevchenko, Phys. Rev. Lett. **72**, 3242 (1994).

[7] J. E. Golub, K. Kash, J. P. Harbison, and L. T. Florez, Phys. Rev. **B41**, 8564 (1990).

[8] U. Sivan, P. M. Solomon, and H. Shtrikman, Phys. Rev. Lett. **68**, 1196 (1992).

[9] G. D. Gilliland, A. Antonelli, D. J. Wolford, K. K. Bajaj, J. Klem, and J. A. Bradley, Phys. Rev. Lett. **71**, 3717 (1993).

[10] L. V. Butov, A. Zrenner, G. Abstreiter, G. Böhm, and G. Weiman, Phys. Rev. Lett. **73**, 304 (1994).

[11] J. P. Eisenstein, L. N. Pfeiffer, and K. W. West, Phys. Rev. Lett. **74**, 1419 (1995).

[12] L. Swierkowski, J. Szymanski, and Z. W. Gortel, Phys. Rev. Lett. **74**, 3245 (1995).

[13] X. Zhu, P. B. Littlewood, M. S. Hybertsen, and T. M. Rice, Phys. Rev. Lett. **74**, 1633 (1995).

[14] A. B. Dzyubenko and G. E. W. Bauer, Phys. Rev. **B51**, 14524 (1995).

[15] G. Vignale and A. H. MacDonald, Phys. Rev. Lett. **76**, 2786 (1996).

[16] Y. Naveh and B. Laikhtman Phys. Rev. Lett. **77**, 900 (1996).

[17] D. W. Snoke, J. P. Wolfe, and A. Mysyrowicz, Phys. Rev. **B41**, 11171 (1990); Jia Ling Lin and J. P. Wolfe Phys. Rev. Lett. **71**, 1222 (1993).

[18] Y. Kuramoto and C. Horie, Solid State Commun. **25**, 713 (1978).

[19] I. V. Lerner and Yu. E. Lozovik, Zh. Éksp. Teor. Fiz. **78**, 1167 (1980) [Sov. Phys. JETP **51**, 588 (1980)]; I. V. Lerner and Yu. E. Lozovik, Zh. Éksp. Teor. Fiz. **80**, 1488 (1981) [Sov. Phys. JETP **53**, 763 (1981)]; A. B. Dzyubenko and Yu. E. Lozovik, Fiz. Tverd. Tela (Leningrad) **26**, 1540 (1984).

[20] D. Yoshioka and A. H. MacDonald, J. Phys. Soc. Jpn. **59**, 4211, (1990).

[21] X. M. Chen and J. J. Quinn, Phys. Rev. Lett. **67**, 895 (1991).

745   Low Temp. Phys. **23** (9), September 1997

S. I. Shevchenko   745

New channels of photon echo relaxation in Y_2SiO_5:Pr^{3+} and LaF_3:Pr^{3+} crystals

Yu. V. Malyukin

Institute of Single Crystals, National Academy of Sciences of the Ukraine, 310001 Kharkov, Ukraine[*]

Experimental results on the investigation of low-temperature optical absorption spectra and temperature dependence of the photon echo (PE) amplitude signal in Y_2SiO_5:Pr^{3+} and LaF_3:Pr^{3+} crystals at the transition $^3H_4(0)-^3P_0$ of the Pr^{3+} ion are presented. It is shown that additional relaxation channels exist for PE in addition to the known phonon mechanisms. This is associated in a LaF_3:Pr^{3+} crystal with the temperature variation of dipole moment at the Pr^{3+} ion transition. In a Y_2SiO_5:Pr^{3+} crystal, this is due to the thermally activated transitions for the Pr^{3+} ion between nonequivalent positions in the crystal lattice. © *1997 American Institute of Physics.* [S1063-777X(97)01109-2]

1. INTRODUCTION

Crystal matrices representing wide-gap insulators with rare-earth impurity ions have been drawing continued attention in view of new aspects of their application, e.g., laser systems with up-conversion,[1–3] high-speed detectors of ionizing radiation,[4] optical memory cells, and Fourier processors.[5] This stimulated scientists to set up and carry out experiments whose main emphasis is shifted towards the dynamics (phase and energy relaxation processes) of optical transitions, which is important for understanding the microstructure of an impurity center and its energy spectrum.

The Pr^{3+} ion has a number of important properties from the application point of view.[2,3] Its optical characteristics are determined by transitions within the $4f$-shell which is split as a result of spin-orbit interaction.[6] It was assumed in Ref. 6 that the crystal field of ligands weakly affects the $4f$-electrons since they are screened by electrons of the outer shells. In spite of this, a transition from one crystal matrix to another gives rise to peculiarities that are manifested most strongly just in the dynamics of optical transitions of the Pr^{3+} ion.[7–9]

In this work, we present the results of experimental investigations of the low-temperature phase relaxation of electron excitations at resonant optical transitions of the Pr^{3+} ion. A relation is established between the structure of optical spectra and peculiarities of photon echo relaxation in Y_2SiO_5:Pr^{3+} and LaF_3:Pr^{3+} crystals.

2. EXPERIMENTAL TECHNIQUE

Absorption spectra of the crystals were recorded on a spectrofluorimeter based on the spectrograph DFS-452. The recording of spectra was carried out by a TV camera connected to a PC of AT-type. The detecting element of the camera was a 542×492 array of optically sensitive elements of charge-coupling type. Since we are interested in the spectral sweep along one coordinate only, we carried out averaging over 542 lines which considerably increased the accuracy of measurements and the signal-to-noise ratio. The experimental technique for recording echo-signals is described in detail in Ref. 10. Low temperatures were produced in an optical helium cryostat in which the sample was held in helium vapor. The objects under investigation were 2 mm-thick crystalline plates cut from the crystals of Y_2SiO_5:Pr^{3+} and LaF_3:Pr^{3+}. The concentration of Pr in both matrices was of the order of 0.3 at.%.

3. DISCUSSION OF EXPERIMENTAL RESULTS

While investigating the temperature dependence of the amplitude of a two-pulse photon- echo (PE) signal at optical resonance transition $^3H_4(0)-^3P_0$ of a Pr^{3+} ion in the matrices of two crystals Y_2SiO_5:Pr^{3+} and LaF_3:Pr^{3+}, we found[8,9] that dephasing of the resonance transition in the LaF_3:Pr^{3+} crystal increases much more sharply with temperature. The temperature range of the existence of PE in Y_2SiO_5:Pr^{3+} is about double the corresponding interval for LaF_3:Pr^{3+} (Fig. 1). It would be expected, however, that the screening of the $4f$-shell must lead to a weak variation of the electron-phonon coupling of $4f$-electrons in Pr upon a transition from one crystal matrix to another.

According to the structure of energy levels of the Pr^{3+} ions (Fig. 1), the temperature dependence of the PE amplitude (and hence the dephasing of the resonance transition $^3H_4(0)-^3P_0$) is determined by the scattering of phonons involving the energy sublevels closest to the resonance transition.[11] For the state $^3P_0$, which does not split since its total angular momentum is equal to zero, the closest sublevel is $^3P_1$, while the one corresponding to $^3H_4(0)$ is $^3H_4(1)$. Under the action of the spin–orbit interaction and the crystal field, the multiplet $^3H_4$ is split into nine components [$^3H_4(0)$, $^3H_4(1)$, etc., correspond to this splitting]. The energy interval separating the sublevels of the states $^3P_0$ and $^3P_1$ is more than 400 cm^{-1}.[12] Hence, we can disregard the levels of the multiplet $^3P_1$ in the temperature range 6–20 K. According to Ref. 11, the phase relaxation time T_2 at the transition $^3H_4(0)-^3P_0$ of the Pr^{3+} ion can be defined[13] by the relation

$$[T_2(T)]^{-1} = \alpha \exp(-\Delta/T), \qquad (1)$$

where α is a constant connected with the half-width of the level $^3H_4(1)$ participating in the phonon scattering, Δ is the energy interval between the sublevels $^3H_4(0)$ and $^3H_4(1)$, and T is the temperature.
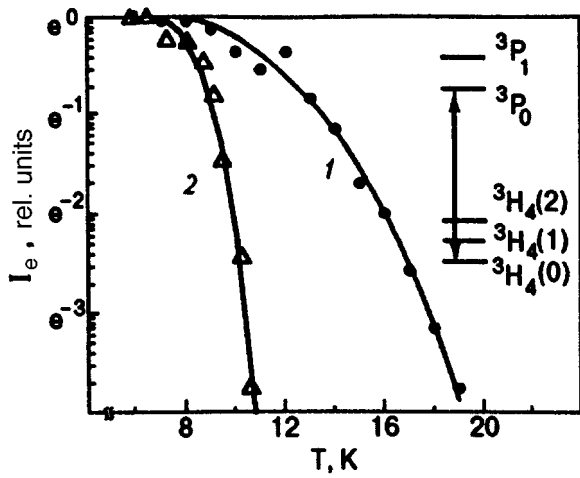
FIG. 1. Temperature dependence of the PE signal amplitude in Y_2SiO_5:Pr^{3+} (curve *1*) and LaF_3:Pr^{3+} (curve *2*) crystals. The inset shows the simplified diagram of energy levels of the Pr^{3+} ion.

The parameters appearing in Eq. (1) for the LaF_3:Pr^{3+} crystal are[6,7] $\alpha = 2.4 \cdot 10^{11}$ s^{-1} and $\Delta = 81.4$ K(57 cm^{-1}). An analysis of the temperature dependence of the PE signal in the LaF_3:Pr^{3+} crystal showed[7] that the experimental dependence may be described by formula (1), in which $\Delta = 58.8$ K(41 cm^{-1}). This was also confirmed by our investigations[8] which completely reproduced the results obtained by Takeuchi.[7] Thus, a decrease in the PE signal intensity occurs more rapidly than what would be expected from the structure of Pr^{3+} ions in the LaF_3 crystal. this disparity was not explained in Refs. 7–9.

The Y_2SiO_5:Pr^{3+} crystal had been investigated sparsely, and the values of α and Δ were not known for it. This circumstance hampered the interpretation of experimental results on PE[8,9] and called for independent evaluation of these parameters.

To achieve these ends, we carried out detailed investigations of the temperature dependence of the absorption spectrum of the Y_2SiO_5:Pr^{3+} crystal and, for of comparison, the LaF_3:Pr^{3+} crystal in the region of the transition $^3H_4(0) - ^3P_0$ of the Pr^{3+} ion. At $T = 6$ K, the absorption spectrum in both crystal matrices consists of a single narrow ($\leqslant 3$ cm^{-1}) spectral line Γ_0 corresponding to absorption from the lowest energy level $^3H_4(0)$ of the multiplet $^3H_4$. Investigation of the spectral contour of the line of resonant transition $^3H_4(0) - ^3P_0$ showed[9] that an absorption peak is observed on the high-frequency side of the spectrum for the Y_2SiO_5:Pr^{3+} crystal (Fig. 2a). No such peak is observed for the LaF_3:Pr^{3+} crystal.

As the temperature of the crystals under investigation is raised, the low-frequency spectral region acquires additional temperature-dependent peaks Γ_1 and Γ_2 (Figs. 2b and 2c) corresponding to absorption from thermally populated energy sublevels $^3H_4(1)$ and $^3H_4(2)$ of the multiplet $^3H_4$. The spectral position of Γ_1 and Γ_2 relative to Γ_0 allows us to determine the splitting of the multiplet $^3H_4$ of the Pr^{3+} ion in the corresponding crystal. The splittings of the multiplet $^3H_4$ observed for the LaF_3:Pr^{3+} crystal coincide with the results obtained in Refs. 6 and 7. For the Y_2SiO_5:Pr^{3+} crystal, the
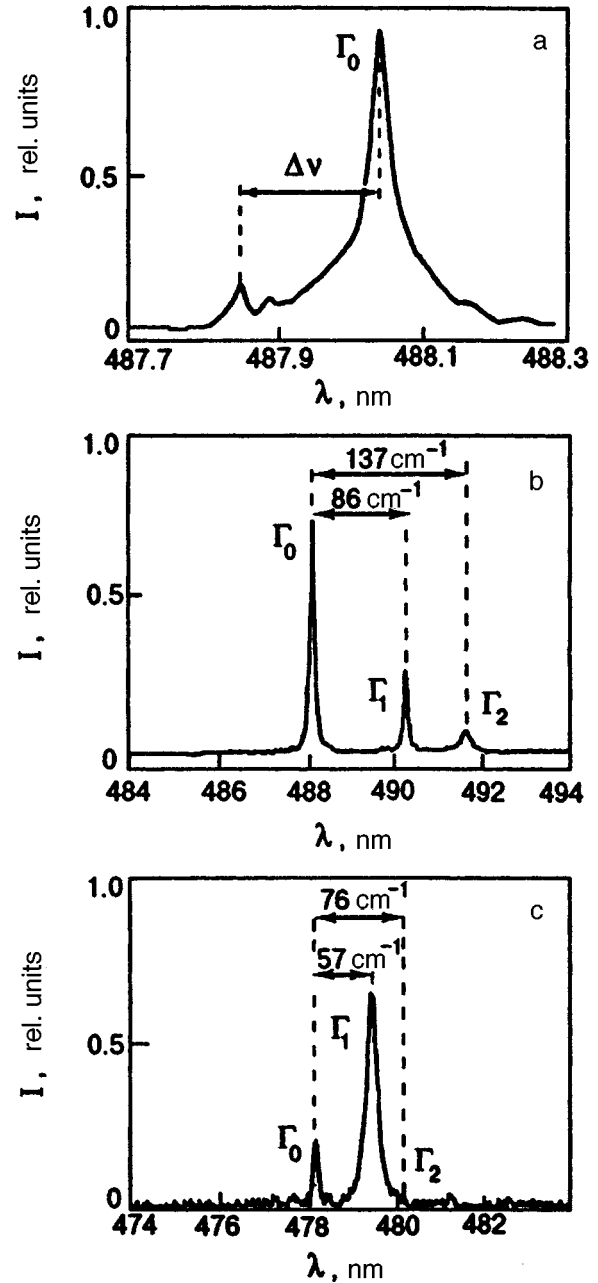
FIG. 2. Fragments of the absorption spectra of the Pr^{3+} ion. Γ_0 corresponds to the resonance transition $^3H_4(0) - ^3P_0$ in Y_2SiO_5:Pr^{3+} at $T = 1.5$ K (a), $T = 80$ K (b) and LaF_3:Pr^{3+} crystals at $T = 80$ K (c).

energy gaps $^3H_4(0) - ^3H_4(1)$ and $^3H_4(0) - ^3H_4(2)$ are equal to 86 and 137 cm^{-1} respectively. These splittings of the multiplet $^3H_4$ are slightly larger than for the LaF_3:Pr^{3+} crystal,[7] which can be treated as a manifestation of the effect of the crystal field on the *f*-shell electrons.

The ratio of intensities of the lines Γ_0, Γ_1, and Γ_2 in the absorption spectrum of the Y_2SiO_5:Pr^{3+} crystal in the temperature range 6–77 K corresponds qualitatively to the Boltzmann population of the sublevels $^3H_4(1)$ and $^3H_4(2)$. No such dependence was observed for the LaF_3:Pr^{3+} crystals. The temperature transformation of the absorption spectrum of the crystal LaF_3:Pr^{3+} is shown in Fig. 3a. It can be seen from the figure that the intensities of the lines Γ_0 and Γ_1
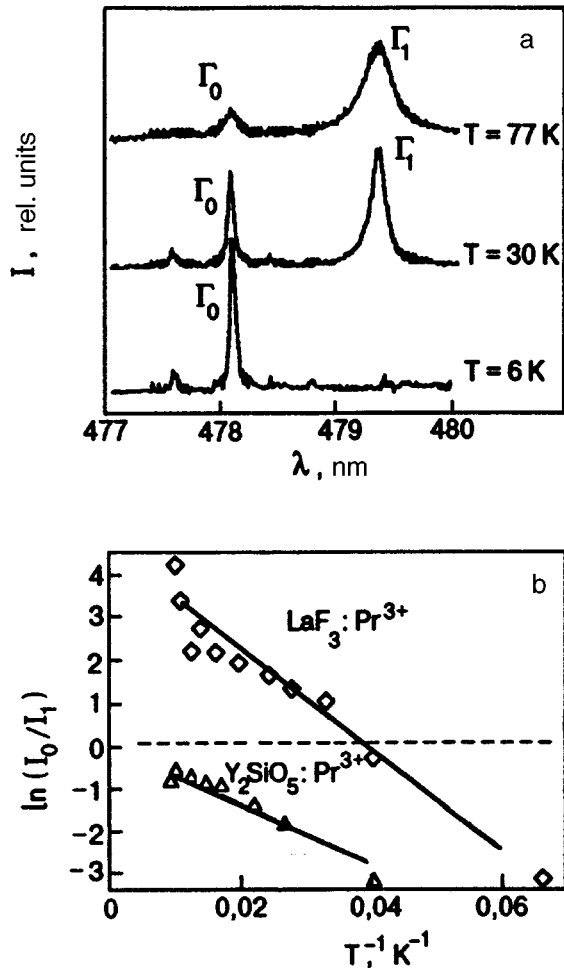
FIG. 3. Temperature transformation of the spectral characteristics of the Pr^{3+} ions: Absorption spectra of LaF_3:Pr^{3+} at different temperatures (a); temperature dependence of the ratio of integral intensities Γ_0 and Γ_1 in Y_2SiO_5:Pr^{3+} and LaF_3:Pr^{3+} crystals (b).

become equal at $T = 30$ K. Upon a further increase in temperature, the absorption at the transition $^3H_4(1) - ^3P_0$ begins to exceed the absorption at the transition $^3H_4(0) - ^3P_0$. A similar behavior of the lines Γ_0 and Γ_1 is preserved in the LaF_3:Pr^{3+} crystals containing 10 at. % Pr^{3+} ions, thus pointing towards the temperature mechanism of intensity redistribution in lines Γ_0 and Γ_1, irrespective of the concentration of Pr^{3+} ions. However, the initial nonuniform broadening of lines in the absorption spectra of LaF_3:Pr^{3+} crystals with different concentrations of Pr^{3+} ions varies from 0.07 cm^{-1} at 0.001 at. % to 10 cm^{-1} at 20 at. % Pr^{3+} ions.[14] Since the broadening of lines Γ_0 and Γ_1 took place in different ways upon an increase in temperature, we constructed the experimental dependences for the ratio of integral intensities of lines Γ_0 and Γ_1 on reciprocal temperature for LaF_3:Pr^{3+} and Y_2SiO_5:Pr^{3+} crystals (Fig. 3b).

Neglecting absorption from higher levels of the multiplet $^3H_4$, we can present the experimental dependences shown in Fig. 3b in the form[15]

$$\frac{I_1}{I_0} = \frac{d_1^2}{d_0^2} \exp(-\Delta/T), \qquad (2)$$

where I_1 and I_0 are the integral intensities of the lines Γ_0 and Γ_1, d_0 and d_1 are the dipole moments of the transitions $^3H_4(0) - ^3P_0$ and $^3H_4(1) - ^3P_0$ respectively, and Δ is the energy gap between the levels $^3H_4(0)$ and $^3H_4(1)$.

Indeed, the slope of the experimental curves for the Y_2SiO_5:Pr^{3+} crystal (Fig. 3b) is of the order of 120 K (84 cm^{-1}), which is in good accord with the magnitude of splitting $^3H_4(0) - ^3H_4(1)$ of the $^3H_4$ multiplet (Fig. 2b). However, under the condition that d_0 and d_1 are constants, the experimental dependence for the LaF_3:Pr^{3+} crystal cannot be described by formula (2), since $I_1/I_0 > 1$ at $T > 30$ K (Fig. 3b). In order to resolve the above-mentioned contradiction, all we have to do is to assume that an increase in the temperature of the LaF_3:Pr^{3+} crystal changes the magnitude of dipole moments at the transitions $^3H_4(0) - ^3P_0$ and $^3H_4(1) - ^3P_0$ of the Pr^{3+} ion. In this case, the value of d_0 decreases and that of d_1 increases in view of a relative decrease in the area covered by the contour of Γ_0 and an increase in the area covered by the contour of Γ_1 (Fig. 3a).

The reason behind the change in the value of the dipole moments is not clear, but it allows a formal explanation of the sharper drop in the echo signal of LaF_3:Pr^{3+} with temperature than what would be expected from the energy splitting of the multiplet $^3H_4$. According to Ref. 13, the amplitude of a two- pulse PE signal is a nonlinear function of the dipole moment of the optical resonance transition:

$$I_e = A_0 \exp(-2\tau_{12}/T_2(T)),$$

$$A_0 = B(\mathbf{k}_1, \mathbf{k}_2, \mathbf{k}_e) N^2 d^2 \sin^2\left(\frac{dE}{\hbar}\delta\right) \sin^4\left(2\frac{dE}{\hbar}\delta\right), \qquad (3)$$

where $B(\mathbf{k}_1, \mathbf{k}_2, \mathbf{k}_e)$ is a quantity that depends on the experimental geometry, d the dipole moment of the optical resonance transition, N the number of particles in the coherent ensemble, δ the duration of laser pulses, E the electric field strength of laser pulses, $\hbar$ the Planck's constant, and τ_{12} the time interval between exciting laser pulses.

While analyzing the drop in the PE signal amplitude with temperature, it is assumed that A_0 is independent of temperature. With increasing temperature, however, the dipole moment of the optical resonance transition decreases in the LaF_3:Pr^{3+} crystal, thus leading to a decrease in the PE signal amplitude in accordance with formula (3). Consequently, the PE signal amplitude in the LaF_3:Pr^{3+} crystal (Fig. 1) decreases not only in accord with the variation of $T_2(T)$ according to formula (1), but also due to a change in the dipole moment of the transition $^3H_4(0) - ^3P_0$ with temperature. This led to an effective decrease in the value of Δ in formula (1) in Refs. 7 and 8.

Using formula (3), we can directly obtain the variation $(T_2(T))^{-1}$ for the Y_2SiO_5:Pr^{3+} crystal (Fig. 4) from the experimental curve presented in Fig. 1. The dependence obtained in this way should also be described by formula (1). However, the parameter α remains undetermined since Δ is obtained directly from the absorption spectrum (Fig. 2b). We can solve the inverse problem, i.e., find the value of α by approximating the experimental points presented in Fig. 4. A satisfactory approximation is attained only in the temperature interval 13–18 K for $\alpha = 9.4 \cdot 10^{10}$ s^{-1}. Analysis of higher
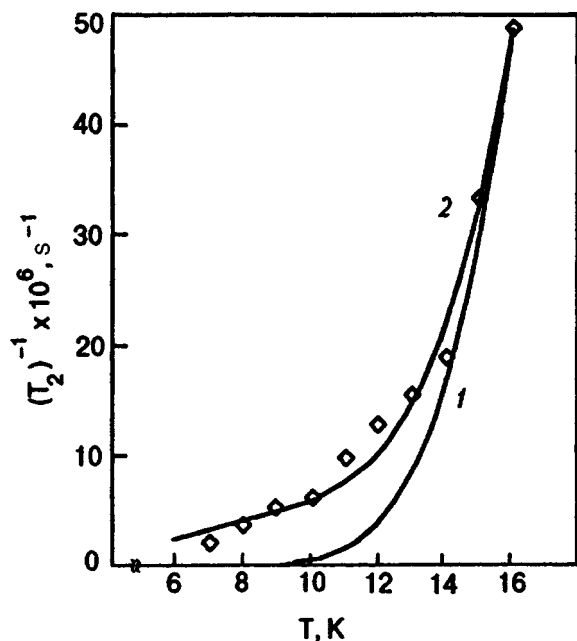
FIG. 4. Temperature dependence of the dephasing time in a $Y_2SiO_5:Pr^{3+}$ crystal. The symbols correspond to the experiment. Curve *1* corresponds to the theoretical dependences taking into account Eq. (1) only, while curve *2* is obtained by taking into account both formulas (1) and (4).

sublevels in the multiplet $^3H_4$ does not improve the description of the experimental curve (Fig. 4) in the temperature interval 6–13 K. It follows from Fig. 4 that the experimental dependence in this temperature interval can be approximated by a linear function of the type $(T_2(T))^{-1} = \beta T$, ($\beta = 1.37$ MHz/K), which does not match with any of the known temperature dependences ($\sim T^{-7}$ or $\sim \exp(-\Delta/T)$) describing the dephasing of optical transitions of impurity centers in crystals at low temperatures.[11]

Hence it should be interesting to consider the two non-equilibrium positions of the yttrium ion that may be occupied by Pr^{3+} ions in the Y_2SiO_5 crystal lattice.[16] The experimental confirmation is provided by an additional absorption peak emerging in the region of resonance transition $^3H_4(0) - ^3P_0$ of Pr^{3+} ions (Fig. 2a). A similar two-center picture is also observed in the optical spectra of Eu^{3+} in the Y_2SiO_5 crystal.[17] Assuming that an increase in temperature of the $Y_2SiO_5:Pr^{3+}$ crystal may cause Pr^{3+} ions to undergo transitions between two nonequivalent positions, this may lead, according to Ref. 11, to the emergence of a new additional dephasing mechanism which exists for amorphous matrices.[18] The elementary excitations associated with the transitions of impurity centers between nonequivalent positions were called tunnelons.[18] Considering the interaction of the optical resonance transition with one tunnelon, the temperature dependence of the phase relaxation time is defined by the expression[18]

$$[T_2(T)]^{-1} = \gamma \sinh^{-1}(\Delta\nu/T), \qquad (4)$$

where $\Delta\nu$ is the activation energy of a tunnelon, and γ is a constant defined exactly in Ref. 18.

For $T > \Delta\nu$, formula (4) gives a linear dependence on temperature. For the $Y_2SiO_5:Pr^{3+}$ crystal, $\Delta\nu = 11.4$ K

(8.1 cm^{-1}) in conformity with Fig. 2a. In this case, the condition $T \sim \Delta\nu$ is satisfied in the temperature interval 6–13 K. However, the functional dependence (4) is close to linear. Taking Eq. (4) into consideration together with formula (1), we obtain a good approximation of the experimental dependences for $\gamma = 14.5 \cdot 10^6$ s^{-1} and $\alpha = 7.5 \cdot 10^{10}$ s^{-1} (Fig. 4).

CONCLUSION

For $Y_2SiO_5:Pr^{3+}$ and $LaF_3:Pr^{3+}$ crystals at low temperatures, new relaxation channels for the photon echo have been established in optical transitions of the Pr^{3+} ion. The reason behind the change in the dipole moments at the transitions $^3H_4(0) - ^3P_0$ and $^3H_4(1) - ^3P_0$ of the Pr^{3+} ion in the LaF_3 crystal remains unclear and requires further investigation. However, independent experimental facts indicate that the low-temperature mechanism of dephasing of optical transitions in $Y_2SiO_5:Pr^{3+}$ crystals may be associated with the tunneling of Pr^{3+} ions between two nonequivalent states. It should be interesting to study these peculiarities and to establish the general regularities governing the phase relaxation of electron excitations of impurity centers in rare-earth silicate crystals by extending the range of objects of investigation, doping Y_2SiO_5 with other rare-earth ions, or by changing the host crystal matrix.

*E-mail: malykin@isc.kharkov.ua

[1] F. Auzel, J. Lumin., **45**, 341 (1990).
[2] V. Schafer, J. Neukum, N. Bodenschatz, and J. Heber, J. Lumin., **60–61**, 633 (1994).
[3] M. Malinowski, M. E. Joubert, and B. Jacquier, J. Lumin., **60–61**, 179 (1994).
[4] G. Blasse J. Lumin., **60–61**, 930 (1994).
[5] È. A. Manykin and V. V. Samartsev, *Optical Echo Spectroscopy* [in Russian], Nauka, Moscow (1984).
[6] W. N. Yen, W. C. Scott, and A. L. Schawlow, Phys. Rev. **A136**, 271 (1964).
[7] N. Takeuchi, J. Lumin., **12–13**, 743 (1978).
[8] Yu. V. Malyukin, N. L. Pogrebnyak, and V. P. Seminozhenko, Fiz. Nizk. Temp. **20**, 610 (1994) [Low Temp. Phys. **20**, 483 (1994)].
[9] Yu. V. Malyukin, È. A. Manykin, N. L. Pogrebnyak *et al.*, Zh. Éksp. Teor. Fiz. **108**, 485 (1995) [JETP **81**, 260 (1995)].
[10] P. N. Zhmurin, N. L. Pogrebnyak, V. P. Seminozhenko, and Yu. V. Malyukin, Ukr. Fiz. Zh. **39**, 791 (1994).
[11] I. S. Osad'ko, Phys. Rep. **206**, 45 (1991).
[12] N. L. Pogrebnyak, P. N. Zhmurin, V. I. Minkov, and Yu. V. Malyukin, Ukr. Fiz. Zh. **40**, 178 (1995).
[13] L. Allen and J. Eberly, *Optical Resonance and Two-Level Atoms*, J. Wiley, New York (1975).
[14] R. M. Macfarlane, J. Lumin., **45**, 1 (1990).
[15] R. Loudon, *The Quantum Theory of Light*, Clarendon Press, Oxford (1973).
[16] B. A. Maksimov, V. V. Ilyukhin, Yu. A. Kharitonov, and N. V. Belov, Kristallografiya **15**, 926 (1970) [Sov. Phys. Crystall. **15**, 806 (1970)].
[17] M. Mitsunaga, T. Takagahara, R. Yano, and N. Uesugi, Phys. Rev. Lett. **68**, 3216 (1992).
[18] I. S. Osad'ko, Adv. Polym. Sci. **114**, 125 (1994).

Translated by R. S. Wadhwa

749   Low Temp. Phys. **23** (9), September 1997

Yu. V. Malyukin   749

PHYSICAL PROPERTIES OF CRYOCRYSTALS

Thermomechanical effects in thermal expansion of Ar–N$_2$-type solid solutions

A. N. Aleksandrovskii, K. A. Chishko, V. B. Esel'son, V. G. Manzhelii,
and B. G. Udovidchenko

*B. Verkin Institute for Low Temperature Physics and Engineering, National Academy of Sciences of the Ukraine, 310164 Kharkov, Ukraine**

The results of analysis of hysteresis in the thermal expansion of solid solutions Ar–4.89 mol. %N$_2$ are considered in the temperature range 1–16 K. A physical model is proposed in order to explain the observed phenomenon. This model is based on the assumption that transformed regions in the form of piles of random stacking faults in the initial fcc lattice are formed in the vicinity of nitrogen impurity. The hysteresis of the thermal expansion coefficient is due to relaxation mechanisms for thermal stresses appearing in the transformed region during thermocycling of the sample. The theoretical estimates of the upper and lower temperature boundaries of hysteresis phenomenon obtained in this model are in good agreement with the experimentally observed values. © *1997 American Institute of Physics.*
[S1063-777X(97)01209-7]

Solidified inert gases and solid solutions based on them form systems with a broad spectrum of unique physical properties. Among other things, thermal expansion of solid solutions based on argon and krypton[1] demonstrate clearly manifested anomalous behavior. The anomaly lies in that the linear thermal expansion coefficient (LTEC) $\alpha = (1/L) \times (\Delta L/\Delta T)$ of the sample (L is the sample length and ΔL the elongation of the sample upon a change in its temperature by ΔT) changes upon thermocycling during measurement. The LTEC of a solid solution held preliminarily at a fixed temperature in the range 4.2–16 K was found to be smaller by a factor of 3–5 than the LTEC of the corresponding crystalline matrix of an inert gas free of impurities. Subsequent thermocycling of the sample near the measuring temperature leads to an increase in the LTEC being recorded, which becomes larger than the LTEC of the pure matrix after three or four thermal cycles. If the sample subjected to such a procedure is again kept for 10–12 h at a constant temperature below 15 K the LTEC is restored. The phenomenon under consideration was observed by us experimentally long ago[1] and was called ''thermoplastic effect.'' In Ref. 1, an attempt was made to construct a physical pattern of the observed phenomenon, and experimental results accumulated by this time received in general a reasonable explanation. Some theoretical models describing the substructure of cryomatrices of inert gases were considered in Ref. 2. We are obviously dealing with a peculiar hysteresis of thermal expansion of a solid solution. Nevertheless, we cannot state that all the aspects associated with the hysteresis of thermal expansion of solid solutions based on inert gases are completely clear. Indeed, the hysteresis of thermal expansion is typical of metallic alloys with a stable heterophase polydomain substructure in a certain temperature range.[3,4] As re-

gards the case of simple molecular cryocrystals we are interested in, no direct experimental proofs of the presence of polydomain structures exist to our knowledge, although we can give arguments in favor of their existence on the basis of reliable indirect data.[1,2] This is primarily due to the fact that direct low-temperature x-ray diffraction analysis whose accuracy is sufficient for the detection and identification of polydomain formation in the matrices of solidified inert gases is difficult for realization. For this reason, the properties of molecular cryocrystals, which are sensitive to the structural variations and provide new information on the substructure of the above-mentioned systems, remain an interesting object for investigations. An analysis of temperature and concentration dependences of LTEC of cryomatrices with impurities is an effective method in this field.

This research aims at obtaining new experimental data on anomalies in the thermal expansion of solid solutions of nitrogen in argon in the temperature range 1–16 K. These results allowed us to propose a physical model providing an interpretation of phenomena observed in this type of solutions, which is free of inherent contradictions.

EXPERIMENTAL TECHNIQUE

Thermal expansion of the solid solutions Ar–4.89 mol. %N$_2$ was measured by a low-temperature capacitive dilatometer.[5] Argon used in experiments was preliminarily purified at a high temperature with the help of a special device based on intermetallic compounds for ultrahigh purification of gases. This method ensures purification of argon to the total concentration of foreign impurities of the order of $10^{-5} - 10^{-6}\%$. The gas purity was controlled chromatographically, and no traces of foreign impurities
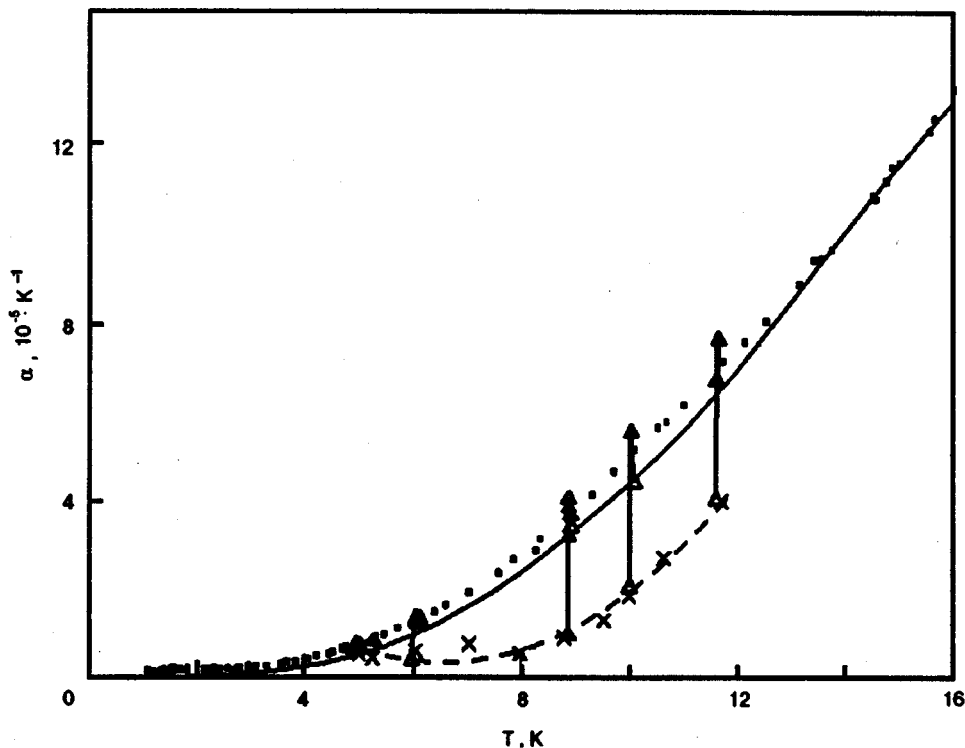
FIG. 1. Values of thermal expansion coefficients for the solid solution Ar–4.89 mol. %N_2 obtained under different conditions of measurements: primary values of the LTEC of the solution (step-wise heating without thermocycling) ($\times$), their smoothed values (dashed curve), in the process of thermocycling ($\triangle$), and the values of LTEC stabilized after thermocycling of this solid solution (■). The solid curve shows the values of LTEC for pure solid Ar.

were detected. The Ar–N_2 mixture was prepared by using nitrogen containing 0.002% of oxygen impurity. The solution under investigation was prepared at room temperature in a special measuring jar made of stainless steel. The rated composition of the solution was monitored by the chromatograph. Solid samples were grown in a glass ampule of the measuring cell of the dilatometer by condensation directly to the solid phase at a temperature ∼49 K. According to phase diagrams[6] (see also Ref. 7), the crystal under investigation must be in the one-phase region and must have a fcc lattice. The sample growth rate was ∼2 mm/h. The process of growing was controlled visually. The sample was transparent and contained no visible defects. It was separated from the walls of the glass ampule by thermal etching and was ultimately in the form of a cylindrical polycrystal with diameter ∼22 mm, height 26 mm, and grain size ∼1 mm. The thermal expansion coefficient was measured along the rotational axis of the sample in the temperature range 1–16 K. The temperature was determined by a germanium resistance thermometer. The thermal expansion coefficient for matrix (pure solid argon) samples grown according to the same technique was measure for comparison on the same dilatometer.

The measurements were made under isothermal conditions since cold influxes to the sample changed insignificantly in the course of measurements, and the required accuracy with which the temperature was maintained at a constant value was ensured by a stabilized power supplied to the heater. The distinguishing feature of this method is that the sample temperature was changed by a jump-wise variation of the power supplied to the heater, which was subsequently maintained at a constant level. The time of stabilization of the new value of temperature and sample length was mainly determined by its thermal diffusivity and amounted

from 0.5 to 1.5 h in this temperature range. In this way, we measured the LTEC during heating and cooling. The data on temperature and length of the sample were recorded every minute by the instruments, processed in real time on a computer, and displayed in graphic or digital form on the screen. A transition to a new temperature value was made automatically after the attainment of a "stable" state of the sample in which the temperature varied by not more than 0.01 K during 10 min. As a rule, thermocycling was carried out during measurements, i.e., the LTEC was measured successively during heating and cooling in a fixed temperature interval from 0.2–0.5 K (but remained unchanged for the same thermal cycle). In each case, the sample temperature was stabilized after each variation. It should be emphasized that the final temperature of the sample in each thermocycling step was attained only by heating (or only by cooling). In this way, we ruled out the possibility of a parasitic thermal cycling which would take place in the process of temperature stabilization with the help of devices with a proportional integro-differential mode for maintaining temperature of the sample.

RESULTS OF MEASUREMENTS

Figures 1 and 2 show the values of the thermal expansion coefficient of the solid solution Ar–4.89 mol. %N_2, obtained in various measuring modes. The solid curve gives the results of our experimental studies of the thermal expansion coefficient for pure solid argon. Triangles denote the variation of the obtained values of LTEC of the solution during thermocycling (the first step of thermal cycle always corresponded to sample heating in all measurements). The smallest values of LTEC correspond to the first measured value on
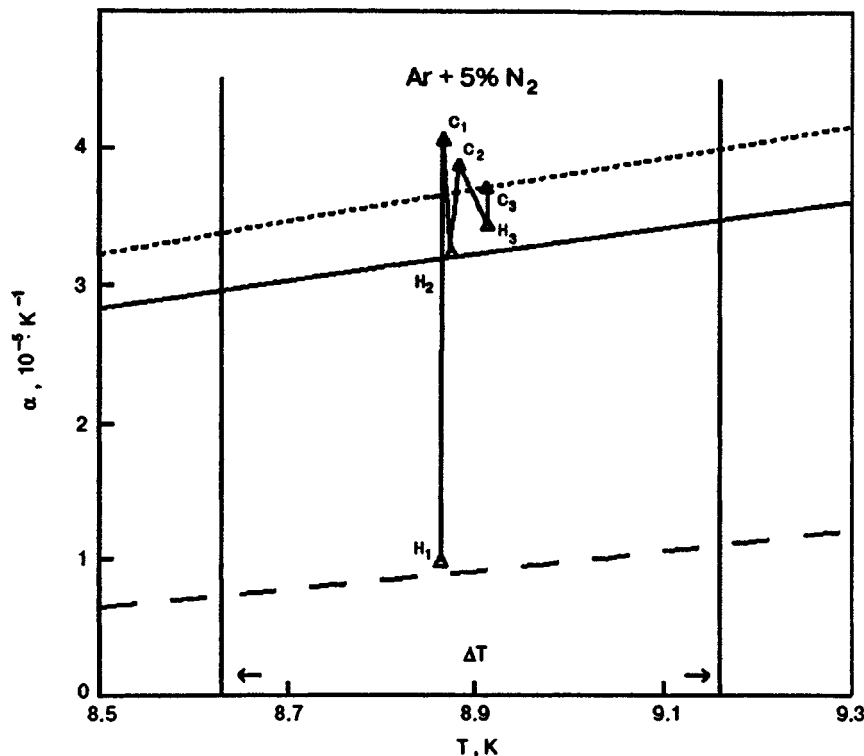
FIG. 2. Fragment of Fig. 1. The dashed line corresponds to the values of LTEC of the solid solution Ar–N_2 stabilized after thermocycling, H and C correspond to the values of LTEC obtained in the course of thermocycling during heating and cooling of the solid solution Ar–4.89 mol. %N_2. The remaining notation is the same as in Fig. 1. Vertical lines indicate the temperature boundaries of thermal cycles.

the initial branch of the thermal cycle. The squares in Fig. 1 denote the final values of the LTEC of the solution, which were obtained after four or five cycles, when the values of the LTEC of the solution remain unchanged during subsequent thermal cycles to within the experimental error. The final values of LTEC at temperatures above 12 K were obtained after thermocycling in the range 4.2–16 K. For this reason, Fig. 1 does not show the initial values of α at $T>12$ K. The crosses denote ''primary'' values of LTEC of the solution, obtained in the measuring mode without thermocycling with the step temperature dependence during heating. Such measurements were made by us only at $T<12$ K. Figure 2 shows a fragment of Fig. 1 (on a magnified scale), in which triangles show the values of LTEC obtained consecutively upon thermocycling at a temperature ~ 8.9 K. The letters H_1, C_1, H_2, C_2, H_3, and C_3 denote the values of the LTEC of the solution during thermocycling for heating (H_1, H_2, H_3) and cooling (C_1, C_2, C_3) of the sample. Vertical straight lines in the figure mark the boundaries of the thermocycling interval ΔT in which these values were obtained. In Fig. 2, the dashed line corresponds, as in Fig. 1, to primary values of the LTEC, while the dotted line corresponds to stabilized values of the LTEC marked by squares in Fig. 1. It can also be seen from Fig. 2 that the average temperature of the sample increased as a result of thermocycling approximately by 0.05 K. This is probably associated with internal friction in the sample.

The figures show that the difference between the final and ''primary'' values (hysteresis) appears at temperatures above 5 K and assumes significant values. The effect is observed above 5 K and up to 16 K. If we analyze the LTEC repeatedly in the temperature range where thermocycling was carried out, no difference between the ''primary'' and

final values of the LTEC is observed. In our experiments, LTEC hysteresis was restored every time after a prolonged (approximately 10–12 h) holding of the sample at the measuring temperature in the interval 4.2–15 K. In other words, by holding the sample after each thermocycling, we can restore the LTEC hysteresis. This process can be repeated many times, and the situation will be reproduced exactly in the same form as in the previous series of measurements. In the course of experiments on thermal expansion, the capacitive pickup used for measuring sample length exerted pressure along the axis of the cylindrical sample, which could be varied from 0.2 to 1 gf/mm^2. The values of LTEC were measured under different pressures from the above interval, and no effect of this pressure on the values being measured was observed. Besides, we carried out test holding of the sample for 10 h at 4.2 K under different axial pressures exerted on the sample (from 0 to 1 gf/mm^2) and did not observe any effect of external pressure on the boundary of hysteresis and temperature corresponding to the formation of this boundary. In some experiments, preliminarily held samples were ''compressed'' by a rod in the above pressure range. We did not observe any influence of this procedure on the magnitude of hysteresis of the LTEC. This leads to the conclusion that the observed phenomena are not associated with the instrumental effects.

At the same time, we made an attempt to analyze the hysteresis by thermocycling in which the first step corresponded to sample cooling from 16 K after 10-h holding of the sample at this temperature. However, in this case the temperature decreased uncontrollably (and the sample length changed accordingly) as a result of contact between the capacitive pickup and the sample and during the stabilization of the working regime in the setup, and hence we could not

obtain a sufficiently reliable ''primary'' value of LTEC. In Fig. 1, the points corresponding to the values of LTEC on different branches of the thermal cycle above 12 K are not shown, and only the final experimental values of LTEC of the solid solution, which were obtained after preliminary thermocycling in the extended temperature range 4.5–18 K are presented. It should be emphasized that we observed no traces of hysteresis in experiments on thermal expansion of pure argon in the temperature range 1–18 K. The sample temperature changed by ΔT during thermocycling. It was mentioned above that the value of this quantity varied from 0.2 to 0.5 K in different cycles of measurements, remaining unchanged for all branches of the same cycle. Thus, in the first run of thermocycling, we increased the measurement temperature from T_0 to $T_1 = T_0 + \Delta T$ and obtained the value of LTEC $\alpha = \alpha_1$. In the second run, the sample was returned to the temperature $T_2 = T_0$, and the value of $\alpha = \alpha_2$ was determined. After this, the cycle was repeated the required number of times, and the LTEC value $\alpha_3, \alpha_4, \dots, \alpha_n$ were recorded. Thus, the points denoted in Fig. 2 as H_1, C_1, H_2, C_2, etc. correspond to the values $\alpha_1, \alpha_2, \alpha_3, \alpha_4$, etc of the LTEC. As a rule the values of LTEC being measured attain saturation after two complete thermal cycles (after four heating–cooling runs), i.e., $\alpha_4 = \alpha_\infty$. The first value (α_1) was always very small as compared to the LTEC for pure argon matrix: $\alpha_1 \approx 0.3\alpha_{Ar}$ in the temperature range 5–9 K and $\alpha_1 \approx 0.5\alpha_{Ar}$ in the temperature range 9–13 K. The values of α_2 from the temperature range 5–9 K differs from α_∞ by less than 15%. If we repeat thermocycling with a new temperature step ΔT_1 after the attainment of LTEC saturation in a cycle of measurements at T_0, the value of LTEC does not change for $\Delta T_1 < \Delta T$, while hysteresis appears again for $\Delta T_1 > \Delta T$, the amplitude of the hysteresis being nonzero in view of the difference in the temperature steps $\delta T = \Delta T_1 - \Delta T > 0$.

As we go over to a new (higher) measuring temperature lying beyond the thermocycling interval in the previous experiments, thermal expansion hysteresis is observed again in a similar form. The distribution of the values of α_i in the forward and backward direction of thermocycling obtained by us is of special importance. The values of α_{2k+1} corresponding to odd branches of a thermal cycle (sample heating by ΔT) in our experiments were found to be smaller in magnitude than the final value of LTEC ($\alpha_{2k+1} < \alpha_\infty$). On the other hand, for even branches of thermal cycle (cooling) we have $\alpha_{2k} > \alpha_\infty$. In this case, the relation

$$|\alpha_{i+1} - \alpha_i| < |\alpha_i - \alpha_{i-1}| \tag{1}$$

was not violated upon an increase in the number i of the thermal cycle, the condition $|\alpha_i - \alpha_\infty| \to 0$ being satisfied in all cases when $i \to \infty$. Pay attention to the fact that the result obtained here differs from the results obtained in Ref. 1: the values measured in Ref. 1 (both for even and odd branches of a thermal cycle) always corresponded to the condition

$$\alpha_1 < \alpha_2 < \alpha_3 \dots < \alpha_n \dots < \alpha_\infty. \tag{2}$$

It should be noted that LTEC hysteresis was observed earlier in Ref. 1 for solid solutions of argon with 1, 2, and 3 mol.% of nitrogen impurity as well as for argon containing 0.5, 1,

and 2 mol.%CO. In the latter case, the effect was somewhat weaker than for the N_2 impurity. It was noted in Ref. 1 that the amplitude of hysteresis for both systems did not depend on the concentration of impurity, and the lower boundary of the effect (~ 8 K) was found to be independent of the impurity concentration. Our present results indicate, however, that the latter statement should be revised: it can easily be seen that an increase in the impurity concentration to 5 mol.% shifts the boundary of the effect towards lower temperatures (to ~ 4 K.

DISCUSSION OF RESULTS

Summarizing the experimentally established regularities of the phenomenon under investigation described above, we can assume that the thermal expansion hysteresis of impurity crystals of argon is due to certain structural transformations occurring in the solid solution during thermocycling. Indeed, the thermal expansion hysteresis is typical, for example, for metallic alloys displaying a tendency to martensite transformation and forming a complex polydomain substructure in the unstressed state.[4] Such a substructure possesses additional internal degrees of freedom which are excited upon a change in temperature or external pressure; this can ultimately lead to a decrease in the LTEC of a macroscopic sample.

This model whose correctness has been verified for classical solid solutions can be rightfully extended to cryocrystals of inert gases. The existence of structurally transformed regions in pure argon and in Ar–N_2 solutions was directly confirmed in experiments.[8,9] The inclusions of the metastable HCP phase in pure argon are observed in x-ray diffraction experiments, which allows us to measure directly its crystallographic parameters.[8] It has been proved experimentally that the introduction of diatomic impurities in the fcc argon matrix stabilizes the hcp phase in the vicinity of impurities.[9] These facts confirm the reality of the existence of an equilibrium polydomain structure in Ar-based solid solutions. Experiments on low-temperature brittle fracture of pure argon single crystals give additional arguments supporting the presence of such a structure.[10] An analysis of these results[2] leads to definite conclusions concerning the role of stacking faults in the formation of plastic properties of cryocrystals. The results of experiments on active deformation of ultrapure hydrogen single crystals at low strain rates[11] can be regarded as most notable in this respect. It was shown in Ref. 11 that the initial segment of the stress–strain curve for H_2 under these conditions is quadratic, followed by a horizontal plateau transformed into the work-hardening state for strains exceeding 0.5–1%. It is remarkable that the removal of loading on any stage of the stress–strain curve led to a complete recovery of the sample. The reason behind such a superelastic behavior of an H_2 single crystal free of impurities can obviously lie in the presence of a thermodynamically equilibrium polydomain substructure similar to those observed in classical systems, which demonstrate shape memory effects.[12]

Pay attention to the fact that the mechanism of LTEC hysteresis under consideration must be a manifestation of the properties of substructure which is in thermodynamic equi-

753   Low Temp. Phys. **23** (9), September 1997

Aleksandrovskii *et al.*   753

librium in the Ar–N_2 solid solution. This follows directly from the fact that the hysteresis vanishing during thermocycling is restored every time after a prolonged isothermal holding of the sample. Thus, the search for possible reasons behind the observed phenomenon should be started from an analysis of the substructure of the Ar–N_2 mixed crystal. The fact that the qualitative nature of the hysteresis changes slightly with the concentration x_{N_2} in the solution is a direct indication of a decisive role of structural factors in the LTEC hysteresis effect. For example, the coefficients α_i for solutions with $1–3\% N_2$,[1] obtained for last branches of the thermal cycle form, in contrast to (1), a monotonically increasing sequence (2) converging to the limiting value a from below. Moreover, according to the results of a recent publication,[13] the finite value of the excess LTEC of the Ar–N_2 solid solution in the temperature range 1–7 K becomes independent of the concentration x_{N_2} of nitrogen molecules for $x_{N_2} > 2.5\%$. This suggests that the substructure of the solid solution undergoes certain structural changes as compared to the substructure of dilute solutions Ar–N_2 starting from N_2 concentrations of the order of a few percent.

Let us now consider the type of the equilibrium substructure that can be formed in N_2–Ar solid solutions. Diatomic nitrogen impurities in the argon atomic lattice are force dipoles creating long-range elastic fields in the surrounding medium. The elastic energy of the impurity subsystem is the athermal (to within a weak temperature dependence of elastic moduli) component of the total energy of the solid solution, which must therefore be manifested most strongly at low temperatures. Let us estimate the energy W of an impurity center for the isotropic continuum,[14] assuming that the N_2 impurity forms at the origin of coordinates a point dipole source of forces whose volume density is given by[15]

$$\mathbf{f}(\mathbf{r}) = -K\Omega_{ik}\nabla_k\delta(\mathbf{r}), \tag{3}$$

where K is the bulk compressional modulus of the argon matrix, $\nabla_k = \partial/\partial x_k$ is the operator of differentiation with respect to the coordinate, and the tensor Ω_{ik} has the form[15]

$$\Omega_{ik} = \Omega_0\delta_{ik} + \Omega_1\left(l_il_k - \frac{1}{3}\delta_{ik}\right), \tag{4}$$

$\mathbf{l}$ being the unit vector in the direction of the dipole axis. The parameters Ω_0 and ω_1 specify the dilatation and deviation (dipole) components of the force action of impurity on the lattice. The order of magnitude estimate of the quantities is $\Omega_0 \simeq \Omega_1 \simeq k(V_{Ar} - V_{N_2})$ (V_{Ar} and V_{N_2} are the specific volumes of argon and nitrogen, and the parameter k is determined by elastic relaxation of the matrix in the vicinity of impurity; an order of magnitude estimate of this coefficient will be given below). Since we are interested in the energy of impurity in the unrelaxed solution, the medium can be regarded as unbounded. Using the standard relations from the theory of elasticity,[14] we can write the strain tensor $\varepsilon_{ik}(\mathbf{r})$ for the crystal with impurity in the form

$$\varepsilon_{ik}(\mathbf{r}) = -\frac{K}{8\pi G}\left\{\frac{1-2\nu}{1-\nu}\left(\Omega_0 - \frac{\Omega_1}{3}\right)\nabla_i\nabla_k\frac{1}{r}\right.$$

$$+ \Omega_1 l_j(l_i\nabla_k\nabla_j + l_k\nabla_i\nabla_j)\frac{1}{r}$$

$$\left. - \frac{\Omega_1}{2(1-\nu)}l_jl_m\nabla_i\nabla_k\nabla_j\nabla_m r\right\}. \tag{5}$$

Here G is the shear modulus and ν the Poisson coefficient of the matrix. Using this relation, we can calculate the elastic energy of the impurity[14]:

$$W = \frac{3K}{2(1+\nu)}\int_a^\infty r^2 dr \int do[\nu\varepsilon_{ll}^2(\mathbf{r}) + (1-2\nu)\varepsilon_{ik}^2(\mathbf{r})] \tag{6}$$

(do is an element of the solid angle). In the continual approximation, a force dipole is regarded as a point source of fields, which leads to the divergence of the integrals in (6) for $r \to 0$. For this reason, the integration limits for r in (6) are bounded from below by the parameter a equal to the separation between nearest neighbors in the densely packed (fcc or hcp) matrix. For the same reason, the terms containing $\delta(\mathbf{r})$ in the integrand of (6) must be omitted. Finally, we have

$$W = \frac{K}{36\pi a^3}\frac{1+\nu}{(1-2\nu)^2}\left\{3\left(\frac{1-2\nu}{1-\nu}\right)^2\Omega_0^2 + \frac{2\Omega_1^2}{15}\left[11\right.\right.$$

$$\left.\left. + \frac{8\nu}{(1-\nu)^2}\right]\right\}. \tag{7}$$

In order to obtain specific estimates, we must know the values of the quantities Ω_0 and Ω_1. Using the results obtained by Ashelby,[16] we can write the following expression in the continual approximation adopted by us:

$$\Omega_0 = 3\frac{1-\nu}{1+\nu}\left(1 + \frac{4G}{3K_{N_2}}\right)^{-1}(V_{Ar} - V_{N_2}), \tag{8}$$

where $K_{N_2} = 2.2\cdot10^{10}$dyne/cm^2 is the bulk compressional modulus for nitrogen.[17] Further, we choose the following values for elastic constants for the fcc argon matrix[18]: $c_{11} = 4.34\cdot10^{10}$ dyne/cm^2, $c_{12} = 1.82\cdot10^{10}$ dyne/cm^2, and $c_{44} = G = 1.61\cdot10^{10}$ dyne/cm^2. These data are taken from ultrasonic experiments and are most suitable (in our opinion) for estimating the elastic response of the medium. The cubic constants listed above should be combined for obtaining two elastic moduli characterizing the matrix in the isotropic medium approximation used here. It is natural to choose for one of such moduli the bulk compressional modulus $K = (c_{11} - 2c_{12})/3 = 2.66\cdot10^{10}$ dyne/cm^2. For the second modulus, we can choose either the shear modulus $G = c_{44}$ or the Poisson coefficient $\nu_1 = (c_{12} + c_{11})/c_{12} = 0.296$. It should be noted that if we choose K and G for isotropic moduli, the effective Poisson coefficient is given by

$$\nu_2 = \frac{3K - 3G}{2(3K + G)} = 0.25.$$

Such a discrepancy is associated with the imperfection of the procedure of transition to the isotropic medium used

by us. It will be shown below, however, that the relative error in the estimates of the value of W obtained in this case does not exceed 10%.

Substituting (8) into (7) and using the above values of elastic moduli, we obtain (recalculating for one impurity) $W_1 = 14.7$ K (for $\nu = \nu_1$) and $W_2 = 15.8$ K (for $\nu = \nu_2$). Thus, the estimate $W \simeq 15$ K per impurity molecule can be regarded as quite reliable. It should be noted that this is approximately equal to the characteristic temperature above which the impurity contribution of N_2 to thermal expansion of the solid solution becomes vanishingly small. Thus, the inclusion of the static elastic energy of impurities is significant in the entire temperature range $T < 15$ K in which the thermal expansion hysteresis is observed. It should be noted that the assumption concerning a significant role of elastic fields of impurities in the formation of the observed physical properties of Ar$-$N$_2$ solid solutions is confirmed by the theoretical interpretation[19,20] of the available experimental results[21] on the heat capacity of these systems.

Obviously, the system tends to relaxation of internal stresses associated with the presence of dilatation centers. The formation of a region with a transformed structure in the form of a pile of stacking faults (SF) lying in densely packed planes (111) can be one of the ways of such a relaxation. These SF are ''threaded'' on the direction $\langle 111 \rangle$ of the valence bond of the impurity diatomic molecule perpendicular to them. The relaxation of internal stresses around an impurity through the formation of a pile of stacking faults can be interpreted as follows: partial dislocations bounding planar SF form a closed cluster whose intrinsic stress fields compensate partly the stress field created by the impurity molecule. We shall not consider in detail the distribution of dislocation loops at the boundary of the transformed region, which corresponds to the best relaxation of the stress field of the anisotropic dilatation center since it requires an independent analysis. In order to get an exact result, special calculations should be made, although some of the results pertaining to this subject can be borrowed from the literature.[22]

Nevertheless, we can consider some estimates illustrating our statements. For this purpose, we take into account the fact that the SF formation in a fcc structure is associated with an elementary shift of the densely packed plane (111) of the set, i.e., with the formation of a local region with the hexagonal symmetry in the fcc crystal. Unfortunately, no reliable experimental or theoretical data pertaining to the SF energy in argon are available. The estimates,[23] based on the calculation of the difference in the static energies of the fcc and hcp Ar lattices $[\Delta = (E_{hcp} - E_{fcc})/E_{fcc} \simeq 0.01\%]$[24] taking into account the known parameters of the Lennard–Jones potential, give low values of SF energy $\gamma_{Ar} \simeq 0.22$ erg/cm^2, which corresponds to the energy ~ 0.18 K per atom. A more realistic estimate can be obtained by using the value $\Delta \simeq 0.065\%$ from Ref. 25: $\gamma_{Ar} \simeq 0.15$ erg/cm^2, i.e., ~ 1.2 K. Experimental observations of split dislocations in xenon[23] lead to the value $\gamma_{Xe} \simeq 1$ erg/cm^2 (Niebel and Venables[26] give a refined value of $\gamma_{Xe} \simeq 1.3$ erg/cm^2), which can serve as the upper boundary for γ_{Ar}. Bullough *et al.*[23] substantiate the conclusion that in actual practice $\gamma_{Ar} < 0.7$ erg/cm^2, i.e., the energy associated with the SF formation in argon is smaller

than 6 K per atom. The inclusion of zero-point vibrations in the energy of atomic interaction in Ar must lower this boundary.

Thus, we can conclude that the energy required for transforming the matrix around an impurity amounts to ~ 3 K. This corresponds to the lower boundary of the emergence of the LTEC hysteresis: the lattice possesses the energy sufficient for the realization or relaxation processes leading to the formation of a thermodynamically equilibrium substructure of solid solution only at $T > 3$ K.

It would be appropriate to make certain remarks about the lower temperature boundary of hysteresis estimated by the above method. The measurements of LTEC for solid mixtures Ar-N$_2$ show that the temperature corresponding to the emergence of the hysteresis decreases from 8 to 4 K upon an increase in the nitrogen concentration from 0.5 to 4–5%. The size of the transformed region in a dilute solution in which impurities can be regarded as isolated is determined by the equilibrium of the boundary (dislocation pile) separating the transformed region from the undistorted matrix in the stress field created by an impurity. This size is independent of temperature and is determined only by the intensity and anisotropy of the impurity dilatation center. For low impurity concentrations, the transformed regions interact as individual inclusions of the ''second phase'' in the matrix of the solid solution, and the LTEC satisfies condition (2) on successive branches of the hysteresis. Starting from the N$_2$ concentration of the order of 5%, transformed regions come in contact, and the dislocation piles embracing individual impurities become coherent boundaries separating the ''territories'' occupied by neighboring impurities. This leads to the formation of a single polydomain substructure of crystallographically conjugate transformed region in the Ar–N$_2$ solid solution with an N$_2$ molecule at the center of each region. Thus, the form of the interaction between impurities changes: a specific mesoscopic ordering of solid solution takes place, for which impurities are ''frozen'' in argon crystallites whose lattice does not possess cubic symmetry any longer (a pile of random stacking faults has a hexagonal symmetry with the third-order axis perpendicular to the basal planes (111)).[4,27] This, in turn, leads to the removal of degeneracy of the rotational states of the impurity molecule and to the emergence the features of an glass-like state.

Thus, a crystallite consisting of the SF pile can be regarded as an inclusion with the hcp structure.[4,27] In contrast to cubic lattices, hexagonal lattices possess, as a rule, a noticeable anisotropy of thermal expansion: the LTEC α_c along the c-axis differs from the LTEC α_b in the basal plane. The ratio $\kappa = \alpha_c / \alpha_b$ for various classical crystals of the hexagonal system has the absolute value $|\kappa| = 0.2-5$; for some lattices, $\kappa < 0$.[28] Consequently, it is natural to expect that the equilibrium substructure of a concentrated solid solution in our model is a set of crystallographically conjugate domains with anisotropy in the thermal expansion coefficient. Naturally, heating or cooling of such a system leads to the emergence of internal stresses concentrated predominantly in the region of domain boundaries in the sample since the c-axes of neighboring domains are not parallel to one another. It should be noted that internal stresses in the boundary region

appear when the transformed region does not come in contact with neighboring domains, but is completely surrounded by the cubic matrix (the latter circumstance is important for understanding that the proposed mechanism is also suitable for the interpretation of the LTEC hysteresis in comparatively dilute Ar–N$_2$ solid solutions). These stresses have the maximum value in the first run of a thermocycle, in which the equilibrium substructure of the solution is in the state described above.

While estimating these stresses, we shall assume that the average strain $\varepsilon \simeq \alpha \Delta T$ emerging in the sample upon a change in its temperature by ΔT takes place in the crystallite tightly pressed between neighboring domains. Naturally, in actual practice the boundaries between crystallites are slightly shifted due to deformation of neighboring domains, but these displacements are the less significant, the stronger the difference between the anisotropy parameter k and unity. This circumstance can be neglected while estimating thermal stresses. In this case, the average stress in the crystallite is of the order of $\sigma \simeq K \varepsilon \simeq K \alpha \Delta T$. Assuming that $\Delta T \simeq 1$ K in experiments, while the excess LTEC observed at temperatures 4–12 K is $\alpha \simeq (4-10) \cdot 10^{-6}$, we find that $\sigma \simeq (4-10) \cdot 10^{-6}$ K $\simeq (1.2-3) \cdot 10^5$ dyne/cm$^2 \simeq 1.2-3$ g/mm^2. It should be noted that the estimated level of internal stresses exceeds typical pressures exerted by the rod on the sample in the course of measurements. Thus, the observed LTEC hysteresis is obviously not associated with the instrumental effects.

An equally important circumstance is that large gradients of internal stresses are created in transformed regions surrounding impurities in view of the extremely small size of these regions (of the order of three-four atomic spacings). The above estimates show that the level and structure of internal stresses are apparently sufficient for initiating microplastic deformation in transformed regions. The deformation includes shear in the basal planes (111), leading to elimination of stacking faults around impurities and to reconstruction of the homogeneous cubic structure of the Ar matrix lattice. The anisotropy of thermal expansion vanishes, and thermal stresses do not appear during thermocycling.

In the first thermal cycle, when deformations in crystallites are suppressed to the maximum possible extent by the presence of neighboring regions, the excess LTEC α_1 has the minimum value and coincides in order of magnitude with the smaller of the values α_b and α_c. Since the anisotropy parameters of transformed regions are unknown, the above consideration can be used for estimating $\kappa \sim \alpha_1 / \alpha_\infty$. As the substructure is destroyed during consecutive steps of a thermal cycle, the value of α_n increases as described above. In this case, in the low-temperature region of hysteresis, in which thermal stresses are comparatively low, only local growth and reorientation of individual domains take place. With increasing temperature (upon a transition to a new thermal cycle), the value of α_1 also increases, while internal stresses become sufficient for restoring the cubic matrix in wider regions even at the first step of a new thermal cycle. As a result of heating from 4 K, hysteresis increases in magnitude until the volume fraction of the initial transformed regions decreases to such an extent that the hysteresis amplitude starts decreasing as we approach the upper boundary of the effect (of the order of 15 K). Above this temperature, the substructure under investigation is not formed in the solid solution since the energy of intrinsic elastic fields of the impurity subsystem becomes smaller than the energy of thermal motion of matrix atoms.

Thus, the model proposed above makes it possible to work out an admissible physical concept for interpreting the LTEC hysteresis in solid solutions of diatomic molecules in matrices of inert gases. Naturally, a number of theoretical and experimental studies are required to clarify the following aspects in order to complete the development of this model.

(1) The substructure of solid solution described above is a stable thermodynamically equilibrium formation. For this reason, an authentic theoretical description of its properties should be obtained not only in the form of estimates, but also by using a more rigorous approach.

(2) Independent experimental verification of sufficient conditions for the existence of the substructure of the solid solution can involve control measurements of the impurity LTEC in systems with spherically symmetric impurities, e.g., with atoms of other inert elements. In this case, we can expect a noticeable decrease or even the disappearance of the LTEC hysteresis.

(3) Finally, independent experimental proofs of the existence of a substructure in the solid solutions under investigation can be obtained, in our opinion, from an analysis of other physical properties of impurity cryocrystals, e.g., heat capacity, thermal conductivity, and also appropriate x-ray diffraction studies.

*E-mail: aalex@ilt.kharkov.ua

[1] A. N. Aleksandrovskii, K. A. Chishko, E. A. Kosobutskaya, and V. G. Gavrilko, Fiz. Nizk. Temp. **12**, 55 (1986) [Sov. J. Low Temp. Phys. **12**, 32 (1986)].

[2] K. A. Chishko, Fiz. Tverd. Tela (Leningrad) **31**, 283 (1989) [*sic*].

[3] J. Christian, *The Theory of Transformations in Metals and Alloys*, Pergamon Press, Oxford (1975).

[4] B. I. Nikolin, *Multilayered Structures and Polytypism in Metallic Alloys* [in Russian], Naukova Dumka, Kiev (1984).

[5] A. V. Soldatov. V. I. Kuchnev, A. M. Tolkachev *et al.*, Pribory Tekhn. Éksp. **4**, 237 (1990).

[6] L. D. Yantsevich, A. I. Prokhvatilov, I. N. Krupskii, and A. S. Baryl'nik, Fiz. Nizk. Temp. **12**, 300 (1986) [Sov. J. Low Temp. Phys. **12**, 170 (1986)].

[7] C. S. Barrett and L. Meyer, J. Chem. Phys. **42**, 107 (1965); *ibid*. **42**, 3502 (1965).

[8] L. Meyer, C. S. Barrett, and P. Haasen, J. Chem Phys. **40**, 2744 (1964).

[9] C. S. Barrett and L. Meyer, J. Chem. Phys. **41**, 1078 (1964).

[10] A. V. Leont'eva, A. V. Romanusha, L. V. Stepanchuk, and È. P. Fel'dman, Ukr. Fiz. Zh. **28**, 1025 (1988).

[11] A. N. Aleksandrovskii, E. A. Kir'yanova, V. G. Manzhelii *et al.*, Fiz. Nizk. Temp. **13**, 1095 (1987) [Sov. J. Low Temp. Phys. **13**, 623 (1987)].

[12] K. A. Chishko, Fiz. Nizk. Temp. **15**, 117 (1989); deposited at VINITI 09.08.1988, dep. No. 6367-B88.

[13] A. N. Aleksandrovskii, V. G. Manzhelii, V. B. Esel'son, and B. G.

Udovidchenko, Fiz. Nizk. Temp. **22**, 345 (1996) [Low Temp. Phys. **22**, 270 (1996)].

[14] L. D. Landau and E. M. Lifshitz, *The Theory of Elasticity*, 3rd ed., Pergamon Press, Oxford 1986.

[15] A. M. Kosevich, *Theory of Crystal Lattice* [in Russian], Vishcha Shkola, Kharkov (1988).

[16] J. D. Eshelby, in Solid State Physics, Vol. 3, p. 79 (1956); Foreign Lang. Publ. House, Moscow (1963).

[17] *Cryocrystals* (ed. by V. G. Manzhelii and Yu. A. Freiman), AIP Press (1996).

[18] B. M. Powell and G. Dolling, in *Rare Gas Solids* (ed. by M. Klein and A. J. Vanables), Academic Press, London, New York, San Francisco (1976).

[19] T. N. Antsygina and V. A. Slyusarev, Fiz. Nizk. Temp. **19**, 102 (1993) [Low Temp. Phys. **19**, 73 (1993)].

[20] T. N. Antsygina, K. A. Chishko, and V. A. Slyusarev, Phys. Rev. B55 3548 (1997).

[21] P. I. Muromtsev, M. I. Bagatskii, V. G. Manzhelii *et al.*, Fiz. Nizk. Temp. **16**, 1058 (1990) [Sov. J. Low Temp. Phys. **16**, 616 (1990)].

[22] K. Teodosiu, *Elastic Models of Crystal Defects*, Springer, Heidelberg (1982).

[23] R. Bullough, H. R. Glyde, and J. A. Venables, Phys. Rev. Lett. **17**, 249 (1966).

[24] L. Jansen, in *Modern Quantum Chemistry*, ed. by O. Sinanoğlu, Acad. Press, 1965 [Russian transl., Mir (1968)].

[25] T. Bricheno and A. J. Venables, J. Phys. **C9**, 4094 (1976).

[26] K. F. Niebel and A. J. Venables, in *Rare Gas Solids* (ed. by M. Klein and A. J. Venables), Academic Press, London, New York, San Francisco (1976).

[27] N. V. Belov, *Structure of Ionic Crystals and Metallic Phases* [in Russian], Izd. Acad. Nauk SSSR, Moscow (1947).

[28] G. Leibfried, *Microscopic Theory of Mechanical and Thermal Properties of Crystals*; (in German) Gittertheorie der mechanischen und thermischen Eigenschaften der Kristalle. Handb. der Physik, B.VIII, Teil 2. Springer-Verlag, Berlin, 1955.

Translated by R. S. Wadhwa

LOW-TEMPERATURE PHYSICS OF PLASTICITY AND STRENGTH

Jump-like deformation of single crystals of Sn−Cd alloys at temperatures ≲1 K

G. I. Kirichenko, V. D. Natsik, V. V. Pustovalov, V. P. Soldatov, and S. E. Shumilin

B. Verkin Institute for Low Temperature Physics and Engineering, National Academy of Sciences of the Ukraine, 310164 Kharkov, Ukraine

The low-temperature jump-like deformation of Sn−Cd single crystals is studied systematically for various concentrations. The effect of temperature (in the range 0.5– 4.2 K), Cd concentration (in the interval 0.01–0.53 at.%), strain, and superconducting transition on manifestations of jump-like deformation is analyzed. The obtained results are considered in the light of modern concepts about the nature of low- temperature instability. The observed basic regularities in macroscopic jump-like deformation contradict the hypothesis of thermomechanical instability. © *1997 American Institute of Physics.* [S1063-777X(97)01309-1]

1. INTRODUCTION

In the case of constant-rate deformation, the work hardening curve $P(\varepsilon)$ (P is the load and ε the strain) can have segments with a negative slope ($dP/d\varepsilon < 0$) corresponding to strains increasing upon a decrease in stress. Such a deformation is known as unstable. Repetition of instability region results in serrated yielding (jump-like deformation JLD). In some cases (phase transformations under stress, twinning, and crack formation), the physical nature of JLD can be interpreted easily. At low temperatures, serrated yielding is often observed for metals and alloys in various manifestations. The conditions for its emergence and kinetics of JLD are very sensitive to a change in the sample parameters and experimental conditions.[1,2] The nature of low-temperature JLD remains unclear. There exist several theoretical models describing low-temperature JLD. The most widely recognized models involve an increase in the probability of formation of dislocation piles in front of various obstacles as a result of a decrease in the probability of thermally activated overcoming of these obstacles[3] and thermomechanical instability in the evolution of dislocation flows, which is associated with the small thermal diffusivity of the sample (see first publications on this subject in Refs. 4–10. In some cases, the low-temperature JLD correlates with effects of localization of dislocation flows, i.e., the formation of large slip bands and constrictions in the sample. The inclusion of geometrical instability proved to be fruitful for describing such effects.[11] The increase in the role of dynamic (including inertial) effects in the dislocation flow, which is associated with a sharp decrease in phonon drag,[1,2] can be an important premise for the formation of low-temperature JLD. Experimental observations indicate a complex and diverse nature of low-temperature JLD processes, which cannot be described by one of the above- mentioned mechanisms. The attempts to explain all the manifestations of JLD completely on the basis of thermomechanical instability mechanism alone were not confirmed by modern experiments[12] and are debated in some theoretical publications.[13] It is often proposed that various manifestations of low-temperature JLD are consequences of joint operation of several simple mechanisms, e.g., the combination of dynamic effects and thermomechanical instability.[13,14]

Further progress in understanding of the nature of low-temperature JLD can be made after accumulation of systematic data on JLD manifestations in various materials, on regularities of its variation with temperature, deformation, strain rate, and doping. Such measurements in combination with a change in physical experimental conditions are of special importance. In this connection, it would be interesting to study the effect of the superconducting transition on JLD since the results of such experiments might be a serious argument in favor of a certain mechanism. It should be noted that the low- temperature JLD was studied, as a rule, for fcc metals and alloys, while bcc and hcp metals and alloys were investigated to a smaller extent since a decrease in temperature of these materials leads to the development of strain twinning initiating a specific type of JLD. In our opinion, single crystals of tin and Sn−Cd alloys are very convenient objects for studying the low-temperature JLD. In these crystals, twinning is absent for some orientations of axis of tensile stresses, and plastic deformation is controlled by the flow of dislocations through Peierls barriers.[15,16] Thus, plastic flow of tin and bcc metals is controlled by similar microscopic mechanisms, and an analysis of the low-temperature JLD in tin can give important new information to supplement the general pattern of the phenomenon.

In this paper, the low-temperature JLD of Sn−Cd alloys observed earlier in experiments on tension of these alloys at $T < 4.2$ K[17] will be analyzed in detail for the first time.

2. EXPERIMENTAL TECHNIQUE

We investigated single crystals of Sn−Cd alloys of several concentrations: 0.01, 0.04, 0.21, and 0.53 at. %. All chosen concentrations correspond to the range of solid solutions. The alloys of required concentration were obtained by alloying high-purity tin (99.9995%) with the appropriate amount of high-purity cadmium. The obtained ingots were cut into small pieces and loaded in a graphite mould in which

10 identically oriented monocrystalline samples with the size of deformable part $1.5 \times 4.5 \times 25$ mm were grown simultaneously by the modified Bridgmann method .[18] The orientation of tensile stress axis corresponded to the $\langle 110 \rangle$ direction and was favorable for slip in the system $(100)\langle 010 \rangle$. For this orientation, plasticity of pure tin[15,16] as well as of Sn–Cd alloys[17] is preserved during cooling.

Deformation was carried out in the temperature range 4.2–0.5 K on an original setup.[19] In the temperature range 4.2–1.8 K, experiments were made in gaseous ^{3}He cooled by liquid ^{4}He filling the outer helium Dewar flask, while experiments in the temperature interval 1.8–0.5 K were made in liquid ^{3}He cooled by pumping its vapor. The temperature was monitored by a gallium arsenide thermometer TSAD-4KM and according to ^{3}He saturated vapor pressure.

The experiments were made mainly for the strain rate $\dot{\varepsilon}_1 = 6.6 \cdot 10^{-5} \mathrm{s}^{-1}$, while some experiments were carried out for $\dot{\varepsilon}_1 = 6.6 \cdot 10^{-6} \mathrm{s}^{-1}$.

Below 3.7 K, pure tin undergoes a transition to the superconducting state, and the superconducting transition temperature for the low-concentration alloys under investigation is apparently close to T_c for pure tin. Consequently, we could study the effect of the superconducting transition on JLD for $T < 3.7$ K: the superconducting transition was made during deformation at a fixed temperature as a result of application and removal of a magnetic field of 35 mT, whose magnitude clearly exceeds the critical field ($H_c = 30.5$ mT for pure tin).

3. EXPERIMENTAL RESULTS

3.1. General characteristic of work hardening curves and serrated yielding

It was established earlier[15–17] that plastic flow in the slip system $(100)\langle 010 \rangle$ at $T > 4.2$ K is smooth both for single crystals of pure tin and β-tin doped with cadmium. The stress–strain curves at such temperatures have a clearly manifested yield stress. easy glide stage, and the stage of linear hardening. High-purity samples of β-tin (99.9995%) preserve smooth plastic flow upon cooling to 0.5 K also (Fig. 1). Doping of tin with Cd increases the yield stress significantly, changes its temperature dependence, and reduces the fracture strain and the length of the easy glide stage. Moreover, doping of tin with cadmium leads to a change from smooth flow to serrated yielding below 4.2 K. Typical stress–strain curves for pure tin and Sn–Cd alloys in the temperature range 4.2– 0.5 K are shown in Figs. 1 and 2. Pure tin as well as alloys with 0.01, 0.04, and 0.21 at. % Cd have a two-stage work hardening curve consisting of stage I of easy glide and stage II of linear hardening. The alloy with 0.53 at. % Cd has no easy glide stage. The strain-hardening coefficient as a function of concentration and temperature changes from 10 to 70 MPa in stage I and from 80 to 190 Mpa in stage II. No systematic regularity in the temperature dependence of the strain-hardening coefficient θ is observed (see Table I). The strain-hardening curves for the alloy with 0.53 at. % Cd have the saw-tooth shape. The coefficient θ for these curves was estimated from the upper envelope. It should also be noted that the visually observed
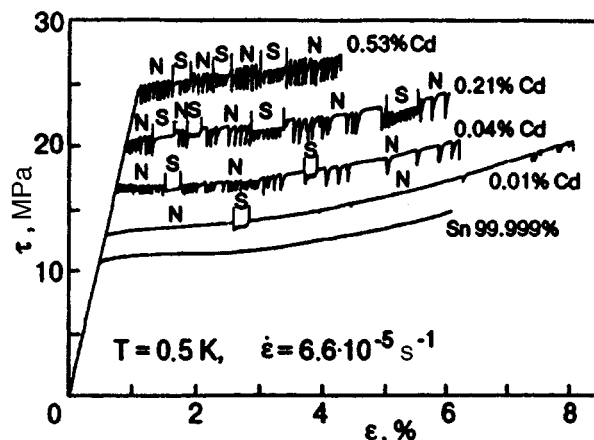

FIG. 1. Work-hardening curves for Sn–Cd alloys with various concentrations recorded under tension. The electronic states of the samples varied in the course of deformation.

deformation of the working part of pure as well as doped samples remain uniform upon heating up to fracture in the entire temperature range under investigation, and no rough traces of slip bands and ''neck'' were observed.

In addition to stress jumps with an amplitude of the order of 1–2 MPa, which are referred to as macroscopic, we managed to detect JLD with a much smaller amplitude of jumps of the order of 0.1 Mpa (see inset to Fig. 2). Such jumps are called microscopic and can be seen clearly only for the alloy with 0.21 at. % Cd at 0.5 and 2.9 K.

3.2. Effect of impurity concentration and strain on JLD

The effect of these two factors on JLD is manifested most clearly at the minimum experimental temperature 0.5 K (see Fig. 1). It can be clearly seen that as the impurity concentration increases, the stress corresponding to the onset of JLD is first displaced to the yield stress, and the amplitude of jumps increases. The microscopic JLD is manifested most clearly in the alloy with the highest impurity concentration of 0.53 at. %. Microscopic jumps observed in the alloy with 0.21 at. % Cd are of a random amplitude and are observed most often for small strains (see Fig. 3 and insets in Fig. 2).

With increasing strain, the amplitude of macroscopic jumps increases, while the amplitude of microscopic jumps remains unchanged. The lower the temperature and the higher the impurity concentration in the alloy, the smaller the strain at which first macroscopic jumps occur. The frequency of macroscopic jumps for the Sn–0.01 at. % Cd alloy increases with strain so that the regions of smooth flow between the jumps become shorter and shorter, especially at temperatures below 1 K. For alloys with a high concentration (0.04 and 0.21 at. % Cd below 1 K, the JLD in the normal state starts directly at the yield stress and immediately becomes of the saw-tooth type. It should be noted that the frequency of macroscopic jumps does not increase but decreases with increasing strain, and the segments of smooth flow appear and grow. For example, the frequency of jumps in the Sn–0.21 at. % Cd alloy at $T = 0.5$ K decreases with increasing strain from 20–25 for 1% strain near the yield stress to 2–5 at the end of the work-hardening curve. The

TABLE I. Strain-hardening coefficients θ, MPa for tin and Sn–Cd alloys at the first and second stages.

T	Sn		0.01 at. % Cd		0.04 at. % Cd		0.21 at. % Cd		0.53 at. % Cd	
	I	II	I	II	I	II	I	II	I	II
0.5	25	75	10	130	50	110	12	90	no	100
0.7	–	–	–	–	–	–	–	–	no	120
0.9	–	–	8	140	–	–	–	–	–	–
1.45	–	–	20	120	–	–	60	–	–	–
1.95	40	190	23	120	–	–	70	95	–	–
2.15	40	170	–	–	35	170	–	–	–	–
2.8	30	180	10	140	–	–	22	75	–	–
4.2	20	170	20	130	17	140	20	80	–	–

work- hardening curve for the Sn–0.53 at. % Cd alloy retains its saw-tooth shape up to fracture (see Fig. 1).

The quantitative relations between the amplitudes of macroscopic and microscopic jumps are shown in Fig. 3 presenting the dependence of these parameters on strain. Table II illustrates the dependence of the amplitude of jumps at 0.5 K on strain, concentration, and the electron state of the sample.

3.3. Effect of temperature and strain rate

With decreasing temperature, The JLD in alloys becomes more and more developed. Individual stress jumps are observed in the Sn–0.01 at. % Cd alloy at temperatures below 3 K only at the strain rate $\dot{\varepsilon}_1 = 6.6 \cdot 10^{-5} \text{s}^{-1}$. The strain corresponding to the first jump decreases at lower temperatures from 6–7% to 3–4%. The number of jumps on the work-hardening curve increases from 2–3 at $T \simeq 3$ K to 10–15 at $T = 0.5$ K. Solitary jumps are observed for the Sn–0.04 at. % Cd alloy even at $T = 4.2$ K after a plastic strain of 1–2%. Their number also increases upon cooling, and at $T < 0.8$ K they start from the yield stress. The Sn–0.21 at .% Cd alloy also behaves similarly, but the JLD in it starts near the yield stress even at 1.4 K. The effect of temperature on the form of JLD for this alloy is illustrated in

Fig. 2. The amplitude of microscopic jumps observed in the alloy of this concentration does not depend on temperature (Fig. 3). The above regularities pertain to deformation in the normal state. The peculiarities in the variation of JLD in the course of the superconducting transition will be considered below.

The JLD variations upon a transition to a lower rate $\dot{\varepsilon}_2 = 6.6 \cdot 10^{-6} \text{s}^{-1}$ were studied in the course of measurement of the strain-rate sensitivity of deforming stress, during which the strain rate decreased by an order of magnitude. In this case, comparatively small segments of the stress–strain curve were recorded. No jumps were observed, as a rule, for alloys with concentration up to 0.21 at. % Cd at $\dot{\varepsilon}_2$. Sometimes, solitary jumps were recorded below 1 K and only in the normal state. Jump-like deformation was observed for the alloy Sn–0.53 at. % Cd at the lowest experimental temperature (0.5 K) in the N- and S-states. A reliable observation of JLD under experimental conditions of strain rate cycling is possible only in the case of a saw-tooth curve since the segment corresponding to $\dot{\varepsilon}_2$ for solitary jumps can coincide in some cases with the interval between the jumps.

3.4. Effect of superconducting transition

A transition from the normal to the superconducting state in a sample under the JLD conditions leads to a considerable change in the regime of macroscopic jumps (see Figs.
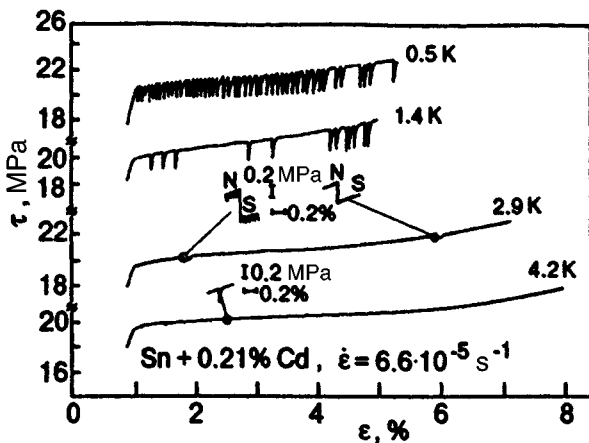

FIG. 2. Work-hardening curves for Sn–0.21 at. % Cd alloys recorded under tension at different temperatures in the normal state. Experiments at 4.2 and 2.9 K were carried out in gaseous ^{3}He and at 1.4 and 0.4 K in liquid ^{3}He. The insets show the segments of the curves on a magnified scale.
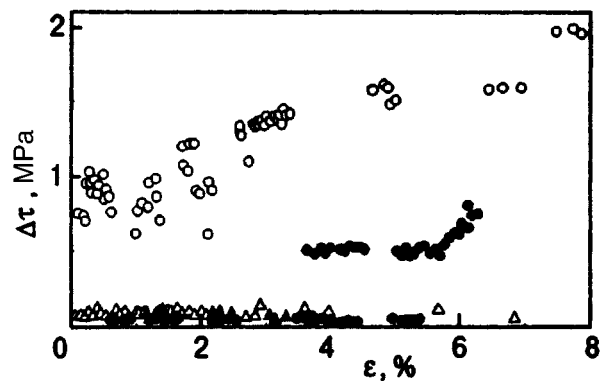

FIG. 3. Amplitude of (macroscopic and microscopic) jumps as a function of strain in the Sn–0.21 at. % Cd alloy at various temperatures, K: 2.9 (triangles) and 0.5 (circles) (light symbols correspond to the N-state and dark symbols to the S- state).

TABLE II. Typical values of the amplitude of macroscopic jumps, MPa, at $T = 0.5$ K.

C, at. %	N-State		S-State	
	low ε	near fracture	low ε	near fracture
0.01	0.25	0.8	0.1	0.25
0.04	0.7	1.5	0.15	0.35
0.21	1.0	2.0	0.5	1.3
0.53	1.5	2.3	0.8	1.4

1 and 4). It is important to note that this effect is correlated to a considerable extent with the action of such factors as strain, impurity concentration, and temperature. In the case of developed JLD as, for example, for the alloy with the highest Cd concentration, the saw-tooth form of the stress–strain curve is preserved during the $N-S$ transition at 0.5 K, but the amplitude of jumps decreases noticeably (see Fig. 1). The most complex and diverse influence of the $N-S$ transition on the nature of JLD is observed for alloys with an intermediate Cd concentration (see Figs. 1 and 4), for which the correlation between the effect of the $N-S$ transition and the strain rate of the sample is manifested clearly. The curves in Figs. 1 and 4 corresponding to the alloy Sn–0.21 at. % Cd illustrate the following facts: (a) the JLD of the sample in the normal state near the yield stress changes to a smooth flow upon a superconducting transition; (b) With increasing strain, jumps are also observed in the S state, but their amplitude is smaller; (c) the frequency of jumps for alloys with 0.04 and 0.21 at. % Cd decreases with increasing strain in the N state, and segments of smooth flow are formed (see Figs. 1 and 2). Since the regularities listed above were observed under multiple changes in the state of the sample, it would be interesting to clarify the effect of experimental conditions on JLD. In test experiments, samples were deformed in one of the states at 0.5 K (see Fig. 4). All these regularities were confirmed qualitatively. Observations of microscopic JLD on
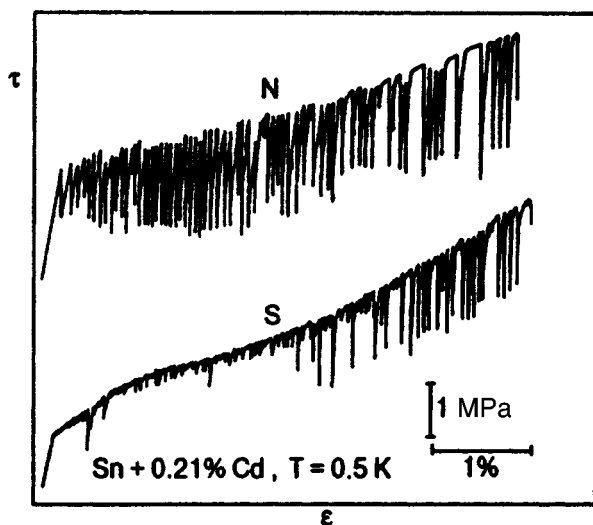
the Sn– 0.21 at. % Cd alloy revealed that it is insensitive to the $N-S$ transition at 2.9 K. Similar observations in pure form at 0.5 K are complicated in view of developed macroscopic JLD. The only thing that can be detected (see Fig. 4) is the presence of microscopic jumps at small strains in the S- state and the absence of microscopic jumps in the N-state at large strains.

3.5. Effect of cooling medium

In cases when JLD is determined by the thermomechanical instability effect, the conditions of heat removal from the sample to the cooling medium must play an important role. A considerable variation in the JLD parameters upon change in the heat-removal conditions can be regarded as an important evidence of the efficiency of the thermomechanical instability mechanism. In this connection, we made the experiments on deforming samples in various cooling media (liquid ^{4}He and gaseous ^{3}He cooled by liquid ^{4}He from outside) at 4.2 K. The experiments were made in the Sn– 0.53 at. % . Cd alloy with the most developed jump-like deformation. In both media, JLD occurs in the form of solitary jumps. Their number is small, namely, six in gaseous ^{3}He (one jump has a small amplitude) and four in liquid ^{4}He (three of these jumps have a small amplitude). A large jump was observed only before the sample fracture. Consequently, jumps occur in the gaseous cooling medium more frequently than in the liquid medium. The specific feature of the cooling technique used by us was that the experiments were carried out in the gaseous state above 2 K and in liquid ^{3}He below this temperature. But the JLD parameters depend considerably on temperature in the range ~ 2 K, and we could not notice the effect of the change of the cooling medium against the background of this dependence.

4. DISCUSSION OF RESULTS

Let us list the most significant regularities in the low-temperature macroscopic JLD for tin and compare them with the regularities of JLD in other materials as well as with predictions of existing theories. The low-temperature jump-like deformation in tin like in other metals begins below a certain temperature, e.g., below 0.5 K in pure tin, below 2–3 K in the alloy of Sn with 0.01 at. % Cd, and near 4.2 K in Sn with 0.04, 0.21, and 0.53 at. % Cd. It is important that JLD begins with the emergence of individual jumps separated by regions of smooth flow, the frequency of jumps increases only upon an increase in strain or upon cooling, and the work hardening curve acquires a saw-tooth shape. The observation of individual isolated jumps is in contradiction with the hypothesis of thermomechanical instability predicting the saw-tooth shape of strain-hardening curves. The hypothesis[20] that individual jumps are consequences of random changes in the experimental conditions (e.g., random mechanical perturbations in the deformation machine) appears as erroneous. The emergence of an individual jump on the strain-hardening curve is indeed a random event, but the average frequency of jumps is repeated from experiment to experiment and varies regularly with strain. This means that while determining the stress and strain corresponding to the
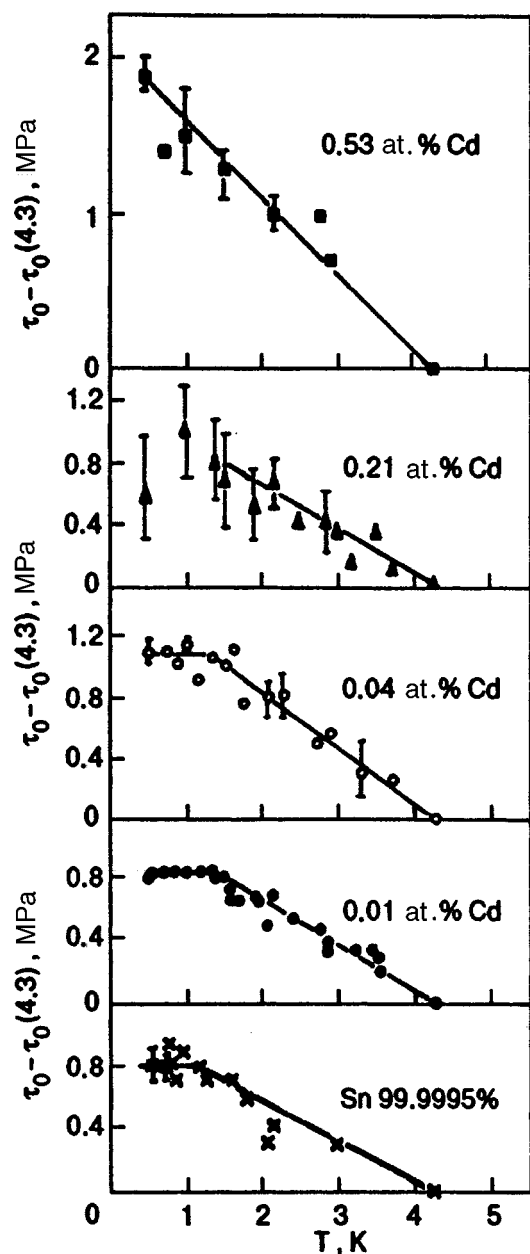

FIG. 4. Work-hardening curves for Sn–0.21 at. % Cd alloys recorded at 0.5 K under tension (N stands for the normal state and S for the superconducting state).

FIG. 5. Temperature dependences of the yield stress τ_0 for Sn–Cd alloys with various concentrations (the origin corresponds to the value of τ_0 at $T=4.3$ K).

emergence of the first jump, we must take into account individual jumps also. The opposite regularity, i.e., a transition from the saw-tooth curve to the stress–strain curve with rare jumps, was also observed in Sn–Cd alloys for the first time.

The jump-like deformation in alloys with concentrations under investigation (except those with 0.01 at. % Cd) at 0.5 K begins immediately after the yield stress. This is convenient for comparing the observed regularities with predictions of the thermomechanical model concerning the relation between the criterion for the emergence of JLD and the temperature dependence of deforming stress since in this case the role of the deforming stress is played by the yield stress $\tau_0(T)$ which can easily be measured at various temperatures. Figure 5 shows the $\tau_0(T)$ curves for pure tin and for Sn–Cd alloys in the temperature range 0.5–4.2 K. It can be clearly

seen that the $\tau_0(T)$ curve for pure tin and alloys with 0.01 and 0.04 at. % Cd has an athermal segment below 1.2–1.4 K, which can be explained by the tunneling of dislocations.[17] The spread in the experimental values of $\tau_0(T)$ observed for alloys with 0.21 at. % Cd does not allow us to determine unambiguously the type of the anomaly of τ_0 (athermal behavior or a decrease in the value of τ_0 with temperature) below 1 K. Finally, the $\tau_0(T)$ curve observed for the alloy with 0.53 at. % Cd down to 0.5 K has the shape typical of a thermally activated plastic flow: the yield stress increases with cooling. Thus, the developed jump-like deformation is observed in the temperature range 0.5–1 K (see Fig. 2) both in the case of athermal behavior of τ_0 and in the case of a strong temperature dependence of τ_0. This means that there is no one-to-one correspondence between the emergence of jump- like deformation and the form of the $\tau_0(T)$ dependence. No correlation is observed between the temperatures corresponding to the beginning of anomaly in $\tau_0(T)$ and the emergence of JLD, which exists for stainless steels.[12]

The effect of the superconducting transition on JLD can hardly be explained on the basis of the hypothesis of thermomechanical instability. An analysis of JLD in the normal and superconducting states as well as its variation in the course of the superconducting transition revealed that the macroscopic JLD is either absent in the superconducting state, or the amplitude of jumps becomes considerably smaller than in the normal state at the same temperature. This regularity is typical of a large number of other superconductors: Nb,[5] Pb–In,[21] Al,[22] Pb,[23] In–Pb,[24] Al–Mg,[25] Cu–Nb,[26] and Al–Li.[27] Consequently, such a form of the effect of the $N–S$ transition on JLD can be regarded as typical. According to the predictions of the model of thermomechanical instability, the criterion for the emergence of JLD at a constant temperature and strain rate is determined by the value of three physical parameters: thermal conductivity K, heat capacity C, and the coefficient h of heat transfer to the cooling medium. Since the value of h is independent of the electron state of the sample, the type of JLD can be affected only by changes in heat capacity and thermal conductivity. The value of C changes significantly only near T_c, while below T_c we can assume approximately that $C_S = C_N$. Consequently, the $N–S$ transition at these temperatures mainly affects JLD through a change in the thermal conductivity K. In Sn single crystals, $K_S < K_N$ in a wide temperature range below T_c.[28] No experimental data on the $K_S(T)$ and $K_N(T)$ dependences are available for Sn–Cd alloys, but similar results were obtained for Sn–In alloys,[28] and in all probability the type of the impurity is immaterial for these dependences. The variation of K during the superconducting transition studied by Geilikman and Kresin[28] on the basis of the model of thermomechanical instability indicates that jump-like deformation must be enhanced in the S state. The opposite effect is observed in experiments. It was proposed[29,30] that this can be due to the sign reversal of $d\tau_0/dT$ during the $N–S$ transition. However, the derivative $d\tau_0/dT$ preserves its sign during the $N–S$ transition for most of metals and alloys. The athermal behavior of the yield stress for the quantum plasticity of pure tin in the normal state is also preserved during the superconducting transition.[17] Thus, this assump-

tion does not remove the contradictions between the observed regularities for JLD and the predictions of the thermomechanical instability model either.

Let us compare the same regularities with the dynamic dislocation hypothesis, although this can be done only qualitatively on the basis of the model proposed by Seger.[3] According to this model, piles of dislocations are formed near obstacles during deformation. A spectrum of piles is formed due to the spectrum of obstacles existing in the sample. As the deforming stress and strain increase in the sample, high stresses emerge at the head of a pile. These stresses cannot be significantly higher than the theoretical shear strength without causing a ''catastrophic'' process such as spontaneous generation of dislocations. The jumps observed in this case form an integral effect of catastrophic processes at piles with close intensities which are distributed over the sample at random. With increasing strain, more and more powerful obstacles can be overcome, and the jump amplitude increases as a result. Such a process can take place in the form of solitary jumps or in the form of saw-tooth curve for any type of the $\tau_0(T)$ dependence. In this model the emergence of JLD does not require a decrease in deforming stress upon heating. Using modern concepts on the motion of dislocations in the normal and superconducting states,[1,2] we can predict qualitatively the possible effect of the superconducting transition on JLD. In the superconducting states, some obstacles are overcome at the expense of inertial effects due to the fact that, in contrast to the normal state, dislocations are undamped. For this reason, jumps are observed later, and their amplitude is smaller for the same strain. The experimentally observed shift in stress at the beginning of JLD towards higher values of strain and the decrease in the jump amplitude during the superconducting transition are in qualitative agreement with this conclusion (see Sec. 3.4 and Fig. 1). Thus, the observed peculiarities do not contradict the dynamic dislocation hypothesis.

In experiments with Sn–Cd alloys, jump-like deformation is not accompanied by macroscopic localization of slip, and hence the observed jumps are not manifestations of geometric instability.[11] A comparative estimation of the deforming stress τ and the strain-hardening coefficient θ supports this conclusion. At the first stage of work hardening, the value of τ is of the order of θ, while at the second state $\tau \ll \theta$, which contradicts the geometrical instability criterion.

In addition to macroscopic jumps whose amplitude was comparable to or larger than the deforming stress jump $\Delta \tau_{NS}$ during the superconducting transition, microscopic JLD whose amplitude was smaller than $\Delta \tau_{NS}$ was observed in one of the alloys (Sn–0.21 at. % Cd). Moreover, this type of JLD was found to be not very sensitive to the superconducting transition and temperature. Jump- like deformation of the same intensity was observed in In–Pb alloys in limited ranges of concentrations and temperatures.[31] However, the results obtained in Ref. 31 indicate that the superconducting transition affects significantly the course of microscopic JLD, the sign of this effect being opposite to that observed for macroscopic jumps. The ambiguous effect of concentration, temperature, and superconducting transition on microscopic JLD apparently indicates that these jumps correspond to another type of instability and have an origin differing from that of macroscopic JLD. Microscopic JLD requires a detailed experimental investigation, which is beyond the scope of this research.

5. CONCLUSIONS

(1) Monocrystalline samples of Sn–Cd alloys subjected to tension at a constant strain rate exhibit below 4.2 K a jump-like deformation with the jump amplitude of the order of 1–2 MPa, which increases upon sample cooling and an increase in the impurity concentration.

(2) The behavior of the jump-like deformation in these alloys is qualitatively similar to the behavior of JLD observed in fcc and hcp metals and alloys.

(3) The jump-like deformation is suppressed considerably as the samples go over to the superconducting state.

(4) In addition to this type of JLD, alloys with a high impurity concentration (0.21 at. % Cd) exhibit microscopic jump-like deformation with a jump amplitude of the order of 0.1 MPa and below. The behavior of such a JLD differs from the behavior of macroscopic JLD.

(5) The basic regularities of macroscopic JLD, including the presence of solitary jumps, the existence of JLD under the conditions of athermal deformation, the suppression of JLD upon a transition to the superconducting state, and the absence of localization of deformation, are in contradiction to the hypothesis of thermomechanical instability.

[1] V. I. Startsev, V. Ya. Il'ichev, and V. V. Pustovalov, *Plasticity and Strength of Metals and Alloys at Low Temperatures* [in Russian], Metallurgiya, Moscow (1975).

[2] V. I. Startsev, in *Dislocations in Solids* (ed. by F. R. N. Nabarro), North-Holland, Amsterdam (1983).

[3] A. Seger, in *Dislocations and Mechanical Properties of Crystals* [in Russian], Foreign Lang. Publ. House, Moscow (1960)

[4] Z. S. Basinski, Proc. Roy. Soc. **A240**, 229 (1957).

[5] L. P. Kubin and B. Jouffrey Philos. Mag. **24**, 437 (1971).

[6] E. Kuramoto, S. Takeuchi, and T. Suzuki J. Phys. Soc. Jpn. **34**, 1217 (1973).

[7] G. A. Malygin Phys. Status Solidi B **61**, K45 (1974)

[8] B. V. Petukhov and Yu. Z. Estrin, Fiz. Tverd. Tela (Leningrad) **17**, 2041 (1975) [Sov. Phys. Solid State **17**, 1333 (1975)].

[9] I. S. Zhitomirskii and I. N. Nechiporenko, Fiz. Nizk. Temp. **4**, 1053 (1978) [Sov. J. Low Temp. Phys. **4**, 499 (1978)].

[10] Y. Estrin and L. P. Kubin Scr. Metall. Mater. **14**, 1359 (1980).

[11] V. I. Eremin and V. D. Natsik Scr. Metall. Mater. **26**, 47 (1992).

[12] B. Obst and A. Nyilas Mater. Sci. Eng. A **137**, 141 (1991).

[13] M. Zaiser Scr. Metall. Mater. **32**, 1261 (1995).

[14] V. S. Bobrov and M. A. Lebedkin, Fiz. Tverd. Tela (St. Petersburg) **35**, 1881 (1993) [Phys. Solid State **35**, 939 (1993)].

[15] G. I. Kirichenko, V. D. Natsik, and V. P. Soldatov, Fiz. Met. Metalloved. **63**, 386 (1987).

[16] G. I. Kirichenko, V. D. Natsik, and V. P. Soldatov, Fiz. Nizk. Temp. **18**, 1270 (1992) [Sov. J. Low Temp. Phys. **18**, 887 (1992)].

[17] V. D. Natsik, G. I. Kirichenko, V. P. Pustovalov *et al.*, Fiz. Nizk. Temp. **22**, 965 (1996) [Low Temp. Phys. **22**, 740 (1996)].

[18] Y. G. Kazarov and F. F. Lavrentev Cryst. Res. Technol. **18**, 1007 (1983).

[19] I. N. Kuz'menko, V. V. Pustovalov, and S. È. Shumilin, Prib. Tekh. Éksp. **1**, 196 (1988).

[20] Y. Gröger, J. Kogout, M. A. Lebyedkin, and L. Dunin-Barkovskij, Rev. Eng. Mater. **97–98**, 251 (1994).

[21] V. V. Pustovalov, V. S. Fomenko, and Yu. I. Gofman, Preprint of Institute for Low Temperature Physics and Engineering, Kharkov (1973).

[22] I. N. Kuz'menko and V. V. Pustovalov, Fiz. Nizk. Temp **5**, 1433 (1979) [Sov. J. Low Temp. Phys. **5**, 676 (1979)].

[23] I. N. Kuz'menko and V. V. Pustovalov, Dokl. Akad. Nauk SSSR **282**, 599 (1985).

[24] I. N. Kuz'menko, S. V. Lubenets, V. V. Pustovalov, and L. S. Fomenko, Fiz. Nizk. Temp. **9**, 85 (1983) [Sov. J. Low Temp. Phys. **9**, 450 (1983)].

[25] V. V. Pustovalov and S. É. Shumilin, Fiz. Met. Metalloved. **63**, 171 (1986).

[26] M. A. Tikhonovskii, V. I. Dotsenko, I. F. Kislyak, and V. T. Petrenko, Metallofizika **8**, 73 (1986).

[27] N. V. Isaev, V. V. Pustovalov, V. S. Fomenko, and S. È. Shumilin, Fiz. Nizk. Temp. **20**, 832 (1994) [Low Temp. Phys. **20**, 640 (1994)].

[28] B. T. Geilikman and V. Z. Kresin, *Kinetic and Transient Phenomena in Superconductors* [in Russian], Nauka, Moscow (1972).

[29] G. A. Malygin, Fiz. Nizk. Temp. **12**, 849 (1986) [Sov. J. Low Temp. Phys. **12**, 481 (1986)].

[30] I. N. Nechiporenko, Fiz. Nizk. Temp. **12**, 75 (1986) [Sov. J. Low Temp. Phys. **12**, 43 (1986)].

[31] V. S. Bobrov and I. V. Vvedenskii, in *Proceeding of the 20th All- Union Conf. on Low Temperature Physics* [in Russian], Part III, Chernogolovka (1978).

Translated by R. S. Wadhwa

Acoustic emission of the HTS ceramic YBa$_2$Cu$_3$O$_{7-\delta}$ in the vicinity of the superconducting transition

P. I. Stoev, I. I. Papirov, and V. A. Finkel'

National Science Center ''Kharkov Physicotechnical Institute,'' 310108 Kharkov, Ukraine*

Acoustic emission (AE) of the HTS ceramic YBa$_2$Cu$_3$O$_{7-\delta}$ is studied under heating from liquid nitrogen temperature. For heating at a high rate, a peak in the AE activity is observed in the temperature interval 100–115 K. The parameters of the peak depend on the oxygen content in the HTS ceramic, heating rate, initial temperature to which the ceramic was cooled, and the sample thickness. The observed AE is associated with the relaxation of microscopic thermal stresses generated at the grain boundaries due to anisotropy of the thermal expansion coefficients and their anomalous behavior at these temperatures. Possible relaxation mechanisms of such stresses are the movement of dislocation groups and the formation of microcracks along the least favorably oriented grain boundaries. © *1997 American Institute of Physics.* [S1063-777X(97)01409-6]

1. INTRODUCTION

The acoustic emission (AE) technique is being used widely for studying the movement of dislocations, formation and propagation of microcracks, as well as phenomena accompanying phase transitions in solids. Soon after the discovery of high-temperature superconductivity (HTS) in 1986, several publications[1–6] were devoted to AE studies in HTS materials in a wide temperature range. Most of these publications were devoted to the HTS ceramic YBa$_2$Cu$_3$O$_{7-\delta}$. It was assumed that the processes involving the movement of dislocations, twinning, crack formation, etc., as well as the crystal structure evolution in the vicinity of the superconducting transition temperature T_c, may be responsible for AE, and studies of the latter can provide new information about the dynamic processes in HTS compounds. Unfortunately, these expectations were later belied on account of a large number of contradictions in the obtained results.

For example, the maximum AE intensity at T_c was considered[1] as a direct consequence of the superconducting transition. However, no explanation could be found for the fact that the temperature interval in which the AE peak is observed is an order of magnitude broader than the superconducting transition width. On the contrary, a joint investigation of the electrical resistance and AE of YBa$_2$Cu$_3$O$_{7-\delta}$ led to the conclusion[2,3] that the peak of the AE activity does not coincide with T_c. Studies of the thermal expansion, magnetic susceptibility, and AE of the YBa$_2$Cu$_3$O$_{7-\delta}$ ceramic[4] show that the peak of the AE activity coincides with the temperature 83K at which anomalous thermal expansion is observed, and the susceptibility jump at T_c is not accompanied by the emergence of AE signals. Some researchers (see, for example, Ref. 5) did not observe any singularities at all in the AE spectra over a wide temperature range 60–240 K. (Note that anomalies in the elastic properties, internal friction, and thermal expansion were also observed near T_c for the ceramic YBa$_2$Cu$_3$O$_{7-\delta}$.[7–13])

Thus, the question about the connection between AE and superconducting transition in HTS materials essentially remains unanswered. The present work aims at an analysis of this problem. It should be remarked at the very outset that in contrast to most of the previous investigations, we have employed a technique that allows not only the recording of overall AE intensity, i.e., the number of pulses per unit time dN/dT, but also the selection of pulses according to amplitudes. We believe that this considerably enhances the possibility of studying complex processes in the vicinity of the superconducting transition temperature.

2. EXPERIMENTAL TECHNIQUE

Samples of the HTS ceramic YBa$_2$Cu$_3$O$_{7-\delta}$ for studying AE were synthesized according to the standard ceramic technology.[14] Cylindrical samples of diameter 18 mm and height 2.5–3.5 mm were pressed from powdered ceramic YBa$_2$Cu$_3$O$_{7-\delta}$. Samples were annealed in air at 940 °C for 24 hours. Some of the samples were cooled with the furnace to room temperature at the rate of $\sim$100 °C/h. Such a thermal treatment led to an HTS YBa$_2$Cu$_3$O$_{7-\delta}$ with oxygen index $7-\delta\sim6.95$ and superconducting transition temperature $T_c\sim92.5$ K. Moreover, some samples were quenched in liquid nitrogen from temperatures 500 °C($7-\delta\sim6.8$, $T_c\sim88.5$ K), 550 °C($7-\delta\sim6.8$, $T_c\sim84.0$ K), and 940 °C ($7-\delta\sim6.28$, nonsuperconducting).[15,16] The specific gravity of the obtained YBa$_2$Cu$_3$O$_{7-\delta}$ samples was $\sim$80% of the theoretical value. The recording of AE signals was carried out on the complex M–400 which allows a recording of pulses of various amplitude over 8 channels.[17] Acoustic measurements were synchronized with the recording of the time of the experiment. The collection and preliminary analysis of the data were carried out with the help of the personal computer ''Elektronika-85.'' The following parameters of AE were used for analyzing the results: the total number of pulses N_Σ and the activity $\dot{N}_\Sigma=dN_\Sigma/dt$, as well as the number of pulses and activity for various amplitude levels (N_i and $\dot{N}_i=dN_i/dt$), and average amplitude A_{av} of AE pulses.

The piezoceramic lead zirconate titanate (TsTS–19) with fundamental resonance frequency ~ 180 kHz was used as the detector. Since noise-type AE occurs in construction elements of the detector at low temperatures, the contact between the detector and the sample was established with the help of a waveguide in the form of a quartz cylinder of diameter 11 mm and length 265 mm. The surface of contact of the sample and the waveguide were polished meticulously, and a thin layer of ''low-temperature'' silicon oil GMN–5 was applied on them (solidification of oil at low temperature was not accompanied by the emergence of AE signals).

The experiments involved cooling of the samples of the HTS $YBa_2Cu_3O_{7-\delta}$ samples in liquid nitrogen from different temperatures followed by warming up in air. The apparatus recording the AE signal was switched on simultaneously with the extraction of the sample from liquid nitrogen, i.e., with the warming up of the sample. It was found that the intensity of the AE signals and even the very existence of AE depend on the rate of heating of the samples. At low heating rates ($v < 0.1$ K/s) characteristic for warming up of samples in nitrogen vapor, there were practically no AE signals, and hence warming up of the samples was carried out in air. The rate of temperature variation was ~ 0.4–0.7 K/s.

A miniature indicator magnet, whose response (termination of repulsion from the sample) allowed a recording of the $S–N$ transition at T_c, was suspended in the vicinity of the sample. The temperature of the sample surface during heating was determined with the help of a semiconductor resistance thermometer of the type TPK (unfortunately, the results of temperature measurement are not very reliable in view of large temperature gradients).

3. DISCUSSION OF RESULTS

Characteristic temperature dependences of the AE activity during first heating from the nitrogen temperature of the HTS samples of $YBa_2Cu_3O_{7-\delta}$ with different oxygen indices (and hence different temperatures of superconducting transition) at the rate of ~ 0.5 K/s are presented in Fig. 1. It can be seen that AE signals of high intensity are recorded in the course of heating. However, the peaks on the curves $\dot{N}_\Sigma(T)$ are observed not at $T = T_c$, but at much higher temperatures 100–115 K. In this case, the temperature at which a peak appears on the dependence $\dot{N}_\Sigma(T)$ increases upon a decrease in oxygen index (or T_c). A tendency towards a decrease in the AE activity upon a decrease in the value of $7 - \delta$ is also observed. In nonsuperconducting samples with $7 - \delta \sim 6.28$, AE activity practically does not occur (weak AE signals are detected only after multiple thermal cycling of the samples).

The magnitude of AE depends significantly on the thermal past history of samples of HTS compound $YBa_2Cu_3O_{7-\delta}$, i.e., on the initial temperature before immersion of samples in liquid nitrogen (we are speaking of the second immersion). By way of an example, Fig. 2 shows the dependence $\dot{N}_\Sigma(T)$ for a $YBa_2Cu_3O_{6.8}$ sample heated to different temperatures before immersion in liquid nitrogen (as a
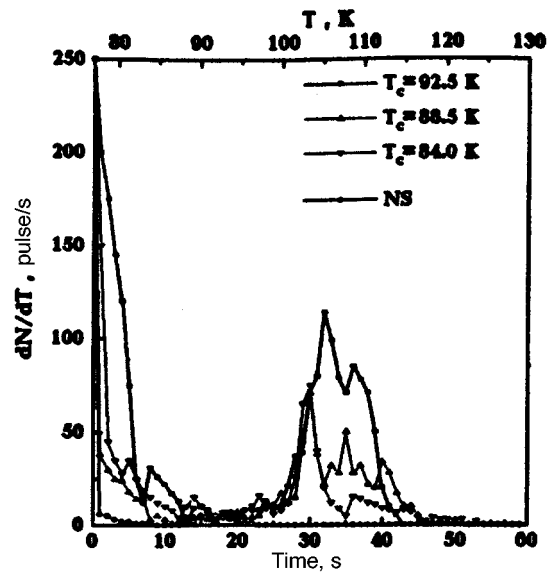

FIG. 1. Dependence of the AE activity dN/dT on time (lower scale) and warming-up temperature (upper scale) for samples with different values of T_c.

matter of fact, the time of warming up after first immersion was recorded reliably instead of the initial temperature). The following tendency was observed. In the first cycle, the AE activity for a small depth of thermal cycling is below the level $\dot{N}_\Sigma$. The AE activity increases upon an increase in initial sample temperature before immersion in liquid nitrogen, and may even exceed the AE activity level in the first cycle. As the thermal cycling depth is increased, the peak on the $\dot{N}_\Sigma(T)$ curve is displaced towards lower temperatures.

An increase in sample thickness lowers the AE activity of samples under identical conditions, and the peak on the dependence of $\dot{N}_\Sigma$ on time is displaced towards longer heat-
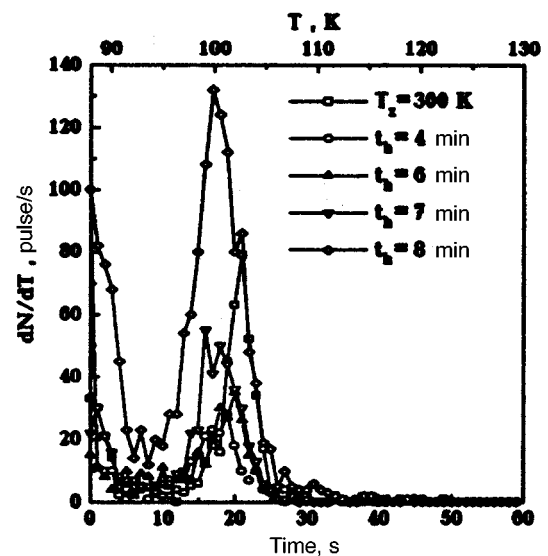

FIG. 2. Dependence of the AE activity dN/dT on time (lower scale) and warming-up temperature (upper scale) for samples ($T_c = 88.5$ K,$h = 3.5$ mm) with different past histories of thermal treatment (see text).
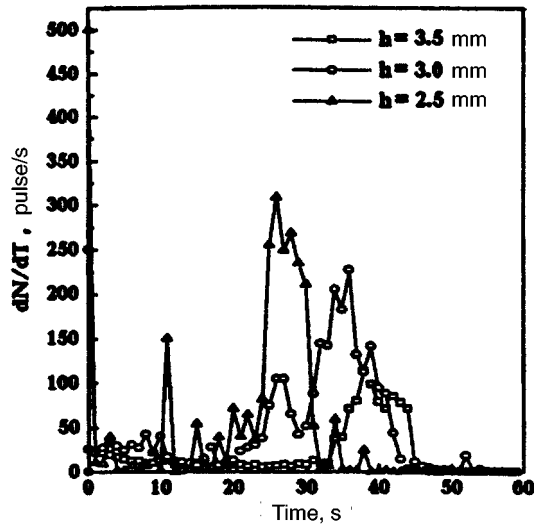
FIG. 3. Dependence of the AE activity dN/dT on warming-up time for samples with different thicknesses ($T_c = 92.5$ K.)

FIG. 4. Amplitude distribution of AE signals being recorded.

ing times (Fig. 3). Obviously, both these effects are associated with a decrease in heating rate of HTS samples upon an increase in their thickness.

The entire range of effects observed in this work, namely, the emergence of an AE peak at $T > T_c$ only for $YBa_2Cu_3O_{7-\delta}$ HTS samples with $T_c > 77$ K, dependence of AE activity and temperature localization of the peak on the $\dot{N}_\Sigma(T)$ dependence, evolution of the $\dot{N}_\Sigma(T)$ dependence upon thermal cycling, and a decrease in AE activity upon an increase in sample thickness, may be a result of the process of relaxation of thermal microstresses associated with the anisotropy of thermal expansion of rhombic HTS crystals at temperatures slightly higher than the superconducting transition temperatures. A nearly complete absence of AE in a nonsuperconducting $YBa_2Cu_3O_{7-\delta}$ sample having a tetragonal lattice (in contrast to superconducting samples which have a rhombic lattice) is quite a serious argument in favor of such an interpretation of results. However, the strong anisotropic variation of thermal expansion coefficient of the superconducting $YBa_2Cu_3O_{7-\delta}$ samples while approaching T_c from higher temperatures has been studied quite extensively (see, for example, Refs. 13 and 18). The qualitative difference in AE spectra of superconducting and nonsuperconducting $YBa_2Cu_3O_{7-\delta}$ samples and the decrease in the AE intensity upon a decrease in the oxygen index accompanied by a decrease in the rhombic distortion $(b-a)/(b+a)$ of the lattice[16] gives serious reasons for the assumption that the relaxation of thermal stresses occurs mainly in the twinning plane, viz., the basal plane (001) of the rhombic lattice of $YBa_2Cu_3O_{7-\delta}$. According to Malygin and Likhachev,[19] the level of thermal stresses σ_t in noncubic crystals upon a change in temperature by ΔT can be estimated with the help of the formula

$$\sigma_t = (\Delta\alpha/\Delta s)\,\Delta T,$$

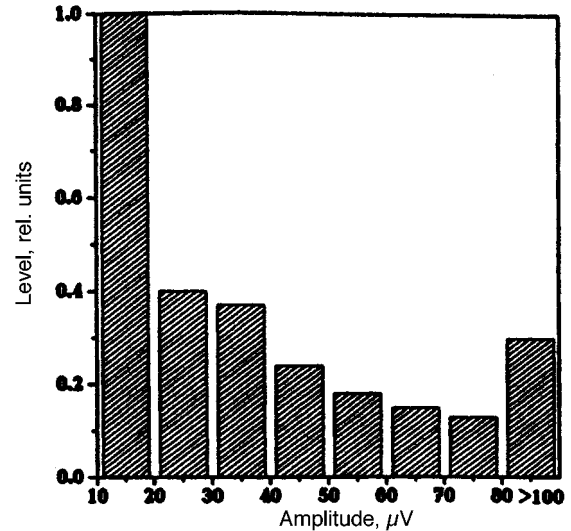where $\Delta\alpha$ is the difference between extremal values of the

coefficients of linear thermal expansion of contacting grains, and Δs is the corresponding quantity for elastic moduli of ductility.

Obviously, the existence of a strong anisotropy of thermal expansion and elastic properties of the HTS $YBa_2Cu_3O_{7-\delta}$ at temperatures exceeding T_c may lead to the growth of notable thermal stresses whose relaxation is responsible for the observed AE signals upon a rapid temperature variation (no AE signals are observed for a slow variation of temperature at a rate $v \sim 0.05$ K/s, see above).

A characteristic feature of all superconducting samples of $YBa_2Cu_3O_{7-\delta}$ under different measuring conditions is that the spectrum of amplitude distribution of AE signals has the same qualitative shape (Fig. 4): the main part of pulses is divided between two small amplitude channels and one large amplitude channel. This circumstance leads to the assumption that the relaxation of microstresses, which is caused by the movement of dislocations and leads to the emergence of AE signals at $T > T_c$, is due to two processes, one of which (low-energy process) is associated with relatively weak stresses at nearly coherent walls of structural domains, while the other (high-energy process) is associated with quite strong thermal stresses at large-angle grain boundaries of various orientations, i.e., with linear thermal expansion coefficients differing most strongly from one another. The thermal stresses for the latter process may be comparable with the ultimate strength. Indeed, multiple thermal cycling of the HTS samples of $YBa_2Cu_3O_{7-\delta}$ at high cycling rate sometimes results in a fracture of the samples. In principle, the relaxation at large-angle grain boundaries could also be observed in nonsuperconducting samples of $YBa_2Cu_3O_{7-\delta}$. but the AE for such samples is very weak in the investigated temperature range.

CONCLUSIONS

(1) The acoustic emission in the metaloxide ceramic $YBa_2Cu_3O_{7-\delta}$ is studied for various values of the oxygen index $7-\delta$ as the sample is warmed up from liquid nitrogen temperature to 130 K.

(2) For the superconducting $YBa_2Cu_3O_{7-\delta}$ samples, the AE activity peak is observed in the temperature interval 100–115K. The AE activity increases upon an increase in the heating rate and decreases upon a decrease in the oxygen index.

(3) Apparently, the behavior of AE spectra in the $YBa_2Cu_3O_{7-\delta}$ ceramic is associated with the relaxation of thermal microstresses originating at the grain boundaries as a result of anisotropy of the thermal expansion coefficients which was observed earlier in this temperature range.

(4) In nonsuperconducting samples of $YBa_2Cu_3O_{7-\delta}$, acoustic emission is practically not observed in the investigated temperature range.

*E-mail: nsc@kipt.kharkov.ua

[1] O. Yu. Serdobol'skaya and G. P. Morozova, Fiz. Tverd. Tela (Leningrad) **31**, 280 (1989) [*sic*].

[2] L. Wozny, B. Mazurek, and J. Ranachowski, Bull. Polish Acad. Sci.: Techn. Sci. **39**, 331 (1991).

[3] B. Mazurek, J. Ranachowski, and L. Wozny, Acoust. Lett. **13**, 201 (1990).

[4] E. A. Dul'kin, Sverkhprovodimost': Fiz. Khim. Tekh. **6**, 314 (1993).

[5] A. L. Gaiduk, S. V. Zherlitsyn, and V. D. Fil', Fiz. Nizk. Temp. **16**, 391 (1990) [Sov. J. Low Temp. Phys. **16**, 217 (1990)].

[6] T. J. Richardson and L. C. De Jonghe, J. Mater. Res. **5**, 2060 (1990).

[7] H. D. Jostarndt, M. Calffy, A. Freimuth, and D. Wohlleben, Solid State Commun. **69**, 911 (1989).

[8] A. L. Gaiduk, S. V. Zherlitsyn, O. R. Prikhod'ko *et al.*, Fiz. Nizk. Temp. **14**, 911 (1988) [*sic*].

[9] P. P. Pal'-Val', V. D. Natsik, and L. N. Pal'-Val', Fiz. Nizk. Temp. **15**, 1296 (1989) [*sic*].

[10] V. D. Natsik, P. P. Pal'-Val', J. Engert, and H. J. Kaufmann, Fiz. Nizk. Temp. **15**, 836 (1989) [Sov. J. Low Temp. Phys. **15**, 463 (1989)].

[11] S. Ewert, S. Guo, and P. Lemmens, Solid State Commun. **64**, 1153 (1987).

[12] S. V. Lubenets, V. D. Natsik, and L. S. Fomenko, Fiz. Nizk. Temp. **21**, 475 (1995) [Low Temp. Phys. **21**, 367 (1995)].

[13] A. I. Prokhvatilov, M. A. Strzhemechnyi, and A. P. Isakina, Fiz. Nizk. Temp. **13**, 1098 (1987) [Sov. J. Low Temp. Phys. **13**, 625 (1987)].

[14] V. N. Golovin, V. A. Finkel', A. A. Blinkin *et al.*, VANT, Ser. Vak., Chist. Mater., Sverkhprovod., No. 1, 85 (1995).

[15] V. M. Arzhavitin, A. A. Blinkin, V. V. Derevyanko *et al.*, Sverkhprovod.: Fiz., Khim., Tekh. **6**, 2095 (1993).

[16] V. A. Finkel', V. M. Arzahavitin, A. A. Blinkin *et al.*, Physica C **235– 240**, 303 (1994).

[17] I. I. Papirov, P. I. Stoev, M. B. Mileshkin, and M. I. Palatnik, Fiz. Met. Metalloved. **57**, 1037 (1984).

[18] A. S. Bulatov, V. F. Dolzhenko, V. V. Eremenko, and V. A. Finkel', Progr. HTSP **24**, 398 (1990).

[19] G. A. Malygin and V. A. Likhachev, Zav. Lab. **32**, 335 (1966).

Translated by R. S. Wadhwa

SHORT NOTES

Localized two-dimensional inhomogeneous states in elastic nematics

A. N. Bogdanov and A. A. Shestakov

A. Galkin Physicotechnical Institute, National Academy of Sciences of the Ukraine, 340114 Donetsk, Ukraine[*]

Analytic solutions of elasticity equations describing a system of localized axisymmetric inhomogeneous states (''isolated threads'') are obtained for nematic liquid crystals. Such structures are compressed into dense threads under the influence of magnetic or electric fields. It is assumed that such structures may be realized in thread-like nematic textures. This model serves as an alternative to the conventional disclination model. The localized states are found to be radially unstable in cholesterics. However, the existence of lattices with thread-like structures cannot be ruled out. © *1997 American Institute of Physics.* [S1063-777X(97)01509-0]

In the planar model for rectilinear disclinations in nematics (the directrix $\mathbf{n}(\mathbf{r})$ rotates in a plane perpendicular to the disclination axis), the solutions have divergent energy at the center and at large distances from the axis.[1] At the same time, axial disclinations with index 2 are unstable in the region of parameters corresponding to real substances.[2] (see also Ref. 3). A model in which the singularity is removed at the axis of such disclinations was considered in Refs. 4, 5. Experimental investigations reported in Refs. 1, 5 confirmed the theoretical conclusions drawn in Refs. 2–4: the inhomogeneous axial structures with index 2 have a nonsingular core. In contrast to disclinations, such structures have a continuous distribution of $\mathbf{n}(\mathbf{r})$ along the axis, but are nevertheless nonlocalized. In the present work, we shall show that the equations of the phenomenological theory of liquid crystals have localized nonsingular solutions possessing axial symmetry. Such localized stationary inhomogeneities in magnets and superconductors are called vortices (see, for example, Ref. 6). The use of such a term for liquids may cause confusion since it is associated with dynamic effects. Hence the localized two-dimensional axial inhomogeneities in liquid crystals studied here will be called threads.

Let us consider the axisymmetric distribution of the directrix for which the vector $\mathbf{n}(\mathbf{r})$ along the symmetry axis (Z) is parallel to this axis and becomes antiparallel as a result of continuous rotation along the radial directions. Unlike the disclinations considered in Refs. 1, and 5, this model describes a nonsingular localized inhomogeneity in the bulk of the liquid crystal.

In the framework of the continual theory, the possible distributions of $\mathbf{n}(\mathbf{r})$ in a thread are determined by the minimization of the elastic energy

$$W = \int w d\mathbf{x} = \int [K_1 (\text{div } \mathbf{n})^2 + K_2 (\mathbf{n} \cdot \text{curl } \mathbf{n} + q_0)^2 + K_3 (\mathbf{n} \times \text{curl } \mathbf{n})^2] dx, \qquad (1)$$

where K_i and q_0 are elastic constants.[3] For $q_0 = 0$, formula (1) describes the energy of a nematic, while for $q_0 \neq 0$, it describes the energy of a cholesteric. The absolute minimum of the system corresponds to the solutions for which the potential (1) vanishes. For a nematic, this is a homogeneous state, while for a cholesteric it is helicoidal structure.[3] Obviously, other distributions of $\mathbf{n}(\mathbf{r})$ minimizing the functional of energy may correspond to local minima, i.e., they describe metastable states.

Introducing cylindrical coordinates $\mathbf{R} = (\rho, \varphi, z)$ for the spatial variable and spherical coordinates ($\mathbf{n} = (\sin\theta\cos\psi, \sin\theta\sin\psi, \cos\theta)$), it can be shown that for states that are homogeneous in z, the variational problem for the functional (1) has axisymmetric solutions of the type $\psi = \psi(\varphi)$, $\theta = \theta(\rho)$. Subsequent calculations show that both for nematics and cholesterics, the solutions $\psi = \varphi + \pi/2$ corresponding to zero divergence are among the solutions minimizing the energy of the system. In the present work, we shall confine ourselves to the analysis of these solutions.

Substituting $\psi = \varphi + \pi/2$ into (1) and integrating the energy with respect to φ and z, we obtain

$$W = \pi L K_2 \int w\rho d\rho = \pi L K_2 \int \left[\left(\frac{d\theta}{d\rho} + \frac{\sin\theta\cos\theta}{\rho} + q_0 \right)^2 + k \frac{\sin^4\theta}{\rho^2} \right] \rho d\rho, \qquad (2)$$

where $k = K_3/K_2$ is the ratio of elastic constants of longitudinal bending (K_3) and torsion (K_2), and L is the length of a thread. It is assumed in formula (2) that $\theta(0) = 0$ along the thread axis, and the vector $\mathbf{n}$ becomes antiparallel at a distance R from the axis where $\theta(R) = \pi$. In particular, formula (2) corresponds to the energy of an isolated thread for $R = \infty$. For the functional (2), the Euler equation

$$\frac{d^2\theta}{d\rho^2} + \frac{1}{\rho}\frac{d\theta}{d\rho} - \frac{\sin 4\theta}{4\rho^2} - k\frac{\sin^2\theta\sin 2\theta}{\rho^2} + 2q_0\frac{\sin^2\theta}{\rho} = 0, \qquad (3)$$

with boundary conditions $\theta(0) = 0$, $\theta(R) = \pi$ describes the distribution $\mathbf{n}(\mathbf{r})$ in the thread.
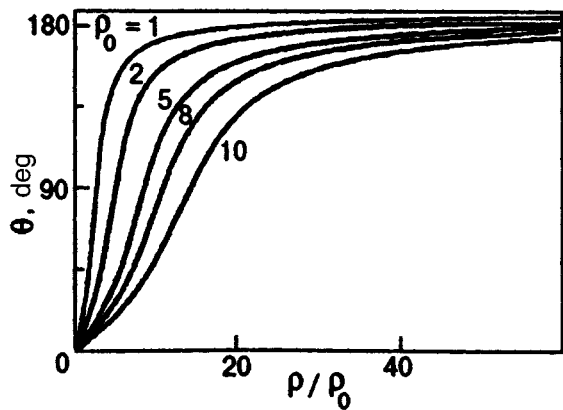
FIG. 1. Dependence of θ on ρ/ρ_0 for $k=4$ and different values of ρ_0.

For isolated threads ($R=\infty$) in a nematic ($q_0=0$), for example, multiplication of Eq. (3) by $\rho^2(d\theta/d\rho)$ and integration with respect to ρ gives the first integral

$$\left(\rho\,\frac{d\theta}{d\rho}\right)^2 = \sin^2\theta[1+(k-1)\sin^2\theta]. \qquad (4)$$

This equation can be integrated in elementary functions

$$\tan\theta = \frac{2(\rho/\rho_0)}{1-k(\rho/\rho_0)^2}, \qquad (5)$$

where ρ_0 is an arbitrary positive number defining the characteristic size of the core of a thread. For small ρ, the angle $\theta\sim\rho$, while for $\rho\to\infty$ the angular variable changes according to the law $\theta\sim\pi-1/\rho$. In the one-constant approximation ($k=1$), formula (5) coincides with the solution for a vortex in an isotropic ferromagnet;[7] for $k\to0$, a singularity is formed in the region $\theta\approx\pi/2$ and for $k=0$ formula (5) is transformed into the expression $\tan\theta=2\rho/\rho_0$ describing a structure in which **n** is turned through $\pi/2$.

For fixed values of k, the solutions of Eq. (5) are a family of functions of the type $\theta(\rho/\rho_0)$. Figure 1 shows the functions $\theta(\rho/\rho_0)$ (5) for $k=4$ (in the thoroughly investigated nematic n-azoxyanizol, the parameter $k=3.95$), ρ_0 varying from 1 to 10. The existence of solutions of the type (5) is a consequence of the invariance of the nematic energy (2) relative to the radial extension $\rho_0>1$ or compression $0<\rho_0<1$ of functions $\theta(\rho)$. Thus, the vortex states obtained for the nematic are ''amorphous'': for a fixed value, the energy (2) of the structure remains constant for an arbitrary radial compression or extension of the profile $\theta(\rho)$.

However, the energy of interaction of a nematic with the magnetic field $\mathbf{H}(\Delta w_H=0.5\Delta\chi H^2\sin^2\theta)$ or the electric field $\Delta w_E=0.5\Delta\varepsilon H^2\sin^2\theta)$ (where $\Delta\chi$ and $\Delta\varepsilon$ are the diamagnetic and dielectric anisotropy respectively) is of quite different type: for scale transformations of the type $\rho\to\rho/\rho_0$ for the functions $\theta(\rho)$, the energies Δw_H and Δw_E are proportional to ρ_0^2. It follows hence that the threads in nematics experience radial instability in a magnetic or electric field. In all known nematics, $\Delta\chi>0$, and hence the energy minimum in a magnetic field is attained for $\rho_0=0$. This means that in a

magnetic field, the axial lines being investigated will be compressed. In the ideal model being considered here, this is a thresholdless process, and even an indefinitely weak magnetic field (e.g., the magnetic field of the Earth) leads to a collapse of the threadlike structures and to the formation of dense localized structures in which the separation between molecules are comparable with their size. It can be assumed that ''black threads'' in filamentary nematic structures are just such formations.

For many years, threadlike textures (which led to the term nematic) as well as other inhomogeneous states in nematics were interpreted on the basis of the disclination theory.[3] However, following the theoretical prediction of axial structures with a continuous core,[4,5] they were detected among inhomogeneous states of schlieren textures.[5]

A similar meticulous analysis of threadlike textures could provide an answer to the question whether these textures contain localized axial structures described in this work.

The energy associated with the structure (5) is calculated by substituting the solution (5) into (2), and has the following form:

$$\frac{E_V}{2\pi K_2 L}$$

$$=\begin{cases} 1+\dfrac{k}{2(1-k)^{1/2}}\ln\dfrac{1+(1-k)^{1/2}}{1-(1-k)^{1/2}}, & 0<k<1, \\[3mm] 1+\dfrac{k}{(k-1)^{1/2}}\arcsin\left(\dfrac{k-1}{k}\right)^{1/2}, & k>1. \end{cases}$$

Both these expressions are identical for $k=1$, while for $k\to0$ the vortex energy tends to the value $2\pi K_2 L$, i.e., half its energy in the one-constant approximation. For large k, the energy of a thread is proportional to $\sqrt{K_2 K_3}$.

In order to analyze the lattices formed by threads in liquid crystals, we can use the circular cell model.[8,9] In this approximation, the unit cell of a lattice with hexagonal (or square) cross-section is replaced by a circular cylinder of the same volume. In this case, the calculation of the lattice structure involves the integration of Eq. (3) followed by minimization of the lattice energy density $w=W/(\pi R)^2$ in R (the
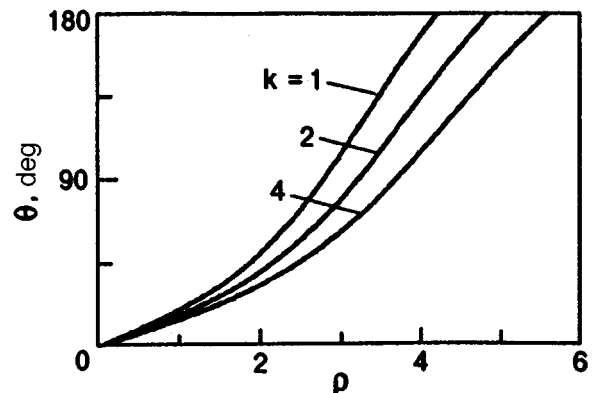

FIG. 2. Calculated values of optimal profiles for different k.

A. N. Bogdanov and A. A. Shestakov   770

energy W is define by formula (2)). Thus the solutions of Eq. (3) with a finite radius correspond to the vortex lattice. It turns out that such solutions exist only for cholesterics. The procedure of numerical solution of an equation of the type (3) was discussed in detail in Ref. 9. Figure 2 shows the results of numerical computation of optimal profiles for several values of k. The equilibrium size R_0 of the lattice increases monotonically with k. For $k=1$, the energy minimum is attained for $R_0 = 4.32 \, q_0^{-1}$, while for $k=4$ the minimum is attained for $R_0 = 5.27 \, q_0^{-1}$. For comparison, it can be mentioned that the period of helicoidal structure in a cholesteric is $L_0 = 2 \pi q_0^{-1}$.[3]

*E-mail: bogdanov@host.dipt.donetsk.ua

[1] I. E. Dzyaloshinskii, Zh. Éksp. Teor. Fiz. **58**, 1443 (1970) [Sov. Phys. JETP **31**, 773 (1970)].

[2] S. I. Anisimov and I. E. Dzyaloshinskii, Zh. Éksp. Teor. Fiz. **61**, 2140 (1972) [Sov. Phys. JETP **36**, 1140 (1972)].

[3] P. de Gennes, *The Physics of Liquid Crystals*, Clarendon Press, Oxford (1974).

[4] P. E. Cladis and M. Kleman, J. Phys. **33**, 591 (1972).

[5] R. B. Meyer, Phil. Mag. **27**, 403 (1973).

[6] A. M. Kosevich, B. A. Ivanov, and A. S. Kovalev, *Nonlinear Magnetization Waves. Dynamic and Topological Solitons* [in Russian], Naukova Dumka, Kiev (1983).

[7] A. A. Belavin and A. M. Polyakov, Pis'ma Zh. Éksp. Teor. Fiz. **22**, 503 (1975) [JETP Lett. **22**, 245 (1975)].

[8] A. Hubert, *Theorie der Domainwande in geodeneten Medien*, Springer, Heidelberg, (1974).

[9] A. N. Bogdanov and A. Hubert, JMMM, **138**, 255 (1994).

Translated by R. S. Wadhwa

Attenuation of phonon–ripplon oscillations in an electron crystal over superfluid ³He–⁴He solutions

V. V. Dotsenko, V. E. Sivokon', Yu. Z. Kovdrya, and V. N. Grigor'ev

B. Verkin Institute for Low Temperature Physics and Engineering, National Academy of Sciences of the Ukraine, 310164 Kharkov, Ukraine[*]

The phonon–ripplon oscillation spectrum of a Wigner crystal with a surface density $1.3 \cdot 10^9$ cm^{-2} of electrons over superfluid ⁴He and ³He–⁴He solutions is studied in the temperature range 70–600 mK. Measurements were made in the frequency range 1–20 MHz. It is shown that resonance frequencies are in good agreement with the theoretical estimates. An analysis of the data shows that the attenuation of capillary waves is not the main mechanism determining the energy losses in a Wigner crystal. A new technique employing the width of the coupled phonon–ripplon resonances is used to determine the mobility of Wigner crystals. © *1997 American Institute of Physics.* [S1063-777X(97)01609-5]

The two-dimensional Wigner solid (WS) discovered first by Grimes and Adams[1] over liquid helium is interesting not only as a model of two-dimensional solids with Coulomb interaction, but also from the point of view of interaction with the surface of a superfluid liquid. Under certain conditions, coupled phonon–ripplon oscillations may be excited in a WS, their characteristics depending on the properties of the WS as well as of the liquid surface. An analysis of such oscillations can provide information about the surface properties of a superfluid liquid. For example, the surface tension of ³He–⁴He solutions can be determined from the position of the resonance frequencies of the oscillations of this type.[2] The width of the coupled phonon- ripplon oscillations, which carries information about the WS mobility and dissipative processes at the liquid surface, was first measured by us over a wide range of temperatures[3] but was not analyzed in detail.

In this work, the spectrum of coupled phonon-ripplon modes of a Wigner crystal with the surface density $n_s = 1.3 \cdot 10^9$ cm^{-2} of electrons over ³He–⁴He solutions containing up to 0.25% ³He is studied in the temperature range 70–600 mK. We measured the response of the experimental cell containing liquid helium surface charged with electrons to a rf signal of amplitude 1 mV in the frequency range 1–20 MHz. The experimental technique and the measuring cell are described in detail in Ref. 4.

The results of measurements for a crystal with $n_s = 1.3 \cdot 10^9$ cm^{-2} at a temperature 78 mK are presented in the inset to Fig. 1 in the form of the frequency dependence of the response amplitude. The points correspond to the measured quantities, and the curves are the result of approximation of the experimental data as the sum of two Lorentzian curves. Series 1 corresponds to pure ⁴He, and series 2 to ³He–⁴He solutions containing up to 0.25% ³He. The results for ³He–⁴He solutions with a lower concentration (0.025%) of ³He are identical with the results for pure ⁴He within the limits of the experimental error. Both curves clearly reveal peaks corresponding to the excitation of coupled phonon–ripplon modes in the cell with different wave vectors depending on the size of the cell. It can be seen that the resonance frequencies for the solution are lower than for pure

⁴He. As the temperature increases, the resonance frequencies for pure ⁴He as well as solutions are displaced towards higher values. It is also important to note that the resonance signal amplitude is smaller for solutions than for ⁴He, while the resonance width is larger. Figure 1 shows the temperature dependences of the width Δf of the observed resonances. It can be seen from the figure that the line width increases sharply with temperature. The dependence of Δf on T is nearly linear for pure ⁴He as well as for solutions. The experiment did not reveal any frequency dependence of the quantity Δf whose value is found to be the same for first and second harmonics.

An analysis of the obtained results is carried out by using the expression for the conductance G of the experimental cell.[4] The real and imaginary parts of the conductance are defined by the following expressions:

$$\text{Re } G = n_s e^2 \sum_{n=1}^{\infty} A_n \frac{n_s e^2 \omega^2 \chi_1}{(m\omega_p^2 - n_s e^2 \omega \chi_2)^2 + (n_s e^2 \omega \chi_1)^2},$$

$$\text{Im } G = \omega \left(n_s e^2 \sum_{n=1}^{\infty} A_n \frac{m\omega_p^2 - n_s e^2 \omega \chi_2}{(m\omega_p^2 - n_s e^2 \omega \chi_2)^2 + (n_s e^2 \omega \chi_1)^2} + g_0 \right). \tag{1}$$

The quantity χ_2 reflects the dynamic characteristics of a Wigner crystal while χ_1 reflects the dissipative characteristics, ω_p are the eigenfrequencies of plasma oscillations, A_n are coefficients depending on the geometrical size of the cell, and g_0 defines the current through the cell in the absence of electrons.

It was shown by Monarkha[5] that the response of a Wigner crystal to a rapidly varying electric field can be described by the dimensionless function Z_1 which depends on the characteristics of the crystal as well as on the intensity of coupling of electrons with ripplons at the surface of the superfluid helium:
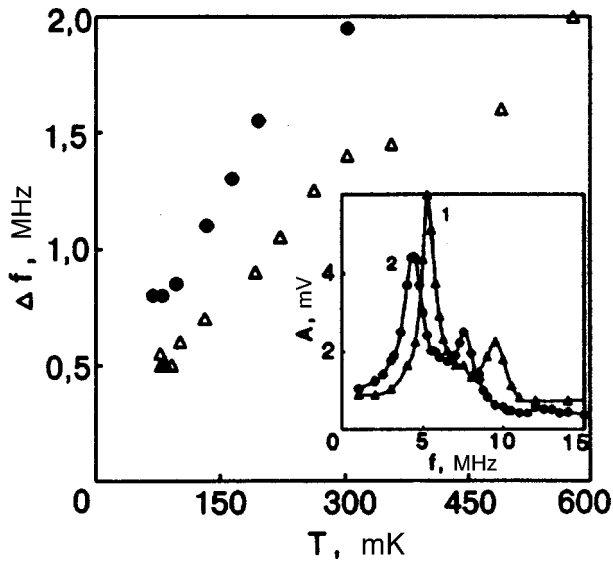
FIG. 1. Temperature dependence of the width of coupled phonon–ripplon resonances for ^{4}He ($\triangle$) and ^{3}He–^{4}He solution ($\bullet$). The inset shows by way of example the experimental dependence of the signal amplitude on frequency.

FIG. 2. Temperature dependence of the mobility of a Wigner crystal over ^{4}He ($\triangle$), ^{3}He–^{4}He solution ($\bullet$), and data from Ref. 8 ($\blacksquare$).

$$\operatorname{Re} Z_1 = \sum_{l=1}^{\infty} C_l \frac{\omega_l^2(\omega^2 - \omega_l^2 + 4\gamma_l^2)}{(\omega^2 - \omega_l^2)^2 + 4\omega^2\gamma_l^2} - 1,$$

$$\operatorname{Im} Z_1 = \sum_{l=1}^{\infty} C_l \frac{2\gamma_l}{\omega} \frac{\omega_l^4}{(\omega^2 - \omega_l^2)^2 + 4\omega^2\gamma_l^2}. \qquad (2)$$

The coefficient C_l characterizes the intensity of coupling of electrons with ripplons, ω_l are the resonance frequencies of capillary waves excited by the electron lattice and corresponding to reciprocal lattice vectors, and γ_l is the coefficient of attenuation of capillary waves with frequency ω_l. Formulas (2) were obtained in the range of applicability of bulk hydrodynamics. It was shown in Ref. 5 that the real part of Z_1 describes the dynamic properties of a Wigner crystal and defines the resonance frequencies of the capillary waves being excited while the imaginary part of Z_1 determines the absorption. Accordingly, χ_1 and χ_2 can be represented in the form

$$\chi_1 = \frac{m\omega}{ne^2} \operatorname{Im} Z_1, \quad \chi_2 = -\frac{m\omega}{ne^2} \operatorname{Re} Z_1. \qquad (3)$$

Formulas (1)–(3) can be used to calculate the signal amplitude at the outlet of the measuring cell which is proportional to $|D| = \sqrt{(\operatorname{Re} G)^2 + (\operatorname{Im} G)^2}$, while a comparison of the frequency dependence of the amplitude in the resonance region with the experimental measured quantities allows us to verify the theoretical estimates. As a result, it was found that the position of resonances defined by the quantity χ_2 from (3) corresponds with a sufficiently high precision to the experimental results in the entire temperature range. The value of the coefficient was obtained by interpolation of the data from Ref. 6. The peak width mainly depends on the quantity χ_1 from (3) which is defined, according to Monarkha,[5] by the attenuation γ_l (2) of capillary waves. The damping factor of capillary waves was measured by Roche et al.[7] The ex-
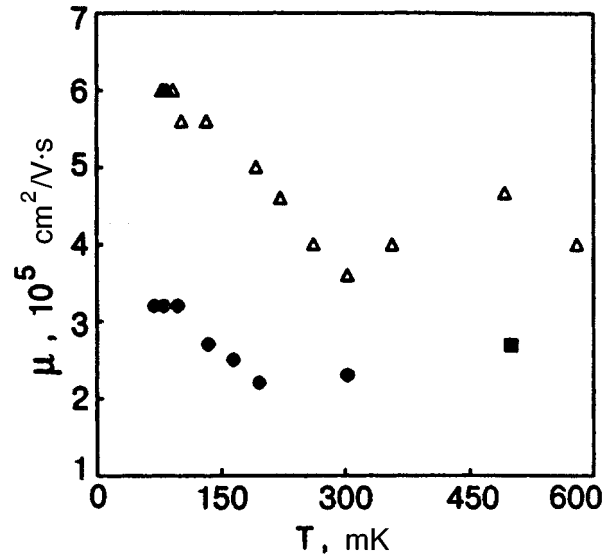
perimental data obtained by them were extrapolated to the region of wave vectors corresponding to the conditions of our experiment ($g \sim 10^5$). Substitution of the value of γ obtained in this way into $|G|$ gives the value $\Delta f \approx 8.5$ kHz for the resonance width which is two orders of magnitude lower than the experimentally observed value. Assuming that the damping factor of capillary waves is determined by surface hydrodynamics, the expressions for Z_1 are modified.[5] In this case, the estimates obtained as a result of an analogous substitution of γ from Ref. 7 also lead to results that are much lower than the experimental value.

Since both bulk and surface hydrodynamics fail to provide a satisfactory interpretation of the experimental data, it can be concluded that the attenuation of capillary waves is not the principal mechanism responsible for energy losses occurring during the movement of WS. However, it can be stated quite authentically that the line width determined in our experiments is mainly associated with dissipative processes. This is confirmed by a good correlation with the mobility data.

The phonon-ripplon resonance width can be connected with the mobility μ of a Wigner crystal by using the relation

$$\chi_1 = (n_s e \mu)^{-1} \qquad (4)$$

and defining χ_1 as a parameter in (1)–(3) for which the width of the resonance curve coincides with the experimentally measured value. The crystal mobilities obtained in this way over ^{4}He and over ^{3}He–^{4}He solution are presented in Fig. 2 as a function of temperature. It can be seen that a decrease in temperature slightly increases the mobility for pure ^{4}He as well as for the solution. Addition of ^{3}He noticeably decreases the mobility. The same figure also shows the mobility of a Wigner crystal measured by Mehrotra et al.[8] over pure ^{4}He for an electron density $9.5 \cdot 10^8$ cm^{-2} (the melting point of the crystal is 0.69 K).

It can be seen that our results are in good agreement with the data obtained in Ref. 8, which confirms the validity of the

procedure used by us for determining the mobility from the width of coupled phonon–ripplon resonances. Thus, we have shown that the attenuation of capillary waves is not the main mechanism determining the energy losses in the phonon-ripplon oscillations of a Wigner crystal. The new technique using the width of the coupled phonon-ripplon oscillations is used for determining the mobility of a Wigner crystal over liquid helium and over ^{3}He–^{4}He solutions.

*E-mail: dotsenko@ilt.kharkov.ua

[1] C. C. Grimes and G. Adams, Phys. Rev. Lett. **42**, 795 (1979).
[2] G. Deville, J. Low Temp. Phys. **72**, 135 (1988).
[3] V. E. Sivokon', V. V. Dotsenko, Yu. Z. Kovdrya, and V. N. Grigor'ev, Fiz. Nizk. Temp. **22**, 1107 (1996) [Low Temp. Phys. **22**, 845 (1996)].
[4] V. E. Sivokon', V. V. Dotsenko, S. S. Sokolov, and Yu. Z. Kovdrya, and V. N. Grigor'ev, Fiz. Nizk. Temp. **22**, 715 (1996) [Low Temp. Phys. **22**, 549 (1996)].
[5] Yu. P. Monarkha, Fiz. Nizk. Temp. **6**, 685 (1980) [Sov. J. Low Temp. Phys. **6**, 331 (1980)].
[6] D. O. Edvards and W. F. Saam, Progr. Low Temp. Phys. **VIIa**, 283 (1978).
[7] P. Roche, G. Deville, K. O. Keshishev et al., Phys. Rev. Lett. **75**, 3316 (1995).
[8] R. Mehrotra, C. J. Guo, Y. Z. Ruan et al., Phys. Rev. Lett. **29**, 5239 (1984).

Translated by R. S. Wadhwa

774   Low Temp. Phys. **23** (9), September 1997

Dotsenko et al.   774

ERRATA

Erratum: Hamiltonian description of the motion of discontinuity surfaces [Low Temp. Physics 23, 89–95 (January 1997)]

A. V. Kats and V. M. Kontorovich

[S1063-777X(97)01709-X]

The following corrections were reported by the authors:

Printed	Should read	
dr	$d\vec{r}$	p. 89, formula (4)
simplis	simplest	p. 90 left, line 5 from the top
$\rho =$	$p =$	p. 90 left, below line 19 from the top
$(v\nabla)$	$(\vec{v}\nabla)$	p. 91 left, over line 9 from the bottom
$\vec{\xi}$	$\dot{\vec{\xi}}$	p. 91, formula (20)
(2)	(20)	p. 91 right, line 12 from the top
$\vec{\mu}(\vec{r},t)=0$	$\vec{\mu}(\vec{r},0)=\vec{r}$	p. 91 right, line 19 from the top
$\vec{\xi}\vert_{\vec{r}}$	$\dot{\vec{\xi}}\vert_{\vec{r}}$	p. 91, formula (23)
$\vec{\lambda}$	$\dot{\vec{\lambda}}$	p. 91, formula (26)
$\vert J'_c\vert$	$[J'_c]$	p. 92 right, line 7 from the top
$[\rho\vec{v}']$	$[\rho v'_n]$	p. 92, formula (37)
$\vec{v}'=\vec{v}-u$	$\vec{v}'=\vec{v}-\vec{u}$	p. 92, formula (39)
$\dot{R}+u\nabla R$	$\dot{R}+\vec{u}\nabla R$	p. 92, formula (40)
$n\nabla_\tau$	$\vec{n}\nabla_\tau$	p. 94, formula (62)
$[j_{\vec{\mu}}]=[j_{\vec{\lambda}/\rho}]=$	$[\vec{j}_{\vec{\mu}}]=[\vec{j}_{\vec{\lambda}/\rho}]=$	p. 94, formula (63)
$j_{\vec{\mu}}\equiv$	$\vec{j}_{\vec{\mu}}\equiv$	p. 94, formula (63)
$j_{\vec{\lambda}/\rho}\equiv$	$\vec{j}_{\vec{\lambda}/\rho}\equiv$	p. 94, formula (63)

Erratum: Noncollinear spin configuration induced by a magnetic field in the surface gadolinium layer of multilayered Gd/Fe films [Low Temp. Physics 23, 346–348 (April 1997)]

S. L. Gnatchenko, A. B. Chizhik, D. N. Merenkov, V. V. Eremenko, H. Szymczak, R. Szymczak, K. Fronc, and R. Zuberek

[S1063-777X(97)01809-4]

The following corrections were reported by the authors:

Printed	Should read	
ferromagnetically	ferrimagnetically	p. 346, left, line 3 from top
moments of Gd layers	moments of other Gd layers	p. 346, left, line 9 from bottom
layers	layer	p. 346, left, line 4 from bottom
in the case of magnetization of the film with p-polarization	during magnetization of the film in the case of the p-polarization	p. 346, right, line 14 from bottom
with the distance	with decreasing of the distance	p. 347, right, line 15 from bottom